



**HAL**  
open science

# Croissance par épitaxie par jets moléculaires d'hétérostructures BiSb/MnGa pour l'étude de la conversion d'un courant de charge en courant de spin

Diana She

► **To cite this version:**

Diana She. Croissance par épitaxie par jets moléculaires d'hétérostructures BiSb/MnGa pour l'étude de la conversion d'un courant de charge en courant de spin. Materials Science [cond-mat.mtrl-sci]. Université Paris-Saclay, 2024. English. NNT : 2024UPASP003 . tel-04585881

**HAL Id: tel-04585881**

**<https://theses.hal.science/tel-04585881>**

Submitted on 23 May 2024

**HAL** is a multi-disciplinary open access archive for the deposit and dissemination of scientific research documents, whether they are published or not. The documents may come from teaching and research institutions in France or abroad, or from public or private research centers.

L'archive ouverte pluridisciplinaire **HAL**, est destinée au dépôt et à la diffusion de documents scientifiques de niveau recherche, publiés ou non, émanant des établissements d'enseignement et de recherche français ou étrangers, des laboratoires publics ou privés.

# Molecular beam epitaxy growth of the BiSb/MnGa heterostructures for the charge current to spin current conversion study

*Croissance par épitaxie par jets moléculaires d'hétérostructures BiSb/MnGa  
pour l'étude de la conversion d'un courant de charge en courant de spin*

## Thèse de doctorat de l'université Paris-Saclay

École doctorale n° 564, Physique en Ile-de-France (EDPIF)  
Spécialité de doctorat : Physique  
Graduate School : Physique. Référent : Faculté des sciences d'Orsay

Thèse préparée dans les unités de recherche : **Laboratoire Albert Fert (Université  
Paris-Saclay, CNRS, Thales),  
Centre de Nanosciences et de Nanotechnologies (Université Paris-Saclay, CNRS),  
Synchrotron SOLEIL (Université Paris-Saclay)**

sous la direction de **Jean-Marie GEORGE**, directeur de recherche,  
la co-direction de **Aristide LEMAITRE**, directeur de recherche,  
le co-encadrement de **Patrick LE FEVRE**, chargé de recherche

Thèse soutenue à Paris-Saclay, le 24 janvier 2024, par

**Diana SHE**

## Composition du Jury

Membres du jury avec voix délibérative

### Alexandra MOUGIN

Directrice de recherche, LPS, Présidente  
Université Paris-Saclay

### Daniel LACOUR

Directeur de recherche, IJL, Rapporteur & Examineur  
Université de Lorraine

### Lisa MICHEZ

Maître de conférence, HDR, CINaM, Rapporteur & Examinatrice  
Aix-Marseille Université

### Sébastien PLISSARD

Chargé de recherche, LAAS, Examineur  
Université de Toulouse

**Titre :** Croissance par épitaxie par jets moléculaires d'hétérostructures BiSb/MnGa pour l'étude de la conversion d'un courant de charge en courant de spin

**Mots clés :** Isolant topologique, épitaxie par jets moléculaires, conversion spin-charge, spin-orbit torque, ARPES, spectroscopie térahertz

**Résumé :** Récemment, les isolants topologiques (TI) ont attiré beaucoup d'attention en raison de leurs propriétés prometteuses potentiellement utiles pour les technologies émergentes, telles que la mémoire MRAM. En effet, les systèmes TI/ferromagnétiques (FM) peuvent réduire considérablement le courant d'écriture en utilisant le renversement par couple spin-orbite (SOT) comme méthode d'écriture. Cet avantage découle de l'utilisation des états de surface topologiques polarisés en spin des TI. Dans ce travail, notre objectif était de faire croître des hétérostructures TI/FM par épitaxie par jets moléculaires (MBE), de réaliser une caractérisation complète des propriétés structurales, magnétiques et électroniques, et d'étudier leurs propriétés de conversion spin-charge.

Nous avons développé une hétérostructure  $\text{Bi}_{1-x}\text{Sb}_x$  (TI)/  $\text{Mn}_x\text{Ga}_{1-x}$  (FM)//GaAs(001) de haute qualité par MBE, malgré la différence de symétrie cristalline. Les films minces FM de  $\text{Mn}_x\text{Ga}_{1-x}$  présentent une anisotropie magnétique perpendiculaire, un champ coercitif faible, une température de Curie élevée, un cycle d'hystérésis carré et une résistivité suffisamment élevée. Cela garantit que la majorité du courant circule à travers la couche  $\text{Bi}_{1-x}\text{Sb}_x$  pendant les expériences SOT. Les mesures SOT suggèrent que les états de volume de  $\text{Bi}_{1-x}\text{Sb}_x$  contribuent principalement aux propriétés de transport. Cependant, nous avons démontré la présence d'états de surface topologiques par ARPES. Ainsi, les états de volume et de surface peuvent coexister. De plus, les résultats préliminaires de la spectroscopie térahertz ont montré une conversion efficace du spin en charge dans la bicouche étudiée, démontrant un potentiel prometteur. En conséquence, nos résultats indiquent que  $\text{Bi}_{1-x}\text{Sb}_x$  présente un potentiel significatif pour les dispositifs spintroniques.

**Title :** Molecular beam epitaxy growth of the BiSb/MnGa heterostructures for the charge current to spin current conversion study

**Keywords :** Topological insulator, molecular beam epitaxy, ARPES, charge-to-spin conversion, terahertz spectroscopy, spin-orbit torque

**Abstract :** Recently, topological insulators (TI) have attracted much attention with their promising properties potentially useful for the emerging memory technologies, as magnetic random-access memory (MRAM). Indeed, TI/ferromagnetic (FM) systems may drastically reduce the writing current using the spin-orbit torque (SOT) switching as a writing method. This advantage stems from the utilization of the spin-polarized topological surface states of the TIs. In this work, we were aiming to grow TI/FM bilayer heterostructures by molecular beam epitaxy (MBE), to perform comprehensive structural, magnetic and electronic characterization, and to study their charge-to-spin interconversion properties.

We developed a high-quality  $\text{Bi}_{1-x}\text{Sb}_x$  (TI)/  $\text{Mn}_x\text{Ga}_{1-x}$  (FM)//GaAs(001) bilayer heterostructure by MBE, despite the difference in crystal symmetries. The FM  $\text{Mn}_x\text{Ga}_{1-x}$  thin films exhibit perpendicular magnetic anisotropy, low coercive field, high Curie temperature, square hysteresis cycle, and sufficiently high resistivity. This ensured that a major portion of the electrical current flows through the  $\text{Bi}_{1-x}\text{Sb}_x$  layer during the SOT experiments. The SOT measurements suggest that bulk states of  $\text{Bi}_{1-x}\text{Sb}_x$  predominantly contribute to the transport properties. However, we demonstrated the presence of topological surface states with ARPES. So, the bulk and surface states may coexist. Additionally, the preliminary results of terahertz spectroscopy showed the efficient spin-to-charge conversion in the studied bilayer, showing promising potential. Consequently, our findings indicate that  $\text{Bi}_{1-x}\text{Sb}_x$  holds significant promise for spintronic devices.

Трём самым главным женщинам в моей жизни:  
моим маме, бабушке и сестре Виктории посвящается.

To the three most important women in my life :  
my mother, my grandmother, and my sister Victoria.



# Remerciements

Une thèse n'est jamais un fleuve tranquille, et c'était plus que vrai pour moi. Mais grâce à toutes les personnes par qui j'ai été entourée pendant cette période, je peux dire sans le moindre doute que c'était une expérience et une école de vie incroyables. Je ne pourrai pas exprimer ma gratitude à la hauteur de laquelle toutes ces personnes y ont contribué, mais je vais quand même essayer.

Tout d'abord, je voudrais remercier Alexandra Mougin, Daniel Lacour, Lisa Michez et Sébastien Plissard d'avoir accepté de faire partie de mon jury de thèse, d'avoir fait le déplacement jusqu'à Palaiseau et d'avoir rendu ma soutenance, malgré ma grande fatigue, plus qu'agréable. Je garderai de meilleurs souvenirs de ce jour-là.

Un énorme merci aux rapporteurs Daniel et Lisa d'avoir rendu les rapports aussi rapidement, ce qui m'a permis de soutenir le plus rapidement possible et de partir en congé maternité sereinement.

Je ne pourrais, bien sûr, pas manquer l'occasion de remercier mes trois directeurs de thèse : Jean-Marie George de "l'UMPhy", Aristide Lemaître de C2N et Patrick Le Fèvre anciennement du Synchrotron SOLEIL et qui est maintenant affilié à l'Institut de Physique de Rennes.

Jean-Marie, merci de m'avoir fait confiance et de m'avoir recrutée en stage de M2. Ma vie aurait été tellement différente si tu ne l'avais pas fait. Tu as toujours été disponible pour moi, sans être sur mon dos, et tu m'as laissé un maximum de liberté dans ma recherche. Cette période de thèse était très tourmentée tant au niveau scientifique que personnel, et tu t'es toujours montré compréhensif et patient envers moi lorsque je rencontrais des obstacles et des problèmes personnels. Merci également pour ta passion pour la recherche et la spintronique, que j'ai toujours admirée. C'est vraiment très inspirant.

Aristide, merci de m'avoir transmis, même si pas entièrement (:P), ta passion pour la MBE. J'appréciais beaucoup nos discussions sur la science, la recherche et les chaînes YouTube de vulgarisation scientifique. Ta bienveillance envers moi, même lorsque je faisais des bêtises à la salle blanche, m'encourageait à m'améliorer.

Patrick, nous n'avons malheureusement pas passé beaucoup de temps ensemble comme je l'aurais voulu (pas par manque de volonté !). En revanche, je garderai de très bons souvenirs de notre séjour à l'école d'été des Houches, merci pour cela, c'était magnifique ! Faire de la science dans un environnement si merveilleux et être si bien entouré, il n'y a rien de plus beau ! Je te rendrai visite en Bretagne, c'est sûr !

Ensuite, je voudrais remercier les permanents et non-permanents de mon laboratoire alma mater : anciennement l'UMPhy ou Unité Mixte de Physique CNRS/Thales ou UMR ou UMR137, qui a enfin convergé vers un seul et unique nom très récemment : Laboratoire Albert Fert.

Tout d'abord, merci à deux directeurs du laboratoire, Paolo Bortolotti et Vincent Cros, qui veillent sur le bon fonctionnement du laboratoire et qui nous ont envoyés en

retraite à la mer ! Un énorme merci à Vincent pour ses remarques pertinentes sur le projet que j'ai mené, l'organisation de ma thèse et le bon déroulement du projet Spicy qui a financé ma thèse.

Merci à l'équipe administrative composée d'Anne Dussart, Florence Hamet, Julien Morain et Nathalie Sauvage. Les deux derniers, malheureusement pour nous, ont quitté le laboratoire. Merci de votre patience, gentillesse et réactivité !

Merci à Nicolas Reyren d'être mon "conseiller" scientifique. Ta rigueur scientifique (c'est ton côté suisse ?) et ta passion pour la recherche sont sans pareilles ! Merci à Henri Jaffrès d'être mon deuxième "conseiller" scientifique. Tu es un chercheur théoricien hors norme !

Merci à Agnès Barthélémy, ma professeure de M2 à Jussieu, de m'avoir transmis sa passion pour la spintronique et le magnétisme et pour ces merveilleux cours dont les fascicules je garde toujours et que je relis de temps en temps. Merci à toi, car tu es une fenêtre vers l'UMPhy pour tous les "SMNOniens", ainsi qu'un modèle d'une femme scientifique à grand succès et d'une extrême humilité malgré toutes tes distinctions.

Merci à Manuel Bibes, avec qui j'ai failli faire mon stage, mais cela ne s'est pas fait, et qui m'a recommandé à Jean-Marie ! Sans toi, je n'aurais pas été là. A Vincent Garcia pour être mon parrain au laboratoire, pour ta bienveillance et ta gentillesse. A Pierre Seneor d'être un mentor pour tous les non-permanents. Chaque fois que j'étais à côté de toi, j'apprenais quelque chose.

Merci à Faycal Bouamrane d'avoir veillé sur mon bien-être au laboratoire, à Marie-Blandine Martin pour toujours prendre de mes nouvelles, à Isabella Boventer pour partager avec moi les peines et les joies d'une jeune maman, à Vincent Humbert pour sa "goofiness" (comment dit-on en français ?), à Frédéric Van Dau, Florian Godel, Bruno Dlubak, Madjid Anane, Sophie Collin, Cécile Carrétéro, Denis Crété, Richard Mattana pour rendre le laboratoire tel qu'il est !

Merci à mes anciens et actuels co-bureaux : Nathan Leroux, Laurette Jerro (tu as laissé un grand vide quand tu es partie), Ruchi Tomar, thanks for being there for me (!), Ayméric Vecchiola pour nos discussions parfois interminables, mais tellement intéressantes ! A Julie Lion pour être toi-même, et, à la dernière nouvelle, Emma Aoustin : bonne chance pour ta thèse ! Un énorme merci à Laëtitia Baringthon qui m'a transmis ses savoirs (et les galères qui vont avec) sur le BiSb. Tu m'as appris beaucoup de choses quand j'étais une stagiaire de M2, merci beaucoup pour ta patience. J'adore ta personnalité, tu m'as toujours fait rire, reste toi-même !

Merci à Nicholas Figueiredo-Prestes, without you my PhD journey would not have been the same. Not only you taught me and helped me a lot with the spin-orbit torque measurements and data treatment so that my PhD increased in quality, but you also became my confidant with whom I shared a lot of my life and you gave me so many precious pieces of advice. Plus, I had a lot of fun with you during the conferences in Obernai and Sendai. Hope to see you soon in Brazil.

Merci à Arnaud De Riz, je ne connaissais pas ton existence car tu étais toujours caché dans ton bureau au fond du laboratoire, mais lorsque je t'ai découvert, ce fut une agréable surprise ! Je peux parler de tout avec toi pendant des heures, mais à un moment donné, il faut aller travailler ! Nous continuerons à assister à des concerts et à des sorties culturelles ensemble (mais tu dois rester à Paris) !

Merci à Sylvain Massabeau pour nos discussions sur tout et sur rien, et bien sûr pour tes mesures THz ! J'espère que la prochaine fois que je te reverrai, tu seras chercheur CNRS !

Merci aux actuels et anciens post-doctorants du laboratoire : Julian Peiro, je n'oublierai

jamais ton soutien pendant une période particulièrement difficile de ma vie. Ping Che, for always asking how my life is going, for your support and your availability, to Eva Grimaldi, Fernando Gallego, Carol De Dios Fernandez, Oliver Paull, Amr Abdelsamie, Xing Chen, David Sanchez Manzano et Christophe Diedonné. Merci à Sachin Krishnia, Pankaj Sethi, Sajid Hussain, Srijani Mallik, Sougata Mallick et Naveen Sodia for bringing India and, of course, each one of your interesting personalities in the lab . Merci à Sara Varotto, je suis tellement heureuse que nous nous soyons rapprochés récemment, tu es incroyable !

Merci à notre promotion de doctorants 2020 : Aya El Kanj, avec qui nous avons partagé les doutes et les joies du doctorat, Kévin Seurre pour ta disponibilité et ton dynamisme, Gaétan Verdierre, Matthieu Grelier et Marie Drouhin.

Merci à la promotion précédente de doctorants : Diane Gouéré et Yanis Sassi, avec qui nous avons commencé ce chemin de stage et de doctorat ensemble, et même si j'ai pris une autre voie, cela ne nous a pas empêché de vivre des expériences ensemble. Merci à Pauline Dufour, Julien Bréhin, Aurélien Lagarrigue, Enzo Rongione pour tes mesures THz dans le BiSb, et Jeremy Laydevant.

Merci à la promotion suivante de doctorants : Sarah Menouni (tu es juste superbe !), Hugo Witt (pour ton rire remarquable que tu devrais breveter, et pour qu'on peut débattre sur des sujets différents pendant des heures, et ça me plaît !), Hao Wei pour ta gentillesse extrême, Frederic Brunnett for being a cool german (;P), Erwan Plouet (pour rendre les déjeuners à la cantine plus joyeux, j'adore ton humour), Katia Ho, Dongshu Liu, Hadi Hassan pour ne pas avoir besoin de stimulants pour être toujours de bonne humeur !

Merci aux deux dernières générations de doctorants : Nicolas Sebe pour ton sens de l'humour remarquable, Benjamin Bony, William Bouckaert, Mohamed Menshawy, Baptiste Carles et Meghan Lecerf. Bonne chance à vous pour la suite !

Je voudrais chaleureusement remercier mon équipe au C2N. Merci à Martina Morassi de m'avoir enseigné les fondamentaux de la MBE, tu es une superbe professeure ! Merci pour ton soutien et d'être mon alliée. Merci également pour ta curiosité et de partager avec moi les défis d'être une femme scientifique et une mère de famille. Tu es super forte !

Merci à Anton Pishchagin de m'avoir toujours aidé sur tous les fronts : scientifique, technique, administratif et personnel. Ma vie au C2N (et en dehors du labo) aurait été beaucoup plus compliquée sans toi !

Merci à Ludovic Largeau pour tes nombreuses mesures TEM et de m'avoir enseigné des choses sur la cristallographie (il était temps !). Merci pour tes blagues parfois douteuses qui me faisaient rire quand même !

Merci à Laurent Travers pour être docteur du bâti MBE dont j'étais locataire. Mais aussi pour avoir apporté ta bonne humeur pendant mes croissances fastidieuses et les avoir rendues un peu plus joyeuses.

Merci à Dyhia Tamsaout pour être ma co-bureau, pour ta curiosité, ta gentillesse et ton bon esprit ! Bonne chance pour la fin de ta thèse !

Merci à Federico Panciera pour ta personnalité espiègle et pour nos discussions passionnantes à la cantine.

Merci également à Jean-Christophe Harmand, Ali Madouri, Antonella Cavanna et Gilles Patriarche.

Merci aux scientifiques et techniciens de la ligne CASSIOPEE au synchrotron SOLEIL : François Bertran, Chiara Bigi et William Breton. Merci à Raphaël Salazar pour ta curiosité et de m'avoir appelée pour parler de l'identité culturelle des Kazakhstaniens ! Depuis, j'adore nos discussions. Je te souhaite beaucoup de réussite dans tes travaux de

post-doctorat.

Je voudrais remercier également ma famille : ma mère, qui est malheureusement partie beaucoup trop tôt et n'a pas pu assister à beaucoup d'événements importants de ma vie d'adulte. Merci de m'avoir appris l'importance du travail, de l'assiduité et de la rigueur. Merci à ma grand-mère, qui a toujours dit à tout le monde que j'allais réussir à être scientifique : j'y suis presque, mamie ! À ma sœur Viktoria et mon beau-frère Oleg pour leur soutien et leur amour inconditionnel, qui sont devenus mes parents de substitution et à qui je dois beaucoup. À mes tantes Svetlana et Irina qui sont toujours de mon côté. À mes oncles Arkadiy et Gennadiy qui ne font, malheureusement, plus partie de ce monde. Merci à mon frère Vitaly.

И, наконец, я хотела бы поблагодарить мою семью: мою маму, которая, к сожалению, ушла слишком рано и не смогла быть на многих важных событиях в моей взрослой жизни. Спасибо, что научила меня значению трудолюбия и усердия. Благодарю мою бабушку, которая всегда говорила всем, что я смогу стать ученым: почти стала, бабушка! Моей сестре Виктории и моему зятю Олегу за их безусловную поддержку и любовь, которые стали для меня заменой родителей, и которым я многим обязана. Моим тётям Светлане и Ирине, которые всегда поддерживали меня. Спасибо моим дядям Аркадию и Геннадию, которые, к сожалению, ушли из жизни. Моему брату Виталию за то, что он мой брат!

Merci à ma belle-famille : Jean-Louis, Elisabeth, Mitra, Samuel, Antoine, Salomé, Edouard, Florence, Agathe et Etienne.

Merci à mes amis pour leur inégalable soutien : à Madina, Assel, Kseniya, Sergey, Yekaterina O, Yekaterina Zh., Marie, Kamshat, Mourad, Iegor, Anastasiia, Kimhee, Andjelika, Caroline et Jeremy.

Merci à mon amour et mon compagnon de vie Boris, qui m'a toujours soutenue et sans qui je n'aurais pas pu faire cette thèse. J'ai beaucoup grandi à tes côtés et grâce à tes précieux conseils, je m'améliore chaque jour. Ensemble, nous avons déjà accompli beaucoup de choses et nous en accomplirons encore plus.

Merci à mon bébé Danil, qui va arriver dans ce monde très bientôt ! Même si, au premier abord, tu ne m'as pas facilité la vie pendant la rédaction de ce manuscrit, tu m'as motivée à persévérer et à ne jamais baisser les bras. Avec papa, on t'aime déjà à la folie et on t'attend avec impatience !

# Contents

|  |           |
|--|-----------|
| <b>General introduction</b>  | <b>17</b> |
| <b>1 The phenomenon of spin-orbit torques</b>  | <b>21</b> |
| 1.1 Spin-orbit interaction   | 21        |
| 1.2 Charge-to-spin current interconversion   | 22        |
| 1.2.1 Spin Hall effect   | 23        |
| 1.2.2 Rashba-Edelstein effect  | 27        |
| 1.2.2.1 Rashba-like physics  | 28        |
| 1.2.2.2 Non-equilibrium Rashba effects: Rashba-Edelstein effect<br>and inverse Rashba-Edelstein effect | 29        |
| 1.3 Generation of spin-orbit torques   | 31        |
| 1.4 Materials for spin-orbit torques   | 32        |
| 1.4.1 Ferromagnet/non-magnetic metal systems   | 33        |
| 1.4.2 Ferromagnet/two-dimensional materials systems  | 34        |
| 1.4.3 Ferromagnet/oxides systems   | 34        |
| <b>2 Topological insulators for spin-orbit torques</b>   | <b>35</b> |
| 2.1 Definition and main properties of topological insulators   | 36        |
| 2.2 Spin-orbit torques in topological insulators/ferromagnet systems                                   | 40        |
| 2.3 Charge-to-spin interconversion in BiSb/ferromagnet systems   | 41        |
| 2.3.1 Crystal structure of $\text{Bi}_{1-x}\text{Sb}_x$  | 42        |
| 2.3.2 Electronic properties of $\text{Bi}_{1-x}\text{Sb}_x$  | 42        |
| 2.3.3 Conversion between spin and charge currents in BiSb/ferromagnet<br>systems                       | 45        |
| <b>3 Growth by molecular beam epitaxy and characterization of BiSb/MnGa//GaAs(001)<br/>bilayer</b>     | <b>51</b> |
| 3.1 Basics of the molecular beam epitaxy   | 51        |
| 3.1.1 Main working principle, benefits and challenges of molecular beam<br>epitaxy                     | 51        |
| 3.1.2 Epitaxial growth modes   | 53        |
| 3.1.3 Growth rate and flux measurements  | 53        |
| 3.2 Growth of BiSb by molecular beam epitaxy on different substrates                                   | 55        |
| 3.2.1 Growth on the InSb(111)B substrate   | 55        |
| 3.2.2 Growth on the GaAs substrates  | 61        |
| 3.3 Growth and characterization of MnGa  | 65        |
| 3.4 Growth and characterization of BiSb/MnGa//GaAs(001)  | 72        |
| 3.5 Chapter conclusion   | 77        |

|          |  |            |
|----------|--|------------|
| <b>4</b> | <b>Electronic characterization of BiSb/MnGa//GaAs(001) bilayer</b>                             | <b>79</b>  |
| 4.1      | ARPES to explore the topological nature of BiSb/MnGa   | 79         |
| 4.1.1    | How does ARPES work?   | 79         |
| 4.1.2    | Surface states in BiSb//GaAs(001) and BiSb/MnGa//GaAs(001) probed by ARPES                     | 82         |
| 4.1.3    | Complementary structural analysis of BiSb/MnGa//GaAs(001) by GIXRD                             | 85         |
| 4.2      | Conductivity properties of BiSb and MnGa thin layers: is there current shunting?               | 88         |
| 4.3      | Magnetotransport measurements  | 91         |
| 4.3.1    | Angular dependence measurements: AMR and SMR effects   | 92         |
| 4.3.2    | Anomalous Hall effect measurements   | 93         |
| 4.4      | Chapter conclusion   | 95         |
| <b>5</b> | <b>Charge-to-spin interconversion in BiSb/MnGa//GaAs(001) bilayer</b>                          | <b>97</b>  |
| 5.1      | Charge-to-spin conversion: SOT in BiSb/MnGa//GaAs(001) heterostructure                         | 97         |
| 5.1.1    | Harmonic Hall voltage technique  | 98         |
| 5.1.2    | SOT efficiency dependence on the BiSb thickness  | 100        |
| 5.1.3    | SOT temperature dependence discussion  | 106        |
| 5.1.4    | Current-induced magnetization switching  | 107        |
| 5.2      | Spin-to-charge conversion in BiSb/MnGa//GaAs(001) heterostructure                              | 110        |
| 5.2.1    | Terahertz time-domain spectroscopy technique to study the spin-to-charge conversion properties | 110        |
| 5.2.1.1  | Experimental results   | 111        |
| 5.3      | Chapter conclusion   | 113        |
|          | <b>General conclusion and perspectives</b>   | <b>115</b> |
|          | <b>Bibliography</b>  | <b>119</b> |
|          | <b>Appendix</b>  | <b>137</b> |

# Résumé étendu

Dans le paysage technologique en constante évolution, la spintronique, un amalgame du spin et de l'électronique, a émergé comme un domaine prometteur qui offre un grand potentiel pour dépasser les limitations de l'électronique traditionnelle basée sur les semi-conducteurs. Contrairement à cette dernière, qui repose principalement sur la charge des électrons, la spintronique exploite à la fois la charge et le spin des électrons pour traiter et stocker l'information. Ainsi, la spintronique offre une nouvelle voie pour développer des dispositifs électroniques qui seront plus rapides, plus petits et plus efficaces.

Un avantage clé de la spintronique réside dans son potentiel d'efficacité énergétique. Les dispositifs spintroniques peuvent réduire significativement la consommation d'énergie. De plus, la spintronique offre la perspective de dispositifs de mémoire non volatile qui permettent de stocker l'information même sans alimentation électrique continue. Les technologies de mémoire basées sur le spin, telles que la mémoire MRAM (Magnetoresistive random-access memory) basée sur des jonctions tunnel magnétiques (Magnetic tunnel junction ou MTJ), offrent des temps d'accès rapides. Elles ont le potentiel de remplacer d'autres mémoires RAM ou d'être intégrées dans des circuits logiques CMOS (Complementary Metal Oxide Semiconductor).

Le développement de la mémoire magnétique MRAM qui exploite le couple de spin-orbite (SOT-MRAM) a été l'une des avancées significatives dans le domaine des technologies de mémoire basées sur la spintronique. Avant cela, la génération de courants de spin reposait sur l'utilisation des matériaux ferromagnétiques (FM) et du phénomène d'interaction d'échange. La SOT-MRAM, cependant, s'appuie toujours sur le concept de magnétorésistance et de couple de transfert de spin (Spin-transfer torque ou STT), mais au lieu d'utiliser la polarisation du spin induite par le courant, elle exploite l'effet de couplage spin-orbite (SOC) pour générer des courants de spin. Cet effet résulte de l'interaction entre le spin de l'électron et son mouvement orbital.

L'avancement important s'est produit en 2011 lorsque Miron et al. ont démontré qu'en faisant passer un courant à travers une couche de métal lourd avec un fort couplage spin-orbite, cela pouvait générer un courant de spin pour agir comme un couple sur la couche magnétique adjacente [110]. Ce couple permettait une commutation efficace de la direction de l'aimantation, conduisant au développement de la SOT-MRAM. Cela a également déclenché la recherche des matériaux pour la conversion de charge en spin.

La SOT-MRAM offre plusieurs avantages par rapport aux technologies MRAM traditionnelles. Elle peut fournir des vitesses d'écriture plus rapides (sur une échelle de quelques ns) et une consommation d'énergie plus faible, car le courant d'écriture requis peut être significativement réduit. En effet, le SOT peut renverser l'aimantation avec un courant critique plus faible, entraînant une efficacité énergétique plus élevée. De plus, contrairement à la STT-MRAM, la SOT-MRAM permet de découpler les mécanismes de lecture et d'écriture, ce qui conduit à une possible optimisation des chemins de lecture et

d'écriture. De plus, elles détiennent un potentiel pour une intégration compatible avec la technologie existante CMOS.

Depuis sa découverte initiale, d'importants efforts de recherche ont été consacrés à l'optimisation des matériaux, des interfaces et des architectures de dispositifs de SOT-MRAM. Divers métaux lourds, tels que Ta, W et Pt, ont été explorés pour améliorer l'efficacité du couple de spin-orbite.

Ces dernières années, la découverte d'isolants topologiques (TIs), des matériaux avec des états de surface uniques qui sont robustes contre les impuretés et le désordre, a encore propulsé le domaine de la spintronique. Les TIs ont montré un grand potentiel pour une utilisation dans les dispositifs SOT-MRAM. Ce sont des matériaux uniques qui sont isolants dans leur volume mais présentent des états de surface conducteurs en raison de leurs propriétés topologiques non triviales. Cette propriété est généralement associée à un SOC important et à un verrouillage du spin au moment (spin-momentum locking) crucial pour générer le couple de spin-orbite requise dans la SOT-MRAM, permettant une manipulation et un contrôle efficaces du spin.

C'est pour ces raisons que nous avons choisi cette classe de matériaux pour notre étude, et plus particulièrement l'alliage  $\text{Bi}_{1-x}\text{Sb}_x$  (BiSb). Le BiSb est le premier isolant topologique tridimensionnel qui a été réalisé expérimentalement. Il présente une petite bande interdite d'énergie du volume (d'environ 30 meV) et une structure de bande globalement complexe, ce qui le rend plus difficile à étudier par rapport à d'autres TI, tels que  $\text{Bi}_2\text{Se}_3$  ou  $\text{Bi}_2\text{Te}_3$ . Cependant, malgré ces complexités, l'effet de quantification peut se produire dans des films ultra minces de BiSb, conduisant à une bande interdite plus large tout en présentant toujours l'inversion de bande près du point M dans la fenêtre de concentration  $x=0.07-0.30$ . Par conséquent, le BiSb peut être un candidat prometteur pour le développement de dispositifs SOT-MRAM réalistes.

En raison de sa structure de bande complexe et de sa petite bande interdite, le BiSb n'a pas été étudié aussi intensivement que d'autres isolants topologiques. Cependant, en 2018, le groupe de Pham Nam Hai a mesuré une efficacité de SOT géante dans la bi-couche BiSb/MnGa, estimée à 52 à température ambiante en utilisant la méthode de coercivité [77]. Cette valeur représente l'efficacité de SOT la plus élevée rapportée dans la littérature à ce jour. De plus, ils ont réussi à démontrer une commutation de l'aimantation induite par SOT dans ce système en utilisant une densité de courant critique relativement faible :  $J = 1,1 \times 10^6 \text{ A/cm}^2$ .

Par la suite, le BiSb a été combiné avec d'autres couches minces ferromagnétiques pour étudier son efficacité de SOT. Cependant, il existe une grande disparité parmi les résultats obtenus, allant de 0,01 à 61. Cette disparité peut être attribuée à des différences dans les techniques de dépôt des couches (épitaxie par jet moléculaire ou pulvérisation), les qualités cristallines et d'interface de l'hétérostructure, et différentes techniques de mesure. La valeur la plus élevée rapportée de l'efficacité de SOT pour la couche de BiSb crûe par pulvérisation est de 10,7.

Néanmoins, la question de la contribution au SOT du volume par rapport à l'interface a été abordée dans une moindre mesure. Chi et al. ont montré que l'efficacité de SOT dans BiSb/CoFeB augmentait avec l'augmentation de l'épaisseur jusqu'à saturation et était indépendante des orientations cristallographiques, suggérant que la contribution dominante au SOT provient du volume [26]. Cependant, le rôle des états de surface topologiques dans la génération de SOT n'est pas encore entièrement compris. Dans ce travail, nous avons essayé d'adresser ce problème.

Ce travail est une collaboration entre trois laboratoires : Laboratoire Albert Fert, Centre de nanosciences et de nanotechnologies (C2N) à Palaiseau et le synchrotron SOLEIL

à Saint-Aubin. Les échantillons étudiés ont été crûs et caractérisés au C2N. Les caractérisations magnétiques, les mesures de transport et de magnéto-transport ont été réalisées au Laboratoire Albert Fert. La caractérisation électronique par spectroscopie photoélectronique résolue en angle (Angle-resolved photoemission spectroscopy ou ARPES) a été effectuée au synchrotron SOLEIL.

Dans ce travail de thèse, l'objectif était donc de développer une hétérostructure BiSb/FM par épitaxie par jets moléculaires (Molecular beam epitaxy ou MBE), dans le but de montrer une conversion efficace d'un courant de spin en courant de charge au sein de ce système. Pour faciliter la distinction entre les effets de couple de spin-orbite et les effets thermiques, l'objectif initial était de faire croître des structures de matériaux BiSb/FM avec une anisotropie perpendiculaire. Nous avons opté pour l'hétérostructure BiSb/MnGa//GaAs(001), car les deux matériaux pouvaient être déposés dans la même chambre MBE, garantissant la préservation de la qualité de l'interface MnGa/BiSb. Une partie de cette thèse était consacrée à la croissance par MBE, impliquant une caractérisation structurale complète à travers diverses techniques expérimentales, notamment diffraction des électrons de haute énergie en incidence rasante (Reflection high-energy electron diffraction ou RHEED), microscopie à force atomique (Atomic force microscopy ou AFM), diffraction des rayons X (X-Ray diffraction ou XRD), diffraction à incidence rasante des rayons X (Grazing incidence X-ray diffraction ou GIXRD) et microscopie électronique en transmission (transmission electron microscopy ou TEM). Compte tenu de notre objectif de fabriquer un matériau ferromagnétique avec anisotropie perpendiculaire, les caractérisations magnétiques utilisant superconducting quantum interference device ou SQUID et alternating gradient field magnetometry ou AGFM ont également guidé cette phase de développement.

La croissance d'une couche ferromagnétique de MnGa d'une épaisseur de 10 nm sur un substrat GaAs(001) avec une anisotropie perpendiculaire a été optimisée, présentant des propriétés magnétiques recherchées. Une aimantation de l'ordre de  $315 \text{ emu/cm}^3$  à basse température, un cycle d'hystérésis avec une rémanence proche de 1, lorsque le champ magnétique est appliqué perpendiculairement au plan des couches, et une coercivité de l'ordre de 0.1 T ont été obtenues. Des études structurales ont démontré la relation épitaxiale avec le substrat. Cependant, réduire l'épaisseur de MnGa à quelques nanomètres a entraîné une détérioration de ses propriétés ferromagnétiques et une instabilité thermique. Nous avons pu observer une anisotropie perpendiculaire jusqu'à 7 nm. La présence d'une couche de mélange à l'interface entre le substrat GaAs et la couche de MnGa a également été observée.

Une couche mince de BiSb de haute qualité, thermiquement stable et épitaxiale a été crûe sur MnGa avec succès. Cependant, les mesures GIXRD ont révélé la présence de deux orientations cristallographiques de BiSb.

Au-delà de cette structure spécifique, au cours de cette thèse, nous nous sommes intéressés à la croissance de BiSb sur divers substrats. Des films minces de BiSb ont été crûs sur InSb, GaAs(001), GaAs(111)A et GaAs(111)B. Pour des mesures de transport qui nécessitent un substrat isolant, une étude de la croissance de BiSb sur un isolant AlInSb, dont le paramètre de maille est proche de celui de BiSb, a été également initiée. Bien que cela présente une alternative prometteuse, une optimisation supplémentaire sera nécessaire.

L'objectif de développer l'hétérostructure BiSb/MnGa était d'étudier les mécanismes impliqués dans la conversion d'un courant de charge en un courant de spin, en particulier à travers le couple de spin-orbite exercé lorsque ce courant de spin est absorbé par un matériau ferromagnétique. En théorie, les propriétés de transport de BiSb, en tant qu'isolant topologique, proviennent de ses états de surface polarisés en spin. Cependant,

en pratique, la petite bande interdite de BiSb peut entraîner un décalage du niveau de Fermi dans la bande de conduction, introduisant une contribution significative des états de volume dans le transport. Ce décalage peut résulter d'un dopage non intentionnel, d'un transfert de charge ou d'effets de courbure de bande à l'interface.

En utilisant les installations de la ligne de faisceau CASSIOPEE du synchrotron SOLEIL, nous avons confirmé la présence d'états de surface sur BiSb lorsqu'il est crû sur MnGa. Il est important de noter que nos observations se limitaient à la surface supérieure, ne fournissant aucun aperçu direct de l'interface MnGa/BiSb.

La conversion de charge en spin a été caractérisée en utilisant la technique de tension de Hall de deuxième harmonique (harmonic Hall voltage technique ou HHV) et le renversement de l'aimantation induite par courant (current-induced magnetization switching). En raison de la plus faible conductivité de MnGa par rapport à celle de BiSb, la majorité du courant passe à travers la couche de BiSb. Cela a permis d'estimer la composante du couple de spin-orbite dite "damping-like" (DLT) plus élevée dans le système BiSb(9 nm)/MnGa(7 nm) par rapport aux systèmes métalliques conventionnels. Cependant, le signal dû à la composante dite "field-like" (FLT) s'est révélée insignifiante. Ces observations suggèrent une origine de SOT dû à l'effet Hall de spin (Spin Hall effect ou SHE). Un soutien supplémentaire à cette conclusion vient de la diminution du DLT en réduisant l'épaisseur de BiSb. Néanmoins, parvenir à une conclusion définitive sur le rôle des états de surface par rapport aux états de volume reste difficile à ce stade. Produire un nombre substantiel d'échantillons avec des épaisseurs variables pour les matériaux TI et FM est nécessaire. Cela se révèle être une limitation avec MnGa sur GaAs, où la réduction de l'épaisseur en dessous de 7 nm semble difficile. Des études supplémentaires sur l'origine du fort DLT sont nécessaires. De plus, l'aimantation n'a été renversée que partiellement, probablement en raison de l'instabilité thermique de MnGa, vu que le chauffage de la couche de MnGa pendant l'expérience de renversement peut détériorer ses propriétés magnétiques.

L'efficacité de conversion du courant de spin en courant de charge (spin-to-charge conversion ou SCC) dans BiSb a été démontrée par spectroscopie térahertz dans le domaine temporel (terahertz time-domain spectroscopy ou THz-TDS). Le signal THz émis est comparable à celui du système SHE Pt/Co conventionnel. Ces résultats préliminaires ouvrent la porte à une caractérisation rapide de SCC (aucune lithographie n'est requise), mais contrairement aux mesures de SOT, une aimantation dans le plan pour la couche ferromagnétique serait une meilleure configuration.

Au cours de ce travail de thèse, nous avons réussi à démontrer que le système MnGa/BiSb fabriqué par MBE présente des caractéristiques intrigantes pour étudier la conversion d'un courant de spin en un courant de charge et vice versa. Néanmoins, ces résultats restent préliminaires, et une compréhension plus approfondie du système est nécessaire. Pour distinguer entre les contributions des états de volume et de surface, la production d'un nombre considérable d'échantillons de haute qualité est essentielle. Surmonter certains défis est, cependant, nécessaire. Premièrement, réduire l'épaisseur du matériau magnétique à quelques nanomètres est crucial, étant donné que l'effet de couple de spin-orbite est interfacial. Atteindre cela sur des substrats GaAs semble difficile, et l'anisotropie élevée représente un obstacle pour minimiser les courants critiques requis pour l'inversion de l'aimantation. Malgré ces défis, MnGa se distingue comme l'un des rares matériaux FM à l'anisotropie perpendiculaire crû en contact direct avec BiSb. Le deuxième point concerne la croissance de BiSb sur MnGa. Bien que le système soit épitaxial, plusieurs orientations cristallines coexistent en raison de la différence de symétries structurales, ce qui complique l'interprétation de la structure de bande en utilisant le modèle de liaisons

fortes (tight-binding model) actuellement disponible.

Pour étudier le rôle des états de surface, il est crucial de contrôler le niveau de Fermi et de le positionner dans la bande interdite de BiSb. Cela reste un domaine d'étude en cours.

Indépendamment de l'origine de la conversion de courant de spin en courant de charge, nous avons montré que le système BiSb est une alternative prometteuse aux matériaux métalliques traditionnels. Sa capacité à moduler les propriétés électroniques à travers des effets de grille ou à se combiner avec des matériaux ferroélectriques en fait un système attrayant. Cependant, la maîtrise des faibles épaisseurs et la démonstration de tels effets sont encore en cours.

Enfin, des études récentes sur la la croissance de BiSb par pulvérisation avec une qualité cristalline comparable à celle obtenue par MBE ont encouragé notre groupe de recherche à entreprendre une nouvelle activité dans ce domaine. Les résultats initiaux sont encourageants, démontrant une efficacité significative de conversion de courant de spin en courant de charge en utilisant la technique de THz-TDS.

Les techniques HHV et THz-TDS offrent des avantages, ainsi que des inconvénients, et améliorer notre compréhension des mécanismes sous-jacents à la conversion de courant de spin en courant de charge importante observée dans l'isolant topologique BiSb nécessite la production d'échantillons de haute qualité. La littérature sur ce sujet reste dispersée et controversée. Pour converger sur cette question et positionner BiSb comme un concurrent des matériaux SHE classiques en spintronique, un contrôle approfondi du matériau est nécessaire. Une partie substantielle de cette thèse a été consacrée à faire avancer cet objectif.



# General introduction

In the ever-evolving landscape of technology, spintronics, an amalgamation of spin and electronics, has emerged as a promising field that holds tremendous potential for surpassing the limitations of traditional semiconductor-based electronics. Unlike the latter, which primarily relies on the charge of electrons, spintronics takes advantage of both the charge and spin of electrons to process and store information. Thus, spintronics offers a new avenue for developing advanced electronic devices that will be faster, smaller, and more efficient.

One key advantage of spintronics lies in its potential for energy efficiency. Spintronic devices can reduce power consumption significantly. Furthermore, spintronics offers the prospect of non-volatile memory devices that retain information even without a continuous power supply. Spin-based memory technologies, such as magnetic random-access memory (MRAM) based on magnetic tunnel junctions (MTJs), provide fast access times and high data retention. So they have a potential to replace other random-access memories or to be embedded in complementary metal-oxide-semiconductor (CMOS) logic.

In addition to energy efficiency and non-volatile memory, spintronics opens up exciting possibilities for new computing paradigms. Spin-based logic and quantum computing architectures leverage the inherent properties of electron spins to perform complex computations. These emerging computing models offer the potential for applications ranging from artificial intelligence to cryptography.

The field of spintronics traces its origins back to the beginning of the 20th century when physicists began to explore the properties and behavior of electrons beyond their charge. The concept of utilizing the spin of electrons for electronic applications emerged as a new frontier in physics and technology. Let us dive into a brief history of spintronics and its key milestones.

- Discovery of electron spin: In 1922, the Stern-Gerlach experiment demonstrated that silver atoms possess only two distinct discrete angular momenta even without having any orbital angular momentum. The existence of electron spin angular momentum was consequently inferred from this experiment.
- Spin-dependent tunneling or tunneling magnetoresistance (TMR): The phenomenon of tunneling magnetoresistance has been known since Julliere's experiments in 1975 [70]. This effect demonstrated that the tunneling of electrons traveling between two ferromagnetic (FM) layers, separated by a thin insulating barrier (a few nanometers or less), could be influenced by the relative orientation of the magnetizations of these two ferromagnetic layers. However, it was only after the study of Yuasa et al. in 2004, where they demonstrated a giant MR ratio up to 180% at room temperature in Fe/MgO/Fe MTJs, that the MTJs based on this phenomenon gained a significant momentum [182].

- Discovery of giant magnetoresistance (GMR): The field of spintronics made a significant leap forward with the discovery of giant magnetoresistance by two independent groups of Albert Fert and Peter Grünberg [9], [19]. In 1988, they demonstrated that alternating layers of ferromagnetic and non-magnetic (NM) materials could exhibit a significant change in electrical resistance when subjected to an external magnetic field. This breakthrough opened the door to using electron spin to sense and manipulate magnetization. In addition, this discovery, awarded by the Nobel Prize in 2007, is generally recognized as the birth of spintronics.
- Spin injection and spin transport: In 1996, Berger [14] and Slonczewski [153] made strides in understanding spin injection and transport. They theoretically explored how to efficiently inject the spin-polarized current exerting a torque on the magnetization of a ferromagnetic layer which can lead to switching of its direction.
- Spin-transfer torque (STT): In 1998, Tsoi et al. experimentally demonstrated the phenomenon of spin-transfer torque, which involves manipulating the orientation of electron spins by transferring angular momentum from a spin-polarized current to a magnetic layer [165] (see Figure 0.1(a)). This phenomenon laid the groundwork for spin-based memory technologies, such as spin-transfer torque magnetic random-access memory (STT-MRAM).
- Further advancements: Spintronics has witnessed continuous advancements and the emergence of various spin-based devices and applications. These include spin valves, magnetic tunnel junctions, spin transistors, and magnetic sensors, among others. Spintronic technologies are being explored for use in non-volatile memory, magnetic field sensors, spin logic devices, and quantum computing architectures.

An MTJ device is composed of two ferromagnetic layers separated by a non-magnetic spacer. One FM layer is the fixed or the reference layer: its magnetization is pinned to an antiferromagnetic layer. The second FM layer is the free layer with magnetization that can be switched either along parallel or anti-parallel direction with respect to the magnetization's direction of the reference layer. These two states corresponding to the parallel and anti-parallel alignments of two magnetizations are two different resistance states as depicted in Figure 0.1(b). They can be associated to 0 and 1 bits, so that one can store or read information.

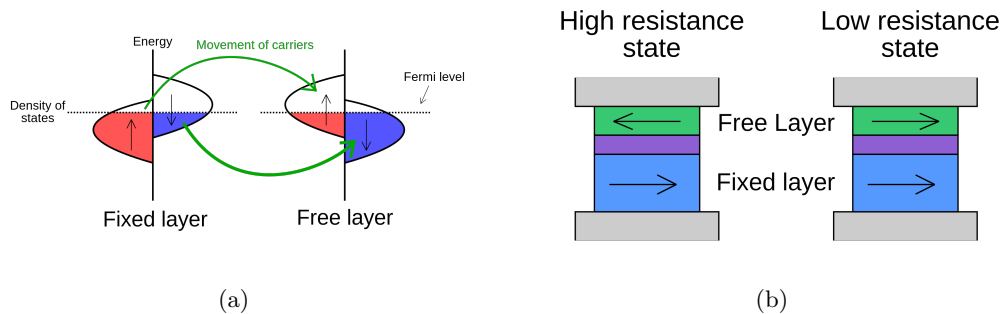


Figure 0.1: (a) Schematic representation of the spin-transfer torque: the spin-polarized current from the reference layer propagates to the free layer, where the majority spins relax into lower-energy states of opposite spins exerting torque. (b) Schematic diagram of two possible resistance states (anti-parallel and parallel) in a basic spin-based device.

The development of spin-orbit torque magnetic random-access memory (SOT-MRAM) has been another significant advancement in the field of spintronics-based memory technologies. Before that, the generation of the spin currents relied on the utilization of the FM materials and the exchange interaction phenomenon. SOT-MRAM, however, still builds upon the concept of magnetoresistance and spin-transfer torque, but instead of utilizing the current-induced spin polarization, it leverages the spin-orbit coupling (SOC) effect to generate spin currents. This effect arises from the interaction between the electron's spin and its orbital motion.

The key breakthrough occurred in 2011 when Miron et al. demonstrated that by passing a current through a heavy metal layer with strong spin-orbit coupling, it could generate a spin current to act as a torque on the adjacent magnetic layer [112]. This torque allowed for efficient switching of the magnetization direction, leading to the development of SOT-MRAM. This also triggered the search for the materials for charge-to-spin conversion.

SOT-MRAM offers several advantages over traditional MRAM technologies. It can provide faster writing speeds (on a timescale of a few ns) and lower power consumption, as the required writing current can be significantly reduced. Indeed, SOT can reverse the magnetization with a lower critical current, leading to a higher energy efficiency. In addition, unlike in STT-MRAM, SOT-MRAM allows to decouple read and write mechanisms leading to a possible optimization of the reading and writing paths. Furthermore, they detain a potential to have an integration compatibility with existing complementary metal-oxide-semiconductor (CMOS) technology.

Since its initial discovery, extensive research efforts have been dedicated to optimizing the materials, interfaces, and device architectures of SOT-MRAM. Various heavy metals, such as Ta, W, and Pt have been explored to enhance the spin-orbit torque efficiency.

In recent years, the discovery of topological insulators (TIs), materials with unique surface states that are robust against impurities and disorder, has further propelled the field of spintronics. TIs have shown great potential for usage in SOT-MRAM devices. They are unique materials that have insulating properties in their bulk but exhibit conducting surface states due to non-trivial topological properties. This property is generally associated with large SOC and allows the realization of large spin-orbit coupling and spin-momentum locking, crucial elements for generating the spin-orbit torque required in SOT-MRAM, enabling efficient spin manipulation and control. We chose this class of materials for our study because of the clear reasons behind their unique properties.

This work is a collaboration between three laboratories: Laboratoire Albert Fert, Centre de nanosciences et de nanotechnologies (C2N) in Palaiseau and SOLEIL Synchrotron in Saint-Aubin. The studied samples were grown and characterized at C2N. Magnetic characterizations, transport and magnetotransport measurements were performed at Laboratoire Albert Fert. Electronic characterization by angle-resolved photoemission spectroscopy was conducted at the SOLEIL Synchrotron.

This manuscript is divided into five chapters. The first chapter provides an overview of the fundamentals of SOTs, including the underlying mechanisms and the materials involved in its generation.

In the second chapter, we delve into the topic of topological insulators, examining their properties and role in generating SOTs, with a specific focus on the  $\text{Bi}_{1-x}\text{Sb}_x$  alloy

and the current state of the art. We also address the challenges related to distinguishing between bulk and surface contributions in SOTs generation and quantifying SOTs.

The third chapter focuses on the experimental results of the growth of the TI/FM bilayer heterostructure, structural analysis, and magnetic characterization of our samples.

Moving to the fourth chapter, we discuss the electronic characterization of the system under investigation, exploring the band structure and magnetotransport properties.

Finally, in the fifth and last chapter, we conduct a detailed characterization of SOTs in the studied heterostructure by exploring charge-to-spin interconversion properties and conclude by discussing the results and presenting future perspectives.

# Chapter 1

## The phenomenon of spin-orbit torques

Spin-orbit torques are a class of phenomena that describe the interaction between the spin and orbital degrees of freedom of electrons in a material. These effects have become increasingly important in recent years due to their potential applications in spintronic devices, which have the potential to improve the way we store and process information.

SOTs arise due to the spin-orbit coupling relativistic effects, which describes the interaction between the spin and motion of electrons in atoms. This interaction is particularly strong in heavy elements, where the high atomic number and large atomic radius lead to strong spin-orbit coupling. In materials with broken inversion symmetry, such as interfaces or surfaces, the spin-orbit coupling can give rise to a torque on the electron spin, which can be used to manipulate the magnetization of a nearby ferromagnetic layer.

SOTs have been experimentally observed in a wide variety of materials, including heavy metals, semiconductors, topological insulators, etc. Recent studies have shown that SOTs can be used to manipulate the magnetization of thin-film MTJs, which are key components in magnetic random-access memory devices.

The ability to manipulate the magnetization of a ferromagnet using SOTs has many potential applications in spintronic devices. For example, SOTs can be used to write data in MRAM devices, which have the potential to be faster, more reliable, and consume less power than conventional memory technologies, such as hard disk drives (HDD) or solid-state drive (SSD).

In this chapter, we will begin by explaining the fundamental notions, such as spin-orbit interaction, the spin Hall effect, and the Rashba-Edelstein effect in order to be able to understand the generation of SOTs. We will then describe the phenomenon of SOTs, including the underlying mechanisms to generate them and their key properties. Finally, we will discuss the materials capable of generating SOTs, which encompass heavy metals, 2D materials, oxides, and topological insulators.

### 1.1 Spin-orbit interaction

Before delving into the subject of spin-orbit torques and mechanisms behind them, it is essential to discuss the fundamental concept at its core, which is the spin-orbit interaction (SOI) or the spin-orbit coupling (SOC).

The spin-orbit interaction arises due to the coupling between an electron's spin and its orbital motion in the presence of an electric field generated by the atomic nuclei. This leads to a shift of electron's atomic energy levels. This phenomenon can be seen as a Zeeman effect, an interaction between two relativistic effects:

1. The effective magnetic field  $\mathbf{B}_{\text{eff}}$  experienced by an electron in its rest frame when moving in an electric field  $\mathbf{E}$  that writes as follows:

$$\mathbf{B}_{\text{eff}} = \mathbf{E} \times \frac{\mathbf{p}}{mc^2} \quad (1.1)$$

where  $\mathbf{p}$  is the electron's momentum,  $m$  is the mass of electron and  $c$  is the speed of light.

2. And the magnetic moment of the electron associated to its spin  $\mu_S$  that writes as follows:

$$\mu_S = -g_s \mu_B \frac{\mathbf{S}}{\hbar} \quad (1.2)$$

where  $\mathbf{S}$  is the spin angular momentum,  $\mu_B$  is the Bohr magneton,  $g_s$  the electron spin gyromagnetic factor, and  $\hbar$  is the reduced Planck's constant.

The spin-orbit potential has two contributions. The first is the Larmor interaction energy which corresponds to the interaction of the spin magnetic moment and the magnetic field of the nucleus experienced by the electron. The second is the Thomas precession.

We will not provide here the complete derivation of the final expression for the total interaction energy. For more details, we recommend that the reader consults quantum mechanics books.

Finally, we obtain the expression of the total spin-orbit interaction energy  $\hat{H}_{\text{SO}}$  in an external electric field  $\mathbf{E} = -\nabla V$ :

$$\hat{H}_{\text{SO}} = \frac{\mu_B}{\hbar m c^2} \frac{1}{r} |\nabla V(r)| \hat{L} \cdot \hat{S} \quad (1.3)$$

with  $\hat{L} = \hat{r} \times \hat{p}$  the angular momentum operator. Here, we made the approximation that the electrostatic potential  $V$  is spherically symmetric:  $V = V(r)$ , i.e., depends only on the radius  $r$ .

The strength of spin-orbit coupling depends on the atomic number of the nucleus and the electron's proximity to it. Therefore, heavier elements with larger atomic numbers tend to have stronger spin-orbit coupling. Additionally, the spatial distribution of the electron's wavefunction and its orbital angular momentum also influence the strength of the coupling.

Spin-orbit coupling has various important applications in the novel emerging field of spintronics, namely spin-orbitronics due to its unique transport properties. Some notable sub-fields of the spin-orbitronics are presented in Figure [1.1](#)

## 1.2 Charge-to-spin current interconversion

It quickly appeared that materials with strong SOC could be very efficient for the generation of spin current by conversion of charge current. It is a fundamental process which is necessary to, e.g., write data in a MRAM: this spin current can generate torques enabling the manipulation of the magnetization (switching).

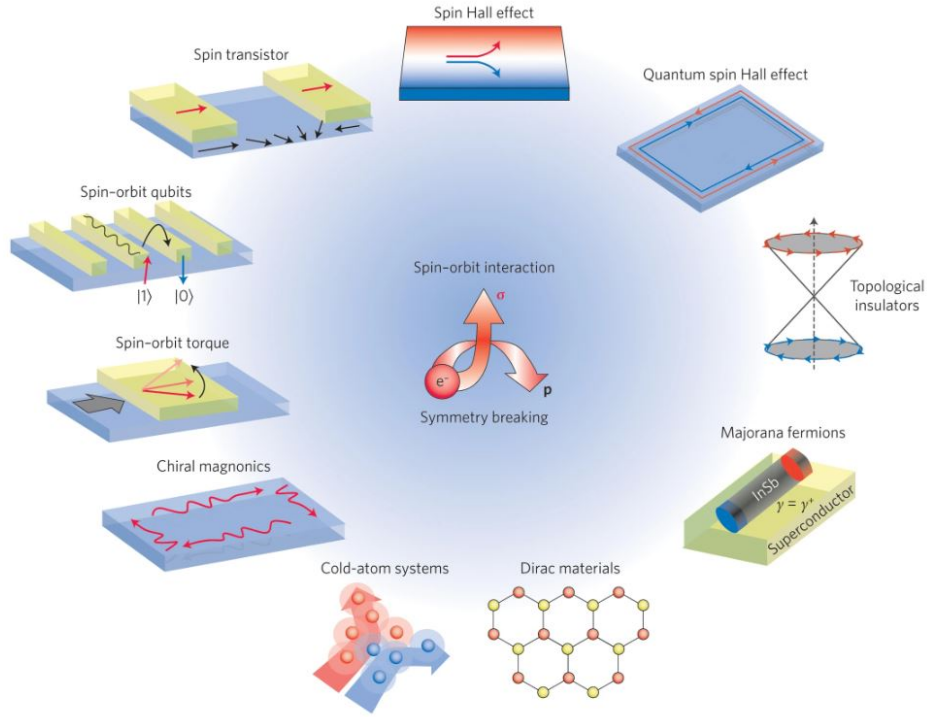


Figure 1.1: Systems with broken inversion symmetry where SOC enables the emergence of various phenomena, as depicted in this Figure. These phenomena give rise to unique transport properties allowing the manipulation of magnetization and spins. Image extracted from [107].

There are several mechanisms through which charge-to-spin conversion can occur. Two prominent processes are the spin Hall effect (SHE) and the Rashba-Edelstein effect (REE) based on the spin-orbit coupling. As we already mentioned, the exploration of these effects lies at the heart of a burgeoning field in spintronics, known as *spin-orbitronics*. This field, as the name suggests, centers on the manipulation of spin through the utilization of spin-orbit coupling.

Let us now discuss more in details the origin of the SHE and the REE.

### 1.2.1 Spin Hall effect

The history of the spin Hall effect can be traced back to 1879 when E. H. Hall made a significant discovery. He observed that when electrons are subjected to both electric and magnetic fields, they experience a lateral displacement, leading them to accumulate on one side of the conductor [54]. This phenomenon was initially recognized as the ordinary Hall effect (OHE). It can be explained by the Lorentz force experienced by the electrons which bend their trajectory. However, it was subsequently observed that the effect is approximately ten times more pronounced in FM materials (such as Ni and Co) compared to non-magnetic metals [69]. This enhanced effect is now referred to as the anomalous Hall effect (AHE). It is proportional to the  $M_z$  component of the magnetization which is perpendicular to both charge current and Hall voltage. Its explanation is not

straightforward. It includes scattering of the spin-polarized electrons by impurities or the introduction of Berry phase\*. These two effects tend to create a Hall voltage perpendicular to the injected current (see Figure 1.2).

SHE is different, since it produces a spin current. The notion and generation of a pure spin current through the SHE in a non-magnetic material was first introduced by Dyakonov and Perel in 1971 [37]. In this work, two main points were emphasized. Firstly, the investigation of spin-dependent asymmetric scattering resulting from Mott scattering of electron beams by nuclei in vacuum [119]. This will be further discussed concerning electrons in a crystal lattice (skew-scattering). Secondly, Mott scattering is regarded as one of the origins of the AHE in ferromagnetic materials [15]. Building upon these two points, it was predicted that the application of an electric current would induce spin-dependent asymmetric scattering in NMs.

The AHE refers to a phenomenon that sorts the charge carriers by their spin direction and generates a transverse voltage in a ferromagnet due to the difference in densities of majority and minority carriers. It results in the generation of a spin-polarized current. The main distinction between the SHE and the AHE is that the SHE does not necessitate a ferromagnetic material. It generates a pure spin current, wherein the densities of spin-up and spin-down carriers are the same, but with opposite polarization on opposite sides.

In SHE, an electric current  $\mathbf{j}_c$  passes through a material with strong spin-orbit coupling. As the current flows, electrons experience a spin-dependent scattering, leading to a separation of spins in the transverse direction perpendicular to the applied electric current. This results in a buildup of spin accumulation on opposite sides of the material. In a heterostructure composed of a SHE material and a FM, the accumulated pure spin current  $\mathbf{j}_s$  can propagate to the adjacent ferromagnetic layer, and by relaxing induces a torque that acts on its magnetization. The reciprocal effect, the inverse SHE (ISHE), converts an injected pure spin current into a transverse charge current. The schematic representation of the SHE is provided in Figure 1.2 (right), alongside the OHE (left) and the AHE (center) for comparison.

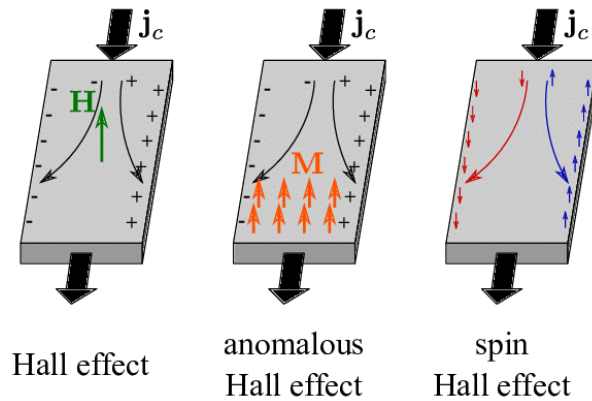


Figure 1.2: Illustration of the spin Hall effect (right) in comparison with the ordinary Hall effect (left) and the anomalous Hall effect (center).

The SHE is solely driven by the spin-orbit coupling of the material and does not require an external magnetic field. This distinguishes it from other spin-related phenomena, such as the magnetoresistance effect. Heavy metals are particularly popular for producing the SHE due to their intrinsically large SOC.

The figure of merit of the SHE is the spin Hall angle  $\theta_{\text{SH}}$ , a material-specific parameter that quantifies the efficiency of the conversion:  $\mathbf{j}_s = \theta_{\text{SH}}(\boldsymbol{\sigma} \times \mathbf{j}_c)$ , with  $\boldsymbol{\sigma}$  denoting spin angular momentum. In other words, it is a ratio of the spin current density and a charge current density, and it is dimensionless.

The SHE can be categorized into two types: intrinsic and extrinsic.

1. The **extrinsic SHE** occurs in materials due to extrinsic mechanisms, such as impurities or defects, present in a lattice or interface effects due to either the asymmetric Mott scattering [115] (also known as skew-scattering) or the side-jump.

Dyakonov and Perel theoretically predicted the extrinsic SHE based on the Mott scattering and the AHE [37].

**Skew-scattering** is a phenomenon in which electrons scatter off a charged (let us say a positive) impurity  $Q$  with a strong SOI and experience different scattering angles based on their spin orientation (up or down). In the reference frame of an electron, the electric field of the impurity behaves like a magnetic field. This magnetic field is perpendicular to both velocity of the electron and electric field. As a result, a magnetic force arises between this magnetic field and the magnetic moments associated with the spins of the electrons. For up spins, this magnetic force points towards the left, while for down spins, it points towards the right. Due to the influence of spin-orbit coupling, the trajectory of the corresponding electrons will be deflected with a higher probability in the same directions as the magnetic force, as shown in Figure 1.3(a).

Let us now discuss the phenomenon of **side-jump** scattering. According to quantum mechanics, an incoming electron wave packet typically follows a straight-line path until it encounters an obstacle, such as an impurity with strong spin-orbit interaction. After the collision, it resumes its straight-line trajectory. However, due to the low symmetry of the SOI, the pre- and post-collision paths of the electron will not coincide. As a result, two possible electron trajectories emerge: 1) the path of the scattered electron forms an angle with the trajectory of the incoming electron, and 2) the two paths are parallel but exhibit a lateral displacement  $\delta_{sj}$ , known as a "side-jump". Figure 1.3(b) depicts these two trajectories. It is important to note that the side-jump process occurs on an infinitesimally short timescale.

2. The **intrinsic SHE** occurs in materials that possess strong spin-orbit coupling inherently within their electronic structure. It occurs even in the absence of scattering.

In crystalline conductors, when we apply an electric field, the usual response of the system will be the following: the electronic wave packet initially centered around a Bloch state will propagate around in space with some Fermi velocity and corresponding phase.

However, there are certain situations where other responses become more important, even in conductors. These responses involve the interaction between different energy bands and are induced by the electric field. One example is the electric-field-induced coherence between Bloch states in different bands or how the Bloch states vary throughout  $\mathbf{k}$ -space. As a consequence, an additional phase is introduced to the usual phase: the Berry phase\*. This introduces an additional component to the group velocity that is perpendicular to the applied electric field. The corrected expression for the group velocity for the  $n$ -th band can be then written, as follows:

$$\frac{d \langle \mathbf{r} \rangle}{dt} = \frac{\partial E_n}{\hbar \partial \mathbf{k}} + \dot{\mathbf{k}} \times \mathbf{b}_n(\mathbf{r}) \quad (1.4)$$

where  $\mathbf{r}$  is displacement vector,  $t$  is time,  $E$  is energy of electrons,  $\hbar$  is reduced Planck constant,  $\mathbf{k}$  is wave vector,  $e$  is elemental charge of electron and  $\mathbf{b}_n(\mathbf{r})$  is Berry-phase curvature.

In Equation 1.4, the first term is the "usual" Fermi velocity. The second term corresponds to an additional component of the group velocity, often referred to as the anomalous velocity. It is called "anomalous", because it is distinct from the usual Fermi velocity. This anomalous velocity is perpendicular to the applied electric field (cf. Figure 1.3(c)) and is associated with the electrons' Berry-phase curvature\*\*, as mentioned earlier. This term leads to the generation of a pure spin current in NMs due to the fact that the Berry-phase curvature acts on electrons as an effective magnetic field.

The SHE was first observed experimentally in 2004 in bulk GaAs and strained InGaAs through magneto-optical Kerr effect 75, more than 30 years after its discovery.

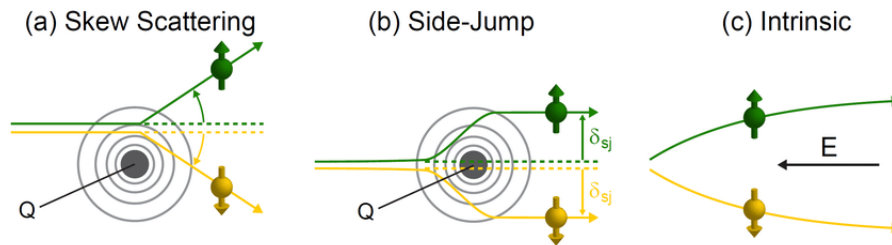


Figure 1.3: Spin-dependent scattering mechanisms responsible for the SHE in NMs: (a) skew-scattering, (b) side-jump, (c) intrinsic.

#### Berry phase\* and Berry-phase curvature\*\*

The **Berry phase**, also known as the geometric phase, was named after the British physicist Sir Michael Berry. In 1984, Berry made a notable contribution to the overall comprehension of geometric phases in systems undergoing adiabatic (very slow) quantum evolution 17. However, this phenomenon was independently described almost 30 years earlier by S. Pancharatnam in the context of polarized light 127 and H. C. Longuet-Higgins in molecular physics 102.

Let us first try to grasp the concept of Berry phase before delving into the quantum mechanics description. Professor D. Natelson from Rice University provides a relatable analogy to intuitively understand the Berry phase 118. He suggests imagining taking a walk while holding an arrow and always keeping it pointing in the same local direction, let us say East. This walk is taken along a closed path. On a flat surface, if we return to the starting point, the arrow will still point East, as shown in Figure 1.4a.

However, if the walk is taken on a curved surface like a sphere, the arrow will rotate from its initial position when we come back to the starting point, even if we consistently maintain the local direction towards the East, as shown in Figure 1.4b. This angle of rotation is analogous to the Berry phase. The crucial point is that the local definition of East varies across the entire surface of the sphere.

Let us now dive into the brief quantum mechanics description of the Berry phase focusing on the essential results. For more details, we recommend referring to the original paper 17. M. Berry considered a basic Schrödinger equation with the

adiabatic  $\boldsymbol{\lambda}$  parameter-dependent Hamiltonian:

$$i\hbar\partial_t |\psi(t)\rangle = \hat{H}[\boldsymbol{\lambda}(t)] |\psi(t)\rangle \quad (1.5)$$

where  $\boldsymbol{\lambda}$  is a set of parameters (such as magnetic field, oscillation frequency, etc.) combined in a vector, which is periodic:  $\boldsymbol{\lambda}(0) = \boldsymbol{\lambda}(T)$ .

Assuming that the system undergoes a slow adiabatic perturbation (e.g. it stays in the ground state ( $n = 0$ ) without transitions and the initial state being:  $|\psi(t=0)\rangle = |n=0, t=0\rangle$ ). In other words, an eigenstate at time  $t$  needs to be proportional to the ground state with a phase  $\phi$ , or mathematically, it writes:

$$|\psi(t)\rangle = e^{i\phi(t)} |0, t\rangle \quad (1.6)$$

Combining the equations [1.5](#) and [1.6](#), it leads to the Schrödinger equation:

$$i\hbar\partial_t |\psi(t)\rangle = E_0(t) |\psi(t)\rangle \quad (1.7)$$

with  $E_0(t)$  energy of the ground state.

As a consequence, a simple solution for  $\phi(t)$  would be written, as follows:

$$\phi(t) = -\frac{1}{\hbar} \int_0^t E_0(t') dt' \quad (1.8)$$

However, Equation [1.8](#) is not entirely correct. There is an additional component missing, because we need to take into account the fact that the state  $|\psi(t)\rangle$  varies locally with  $\boldsymbol{\lambda}(t)$ . After adding this component  $\mathbf{b}$  to the equation [1.8](#) and plugging the latter in Equation [1.7](#), we can derive it and solve for  $\mathbf{b}(t)$ . And finally, we can express  $\mathbf{b}(t)$  in terms of  $\boldsymbol{\lambda}$  and get the final expression:

$$\mathbf{b} = i \oint_C \langle 0, \boldsymbol{\lambda} | \partial_{\boldsymbol{\lambda}} | 0, \boldsymbol{\lambda} \rangle d\boldsymbol{\lambda} \quad (1.9)$$

This integral is a line integral around some closed path in  $\boldsymbol{\lambda}$ -space, corresponding to the **Berry phase**.

We can define the vector potential  $\mathbf{A}(\boldsymbol{\lambda})$  as follows:

$$\mathbf{A}(\boldsymbol{\lambda}) = \langle 0, \boldsymbol{\lambda} | \partial_{\boldsymbol{\lambda}} | 0, \boldsymbol{\lambda} \rangle \quad (1.10)$$

The curl of this vector potential is an effective field called the **Berry-phase curvature**. So the integral of this effective field around the closed path corresponds to the flux of this effective field.

### 1.2.2 Rashba-Edelstein effect

Another more recent mechanism that enables the conversion of charge currents into spin currents and vice versa is the Rashba-Edelstein effect (REE). It was first theoretically introduced by V.M. Edelstein in 1990 [38](#) and experimentally demonstrated for the first time in 2013 by J.C. Rojas Sanchez et al. at the Bi/Ag interface [159](#). However, before diving into the topic of charge-to-spin interconversion, which is a non-equilibrium effect, let us first concentrate on the fundamental concepts of systems in equilibrium what is commonly referred to as Rashba-like physics.

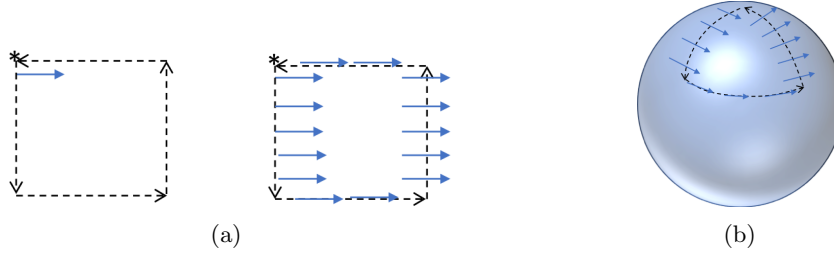


Figure 1.4: Intuitive explanation of the Berry phase: (a) On a flat surface, when we return to the initial point (represented by \*), the arrow points to the East, as initially. (b) On a curved surface, when returning to the initial point, the arrow rotates to a position different from an initial one. This angle of rotation represents the Berry phase. Adapted from [118].

### 1.2.2.1 Rashba-like physics

In 1955, Dresselhaus demonstrated that the structural inversion symmetry breaking, also known as structural inversion asymmetry (SIA), can lead to a spin-orbit splitting of bands in non-centrosymmetric bulk zinc-blende semiconductors [34]. This effect is what we now call the Dresselhaus effect. Examples of such materials include GaAs, InSb, CdTe, among others. The Dresselhaus effect results in a spin-dependent splitting of the energy dispersion relation  $E(\mathbf{k})$ , which is cubic in  $\mathbf{k}$  for energy bands with the symmetry  $\Gamma_6$ .

Subsequently, Rashba and Sheka demonstrated that the spin splitting of bands associated with s-electrons near the  $\Gamma$  point is linear in  $\mathbf{k}$  and isotropic when  $\mathbf{k}$  is perpendicular to the crystal's  $c$  axis [135]. This leads to a circular "cross section" of the energy dispersion  $E(\mathbf{k})$ . This phenomenon is now known as Rashba spin-orbit coupling.

Later on, this concept was extended to the two-dimensional electron gas (2DEG) by Vas'ko [170] and Bychkov and Rashba [21]. Under the influence of the Rashba effect, the electron's spin and momentum become coupled in such a way that the direction of electron motion affects its spin orientation and vice versa. In other words, the electron's spin is entangled with its momentum.

We can naively think that at an interface, the description of Rashba SO coupling states is under dominating effect of the electric field normal to the interface, e.g.  $\mathbf{E} = -\nabla V = -\partial_z V \mathbf{z}$ , where  $\mathbf{z}$  is unity vector normal to the interface. According to a simple Bychkov-Rashba model, the Rashba Hamiltonian  $\hat{H}_R$  at interfaces (surfaces) has then the following form:

$$\hat{H}_R = \alpha_R \boldsymbol{\sigma} \cdot (\hat{\mathbf{k}} \times \hat{\mathbf{z}}) \quad (1.11)$$

where  $\alpha_R = -\frac{g\mu_B E_0}{2mc}$  is material-dependent Rashba coefficient and  $\boldsymbol{\sigma}$  is Pauli spin matrix vector.

However, in crystals, the electrostatic potential gradient still remains spherical (the approximation that we made in Section [1.1]), even at the interfaces:  $\mathbf{E} = -\nabla V(\mathbf{r}) \approx \frac{1}{r} V \mathbf{r}$ . It means that the interface does not affect the spin-orbit coupling, but rather the Bloch electrons acquire a momentum-dependent angular momentum  $\mathbf{L}(\mathbf{k})$ . It is due to the inversion symmetry breaking.

In an atom, the Rashba SOC term writes, if projected to the Bloch states  $|\phi_{n,\mathbf{k}}\rangle$ :

$$\langle \phi_{n,\mathbf{k}} | H_{SO} | \phi_{n,\mathbf{k}} \rangle = \lambda_{SO} \boldsymbol{\sigma} \cdot \mathbf{L}_n(\mathbf{k}) = \mu_B \boldsymbol{\sigma} \cdot \mathbf{B}_{SO}^n(\mathbf{k}) \quad (1.12)$$

where  $\lambda_{SO}$  is the SOC parameter that is proportional to the atomic number  $Z$  (it

results in a larger SOC in heavy atoms comparing to lighter ones, as we mentioned in Section 1.1) and  $\mathbf{B}_{\text{SO}}^n(\mathbf{k})$  is Rashba SOC effective field.

This effective field is odd in momentum  $\mathbf{k}$ :  $\mathbf{B}_{\text{SO}}^n(\mathbf{k}) = -\mathbf{B}_{\text{SO}}^n(-\mathbf{k})$ , which is a consequence of an inversion symmetry breaking.

While this simple model provides correct analytical form of the Rashba Hamiltonian, it remains unsatisfactory regarding the control of the magnitude of the Rashba parameter  $\alpha_{\text{R}}$ . This approach does not take into account interband mixing, which is crucial when it comes to develop materials with large Rashba SOC.

According to this model, it is clear that the materials with heavy elements (such as Pt, Au, Bi, etc.) exhibit larger spin splitting due to strong atomic spin-orbit coupling, but the role of the non-centrosymmetric electrostatic potential or the crystal field in which atoms are submerged is not fully understood. Achieving an optimal compromise between atomic spin-orbit coupling and the crystal field is essential for maximizing Rashba-like spin splitting. PtCoO<sub>2</sub> is suggested to achieve a maximal Rashba spin splitting [158]. Orbital mixing is crucial for designing materials with significant Rashba-like spin-orbit coupling. Although a complete theory is yet to be established, these studies provide inspiring directions for further development.

### 1.2.2.2 Non-equilibrium Rashba effects: Rashba-Edelstein effect and inverse Rashba-Edelstein effect

As mentioned previously, the combination of the spin-orbit coupling and Rashba spin splitting is the origin of the charge current to pure spin current interconversion in certain systems lacking inversion symmetry, for example at the interface of a NM/FM bilayer.

When injecting a 2D charge current  $\mathbf{j}_c^{2\text{D}}$  along  $x$  direction in such a bilayer, the Fermi contour will experience a shift  $\Delta\mathbf{k}$ . It results in non-equilibrium spin accumulation along  $y$  direction, as shown in the Figure 1.5 (a). The 3D spin current  $\mathbf{j}_s^{3\text{D}}$  will propagate and relax in the adjacent FM layer. In the reciprocal effect, called inverse Rashba-Edelstein effect (IREE), the injection of a 3D spin current along  $y$  direction will lead to a shift  $\Delta\mathbf{k}$  of the Fermi contour and non-equilibrium charge population, as well as a 2D charge current  $\mathbf{j}_c^{2\text{D}}$  along  $x$  direction in the Rashba material, as shown in the Figure 1.5(b).

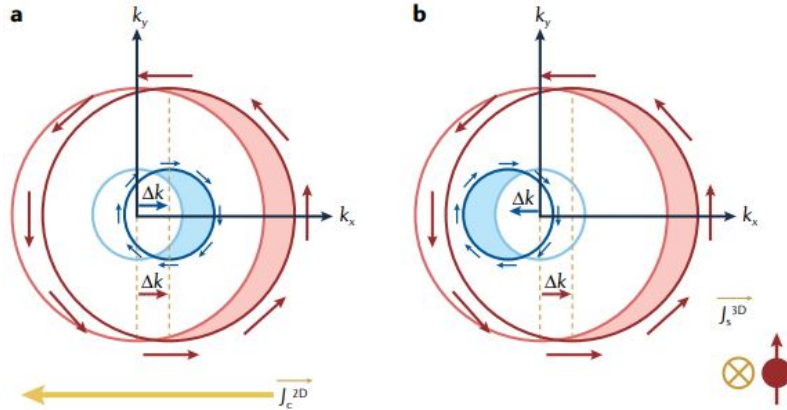


Figure 1.5: Schematic illustration of a Fermi contour under a) a Rashba-Edelstein effect, and b) an inverse Rashba-Edelstein effect. Adapted from [18].

The figure of merit of the REE is its conversion efficiency:  $q_{\text{REE}} = \frac{j_s^{3\text{D}}}{j_c^{2\text{D}}}$ , which is expressed in  $\text{m}^{-1}$ .

While the SHE arises from bulk spin-orbit coupling, the REE arises from interface spin-orbit coupling. In metallic bilayers, these two effects usually coexist together. Both effects lead to the generation of a pure spin current that enable to manipulate spins by spin-orbit torque. This makes the disentangling of these two effects a challenging task. The main difference between them is that the REE converts a 2D charge current into a 3D spin current, whereas the SHE converts a 3D charge current into a 3D spin current. As a consequence, the SHE conversion efficiency  $\theta_{\text{SH}}$  is dimensionless, whereas the dimension of the REE conversion efficiency  $q_{\text{REE}}$  is  $L^{-1}$ .

In a NM/FM bilayer, the interface transparency plays an important role in the charge-to-spin conversion, for example, through the spin mixing conductance [184]. Considering transparent enough interfaces, the transferred spin current  $j_s^{3\text{D}}$  is related to the charge current  $j_c^{3\text{D}}$  in the SHE material in the following way [100], [154], [80]:

$$j_s^{3\text{D}} = \theta_{\text{SH}}(1 - \text{sech}(t_{\text{NM}}/\lambda_{\text{sf}})) \times j_c^{3\text{D}} \quad (1.13)$$

where  $t_{\text{NM}}$  is the thickness of the SHE non-magnetic material, and  $\lambda_{\text{sf}}$  is its spin diffusion length.

Considering that  $j_c^{2\text{D}} = t_{\text{NM}} j_c^{3\text{D}}$ , Equation [1.13] becomes:

$$j_s^{3\text{D}} = \theta_{\text{SH}}(1 - \text{sech}(t_{\text{NM}}/\lambda_{\text{sf}})) \frac{1}{t_{\text{NM}}} \times j_c^{2\text{D}} \quad (1.14)$$

So in order to compare the SHE and REE efficiencies, it was proposed to compare the maximum ratio of the conversion obtained after integrating the 3D current in the SHE case into an equivalent 2D current for  $t_{\text{NM}} \cong 1.5\lambda_{\text{sf}}$  [137]. We then obtain :

$$q_{\text{REE}} = \frac{j_s^{3\text{D}}}{j_c^{2\text{D}}} = 0.38 \frac{\theta_{\text{SH}}}{\lambda_{\text{sf}}} \quad (1.15)$$

The REE is a non-equilibrium effect, so the conversion efficiency depends on the spin relaxation time  $\tau_t$  across the interface. A short spin relaxation time leads to a large 3D spin current. The REE conversion efficiency writes, as follows [65]:

$$q_{\text{REE}} \propto \frac{\alpha_{\text{R}}}{v_F^2 \hbar \tau_t} \quad (1.16)$$

where  $v_F$  is the Fermi velocity.

As for the inverse Rashba-Edelstein effect, the conversion efficiency  $\lambda_{\text{IREE}}$  writes as:  $\lambda_{\text{IREE}} = \frac{j_c^{2\text{D}}}{j_s^{3\text{D}}}$  in  $\text{m}$ . In addition, relation between  $\lambda_{\text{IREE}}$  and  $\theta_{\text{SH}}$  is:

$$\lambda_{\text{IREE}} = \theta_{\text{SH}} \lambda_{\text{sf}} \quad (1.17)$$

And finally, the IREE conversion efficiency can be written as [65]:

$$\lambda_{\text{IREE}} \propto \frac{\alpha_{\text{R}}}{\hbar} \frac{\tau_p \tau_t}{\tau_p + \tau_t} \quad (1.18)$$

where  $\tau_p$  is the spin transmission time across the interface. Therefore, long spin relaxation time and spin transmission time across the interface leads to a large efficiency coefficient.

### 1.3 Generation of spin-orbit torques

Previously, we have described two predominant microscopic mechanisms that could produce the spin currents necessary for the generation of spin-orbit torques: the spin Hall effect and Rashba-Edelstein effect. These two effects can coexist in combination with additional effects arising from electron scattering at the interface between ferromagnetic and non-magnetic materials, or the generation of spin currents within a magnetic material.

Recently, a new proposition has emerged, suggesting that the orbital effect can also contribute to the generation of SOTs. In this scenario, the spin-orbit interaction enables the conversion of orbital current into a spin current, thus introducing an additional mechanism for SOT generation [52].

The magnetization dynamics is governed by the Landau-Lifchitz-Gilbert equation (LLG):

$$\frac{d\mathbf{m}}{dt} = -\gamma\mathbf{m} \times \mathbf{B}_M + \alpha\mathbf{m} \times \frac{d\mathbf{m}}{dt} + \frac{\gamma}{M_s}\mathbf{\Gamma} \quad (1.19)$$

where  $\mathbf{m}$  is the magnetization direction,  $\mathbf{B}_M$  is the effective field that corresponds to a sum of the external magnetic field and magnetic anisotropy,  $\gamma$  is the gyromagnetic ratio of electron,  $\alpha$  is the Gilbert damping parameter,  $M_s$  is the saturation magnetization and  $\mathbf{\Gamma}$  is the torque that we will discuss further.

The first term on the right side of Equation 1.19 corresponds to the precession of the magnetization  $\mathbf{m}$  around the effective field  $\mathbf{B}_M$ . The second term corresponds to the relaxation of the magnetization towards its equilibrium position. And finally, the third term will be at the center of our interest. It represents the torques that may be induced by an electrical current.

The spin-orbit torque  $\mathbf{\Gamma}$  can be decomposed into at least two mutual perpendicular components (see Figure 1.6):

1. The first experimental studies conducted by Miron et al. [112] in Co/Pt/AlO<sub>x</sub> and by Liu et al. in Co/Pt thin layers [98] proposed a longitudinal damping-like torque (DLT), also known as Slonczewski-like torque. The DLT, as suggests its name, acts on the magnetization as an effective magnetic damping term.
2. And a transverse field-like torque [7] (FLT) that acts as an effective magnetic field.

As a result,  $\mathbf{\Gamma}$  has the following form:

$$\mathbf{\Gamma} = \tau_{DL}\mathbf{m} \times (\mathbf{m} \times \boldsymbol{\sigma}) + \tau_{FL}(\mathbf{m} \times \boldsymbol{\sigma}) \quad (1.20)$$

where  $\boldsymbol{\sigma}$  is the spin polarization vector (it usually lies in the plane and perpendicular to both charge and spin currents) and  $\tau_{DL,FL}$  is the amplitude of the respective torques.

We can also express the SOT as follows:  $\mathbf{\Gamma} = \mathbf{M} \times \mathbf{B}$ . So that the DLT and FLT can be expressed in terms of the effective magnetic fields (see Figure 1.6):

$$\mathbf{B}_{DL} = B_{DL}(\mathbf{m} \times \boldsymbol{\sigma}) \quad (1.21)$$

$$\mathbf{B}_{FL} = B_{FL}\boldsymbol{\sigma} \quad (1.22)$$

Using the expression of the effective fields, we can write the SOT efficiency  $\xi_{DL,FL}^j$  as follows [106]:

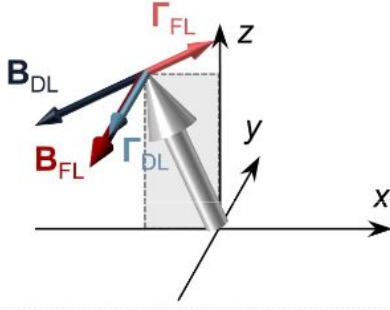


Figure 1.6: Schematic representation of the spin-orbit torques that can be decomposed into two components: damping-like and field-like torques, as well as their respective effective fields induced by the current injected along the  $x$  direction. Adapted from [88].

$$\xi_{\text{DL,FL}}^j = \frac{2e}{\hbar} \frac{M_s t_{\text{FM}}}{j} B_{\text{DL,FL}} \quad (1.23)$$

where  $j$  is current density, and  $t_{\text{FM}}$  is thickness of a FM layer.

This parameter is of utmost importance, as it quantifies the effective magnetic field per unit of charge current for a given system. Consequently, it becomes essential when comparing the charge current densities required to switch the magnetization in different systems. Understanding and accurately determining this parameter enable efficient and reliable control of magnetic materials in spintronic devices.

However, oftentimes when comparing different systems, one needs to take extra precautions, as there is a crude approximation that assumes that all current flows uniformly in the NM layer using a parallel resistor model. In reality, this assumption is not always true, and the actual current distribution can be more complex and non-uniform within the material layers. It is essential to consider these deviations from an ideal system to accurately analyze and interpret the results when studying devices and their behavior under different conditions.

Another nuance is that in general, experimental studies attribute the origin of the DLT to the spin Hall effect, whereas the origin of the FLT is attributed to the Rashba-Edelstein effect. This association stems from the assumption that torques involving the transfer and absorption of spin angular momentum, such as those arising from the SHE, exhibit damping behavior. On the other hand, torques originating from the REE exhibit field-like behavior.

However, these assumptions are not entirely accurate. The SOT can be influenced and altered by various factors, such as interband transitions, spin-dependent scatterings, spin relaxation, and spin precession. These additional mechanisms can significantly affect the behavior of the spin-orbit torque experienced by magnetic materials, making the disentangling of the two contributions of the SOT more complex and nuanced. We will come back to this discussion in Section 5.1.2.

## 1.4 Materials for spin-orbit torques

In this section, we will discuss materials capable of generating SOTs, such as heavy metals, two-dimensional materials, oxides. We will focus on topological insulators in the

next chapter, which are of central interest. However, it is important to note that this section does not provide an exhaustive list of all SOT materials. For a more comprehensive list, we recommend readers to consult the corresponding reviews in the field [106], [149], [155], [55].

### 1.4.1 Ferromagnet/non-magnetic metal systems

The pioneering studies of the SOTs were conducted in FM/NM metal layers, usually capped with an oxide layer. The first observation of the SHE-induced DLT was made in Pt/NiFe bilayer by Ando et al. [5] in 2008. The system was excited by a microwave field, and the resulting change in magnetic damping was measured.

As for the FLT, its first evidence was reported by Miron et al. in 2010. They observed the current-driven nucleation of magnetic domains upon magnetic field in Pt/Co/AlO<sub>x</sub> system [110]. The origin of this effect was attributed to the REE.

Another milestone in the history of SOTs was reached in 2011 when Miron et al. observed SOT-driven magnetization switching in the Pt/Co/AlO<sub>x</sub> system [112]. This demonstration of magnetization switching underscored its significance for SOT applications. They noted that the origin of the DLT of this magnitude could not solely be attributed to the SHE in Pt. However, Liu et al. asserted that the SHE was the sole origin of the DLT [98]. This disagreement marked the beginning of an ongoing debate regarding the origin of the DLT and the FLT in SOTs research.

Quickly after this, another systems, such as Ta/CoFeB/MgO [100], [50], [7], W/CoFeB/Ti [126], Hf/CoFeB/MgO [164], [2], [134], Pd/Co/AlO<sub>x</sub> [51] were studied in terms of the quantification of the SOTs.

Large SOT efficiencies were obtained from the 5*d* metals, such as highly resistive  $\beta$ -W, Ta, and Pt. The commonly accepted SOT efficiency for Pt is around  $\theta_{\text{SH}} \approx 0.10$  [99], [5], [50], [185], [120]. As for  $\beta$ -W and Ta, their SOT efficiencies correspond, respectively to  $\theta_{\text{SH}} \approx -0.33$  [126] and  $\theta_{\text{SH}} \approx -0.10$  [50], [100], [132].

It is important to note that  $\theta_{\text{SH}}$  includes SOT-generating mechanisms other than the SHE, as disentangling the individual contributions of different mechanisms can be challenging. Therefore, the total spin Hall angle  $\theta_{\text{SH}}$  is a collective parameter that accounts for the combined effects of various mechanisms responsible for generating spin-orbit torques in a given system.

If the SOTs originate from the intrinsic SHE,  $\theta_{\text{SH}}$  is directly proportional to the material's resistivity  $\rho$ :  $\theta_{\text{SH}} = \sigma_{\text{SH}}\rho$ , where  $\sigma_{\text{SH}}$  represents the SHE conductivity. Interestingly, despite the moderate resistivity exhibited by Pt and Pd layers, their SOT efficiency is quite large, indicating that they possess a substantial intrinsic spin Hall conductivity and density of states at the Fermi level [120], [51].

Other ways to enhance the SOT efficiency exist, such as:

- Varying the thickness of the FM [81], [44], [45] and the NM layers [99], [51], [164], [120], [57],
- Interfacial tuning (e.g. insertion of different spacer layers [44], [125], [186], annealing and intermixing between layers [50], [7], oxidation [112], etc.),
- Measuring the SOT efficiency as a function of temperature [132], [80].

### 1.4.2 Ferromagnet/two-dimensional materials systems

Some two-dimensional (2D) Van der Waals materials, such as transition metal dichalcogenides, possess strong spin-orbit coupling and broken inversion symmetries, enabling them to generate SOTs through the Rashba-Edelstein effect.

In 2016, Shao et al. demonstrated a large field-like torque in monolayers of MoS<sub>2</sub> and WSe<sub>2</sub> combined with a CoFeB ferromagnetic layer, with field-like efficiency values of  $\xi_{DL} = -0.14$  and  $\xi_{DL} = -0.3$ , respectively [150]. However, the damping-like torque was found to be negligible.

A significant damping-like torque was observed in the Weyl semi-metal WTe<sub>2</sub> combined with NiFe layers, with a value of  $\xi_{DL} = 0.04$ , as reported by MacNeill *et al.* [105]. This work is particularly intriguing as it achieved an out-of-plane spin polarization in WTe<sub>2</sub>, which is a result of its reduced crystal symmetry (lack of two-fold rotational invariance around the *c* axis) when a current is applied along a low-symmetry axis of the surface. In contrast, in NM/FM systems, only in-plane spin polarization is allowed due to symmetry constraints. Consequently, an external magnetic field is typically required to switch the magnetization perpendicular to the plane.

This finding indicates that 2D materials have the potential to offer field-free switching of perpendicular magnetization, which could lead to more energy-efficient magnetic devices.

### 1.4.3 Ferromagnet/oxides systems

One of the most extensively investigated oxide systems is the two-dimensional electron gas (2DEG) formed at the interface between two insulators: SrTiO<sub>3</sub> (STO) and LaAlO<sub>3</sub> (LAO). The 2DEG at the LAO/STO interface can exhibit a strong Rashba spin-orbit coupling, as experimentally demonstrated by the presence of a robust current-induced Rashba field in the 2DEG [117]. This behavior is attributed to the strong electric field perpendicular to the conduction plane that the 2DEG experiences due to its confinement at the LAO (polar)/STO (non-polar) interface [22].

Remarkably, a giant SOT efficiency was observed at room temperature in the STO/LAO/CoFeB heterostructure ( $\theta_{SH} = 6.3$ ) [173]. This efficiency value is two orders of magnitude larger than that found in heavy metals, such as Pt and Ta.

Furthermore, the inverse Rashba-Edelstein effect at the STO/LAO interface was demonstrated through a spin-pumping experiment, which revealed a significantly large  $\lambda_{IREE}$  [96], [156]. This was achieved by tuning the Fermi level. Moreover, it has been shown that the 2DEG exhibits a large spin diffusion length, reaching 300 nm [67], [123].

Due to all of these observations, 2DEGs represent a promising alternative to heavy metals for SOT generation, as they offer the opportunity to control the SOT efficiency by tuning the Fermi level.

After discussing the mechanisms and materials for SOT, let us now dive into the exciting subject of topological insulators, which offer an alternative as SOT generators.

## Chapter 2

# Topological insulators for spin-orbit torques

Previously, we discussed the materials used to generate efficient SOTs. In this chapter, we will particularly focus on a specific class of materials: topological insulators (TIs).

TIs are a class of materials that have attracted significant attention in recent years due to their particular electronic properties. They are a unique type of insulators in which the bulk material is non-conductive, but the surface is topologically protected and conductive. The topological metallic surface states are robust against impurities and disorder, making them potentially useful for applications in advanced spintronics devices.

The discovery of TIs has opened up new avenues for exploring exotic quantum phenomena, such as the quantum spin Hall effect and Majorana fermions.

In this context, research on TIs has been growing rapidly, with a focus on understanding their fundamental physics and exploring their potential applications in novel electronic devices. This includes efforts to develop methods for synthesizing and engineering TIs, as well as techniques for characterizing and manipulating their electronic properties.

TIs are of great interest for spin-orbit torques applications. TIs are characterized by an energy band structure that exhibits a bulk bandgap, similar to conventional insulators, but also has gapless metallic states at the surfaces or edges of the material. The topological surface states in TIs have a helical spin texture, where spin is locked to the momentum and protected by time-reversal symmetry. This spin texture that arises from a strong spin-orbit coupling can be exploited to generate SOTs. The topological protection of these states also makes them less susceptible to scattering and other forms of decoherence, which is crucial for SOT-based devices. In addition, TIs can be combined with magnetic materials to create hybrid structures that can exhibit strong SOTs. Recent research has shown that TIs can be used to create highly efficient spin-to-charge current interconversion and spin-orbit torque devices, indicating that they hold great potential for the development of advanced electronic technologies. That was the main motivation behind our research topic.

In this chapter, we will describe the main properties of TIs, will then review different TIs and compare their spin-to-charge-current interconversion efficiency. And finally, we will focus on a particular TI, i.e.  $\text{Bi}_{1-x}\text{Sb}_x$  by discussing its crystal and electronic structures, as well as providing the recent state of the art on the material.

## 2.1 Definition and main properties of topological insulators

Traditionally, Landau's approach is used to describe the states that are characterized by symmetries they break. However, the quantum Hall effect introduced a new classification based on **topological order** [163], [175]. In this context, certain properties, like quantized Hall conductance and number of gapless boundary modes, stay invariant despite gradual changes in materials properties, only changing during quantum phase transitions. Topological insulators can be thus characterized by this new kind of order: topological order, which cannot be described by the standard symmetry breaking approach.

### Trivial vs. non-trivial insulators

An insulator is a material where valence electrons are strongly bound to atoms in closed shells. As a result, the occupied valence-band states are separated from the empty conduction-band states by an energy gap. These states can be described by Bloch states defined in a periodic Brillouin zone, which are the eigenstates of the Bloch Hamiltonian  $H(\mathbf{k})$ .

It's important to note that even though some insulators may have a larger energy gap than others, they belong to equivalent phases. This means that by adjusting the Hamiltonian  $H(\mathbf{k})$ , one can continuously transform one insulator into another without closing the energy gap. There is a topological equivalence between different insulating phases, indicating that all conventional insulators are equivalent to one another and also to the vacuum, making them trivial. However, there are states with an energy gap that are not topologically equivalent to the vacuum. These are non-trivial insulators and are the focus of our interest.

### The quantum Hall state

In 1980, it was discovered that, in a system made of electrons confined in a bi-dimensional film and exposed to a strong perpendicular magnetic field  $H$ , the Hall resistance was quantized. This phenomenon is known as the quantum Hall effect (QHE).

In the strong magnetic field, the electrons undergo a cyclotron orbital motion due to the Lorentz force [83]. On the edges of the system, the electrons cannot complete the full rotation and bounce on the edges, creating edge conduction channels, as shown in Figure 2.1 (left). It means that electrons flow in one direction on one side and in the other direction on the other side.

The orbital motion is quantized at the cyclotron frequency  $\omega_c$ , resulting in energy spectra composed of quantized Landau levels:  $E_m = \hbar\omega_c(m + \frac{1}{2})$ , where  $m$  represents the Landau level index. These Landau levels can be seen as a band structure. When  $N$  Landau levels are occupied and the remaining levels are empty, the "Fermi level" resides within the energy gap that separates occupied and empty states. When  $H$  increases,  $\omega_c$  also increases, changing the positions of the Landau levels with respect to the Fermi level. When the latter is in between two Landau levels, the "bulk" electrons circular orbitals are trapped on the impurities and do not participate to the conduction, which is only ensured by the edge states, insensitive to disorder: the transmission is perfect, the resistivity is quantized and forms a plateau. The system is a bulk insulator and a perfect metal on its edges. When the Fermi level aligns with a Landau level, the bulk states spatially extend and back-scattering from one edge state to the other edge becomes possible. The resistivity increases and one edge state is destroyed to fill the new Landau level.

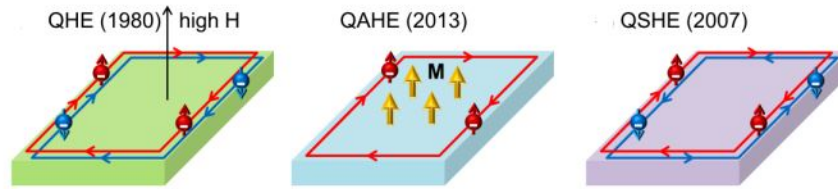


Figure 2.1: From left to right: **-The quantum Hall effect (QHE)**. When exposed to a high magnetic field  $H$ , the energy of electrons becomes quantized into discrete Landau levels. **-The quantum anomalous Hall effect (QAHE)**. It corresponds to the quantized version of the anomalous Hall effect, described in Section 1.2.1. When the magnetization of the film is perpendicular to the plane, only spin-up electrons flow clockwise along the edge. **-The quantum spin Hall effect (QSHE)**. It exists in bi-dimensional semi-conductors with a pure quantized spin Hall conductance in the absence of an external magnetic field.

Materials exhibiting the quantum Hall effect have great potential for low-power consumption devices because impurities do not scatter conductive electrons. The quantization arises from the presence of dissipationless one-dimensional conduction channels along the edges, with the rest of the film behaving as an insulator. This arrangement prevents electrons from backscattering, as the backward channel exists only on the opposite side of the film, separated by an insulating state. Despite the existence of these lossless conduction channels, it is important to note that the QHE still necessitates a strong external magnetic field.

In 1988, Haldane et al. theoretically predicted the possibility of quantized transverse resistance without the need for an external magnetic field in a bi-dimensional lattice [53]. This prediction was experimentally confirmed in 2013 by Chang et al. using a thin ferromagnetic topological insulator [23]. This phenomenon is known as the quantum anomalous Hall effect (QAHE). When the magnetization of a ferromagnet is perpendicular to the plane, only spin-up electrons flow clockwise along the film's edge, as depicted in Figure 2.1 (center).

In 2007, it was shown that the lossless edge channels appear in HgTe/CdTe quantum well structures still without an external magnetic field [93]. Due to the spin-orbit coupling present in heavy atoms, there exists two conduction edge channels: clockwise and counterclockwise. The directions of these conduction channels are defined by the spin orientation (up or down), as shown in Figure 2.1 (right). It corresponds to the quantized version of the spin Hall effect, known as the quantum spin Hall effect (QSHE).

### The Chern number

The quantum Hall effect gives a first example of a non-trivial topological insulator. It can be characterized by a so-called Chern number.

Mathematically speaking, one can group geometrical objects into broader topological classes. For example, a mug can be smoothly deformed into a donut because they both have the same number of holes (one), so they belong to the same topological class (see Figure 2.2). However, it is not possible to smoothly deform a donut into an orange because they do not have the same number of holes, meaning that it must undergo a discontinuous deformation. So, they belong to different topological classes.

The topological classes can be described by the means of a concept of a topological



Figure 2.2: An example of two geometric objects that are topologically equivalent. A mug can be smoothly deformed into a donut because they both have the same number of holes (one), so they belong to the same topological class. Image credit: [133].

invariant [58]. Two geometric objects that are topologically equivalent have the same topological invariant. In other words, a topological invariant is a property of an object that does not change when the object undergoes a smooth, continuous deformation. It is the Chern invariant  $n \in \mathbb{Z}$  (set of integers). It derived from what is used to be called the TKNN invariant, named after Thouless, Kohmoto, Nightingale and den Nijs [163]. In this case, the topological invariant can be expressed as the integral of the object's curvature over the entire surface of the object.

In solid-state physics, the Chern invariant can be seen in terms of the Berry phase described in Section 1.2.1. The Bloch states  $|u_m(\mathbf{k})\rangle$  are invariant under transformation along a closed loop. Their Berry phase is the line integral of the vector potential  $\mathbf{A}_m = i \langle u_m | \partial_{\mathbf{k}} | u_m \rangle$ , and the Berry curvature is the curl of this vector potential:  $\mathbf{F}_m = \nabla \times \mathbf{A}_m$ . The Chern number corresponds to the total Berry flux over the Brillouin zone:

$$n_m = \frac{1}{2\pi} \int_{\text{BZ}} d^2\mathbf{k} \mathbf{F}_m \quad (2.1)$$

It is a topological invariant, since it remains unaltered when the Hamiltonian varies smoothly.  $n = 0$  corresponds to a trivial state, while  $n \neq 0, n \in \mathbb{Z}$  corresponds to Chern insulating states.

A simple example of the quantum Hall effect is a Haldane model in a graphene under a periodic magnetic field [53].

## 2D topological insulator

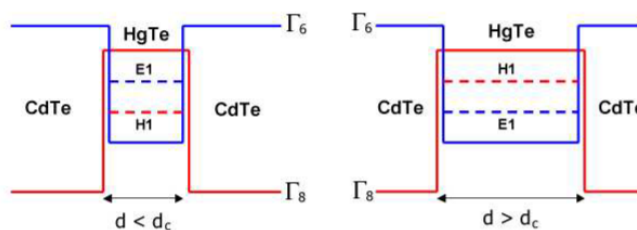
The concept of a quantum Hall spin insulator was first introduced theoretically in graphene by Kane and Mele in 2005 [73]. Subsequently, this state was experimentally observed in HgCdTe quantum well structures [16]. The quantum Hall spin insulator is known as a 2D topological insulator. A stronger spin-orbit coupling in these structures than in graphene allows for a particular topological class of insulators, as long as time-reversal symmetry is preserved, i.e. in the absence of an external magnetic field. This is referred to as the **Z<sub>2</sub> invariant**, which is of particular interest [58].

In 2006, Bernevig, Hughes, and Zhang studied a quantum well structure: CdTe/HgTe/CdTe [16]. While CdTe has a "classic" semi-conductor band structure where the conduction band is formed from  $s$ -electrons and the valence band is formed from  $p$ -electrons, HgTe has a strong spin-orbit interaction that results in  $p$ -orbitals levels rising above the

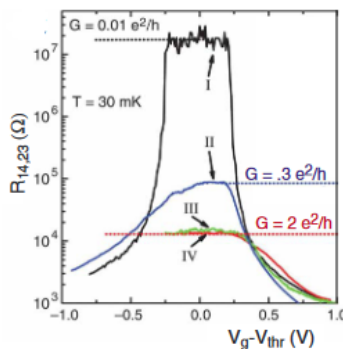
$s$ -orbitals levels. It leads to a band inversion, when the thickness of the HgTe layer  $d$  is larger than the critical thickness  $d_c$ :  $d > d_c = 6.3$  nm. However, when  $d < d_c$ , the quantum well structure has a normal band and behaves as a trivial insulator. The band structures in both regimes are shown in Figure 2.3(a).

They measured quantum well structure's resistance as a function of a gate voltage. The gate voltage can tune the Fermi energy through the bulk energy gap in both regimes. These results are shown in Figure 2.3(b). In the normal regime the film resistance is large at zero gate voltage. This indicates a trivial insulating state. In the inverted regime, however, the resistance is quantized associated to the edge states.

Thus, Bernevig, Hughes, and Zhang showed that depending on the thickness  $d$ , there is a quantum phase transition between the trivial and QSH insulators, as well as the existence of the edge states of the QSH insulator.



(a)



(b)

Figure 2.3: (a) The CdTe/HgTe/CdTe quantum well structure in the normal regime (left), when  $d < d_c$  and in the inverted regime, when  $d > d_c$  (right). Adapted from [16]. (b) The structure's resistance measurements as a function of a gate voltage: maximal resistance at zero gate voltage in the normal regime indicates an insulating behaviour (sample I) and quantized resistance in the inverted regime corresponding to the edge states (samples III and IV). Adapted from [93].

### 3D topological insulator

Later, the extension of the quantum spin Hall insulator to three dimensions was theoretically discovered by three independent groups: Fu, Kane, and Mele [49], Moore and Balents [114], and Roy [140]. Fu, Kane, and Mele showed the presence of the conductive states in the bulk topological order. In 2008, Hsieh et al. experimentally discovered the

first 3D topological insulator  $\text{Bi}_{1-x}\text{Sb}_x$  [61]. Later, the second generation Bi-based topological insulators, such as  $\text{Bi}_2\text{Se}_3$  [179],  $\text{Bi}_2\text{Te}_3$ , and  $\text{Sb}_2\text{Te}_3$  [58], were discovered. The distinctive signature of a 3D topological insulator is the presence of gapless surface states in the shape of a Dirac cone (cf. Figure 2.4(b)) within the bulk energy band gap (cf. Figure 2.4(a)).

We will discuss the electronic properties of the 3D topological insulator of our interest  $\text{Bi}_{1-x}\text{Sb}_x$ , as well as the methods for probing its surface states using ARPES in Section 2.3.2.

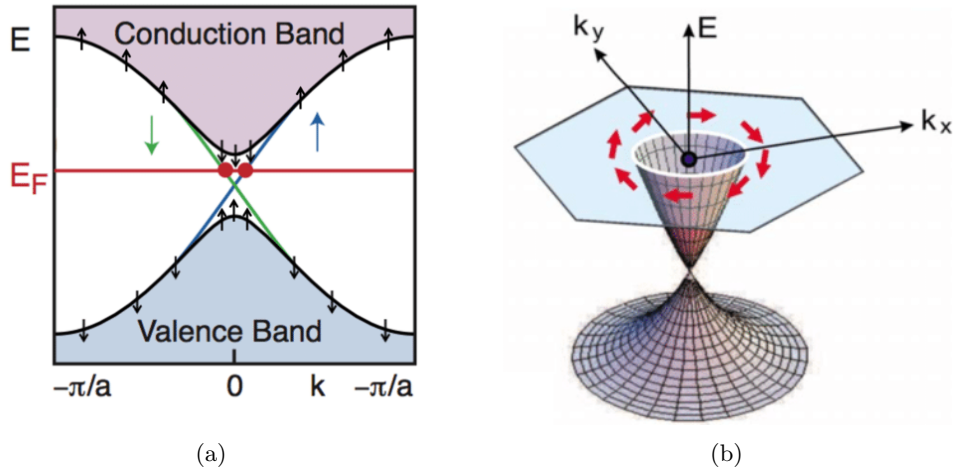


Figure 2.4: (a) Schematic representation of a band inversion in a 3D topological insulator. The band inversion leads to the emergence of topologically protected surface states within the bulk energy gap, with spins up and down oriented in opposite directions. Adapted from [58]. (b) Topological surface states of a 3D TI take the shape of a Dirac cone with spin-momentum locking. Adapted from [61].

## 2.2 Spin-orbit torques in topological insulators/ferromagnet systems

As mentioned previously, topological insulators possess spin-polarized surface states that are topologically protected by time-reversal symmetry, resulting in spin-momentum locking. Additionally, TIs are conductive on their surface while being insulating in the bulk. These unique properties make TIs a promising candidate for more efficient SOT compared to heavy metals. In fact, TIs have the potential to reduce the switching current by one order of magnitude, offering the possibility of low-power magnetic memory devices.

The TIs are also characterized by a hexagonal warping of the Dirac cone [91]. As a consequence, TIs have the ability to generate both in-plane and out-of-plane spin current density, which, in turn, can lead to the generation of both in-plane and out-of-plane torques.

The first demonstrations of large SOT in a TI were made in 2014. Fan et al. demonstrated it in the  $(\text{Bi}_x\text{Sb}_{1-x})_2/\text{Cr}-(\text{Bi}_x\text{Sb}_{1-x})_2\text{Te}_3$  bilayer [46], while Mellnik et al. did so in the  $\text{Bi}_2\text{Se}_3/\text{Ni}_{80}\text{Fe}_{20}$  bilayer [109]. The SOT efficiencies in these systems were found to

be  $\theta_{\text{SH}} = 425$  at  $T = 1.9$  K and  $\theta_{\text{SH}} = 2.0 - 3.5$ , respectively. Additionally, the switching current density was found to be  $J \approx 8.9 \times 10^4 \text{ A/cm}^2$ , which is two orders of magnitude lower than the current density necessary to switch the magnetization in FM/heavy metal systems.

As for the spin-to-charge conversion, it was measured in TIs, as well, by using the spin-pumping technique: in  $\text{Bi}_2\text{Se}_3$  [32],  $\text{Bi}_{1.5}\text{Sb}_{0.5}\text{Te}_{1.7}\text{Se}_{1.3}$  [152],  $(\text{Bi}_{1-x}\text{Sb}_x)_2\text{Te}_3$  [86], and  $\alpha\text{-Sn}$  [137].

Among all the studies involving TIs, there is a large discrepancy in the observed SOT efficiencies, ranging from 0.001 to 425. In TIs, the surface states lie within the bulk energy gap, and so does the Fermi level. Consequently, the Fermi level only intersects with the surface states. As a consequence, as TIs possess a narrow bulk band gap, which makes them sensitive to crystalline defects and doping by impurities, it can cause the Fermi level to shift into the conduction band, affecting the electronic structure. Therefore, the discrepancy in the observed SOT efficiencies can be attributed to the different TI crystalline quality. Moreover, the presence of defects and impurities can lead to the formation of a two-dimensional electron gas (2DEG) with a strong Rashba spin-splitting [82]. This can also significantly influence the SOT efficiency.

As topological insulators are sensitive to the crystalline quality and the presence of disorder and impurities, it appeared that synthesizing TIs using molecular beam epitaxy helps minimizing the presence of defects. However, this fabrication method is laborious and not industry-friendly. As a result, there have been attempts to grow TIs using magnetron sputtering. In particular, sputtered  $\text{Bi}_2\text{Se}_3$  possesses a large resistivity, allowing the charge current to flow on the interface rather than "inside" the TI layer [31]. This enhances the SOT efficiency (in [31],  $\theta_{\text{SH}} = 18.8$ ). However, the role of their topological surface states in SOT generation has not been completely understood yet.

Another issue that can arise when using TI/FM bilayer systems is the complex electronic hybridization induced by the proximity of a ferromagnet and a topological insulator. Theoretical studies have shown that in  $\text{Bi}_2\text{Se}_3$ /3d-transition ferromagnet systems (such as Co, Ni, Cu), the Fermi level shifts to the conduction band of bulk  $\text{Bi}_2\text{Se}_3$ , and the electronic hybridization between the topological surface states and the metallic bands can destroy or distort the helical spin texture of the TI surface states [183]. These considerations must be taken into account when analyzing the experimental data in such systems.

Let us now focus on the SOT generation in a specific TI:  $\text{Bi}_{1-x}\text{Sb}_x$ .

### 2.3 Charge-to-spin interconversion in BiSb/ferromagnet systems

$\text{Bi}_{1-x}\text{Sb}_x$  (BiSb) is the first 3D topological insulator that was experimentally realized [61]. It exhibits a narrow bulk band gap (around 30 meV) and an overall complex band structure [101], which makes it more challenging to study compared to other TIs, e.g.,  $\text{Bi}_2\text{Se}_3$  or  $\text{Bi}_2\text{Te}_3$ . However, despite these complexities, as we will see later, the quantization effect can occur in ultra thin films of BiSb leading to a larger band gap while still exhibiting the band inversion near  $\bar{M}$  point in the  $x = 0.07 - 0.30$  concentration window [11]. As a result, BiSb can be a promising candidate for the development of realistic SOT-MRAM devices.

In this section, we will first introduce the crystal structure of BiSb. We will then discuss the band structure of BiSb and how it evolves depending on the Sb concentration

and the thickness of BiSb. Finally, we will describe the recent state of the art on the charge-to-spin interconversion properties in BiSb thin films.

### 2.3.1 Crystal structure of $\text{Bi}_{1-x}\text{Sb}_x$

Bismuth (Bi) and antimony (Sb) are semi-metals located in column V of the periodic table. In their pure form and their alloys, both Bi and Sb adopt a rhombohedral crystal structure, specifically known as the  $A_7$  structure of the  $R\bar{3}m$  point group. This crystal structure consists of two atoms per unit cell and can be seen as a slightly distorted cubic lattice, as illustrated in Figure 2.5(a).

To describe this rhombohedral structure, commonly used coordinate systems are as follows: the binary axis with  $C_2$  symmetry, the trigonal axis with  $C_3$  symmetry and the bisectrix axis, normal to the two other axes.

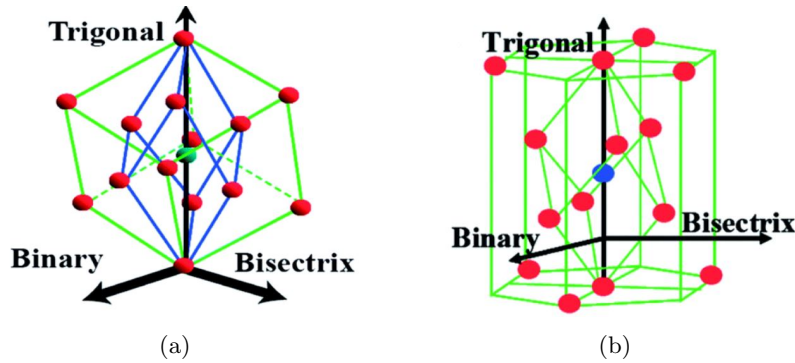


Figure 2.5: (a) The rhombohedral structure of Bi and Sb under a distorted cubic system. (b) The rhombohedral structure of Bi and Sb under a hexagonal framework. Adapted from [162].

Because of the  $C_3$  symmetry of the trigonal axis, the hexagonal notation is commonly used to describe different crystalline directions in the rhombohedral crystal structure. In this notation, the trigonal, binary, and bisectrix axes are respectively denoted by  $[0001]$ ,  $[\bar{1}\bar{2}10]$ , and  $[10\bar{1}0]$ , as illustrated in Figure 2.5(b).

As Bi and Sb have similar lattice parameters (presented in Table 2.1),  $\text{Bi}_{1-x}\text{Sb}_x$  alloys form a solid solution. Moreover, the hexagonal lattice parameters of  $\text{Bi}_{1-x}\text{Sb}_x$  follow Vegard's law when  $0 \leq x \leq 0.3$  [29]. Vegard's law is an empirical rule stating that the lattice parameters of a solid solution alloy vary linearly with the composition of the alloy  $x$ . This linear relationship allows to predict and control the lattice parameters of  $\text{Bi}_{1-x}\text{Sb}_x$  alloys with different compositions. As we can see in Figure 2.6(a), this is especially true at  $298 \pm 3\text{K}$ . However, when the temperature decreases, the lattice parameter  $c$  slightly deviates from the Vegard's law (cf. Figure 2.6(b),(c)). The relationships between the lattice parameters and the Sb concentration  $x$  at different temperatures are visible in Figure 2.6(a)-(c) as well.

### 2.3.2 Electronic properties of $\text{Bi}_{1-x}\text{Sb}_x$

In this section, we will discuss the electronic properties of pure Bi and Sb and how the incorporation of Sb into Bi lattice changes the band structure of Bi. We will also discuss the variation of the band structure of BiSb, when varying the thickness of the layers.

| Lattice parameter |   | 298±3K | 78K    | 4.2K   |
|-------------------|---|--------|--------|--------|
| Bi                | c | 11.862 | 11.814 | 11.797 |
|                   | a | 4.546  | 4.535  | -      |
| Sb                | c | 11.273 | 11.23  | 11.21  |
|                   | a | 4.308  | 4.30   | -      |

Table 2.1: Lattice parameters of pure Bi and Sb at different temperatures (Å). Extracted from [29].

The first Brillouin zones of Bi and Sb can be visualized as a Brillouin zone for the face-centered cubic (fcc) lattice elongated along the trigonal axis. In Bi, the electronic band structure exhibits a hole pocket at a single T-point in the Brillouin zone, while three equivalent electron pockets are present at the L-points, as illustrated in Figure 2.7(a). The hole Fermi surface corresponds to an ellipsoid of revolution along the trigonal axis, and the electron Fermi surfaces correspond to three quasi-ellipsoids elongated along a direction near the bisectrix axis. This anisotropic shape of the Fermi surfaces results in unusually small effective masses along certain directions, contributing to large electron mobilities in the material.

On the other hand, in Sb, the electronic band structure reveals electron pockets located at the L-points, similar to Bi, but with six equivalent hole pockets at the H-points.

Bi-Sb alloys are formed by the substitution of Bi atoms with Sb atoms in the Bi lattice. This process significantly modifies the band structure of Bi, leading to varying electronic properties as the composition of the alloy changes.

The band structure evolution of Bi-Sb alloys with varying Sb concentration ( $x$ ) at low temperature is depicted in Figure 2.7(b). The process of alloying can significantly influence various band parameters, leading to changes in the electronic structure of the material. Key band parameters that are affected by alloying include: the overlap between the L and T bands, the value of the energy gap  $E_g$  and the energy of the top of the H bands.

In Figure 2.7(b), the following observations can be made:

- When  $0 \leq x < 0.04$ , the overlap between the L and T bands decreases, and the band gap narrows with a semi-metallic character.
- At  $x \approx 0.04$ , the band structure becomes gapless, indicating a transition point.
- When  $0.04 < x < 0.07$ , the bonding  $L_s$  and  $L_a$  bands are inverted, leading to an increase in the band gap.
- At  $x \approx 0.07$ , the top of the T-band coincides with the top of the  $L_a$ -band. The alloy is now a semiconductor with an indirect gap between T and  $L_s$ .
- At  $x \approx 0.22$ , there is a second transition as the top of the H band increases.
- When  $x \geq 0.22$ , the band structure evolves towards that of pure Sb with a metallic character.

As a result, when the concentration of Sb is between 0.07 and 0.22, Bi-Sb alloys exhibit semiconductor behavior with a narrow band gap. The maximum band gap (30 meV) is observed at  $x = 0.15 - 0.17$ .

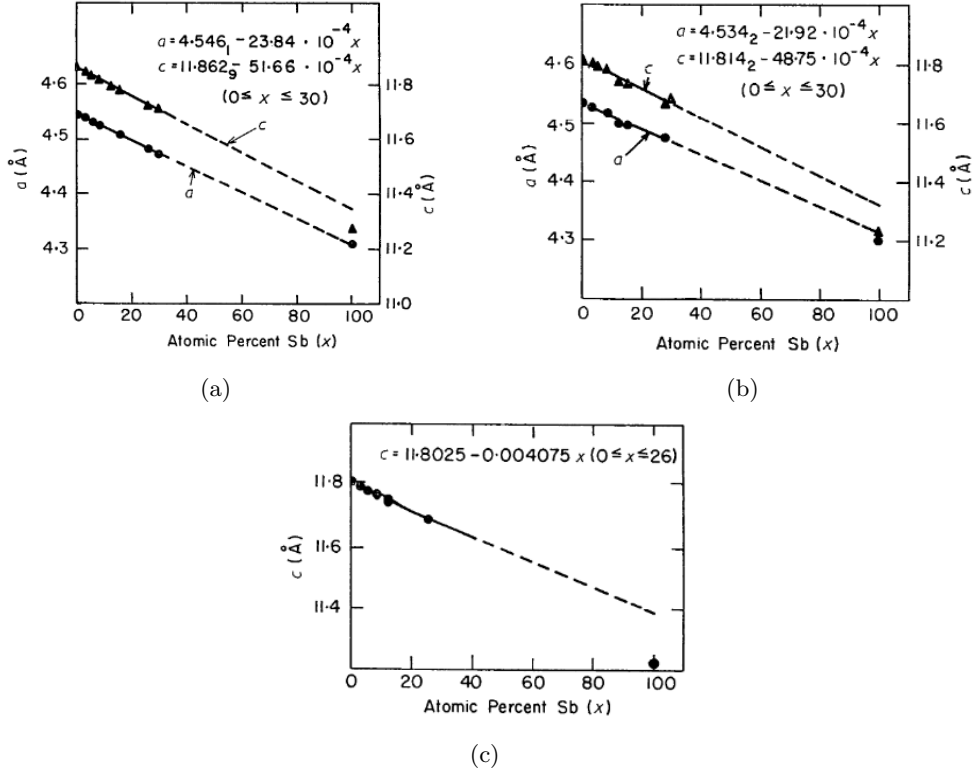


Figure 2.6: Hexagonal lattice constants of Bi-Sb alloys at: (a)  $298 \pm 3$  K, (b) 78 K, (c) 4.2 K. Adapted from [29].

As the electron energy gap is small in Bi-Sb alloys, the electron band parameters exhibit strong temperature dependence. The extrema of  $L_s$  and  $L_a$  bands increase and decrease, respectively, with increasing temperature [34]. Additionally, the effective masses at the extrema of the L bands also vary with temperature. However, the temperature dependence of band parameters for the T and H bands is not yet fully understood.

Due to these complexities and the strong temperature dependence of band parameters, it becomes challenging to analyze the transport properties of Bi-Sb alloys. The temperature-dependent variations in the band structure can significantly influence electron mobility, conductivity, and other transport properties. As a result, a comprehensive understanding of the temperature-dependent electronic properties of Bi-Sb alloys is important for their effective utilization in various applications.

In this study, our focus will be on the semiconductor phase of  $\text{Bi}_{1-x}\text{Sb}_x$  with  $0.07 \leq x \leq 0.22$ , where the bulk energy gap is maximized, and where a band inversion is observed, making it a promising candidate to exhibit topological surface states. Consequently, precise control over the Sb concentration in the alloy becomes crucial.

Figure 2.8(a) shows an experimental Fermi surface for a 15 nm-thick  $\text{Bi}_{0.85}\text{Sb}_{0.15}/\text{Si}(111)$  thin film measured by ARPES at Synchrotron SOLEIL by L. Baringthon et al. [11]. The obtained Fermi surface has a hexagonal core centered at  $\bar{\Gamma}$  with a six-fold symmetry, which is in excellent agreement with the tight-binding calculations, shown in Figure 2.9(b) [11]. It is surrounded by petals along the  $\bar{\Gamma M}$  directions. The hexagonal core, denoted by P1,

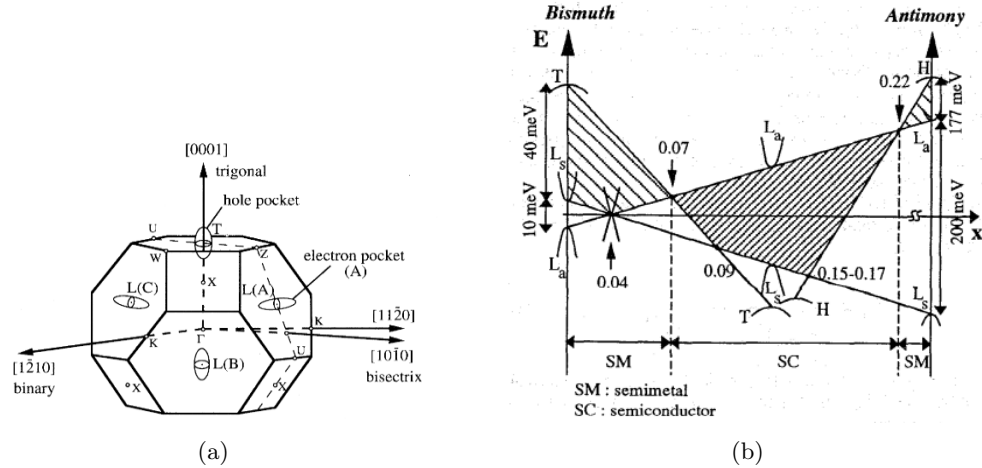


Figure 2.7: (a) Schematic representation of the Brillouin zone of Bi. Adapted from [63]; (b) Schematic diagram of the band edge configuration of Bi-Sb alloys as a function of Sb concentration  $x$  at low temperature. Adapted from [95].

is associated to the  $S_1$  state, whereas the hole pockets, denoted by P2, are associated to the  $S_2$  state. The P3 petal is also formed by the  $S_1$  state. Tight-binding calculations of the band structure of a 5 nm-thick  $\text{Bi}_{0.93}\text{Sb}_{0.07}$  along  $\bar{\Gamma M}$  showing two surface states,  $S_1$  and  $S_2$ , are demonstrated in Figure 2.9(a). The experimental band structure  $\bar{\Gamma M}$  is shown in Figure 2.8(b).

The topological and trivial phases are characterised, respectively, by an odd and even number of crossings of the Fermi level [12], [61]. Baringthon et al. considered the  $S_2$  surface state to be trivial, as it always crosses the Fermi level twice, regardless the concentration of Sb (cf. Figure 2.10 (right)). For all concentrations, excluding 7% and 30% of Sb, by counting the number of crossing of the Fermi level, the  $S_1$  surface state is found to be topologically non-trivial (cf. Figure 2.10). The topological nature of  $S_1$  is not obvious for the small (7%) and large (30%) concentrations [11].

Another approach to enhancing the band gap involves confining electron states. Indeed, reducing the dimensions of an infinite potential well can lead to an increased energy gap between levels. Thus, by reducing the thickness of the thin film, there is a potential to amplify the band gap. Baringthon et al. demonstrated the variation of the band structure of  $\text{Bi}_{0.79}\text{Sb}_{0.21}$  as a function of thickness of BiSb ranging from 2.5 to 15 nm (cf. Figure 2.11). They observed a well-defined P3 petal closing at  $\bar{M}$  for a 15 nm-thick BiSb layer. With decreasing thickness this petal opens at  $\bar{M}$ , indicating that the  $S_1$  surface state energy might shift downward below the Fermi level. These observations suggest that by reducing the thickness of the film, effects due to the quantum confinement appear.

### 2.3.3 Conversion between spin and charge currents in BiSb/ferromagnet systems

As mentioned previously, due to its complex band structure and narrow band gap, BiSb has not been studied as extensively as other topological insulators. However, in 2018, the group of Pham Nam Hai measured a giant SOT efficiency in the BiSb/MnGa bilayer to be  $\theta_{\text{SH}} \approx 52$  at room temperature using the coercivity method [77]. This value represents the

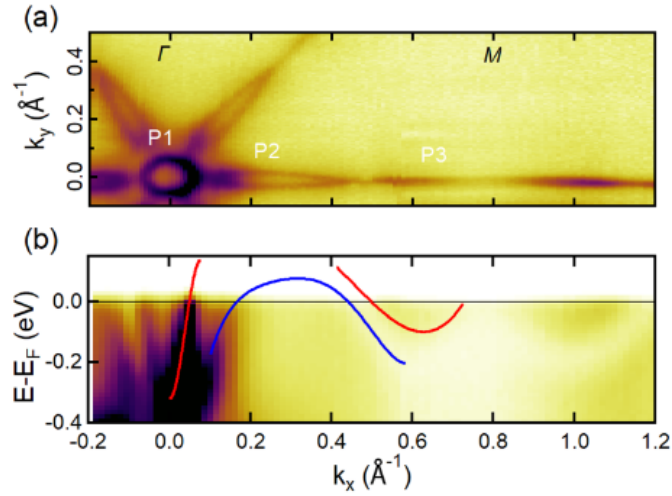


Figure 2.8: ARPES measurements for a 15 nm-thick  $\text{Bi}_{0.85}\text{Sb}_{0.15}/\text{Si}(111)$  thin film performed at room temperature with linearly vertical polarized light at 25.2 eV. (a) Recorded Fermi surface and (b) band structure along  $\overline{\Gamma M}$ . Red and blue lines correspond respectively to the two surface states:  $S_1$  and  $S_2$ . Adapted from [11].

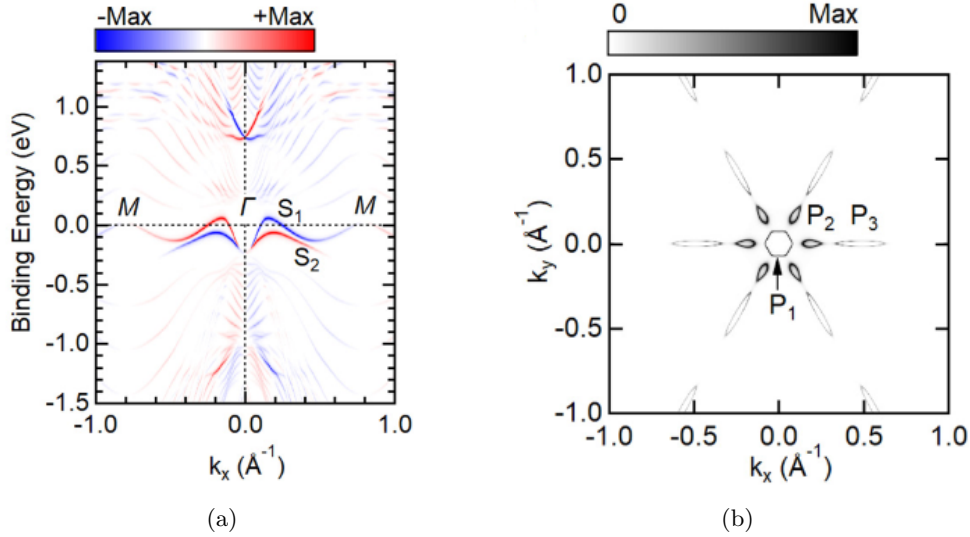


Figure 2.9: Tight binding calculations of the band structure of a 5 nm-thick  $\text{Bi}_{0.93}\text{Sb}_{0.07}$  (a) Electronic band structure along  $\overline{\Gamma M}$  showing two surface states:  $S_1$  and  $S_2$ . (b) Fermi surface showing three electron (P1, P3) and hole pockets (P2). Adapted from [11].

largest reported SOT efficiency in the literature to date. Furthermore, they successfully demonstrated SOT-driven magnetization switching in this system using a relatively low critical current density:  $J = 1.1 \times 10^6 \text{ A.cm}^{-2}$ .

Subsequently, BiSb was combined with other ferromagnetic thin layers to investigate its SOT efficiency [147], [64], [43], [78], [146]. However, there is a large discrepancy

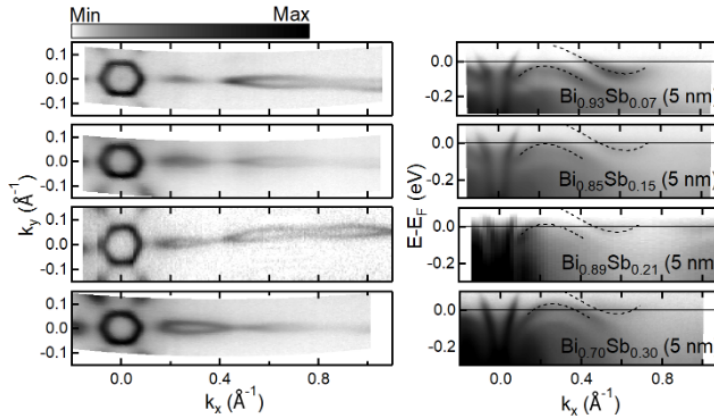


Figure 2.10: ARPES measurements for  $\text{Bi}_{1-x}\text{Sb}_x$  (5 nm) as a function of various concentrations of Sb  $x$ : 7%, 15%, 21% and 30%. Left panel: Fermi surfaces along the  $\Gamma\bar{M}$  direction. Right panel: Corresponding cross sections. Adapted from [11].

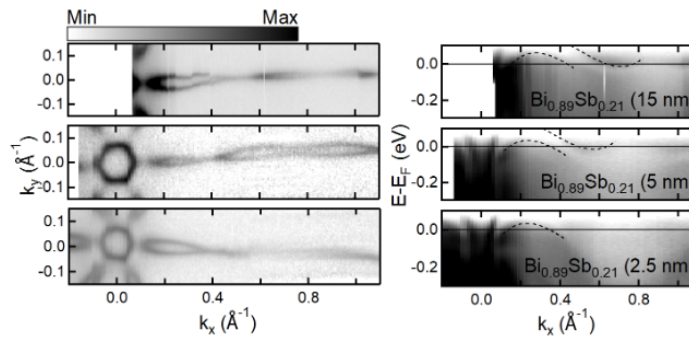


Figure 2.11: ARPES measurements for  $\text{Bi}_{0.79}\text{Sb}_{0.21}$  thin film as a function of various BiSb thicknesses: 2.5 nm, 5 nm, 15 nm. Left panel: Fermi surfaces along the  $\Gamma\bar{M}$  direction. Right panel: Corresponding cross sections. Adapted from [11].

among the obtained results, ranging from 0.01 to 61. This discrepancy can be attributed to differences in the layer deposition techniques (molecular beam epitaxy or magnetron sputtering), the crystalline and interface qualities of the heterostructure, and different measurement techniques. The largest reported value of the SOT efficiency for the sputtered BiSb layer is found to be 10.7 [79], [43].

Nevertheless, the question of the bulk versus interface contribution to the SOT has been addressed to a lesser extent. Chi et al. showed that the SOT efficiency in BiSb/CoFeB increased with increasing thickness until reaching saturation and was facet independent, suggesting that the dominant contribution to the SOT comes from the bulk [26]. However, the role of the topological surface states in SOT generation is not yet fully understood.

To shed light on this matter, in our previous study we attempted to pair measurements of the helical spin texture of the topological surface states of BiSb using spin- and angle-resolved photoemission spectroscopy (SARPES) with measurements of spin-to-charge conversion using THz emission spectroscopy in the time domain (THz-TDS)

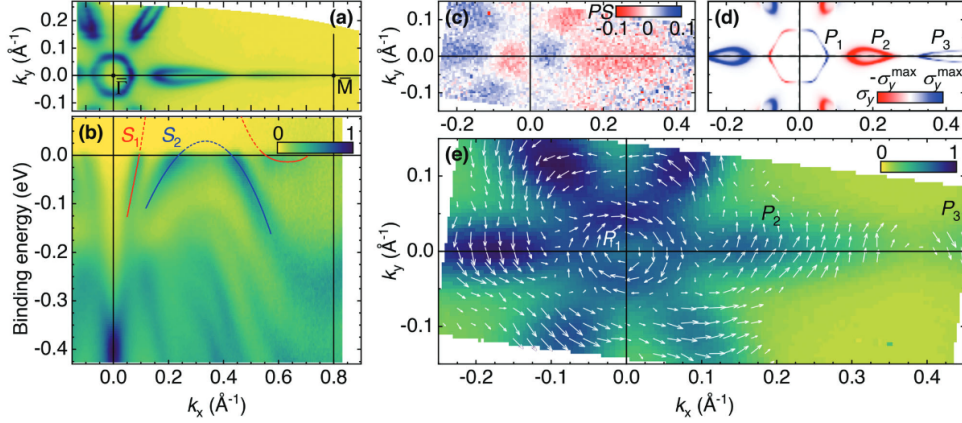


Figure 2.12: Spin-and angle-resolved photo-emission spectroscopy of a 5-nm thick  $\text{Bi}_{0.85}\text{Sb}_{0.15}$  film grown on  $\text{Si}(111)$ : (a) ARPES map at the Fermi level. The red and blue lines are used as guide to the eye to underline respectively two surface states  $S_1$  and  $S_2$ . (b) ARPES energy dispersion along the  $\bar{\Gamma}\bar{M}$  direction. The color bar designates the density of states in a.u. (c) Spin polarization at the Fermi level projected along  $\mathbf{y}$  axis measured by SARPES at room temperature. (d) Tight-binding calculations of the spin density of states projected on the first Brillouin zone.  $P_1$  and  $P_3$  are electrons pockets and  $P_2$  is a hole pocket. (e) Two spin density of states components measured by SARPES represented as a vector field with arrows representing spin polarization direction. Adapted from [138].

[138].

First, we confirmed the presence of surface states in  $\text{Bi}_{0.85}\text{Sb}_{0.15}$  (5 nm)/Co(2 nm)/ $\text{AlO}_x$  (3 nm) grown and measured by L. Baringthon et al. at SOLEIL synchrotron [11]. Figure 2.12(a) shows the measured ARPES map at the Fermi level in the first Brillouin zone, while (b) illustrates the energy dispersion along the  $\bar{\Gamma}\bar{M}$  direction, displaying two surface states within the bulk gap:  $S_1$  and  $S_2$ .

Figure 2.12(c) shows the measured spin polarization at the Fermi level projected along the  $\mathbf{y}$  axis, as measured by SARPES at room temperature, along with its corresponding tight-binding calculations (refer to Figure 2.12(d)). In Figure 2.12(e), two components of the spin density of states, as measured by SARPES, are represented as a vector field with arrows indicating the direction of spin polarization.

Figure 2.13 demonstrates that the amplitude of the THz signal from the same sample measured by (S)ARPES is 1.5 times larger than in the Co(2nm)/Pt(4nm) system. We, thus, demonstrated an efficient spin-to-charge conversion in BiSb/Co, attributable to the spin texture of the robust surface states of BiSb.

In the study conducted by Roschewsky et al. where the BiSb/Co heterostructure [139] was investigated, they found that the SOT signal measured by the second harmonic Hall voltage technique was dominated by contributions from the ordinary Nernst effect (ONE). The ONE is associated with the generation of a voltage when both a thermal gradient and an external magnetic field are present [6]. Since the voltage related to the ONE and the SOT have the same symmetry, distinguishing between them becomes highly challenging. Thus, they suggested that the previously reported spin Hall angle in other studies was mostly dominated by the ONE effect.

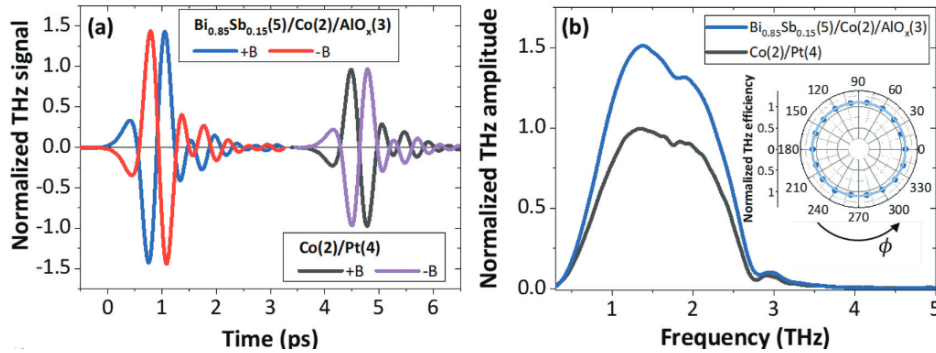


Figure 2.13: (a) THz emission signal in the time domain from Bi<sub>0.85</sub>Sb<sub>0.15</sub>(5 nm)/Co(2 nm)/AlO<sub>x</sub>(3 nm) in two directions of the in-plane saturating magnetic field ( $\pm B$ ). (b) Spectral components of the THz emission from Bi<sub>0.85</sub>Sb<sub>0.15</sub>(5 nm)/Co(2 nm)/AlO<sub>x</sub>(3 nm) for +B. Adapted from [138].

To overcome this challenge and distinguish between the SOT and the ONE contributions, measuring the harmonic Hall voltage as a function of the amplitude of the external magnetic field becomes necessary. To perform such measurements, a ferromagnet with perpendicular magnetic anisotropy is typically used. These efforts are crucial to gain a deeper understanding of the SOT mechanisms in BiSb-based heterostructures.

For the reasons mentioned above, it is highly important to ensure the high crystalline and interface quality of the studied heterostructure. Therefore, our goal was to develop high-quality thin layers of BiSb and a ferromagnet with a perpendicular magnetic anisotropy to study its SOT efficiency. For that purpose, we employed the molecular beam epitaxy technique to grow the entire heterostructure in the same growth chamber to preserve the interface quality. In the next chapter, we will focus on the MBE growth of these thin layers and their structural and magnetic characterization.



## Chapter 3

# Growth by molecular beam epitaxy and characterization of BiSb/MnGa//GaAs(001) bilayer

The high quality of the investigated heterostructure, as well as the interface between the topological insulator and ferromagnet, is crucial for efficient SOT generation. To ensure this, we employ the molecular beam epitaxy technique, which offers high-quality thin films.

In this chapter, we will begin by explaining the basics of MBE. The crystal structure of BiSb was detailed in Section 2.3.1, so we will directly pass to justifying the choice of a substrate, and explore the growth optimization conditions of B, as well as its structural BiSb. Afterward, we will focus on the choice of a ferromagnet material, explain its crystal structure, and discuss its growth conditions along with its structural and magnetic characterization. Finally, we will dive into the growth and characterization of the two layers combined, forming the BiSb/FM heterostructure.

### 3.1 Basics of the molecular beam epitaxy

Molecular beam epitaxy is a sophisticated and versatile thin-film deposition technique used to grow high-quality crystalline films with atomic precision. It is widely employed in the fabrication of semiconductor devices, quantum structures, and complex heterostructures due to its ability to precisely control the growth process at the atomic level.

#### 3.1.1 Main working principle, benefits and challenges of molecular beam epitaxy

The MBE process involves the deposition of atoms or molecules onto a heated substrate in an ultrahigh vacuum (UHV) chamber. The vacuum environment is essential to minimize the presence of contaminants and ensure the growth of clean and pure films. Usually, the UHV is achieved by using a cryogenic, an ionic, and a Ti sublimation pumps. Moreover, the residual molecules/species can be trapped by the hollow cryopanel situated in proximity of the effusion cells to prevent their re-evaporation. As a result, the residual pressure inside the growth chamber can reach  $10^{-10} - 10^{-11}$  Torr. Thanks to these conditions, one

can monitor the growth process using in-situ techniques, such as: reflection high-energy electron diffraction (RHEED), mass spectrometry, X-ray photoemission spectroscopy, etc.

Indeed, the real-time monitoring of the growth process is of high importance in MBE. For this, we employed the RHEED technique, which is commonly used to observe the surface reconstruction and crystal quality of the growing film. This technique provides valuable information about the film's thickness, surface roughness, and epitaxial relationship with the substrate. The working principle of the RHEED technique is given in Appendix.

In the MBE chamber, multiple effusion cells or sources containing elemental materials or compounds are heated. This leads to the evaporation of atoms or molecules from these sources. The evaporated species then travel in the vacuum chamber and interact with the substrate surface. The temperature of each source can be precisely controlled, enabling the deposition of different materials in a controlled manner. The principal elements of the MBE system are represented in Figure 3.1(a) and the photography of the actual system used for growing our samples is in Figure 3.1(b).

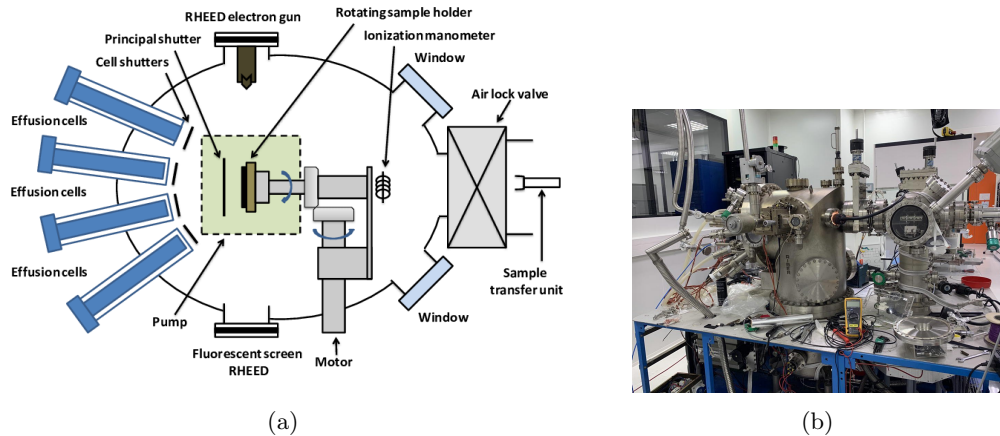


Figure 3.1: (a) Schematic representation of the principal elements of a molecular beam epitaxy system. (b) Photography of the molecular beam epitaxy system (Riber R2300) used to grow our samples at the C2N laboratory.

During the deposition process, the atoms or molecules arriving at the substrate surface adhere and form a crystalline layer, following the lattice structure of the substrate. The deposition rate and flux of each species can be relatively slow (about 0.1-1 Å/s) and accurately adjusted, allowing for precise control of the film thickness and composition.

One of the major advantages of MBE is its ability to achieve atomic-scale control over the film structure. The highly controlled growth conditions result in films with excellent crystalline quality, uniform thickness, and well-defined interfaces, making MBE an ideal technique for the growth of heterostructures and quantum structures.

However, MBE also has some challenges. It requires an elaborate UHV system to maintain a clean environment, and the growth rates can be slow compared to other deposition methods. Additionally, it may require the use of toxic or reactive materials, necessitating stringent safety measures.

### 3.1.2 Epitaxial growth modes

When growing a heterostructure, one can observe three main growth modes, which primarily depend on various parameters, such as lattice mismatch between different materials and the substrate and thermodynamic properties, such as surface energies, growth temperature, etc. The three epitaxial growth modes are the following:

1. **Volmer-Weber (VW) growth mode** refers to the three-dimensional growth mode that results in the formation of islands through local nucleation. Subsequently, the islands undergo further nucleation, leading to the formation of an epitaxial layer, as shown in Figure 3.2(a). When the deposited materials have a large lattice mismatch and the growth reaches a critical thickness, the strain accumulated in the film due to the mismatch becomes significant. As a result, the film undergoes strain relaxation, leading to the formation of dislocations. These dislocations allow the film to accommodate the lattice mismatch and reduce the strain energy, but they also introduce defects and imperfections in the crystal structure, which can affect the film's properties and performance.
2. **Frank-Van der Merwe (FVM) growth mode** offers a two-dimensional layer-by-layer growth. When atoms reach the surface of the substrate, they incorporate into the step kinks. The atoms smoothly cover the entire surface of the substrate, resulting in a continuous and uniform layer. This layer-by-layer process repeats until the desired film thickness is achieved, as portrayed in Figure 3.2(b).
3. **Stranski-Krastanov (SK) growth mode** combines the VW and FVM growth modes. The growth starts with a 2D layer-by-layer mode, where atoms incorporate into the existing lattice without forming islands, resulting in a smooth and continuous layer. However, when the critical thickness is reached, the strain between the film and the substrate becomes significant, leading to strain relaxation. At this point, the growth mode transitions to the formation of 3D islands, resulting in a more complex and rougher surface morphology (cf. Figure 3.2(c)). This combination of growth modes allows for the accommodation of lattice mismatch between the film and the substrate, while still achieving a continuous and coherent layer initially.

### 3.1.3 Growth rate and flux measurements

One of the most crucial growth parameters in epitaxial thin film deposition is the material flux. The material flux alone is not an intuitive parameter to directly understand how fast the layer is growing. To establish a clear relationship between the material flux and the growth rate, it is essential to clarify what these parameters represent when we refer to them in the context of thin-film deposition.

The manipulator equipped with an ion gauge inside an MBE growth chamber can be positioned in front of the effusion cells at the sample growth position to measure the pressure  $P_i$ , which corresponds to the beam flux of a specific molecular species  $i$ . This flux is emitted from a source at given temperature and/or valve opening. This pressure is commonly called the beam equivalent pressure (BEP). The BEP depends mainly on the ionization cross section, the thermal velocity of the atoms, as well as on the solid angle of the beam intercepted by the ionisation volume of the gauge.

The growth rate is a crucial metric that informs us about the speed at which the film is being deposited on the substrate. It represents the change in film thickness over a specific

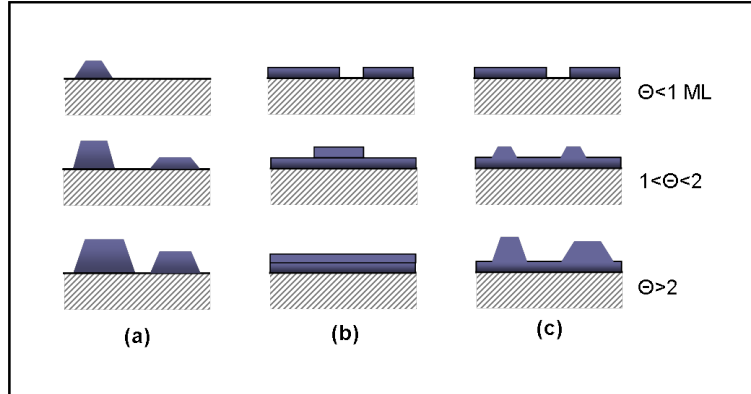


Figure 3.2: Schematic representation of the cross section of the thin layers in three main growth modes: (a) Volmer-Weber (VW), (b) Frank-Van der Merwe (FVM), (c) Stran-ski-Krastanov (SK).

time interval, typically measured in units of angstroms per second ( $\text{\AA}/\text{s}$ ) or nanometers per minute ( $\text{nm}/\text{min}$ ). It can be estimated either by performing the RHEED calibration, either by using some ex-situ techniques, such as TEM, X-ray reflectivity, secondary-ion mass spectroscopy (SIMS), X-ray diffraction, etc.

To establish the relationship between the growth rate and the BEP, we must take into account the effective deposition area on the substrate, as well. Instead of solely focusing on the growth rate, it is essential to consider the absolute atomic flux  $F_i$  for each specific molecular species  $i$ . It is expressed as the number of atoms or molecules arriving at the substrate surface per unit area and time (atoms or molecules per  $\text{cm}^2$  per second, for example).

The relationship between the BEP and the absolute atomic flux (or the growth rate) is the following. In the limited range of a temperature of a source, the growth rate can be considered as directly proportional to the material flux:  $F_i = \eta_i P_i$ , where  $\eta_i$  is a constant that varies from one material source to another. This relationship is a fundamental principle in MBE and other thin film deposition techniques.

To achieve precise control over the growth process and obtain the desired film thickness, it is essential to accurately regulate the material flux. The growth rate can be controlled by adjusting the temperature of the effusion cells or sources containing the material to be deposited. By increasing or decreasing the temperature, the evaporation rate of the material can be controlled, thereby controlling the material flux and consequently the growth rate. The classic method of flux calibration using RHEED oscillations is not suitable for determining the growth rate of BiSb and MnGa thin layers. Instead, we will employ the X-ray reflectivity and/or X-ray diffraction technique.

Now that we have covered the basic notions of MBE, we can discuss the development of the desired heterostructure.

## 3.2 Growth of BiSb by molecular beam epitaxy on different substrates

To achieve the growth of a high-quality heterostructure using MBE, the selection of a suitable substrate is of great importance. Significantly mismatched lattice parameters can introduce strain, dislocations, and misorientated grains, among other undesirable effects.

BiSb thin layers adopt a rhombohedral crystal structure, close to the hexagonal structure, that is why the use of a substrate with a hexagonal surface lattice is a natural choice. The common substrates used to grow BiSb in the literature are BaF<sub>2</sub>(111) [63], mica [171], [68], InSb(111) [27], GaAs(001) [143], [180], GaAs(111)A [180], [142], GaAs(111)B [180] and Si(111) [60], [85].

To grow our samples of BiSb, we chose InSb(111)B, GaAs(001), GaAs(111)A, and GaAs(111)B substrates. The choice of these substrates will be discussed in following Sections.

### 3.2.1 Growth on the InSb(111)B substrate

InSb crystallizes in a cubic zinc-blende structure, as shown in Figure 3.3(a). The InSb(111) surface can have two faces, denoted as A and B, with the A face terminated by In atoms and the B face terminated by Sb. While the lattice parameter of bulk InSb is  $a = 6.478 \text{ \AA}$ , the hexagonal representation of the (111) planes yields an in-plane interatomic distance of  $4.580 \text{ \AA}$ , as shown in Figure 3.3(b).

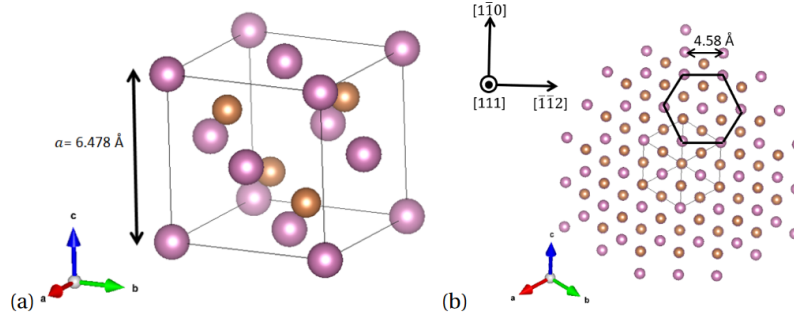


Figure 3.3: (a) Unit cell structure of InSb. Purple and yellow spheres represent In and Sb atoms, respectively. (b) (111) plan of InSb. Extracted from [10].

Utilizing the empirical relation established by Cucka et al. [29] at room temperature, as depicted in Figure 2.6(a), it becomes possible to calculate the lattice parameter of Bi<sub>1-x</sub>Sb<sub>x</sub> for a given Sb concentration. Consequently, for Sb concentrations ranging from  $0 < x < 0.3$ , the lattice parameter is predicted to fall within the range of  $4.546 \text{ \AA}$  to  $4.474 \text{ \AA}$ . Thus, the calculated in-plane lattice mismatch between BiSb and InSb(111) is estimated to be between  $-0.74\%$  and  $-2.3\%$ .

Given this relatively modest lattice mismatch, it was a logical step to initiate the growth optimization of BiSb thin layers on InSb substrates. Nonetheless, it's important to note that InSb is itself a semiconductor characterized by a narrow band gap ( $175 \text{ meV}$ ), rendering it unsuitable for our intended measurements, as we require an insulating

substrate.

### Substrate preparation

Before starting the growth process, substrate preparation is essential. First, the wafer is introduced into the MBE preparation chamber for degassing at 300°C for approximately an hour. Then, it is loaded into the main chamber where it needs to undergo a crucial step that involves the removal of the surface oxide layer through a deoxidation process applied to the substrate's surface. To achieve this, the substrate is heated to approximately 400°C for a brief period. As a result of this process, the RHEED pattern undergoes a transformation, transitioning from an absence of discernible pattern to manifesting streaky and spotty characteristics. This alteration in the RHEED pattern serves as an indication that the oxide layer has been successfully removed from the substrate's surface.

Subsequently, to achieve a smooth and flat surface, the growth of an InSb buffer layer is initiated. For this, the temperature is lowered to 390°C, and the shutters of both the In and Sb effusion cells are simultaneously opened for one minute.

An alternative method for achieving even smoother surface through chemical etching was also employed. This involved treating the surface by rinsing the substrate with a solution of lactic acid ( $\text{CH}_3\text{COOH}$ ),  $\text{HNO}_3$ , and HF (25:4:1). The subsequent steps included deoxidation inside the MBE growth chamber and the deposition of an InSb buffer layer, as previously described.

### Growth of BiSb and ex-situ characterisation

We started the BiSb growth process by investigating the impact of growth temperature on the thin film's quality. A series of samples was grown over a temperature range of 100°C to 250°C and at the growth rate of 0.5 Å/s, calibrated by X-ray reflectivity (XRR) and X-ray diffraction (XRD). The V/III (Sb/In) BEP flux ratio is 7. Note that we chose this temperature range according to the phase diagram of the Bi-Sb alloy (cf. Figure 3.4). In addition, the thickness of the thin films was estimated to be 15 nm, and the Sb concentration was estimated using the empirical law by Cucka et al. [29]: 18%. The estimation of the film's thickness, lattice parameter  $c$ , as well as Sb concentration will be discussed later.

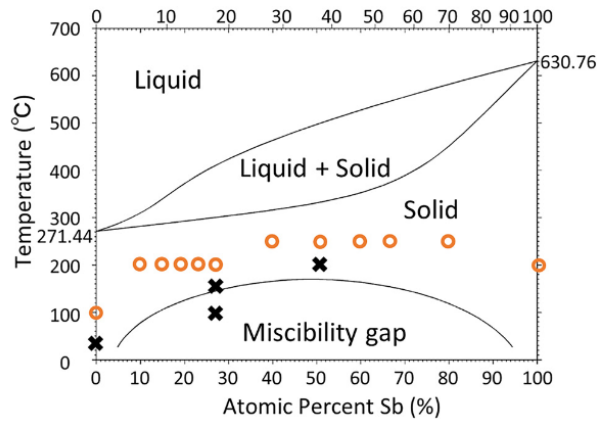


Figure 3.4: Phase diagram of  $\text{Bi}_{1-x}\text{Sb}_x$ . The epitaxial samples are represented by "o", while amorphous or polycrystalline samples are represented by "x". Extracted from [167].

The samples surface was characterized ex situ by the atomic force microscopy (AFM).

The working principle of AFM is described in Appendix. The scan field is  $1 \times 1 \mu\text{m}^2$ , which is representative of the whole film. All samples show triangular pits which is consistent with the hexagonal symmetry of the material. Moreover, all the triangular pits exhibit the same orientation, as shown in Figure 3.5. It indicates that the films are single crystalline.

The root-mean-square roughness  $R_q$  was also measured using AFM and is plotted in Figure 3.6. We can observe that when the growth temperature is maintained within the range of  $200^\circ\text{C}$  to  $230^\circ\text{C}$ , the triangular pits exhibit greater dimensions, leading to minimized root-mean-square roughness  $R_q$  values (0.605 nm and 0.646 nm, respectively).

The sample with the lowest surface roughness was characterized using X-ray diffraction. In this work, the XRD measurements were performed using a Bruker D8-Discover diffractometer with a copper source ( $K_{\alpha 1} = 1.54056 \text{ \AA}$ ). The working principle of XRD is given in Appendix. Figure 3.7 displays the  $\theta - 2\theta$  XRD spectra of a 15 nm-thick  $\text{Bi}_{0.82}\text{Sb}_{0.18}$  thin film grown on the  $\text{InSb}(111)\text{B}$  substrate. The observed peaks exclusively correspond to the  $\text{BiSb}(001)$  phase, suggesting that the film is a single crystal. Moreover, the presence of Laue oscillations in the film can be an indicator of a high-quality crystallographically aligned film.

After determining the optimal growth temperature, a series of samples was grown:

- a: **Bi//InSb(111)B**: as we mentioned previously, growing BiSb alloys consists in a simple substitution of Bi atoms by Sb atoms, so that a single Bi layer will serve us as a reference layer. The film was grown on the InSb substrate prepared without chemical etching at  $130^\circ\text{C}$ .
- b: **BiSb//InSb(111)B**: A layer of BiSb grown on the InSb substrate prepared without chemical etching at  $200^\circ\text{C}$ .
- c: **BiSb//InSb(111)B with chemical etching**: A layer of BiSb grown on the InSb substrate prepared with chemical etching at  $200^\circ\text{C}$ .

The samples were characterized ex situ by AFM, as well as by XRD. Figure 3.8 shows the AFM images of the three samples. The root-mean-square roughness  $R_q = 0.66 \text{ nm}$  is minimal for the sample (b) grown on  $\text{InSb}(111)\text{B}$  prepared without chemical etching.

Figure 3.9 illustrates the  $\theta - 2\theta$  X-ray diffraction spectra of samples a, b, and c. Each diffractogram exhibits peaks corresponding to the (001) phase, indicating that all samples are single crystals. The XRD spectra enable the calculation of lattice parameter  $c$  and layer thickness. The lattice parameter  $c$  can be calculated using the Bragg's law:

$$2d_{\text{hkl}} \sin \theta = n\lambda \quad (3.1)$$

where  $n$  is the diffraction order,  $\lambda$  is the wavelength of the incident X-rays,  $d_{\text{hkl}}$  is the interplane spacing,  $\theta$  is the angle between the incident ray and the surface of the sample. Moreover,  $d$  is related to the Miller indices  $h$ ,  $k$  and  $l$ , as follows:

$$\frac{1}{d^2} = \frac{h^2}{a^2} + \frac{k^2}{b^2} + \frac{l^2}{c^2} \quad (3.2)$$

Using these relations and knowing  $\theta$  of the observed pics ( $hkl$ ), we can thus calculate the lattice parameter  $c$ .

The thickness of thin films can be determined by fitting the Laue oscillations near the diffraction pics using the following relation:

$$I(\theta) = \left[ \frac{\sin(\pi N d \sin \theta / \lambda)}{\sin(N d \sin \theta / \lambda)} \right]^2 \quad (3.3)$$

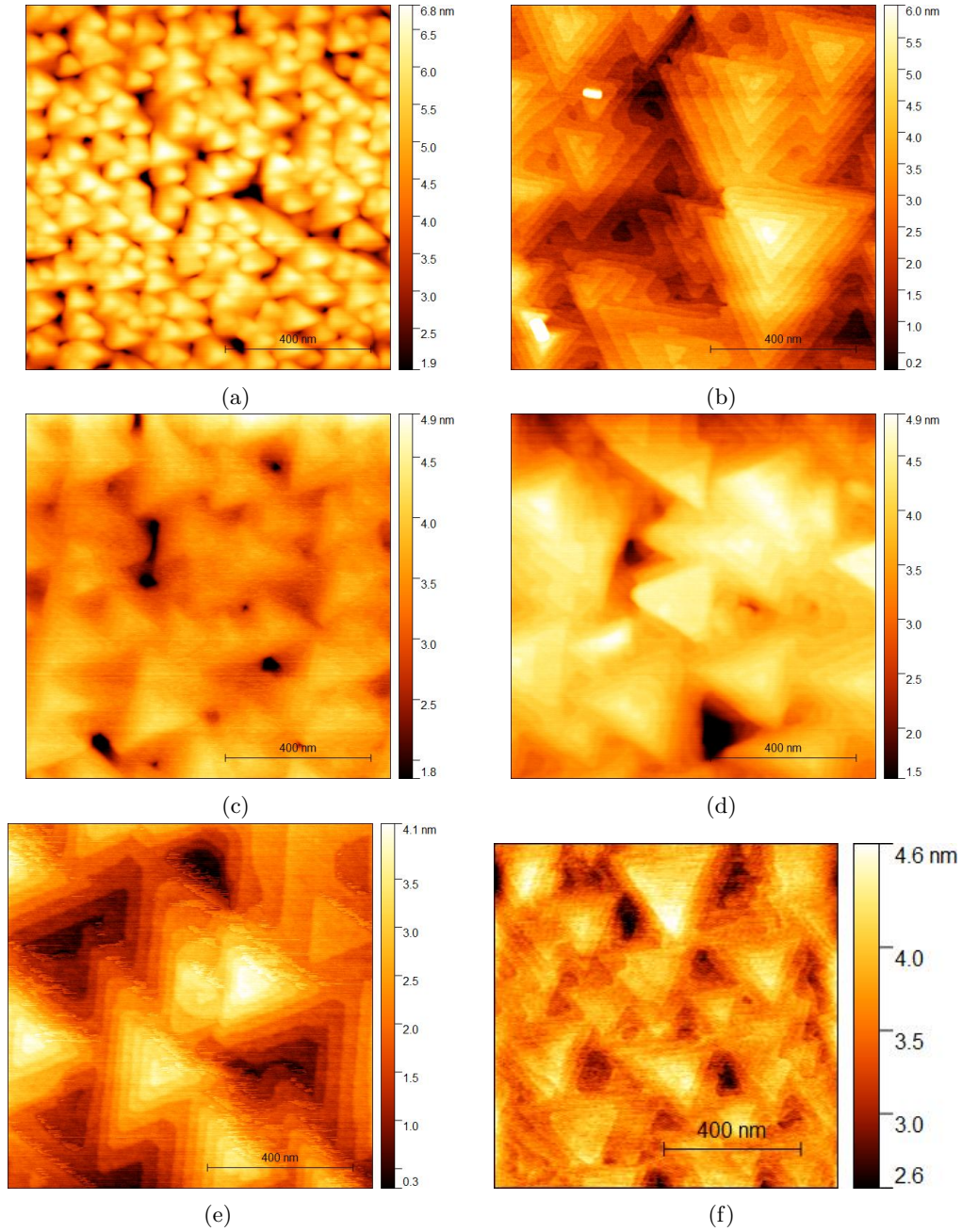


Figure 3.5: AFM images of  $\text{Bi}_{0.82}\text{Sb}_{0.18}$  thin films grown on the  $\text{InSb}(111)\text{B}$  substrates at various growth temperatures: (a) 100°C, (b) 120°C, (c) 150°C, (d) 180°C, (e) 200°C, (f) 230°C. All samples show triangular pits which is consistent with the hexagonal symmetry of the material. The triangular pits have the same orientation indicating single crystalline thin films. The scan field is  $1 \times 1 \mu\text{m}^2$ .

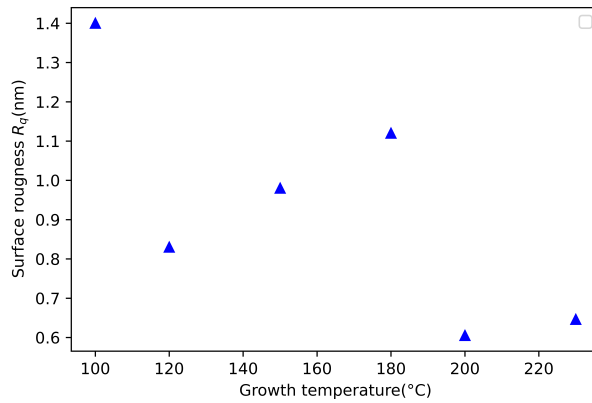


Figure 3.6: The relationship between surface roughness  $R_q$  of 15 nm-thick  $\text{Bi}_{0.82}\text{Sb}_{0.18}/\text{InSb}(111)\text{B}$  thin film and sample growth temperature was determined using AFM. It was observed that the minimal roughness, indicative of a superior surface quality, is achieved, when the growth temperature is between  $200^\circ\text{C}$ - $230^\circ\text{C}$ .

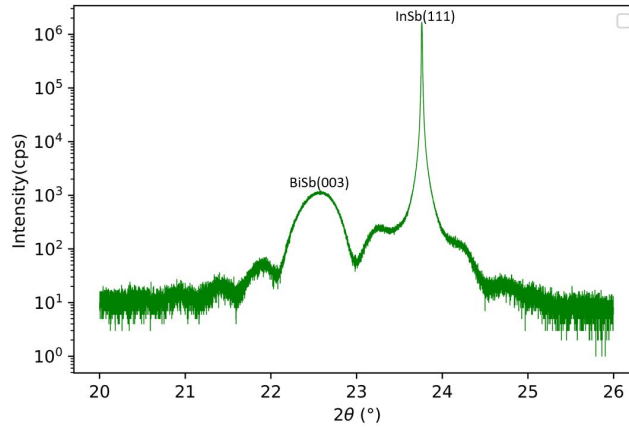


Figure 3.7:  $\theta - 2\theta$  X-ray diffraction spectra of a 15 nm-thick  $\text{Bi}_{0.82}\text{Sb}_{0.18}$  thin film grown on the  $\text{InSb}(111)\text{B}$  substrate. The observed peak exclusively corresponds to the  $\text{BiSb}(001)$  phase, suggesting that the film is a single crystal. The presence of Laue oscillations can be an indicator of a high-quality crystallographically aligned film.

where  $I$  is the intensity and  $N$  is the number of planes.

Furthermore, the thickness was determined using X-ray reflectivity data (see Figure 3.10). Due to the refractive index of materials being less than 1, X-rays incident on a smooth surface at a grazing angle undergo total reflection. By measuring the total reflection as a function of the incident angle relative to the thin film surface, a periodic oscillation profile is obtained. This profile can be fitted using parameters like density, roughness, and film thickness.

All these values for samples a, b, and c are presented in Table 3.1. Using the calculated cell parameter  $c$  and the empirical law of Cucka et al., the concentration of Sb in these

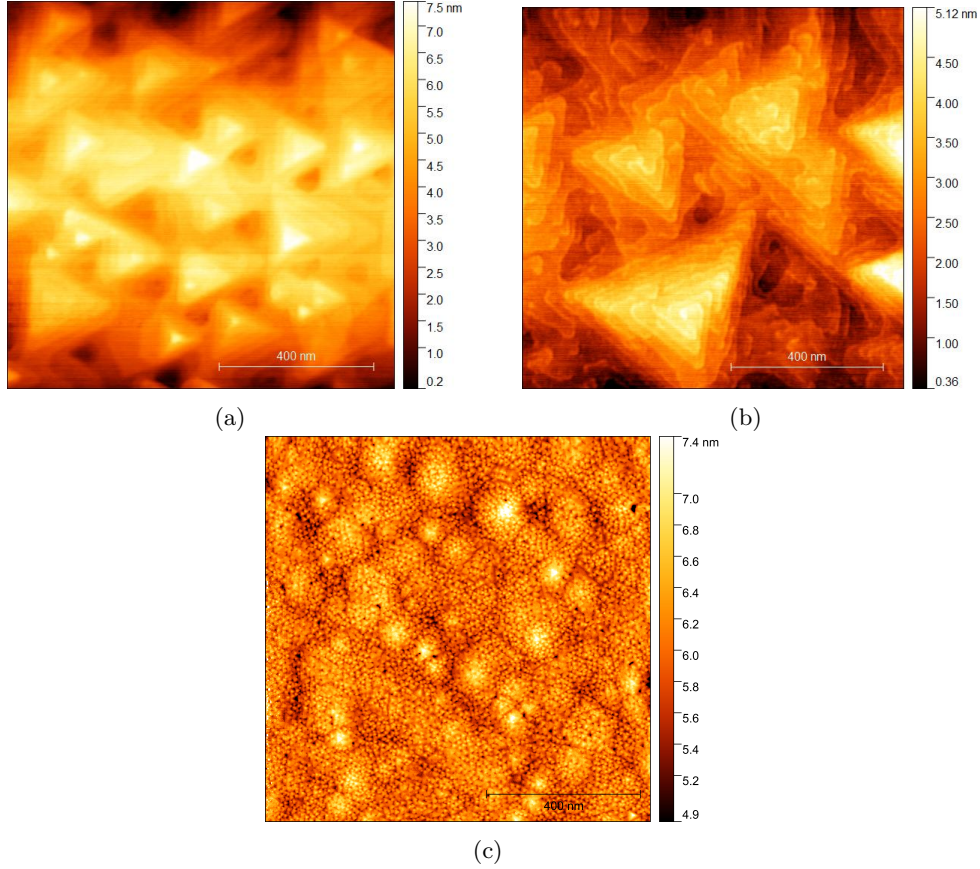


Figure 3.8: AFM images of: (a) Bi/InSb(111)B, (b)  $\text{Bi}_{0.82}\text{Sb}_{0.18}/\text{InSb}(111)\text{B}$ , (c)  $\text{Bi}_{0.82}\text{Sb}_{0.18}/\text{InSb}(111)\text{B}$  with chemical etching. The scan field is  $1 \times 1 \mu\text{m}^2$ .

films is  $\sim 18\%$ . The estimated thickness was used to calibrate the growth rate.

| Samples                                      | Incident XRD angle $\theta$ | $c$                  | Thickness (XRD)       | Thickness (XRR) |
|--|-----------------------------|----------------------|-----------------------|-----------------|
| a: Bi//InSb(111)B                            | $11.24^\circ$               | $11.855 \text{ \AA}$ | $30 \pm 2 \text{ nm}$ | 29.86 nm        |
| b: BiSb//InSb(111)B                          | $11.28^\circ$               | $11.812 \text{ \AA}$ | $40 \pm 2 \text{ nm}$ | not able to fit |
| c: BiSb//InSb(111)B<br>with chemical etching | $11.20^\circ$               | $11.897 \text{ \AA}$ | $41 \pm 2 \text{ nm}$ | 38.68 nm        |

Table 3.1: Calculated lattice parameter  $c$  and thickness using XRD and XRR techniques for samples a, b, and c.

These structural characterizations showed that we could optimize the growth conditions of high-quality BiSb thin layers on InSb(111)B substrates. The substrate preparation with chemical etching does not improve the quality of the thin layers. As mentioned previously, an insulating substrate is, however, necessary for further magnetotransport measurements. For this purpose, we attempted to incorporate Al into the InSb layer. Al would serve as an impurity to reduce the conductivity. To grow this layer, we chose a

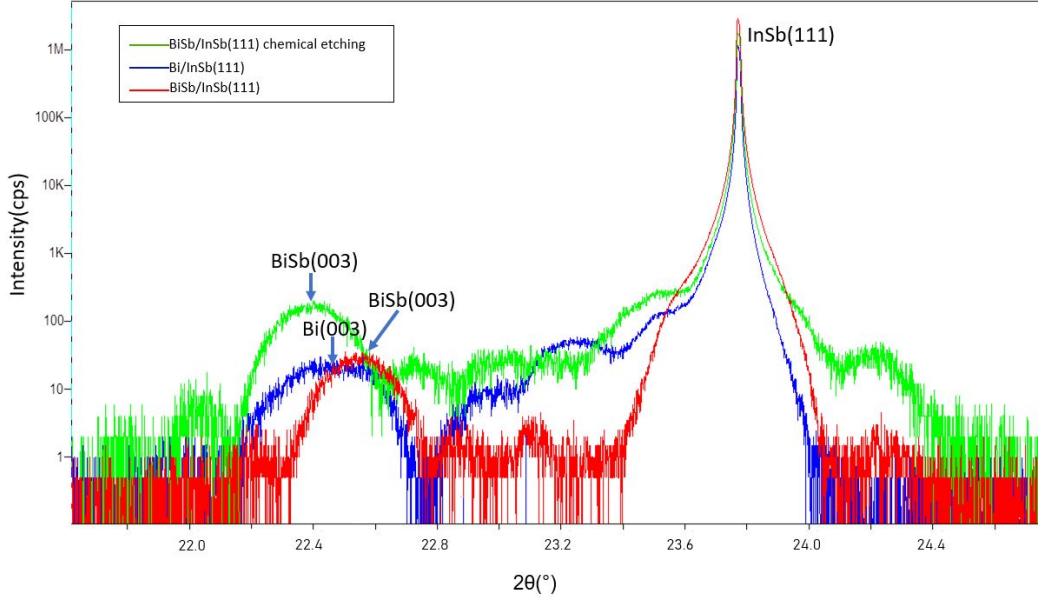


Figure 3.9:  $\theta - 2\theta$  X-ray diffraction spectra. The blue curve corresponds to the sample a (Bi//InSb(111)B), the red curve to the sample b ( $\text{Bi}_{0.82}\text{Sb}_{0.18}$ //InSb(111)B) prepared without chemical etching and the green curve corresponds to the sample c ( $\text{Bi}_{0.82}\text{Sb}_{0.18}$ //InSb(111)B) prepared with chemical etching.

GaAs(111)B substrate. The procedure for preparing the substrate is described in Section 3.2.2. After growing the GaAs buffer layer, we deposited a 100 nm-thick  $\text{Al}_{0.10}\text{InSb}$  layer at 370°C with a growth rate of 0.268 ML/s. Then, a layer of BiSb was grown on top of it at 200°C.

The layer was characterized by AFM and XRD. AFM images revealed the presence of holes in the BiSb layer and an overall rough surface, as seen in Figure 3.11(a). The XRD measurements did not show characteristic distinguishable peaks of the BiSb layer, which can be an indicator of an amorphous layer.

Despite the fact that the growth of a BiSb layer on top of the  $\text{AlInSb}$  layer has not been yet optimized, the electrical measurements that we performed were very promising. Indeed, the sheet resistance  $R_{\text{sheet}}$  of the  $\text{Al}_{0.10}\text{InSb}$ //GaAs(111)B layer is of the order of  $10^5 \Omega/\text{sq}$  (cf. Figure 3.11(b)) at room temperature. This is three orders of magnitude larger than the sheet resistance of BiSb (transport measurements of BiSb will be discussed in Chapter 4). These results open up prospects for the  $\text{Al}_{0.10}\text{InSb}$ //GaAs(111)B layer to serve as an insulating substrate for growing a BiSb layer with a small lattice mismatch. It holds a great potential for growing high-quality thin films of BiSb with fewer defects to obtain a large low-current SOT efficiency. Further investigation into the growth optimization conditions is necessary.

### 3.2.2 Growth on the GaAs substrates

The thin layers of BiSb were also grown on GaAs substrates: GaAs(001), GaAs(111)A (terminated with Ga) and GaAs(111)B (terminated with As). As mentioned earlier, BiSb thin layers adopt a rhombohedral crystal structure, closely resembling the hexagonal

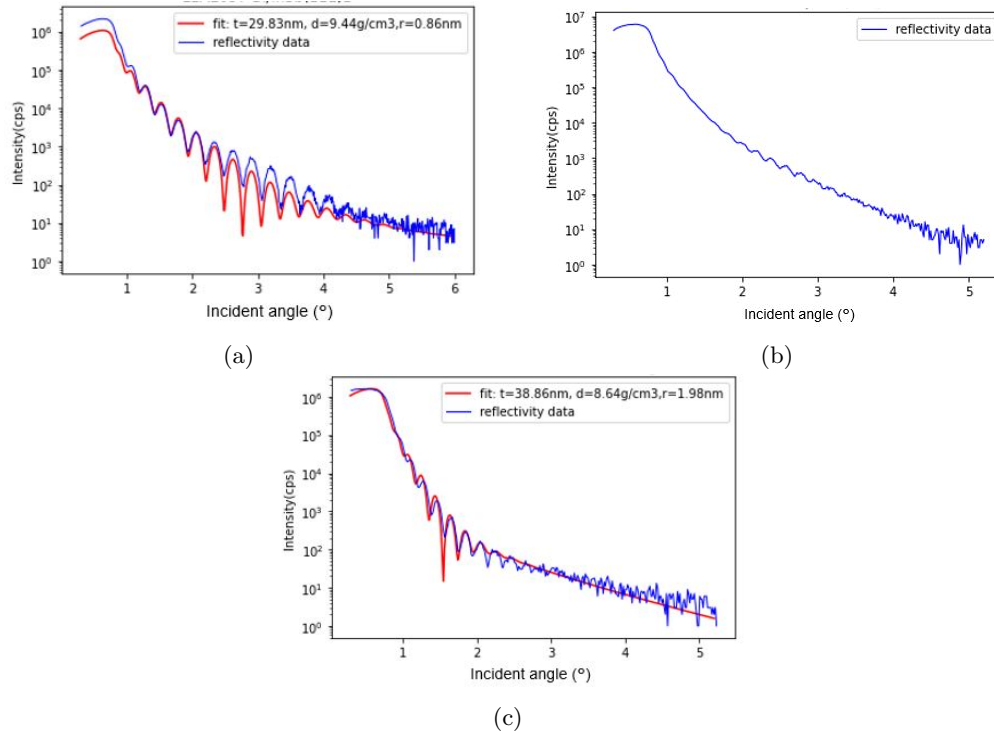


Figure 3.10: X-ray reflectivity measured profile of: (a) Bi//InSb(111)B; (b)  $\text{Bi}_{0.82}\text{Sb}_{0.18}$ //InSb(111)B; (c)  $\text{Bi}_{0.82}\text{Sb}_{0.18}$ //InSb(111)B prepared with chemical etching.

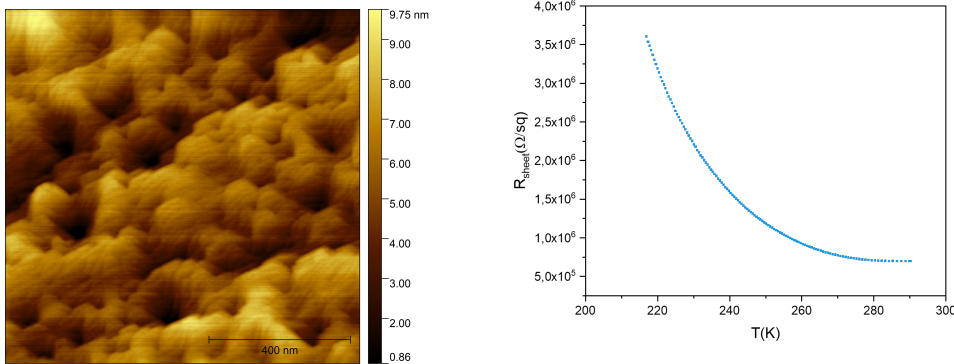


Figure 3.11: (a) AFM image of the BiSb/Al<sub>0.10</sub>InSb//GaAs(111)B layer: we observe the presence of holes in the layer and an overall rough surface. The scan field is  $1 \times 1 \mu\text{m}^2$ . (b) Sheet resistance  $R_{\text{sheet}}$  as a function of temperature of the Al<sub>0.10</sub>InSb//GaAs(111)B layer: the Al<sub>0.10</sub>InSb layer is more resistive than the BiSb layer.

structure, making the use of a GaAs substrate with the (111) plane a natural choice. However, for the reasons we will discuss later, since we need to grow the BiSb layer on top of the MnGa layer that adopts a tetragonal structure, the most appropriate substrate

choice for growing BiSb(top)/MnGa(bottom) heterostructure will be GaAs(001).

GaAs has a cubic zinc blende crystalline structure. Its structure with (001) and (111) orientation, as well as the structure of BiSb with (001) orientation are presented in Figure 3.12.

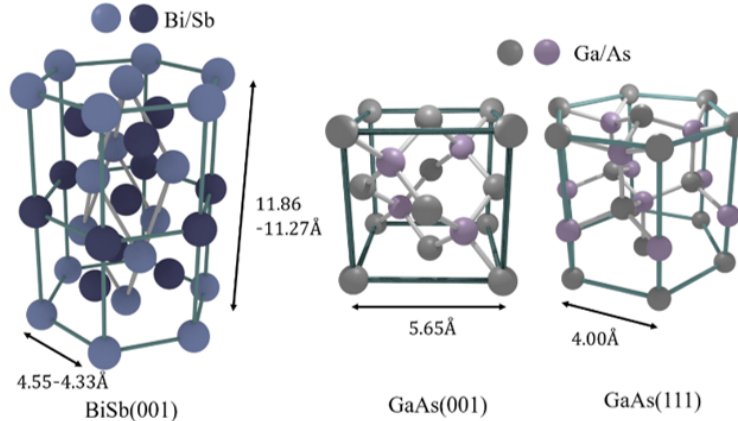


Figure 3.12: Crystal structures of BiSb with (001) orientation and GaAs with (001) and (111) orientations. Adapted from [180].

#### Substrate preparation and growth of $\text{Bi}_{0.90}\text{Sb}_{0.10}$

- GaAs(001): After degassing the substrate at  $300^\circ\text{C}$  for approximately an hour, it was introduced into the growth chamber. Subsequently, the surface oxide layer was removed at  $640^\circ\text{C}$  for one minute under an As flux of  $2.4 \times 10^{-6}$  Torr. The RHEED pattern appears at this moment, indicating the desorption of the oxide layer. The temperature was then lowered to  $570\text{-}580^\circ\text{C}$ , and a 100 nm-thick GaAs buffer layer was grown at a rate of  $1 \text{ \AA/s}$  with V/III = 10 BEP flux ratio to obtain an atomically smooth surface. The RHEED pattern exhibited a  $(2 \times 1)$  surface reconstruction.

The temperature was then reduced to room temperature. The As shutter is closed when the temperature is under  $500^\circ\text{C}$ . Next, a 13 nm-thick layer of  $\text{Bi}_{0.90}\text{Sb}_{0.10}$  was deposited at a growth rate of  $0.37 \text{ \AA/s}$  and subsequently annealed at  $200^\circ\text{C}$  for 10 minutes. After annealing, the RHEED pattern displays a smooth  $(1 \times 1)$  surface reconstruction.

- GaAs(111)A: Following degassing and deoxidation steps, a 3.6 nm-thick GaAs buffer layer is grown at  $570^\circ\text{C}$  with a growth rate of  $1.9 \text{ \AA/s}$ . The RHEED pattern exhibits a  $(2 \times 2)$  surface reconstruction. The temperature is subsequently lowered to room temperature. Following this, a 13 nm-thick layer of  $\text{Bi}_{0.90}\text{Sb}_{0.10}$  is deposited at a growth rate of  $0.37 \text{ \AA/s}$ , followed by an annealing process at  $200^\circ\text{C}$  for 10 minutes. After annealing the RHEED pattern displays a smooth  $(1 \times 1)$  surface reconstruction.
- GaAs(111)B: Following degassing and deoxidation procedures, a 2 nm-thick GaAs buffer layer is grown at  $560^\circ\text{C}$  with a growth rate of  $1.9 \text{ \AA/s}$ . The RHEED pattern displays a  $(2 \times 2)$  surface reconstruction. The temperature is then reduced to room temperature. Subsequently, a 13 nm-thick layer of  $\text{Bi}_{0.90}\text{Sb}_{0.10}$  is deposited at a

growth rate of  $0.37 \text{ \AA/s}$ , followed by an annealing process at  $180^\circ\text{C}$  for 10 minutes. After annealing the RHEED pattern displays a smooth  $(1 \times 1)$  surface reconstruction.

### Structural ex-situ characterisation

Figure 3.13(a)-(c) shows the AFM images of the three samples. All three samples exhibit triangular pits and the root-mean-square roughness values of BiSb on GaAs(001), GaAs(111)A and GaAs(111)B are 0.81 nm, 1.11 nm and 0.57 nm, respectively.

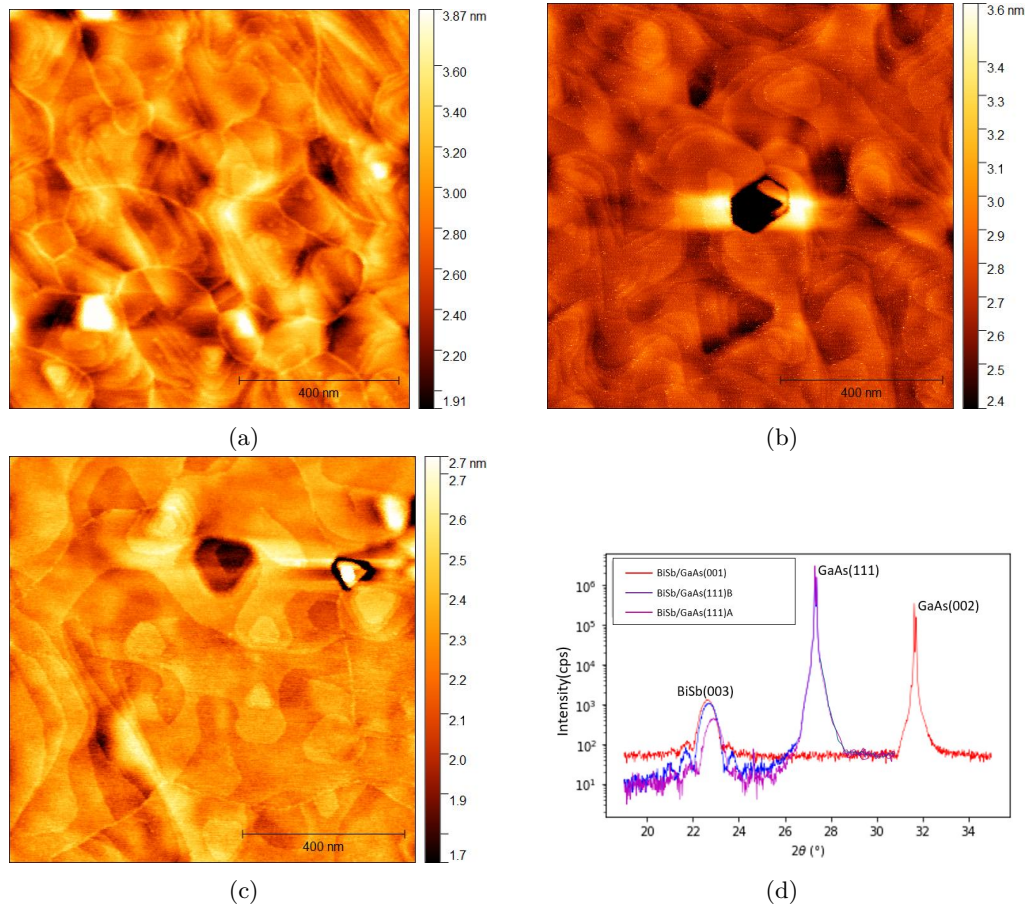


Figure 3.13: AFM images of: (a)  $\text{Bi}_{0.90}\text{Sb}_{0.10}/\text{GaAs}(001)$ , (b)  $\text{Bi}_{0.90}\text{Sb}_{0.10}/\text{GaAs}(111)\text{A}$ , (c)  $\text{Bi}_{0.90}\text{Sb}_{0.10}/\text{GaAs}(111)\text{B}$  heterostructures. The scan field is  $1 \times 1 \mu\text{m}^2$ . (d)  $\theta - 2\theta$  X-ray diffraction spectra of BiSb thin layers on GaAs substrates. The red, purple, and magenta curves correspond to  $\text{Bi}_{0.90}\text{Sb}_{0.10}/\text{GaAs}(001)$ ,  $\text{Bi}_{0.90}\text{Sb}_{0.10}/\text{GaAs}(111)\text{A}$ , and  $\text{Bi}_{0.90}\text{Sb}_{0.10}/\text{GaAs}(111)\text{B}$ , respectively.

Figure 3.13(d) depicts the  $\theta - 2\theta$  X-ray diffraction spectra of BiSb thin layers on GaAs substrates. Besides the peaks attributed to the substrates, we can observe a peak corresponding to BiSb(003). It indicates that all samples exhibit characteristics of single crystals, and notably, the GaAs(111)B substrate might be the most suitable choice for producing high-quality, crystallographically aligned films, likely attributed to the presence of Laue oscillations.

These results differ from the observations made by Yao et al. [180]. They found that thin films of BiSb grow with (012) orientation on GaAs(111)B and exhibit strong texture. In contrast, BiSb(001) thin films exhibit an epitaxial mode on GaAs(111)A. This difference might be explained by the fact that the GaAs(111)A surface is terminated with Ga atoms and has a stable hexagonal reconstruction lattice [124], which promotes the epitaxial growth of BiSb(001). On the other hand, the GaAs(111)B surface has a more complex surface reconstruction with hexagonal, square, and disorder structures [124], which may compromise the quality of BiSb thin layers on the GaAs(111)B substrate compared to its growth on the GaAs(111)A.

Regarding the growth on GaAs(001) substrates, one might expect BiSb to grow with (012) orientation due to symmetry arguments. However, our results show that it grows with (001) orientation, consistent with the findings of Yao et al. [180] and Sadek et al. [143]. They also reported that BiSb(001) thin films exhibit texture when grown on GaAs(001).

Our results provide insights into the choice of the most suitable substrate for growing BiSb thin films, but further in-depth analysis is needed.

### Conclusion

The BiSb thin films were grown on InSb(111)B, GaAs(001), GaAs(111)A, and GaAs(111)B substrates. The growth of BiSb on InSb(111)B exhibited an epitaxial growth mode with a small surface roughness and a high crystalline quality. However, InSb substrates have a narrow bandgap, which is not suitable for SOT measurements. To address this, we attempted to introduce Al as an impurity into the InSb layer to reduce its conductivity. Transport measurements demonstrated promising results, suggesting that AlInSb could serve as an insulating substrate.

Furthermore, our experiments revealed that BiSb consistently grows with a (001) orientation on all three GaAs substrates. Despite the different symmetries of the cubic GaAs(001) substrate and rhombohedral BiSb, it is still possible to choose this substrate for growing BiSb. This suggests that the growth of BiSb on top of MnGa is also feasible (see Section 3.4). However, AFM and XRD measurements indicated that the growth of BiSb on GaAs(111)B resulted in a smoother surface and better crystalline quality compared to the other substrates.

It is important to note that our study of BiSb growth on different substrates was far from being complete, as our primary goal was to create a BiSb/FM heterostructure. Nonetheless, it constituted an important step to serve as the foundation for our further study, allowing us to familiarize ourselves with the material. In addition, this study may provide some valuable insights for further investigations and hints at the most suitable substrate for achieving efficient SOT.

We will now pass to the next step of growth of the heterostructure: the ferromagnetic thin layers.

## 3.3 Growth and characterization of MnGa

Mn-Ga alloys are promising materials for spintronic applications due to their large spin polarization, square-like hysteresis loops, high magnetization, Curie temperature above room temperature, perpendicular magnetic anisotropy (PMA), large spin polarization at Fermi level, and high enough resistivity comparing to the conventional ferromagnetic metals, such as Co or Ni [160], [161], [169], [177], [187], [190], [189], [136], [92], [113]. The latter is of high importance in order to minimize current flowing through the ferromagnetic

layer instead of the TI layer during the SOT experiments. This way, the maximum charge current can be utilized to generate a spin current. In addition, our choice of the ferromagnetic material was also influenced by the availability of materials in our MBE growth chamber. Indeed, one of the goals of this work was to grow and develop the TI/FM heterostructure inside the same MBE chamber to preserve the structural quality of the TI/FM interface, and thus the spin-polarized surface states. This is particularly important for magnetotransport measurements.

It has been observed that  $\text{Mn}_x\text{Ga}_{1-x}$  (MnGa) alloys exhibit two main phases at room temperature: the  $\text{L1}_0$  ferromagnetic phase for  $0.43 \leq x < 0.66$  and the  $\text{D0}_{22}$  ferrimagnetic phase for  $0.66 \leq x < 0.75$  [36]. Both of these phases crystallize in a tetragonal structure, as illustrated in Figure 3.14

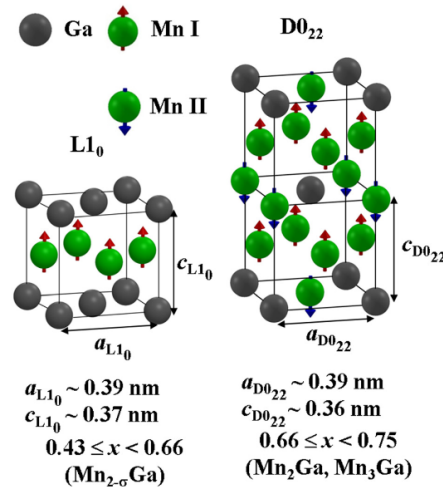


Figure 3.14: Tetragonal crystal structures of two phases of  $\text{Mn}_x\text{Ga}_{1-x}$  alloys: the  $\text{L1}_0$  ferromagnetic phase (left) and the  $\text{D0}_{22}$  ferrimagnetic phase (right). The blue and red arrows represent the direction of magnetic moments of Mn atoms. Adapted from [36].

We are particularly interested in the  $\text{L1}_0$  ferromagnetic phase. Note that in the (001) orientation, the crystal is a stack of pure Mn and Ga layers. To achieve the FM phase with a PMA, we observed that precise control of stoichiometry is essential, as it significantly influences magnetic properties such as magnetization, coercive field, and PMA. Another crucial growth parameters to manage are the growth temperature and the annealing temperature. Indeed, it can substantially impact not only the aforementioned magnetic properties but also the crystal quality of the MnGa thin films. As we will discuss later, achieving high-quality thin films necessitates an annealing temperature above  $350^\circ\text{C}$ . However, it is worth noting that the melting temperature of  $\text{Bi}_{1-x}\text{Sb}_x$  is relatively low (around  $280^\circ\text{C}$ - $290^\circ\text{C}$ ) [36] according to the phase diagram shown in Figure 3.4. Consequently, the BiSb layer should be deposited on top of the MnGa layer.

The MBE growth of MnGa thin layers in its stable ferromagnetic phase can be integrated onto GaAs(001) substrates. This integration is facilitated by the fact that the interatomic distance between Mn atoms in the basal plane is  $\sim 0.27 \text{ nm}$ , which is nearly half of the lattice constant of GaAs ( $0.28 \text{ nm}$ ). As a result, the lattice mismatch is relatively small, at only 3.8 %.

### Growth procedure

The growth procedure was inspired by the already existing technique for growing stable  $L1_0$ -ferromagnetic thin layers of MnGa developed by Tanaka et al. [160]. However, crucial growth parameters, such as stoichiometry, growth temperature, and annealing temperature, had to be significantly adjusted to attain the desired magnetic properties and a high-quality crystalline structure. So, we optimized growth conditions based on structural characterizations (RHEED, AFM, XRD) and magnetic characterizations (alternating gradient force magnetometry (AGFM) and superconducting quantum interference device (SQUID) magnetometry).

The growth rate of Mn was determined through ex-situ XRR measurements of MnAs thin films. The growth process for MnAs thin films on GaAs(111)B substrates has been well-established within our group. Fitting parameters of the XRR curve included density, roughness, and film thickness are listed in the inset of Figure 3.15. Consequently, we were able to deduce the growth rate of Mn for the given flux of  $1 \times 10^{-8}$  Torr, which is 0.17 Å/s.

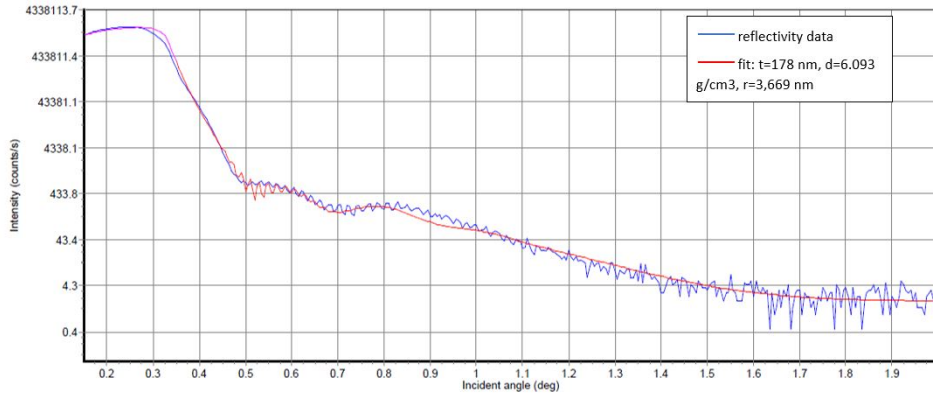


Figure 3.15: XRR measurements of the MnAs thin film (blue curve) and its fit (red curve). Fitting parameters include density  $d$ , roughness  $r$ , and film thickness  $t$ . It allows to determine the growth rate of Mn.

To grow MnGa thin layers, we initially prepared the semi-insulating GaAs(001) substrates using the same procedure described in Section 3.2. It is important to mention that after growing the buffer of GaAs, the As flux should be significantly reduced, as even residual As flux can potentially react with Mn, leading to the formation of MnAs layers.

Then, the substrate was cooled down to room temperature, and we employed the so-called "template" method by depositing the first four alternating monolayers of Mn and Ga. There is no RHEED pattern, indicating an amorphous layer.

Following the deposition of the template, it was annealed at temperatures ranging from 220°C to 300°C. At an annealing temperature of 300°C, we observed a streaky RHEED pattern with a  $2 \times 3$  surface reconstruction.

Then, the sample temperature was lowered to a range of 130°C to 250°C to grow a thin layer of MnGa with a total thickness of 15 nm, followed by a final annealing step within the temperature range of 250°C to 400°C. The RHEED pattern exhibited a streaky and spotty appearance at a growth temperature of 130°C and a streaky appearance at final annealing temperature of 400°C indicating improved flat 2D surface. All these steps,

along with their corresponding RHEED patterns, are illustrated in Figure 3.16

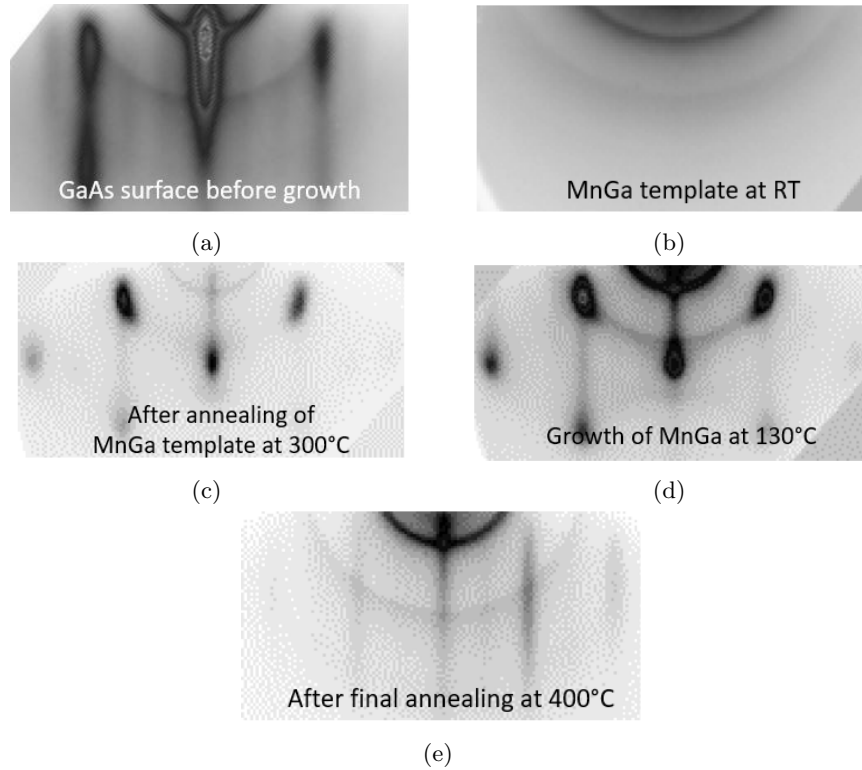


Figure 3.16: In-situ RHEED patterns along the  $\langle 110 \rangle$  azimuth during growth process of MnGa//GaAs(001): (a) GaAs buffer surface before the growth of MnGa. (b) Growth of the "template" layer: four alternating monolayers of Mn-Ga-Mn-Ga. No observable pattern: the layer is amorphous. (c) After annealing of the "template" layer at  $300^\circ\text{C}$ . The pattern is streaky with  $2 \times 3$  surface reconstruction. (d) During the growth of MnGa at  $130^\circ\text{C}$  with a total thickness of 15 nm. The pattern is streaky and spotty. (e) After annealing of 15 nm-thick MnGa layer at  $400^\circ\text{C}$ . The pattern is streaky indicating improved flat 2D surface.

#### Stoichiometry control of MnGa to achieve the ferromagnetic phase

Now that we have an indication of a bi-dimensional flat surface, we must control the stoichiometry of the MnGa layer to obtain the  $L1_0$  ferromagnetic phase. To achieve this, we grew a series of samples with a Mn/Ga BEP flux ratio equal to 0.950, 1.108, 1.118, 1.133, 1.176, and 1.200. Note that in the following, when we discuss the Mn/Ga ratio, we will refer to its BEP flux ratio. The precise stoichiometry will be then determined by using energy dispersive X-ray spectroscopy analysis in transmission electron microscopy (STEM-EDX).

Each sample underwent characterization through in-situ RHEED and ex-situ techniques, including AFM, XRD, and AGFM. The most promising samples, exhibiting superior magnetic and structural properties, were also subjected to SQUID characterization in order to quantitatively measure magnetisation, coercive field, and Curie temperature. The working principle of AGFM and SQUID are given in Appendix. The magnetotransport characterization, including AHE, will be presented in Chapter 4

Figure 3.17 displays the AFM topography of this series of samples. It is shown that for Mn/Ga ratios 0.950 and 1.108, the surface exhibits greater homogeneity, and all the grains are coalesced.

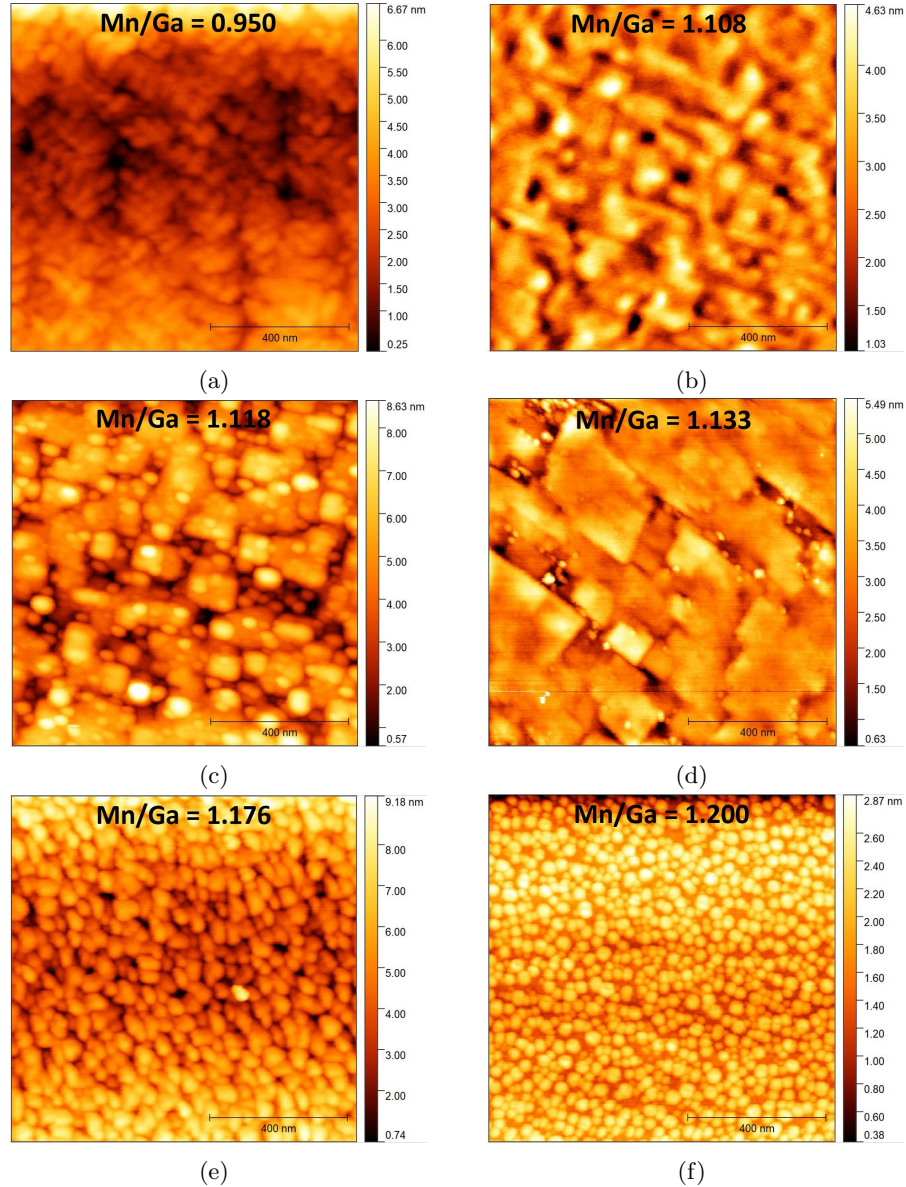


Figure 3.17: AFM images of a series of samples of MnGa thin layers with different Mn/Ga BEP flux ratios: (a) 0.950, (b) 0.108, (c) 1.118, (d) 1.133, (e) 1.176, (f) 1.200.

Figure 3.18(a) shows the  $\theta$ - $2\theta$  scan. The most defined peaks are for Mn/Ga ratio = 0.950 and 1.108. There is no detectable peak due to the MnGa film for Mn/Ga ratio = 1.200. We can also observe the peaks due to  $\text{Mn}_2\text{As}$  that will be discussed in Section 3.4. Based on this data, we were able to estimate the cell parameter  $c$ , that are presented in Table 3.2. As a reminder, the ferromagnetic phase of MnGa has a lattice parameter  $c$  of

3.700 Å [36].

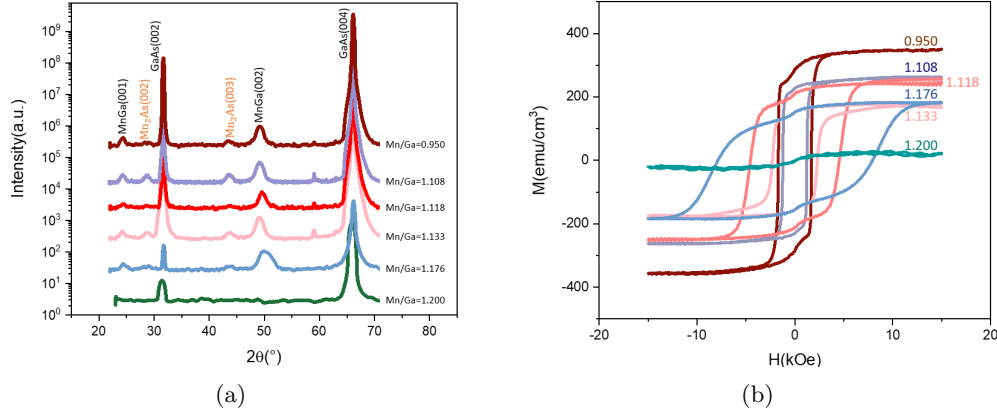


Figure 3.18: Ex-situ characterization of a series of samples of MnGa//GaAs(001) thin layers with different Mn/Ga BEP flux ratios: (a)  $\theta$ - $2\theta$  scan. The curves were smoothed and vertically shifted in an arbitrary manner to enhance clarity. (b) Hysteresis cycles  $M(H)$  measured with AGFM under the external field applied out of plane.

| Mn/Ga BEP flux ratio | Lattice parameter $c$ of MnGa |
|----------------------|-------------------------------|
| 0.950                | 3.703 Å                       |
| 1.108                | 3.701 Å                       |
| 1.118                | 3.671 Å                       |
| 1.133                | 3.707 Å                       |
| 1.176                | 3.636 Å                       |
| 1.200                | -                             |

Table 3.2: Estimated lattice parameter  $c$  of MnGa thin layers grown on GaAs(001) with different Mn/Ga BEP flux ratios from XRD data presented in Figure 3.18(a).

Figure 3.18(b) shows hysteresis cycles of magnetization  $M$  as a function of the external field  $H$  applied out of plane of the sample. Samples with Mn/Ga ratios of 0.950 and 1.108 exhibit the lowest coercive field (1.69 kOe and 1.23 kOe, respectively) and the highest saturation magnetization (283 emu/cm<sup>3</sup> and 198 emu/cm<sup>3</sup>, respectively).

These two samples were then characterized by SQUID. Hysteresis cycles with the external field applied out of plane for Mn/Ga ratio = 0.950 and 1.108 at 10K and 300K are presented in Figure 3.19(a) and (b), respectively. Magnetization as a function of temperature is presented in Figure 3.19(c) and (d). It is evident that the squareness is larger for Mn/Ga ratio = 1.108, approaching a value of 1, and similarly, the saturation magnetization  $M_s$  is also higher. The coercive field  $H_c$  is smaller for Mn/Ga ratio = 1.108. The Curie temperature is above room temperature for both samples.

The magnetic properties of these two samples are summarized in Table 3.3

It is clear that the sample with a Mn/Ga ratio of 1.108 exhibits superior magnetic properties. Consequently, we have successfully achieved a MnGa ferromagnetic thin layer with perpendicular magnetic anisotropy and high Curie temperature.

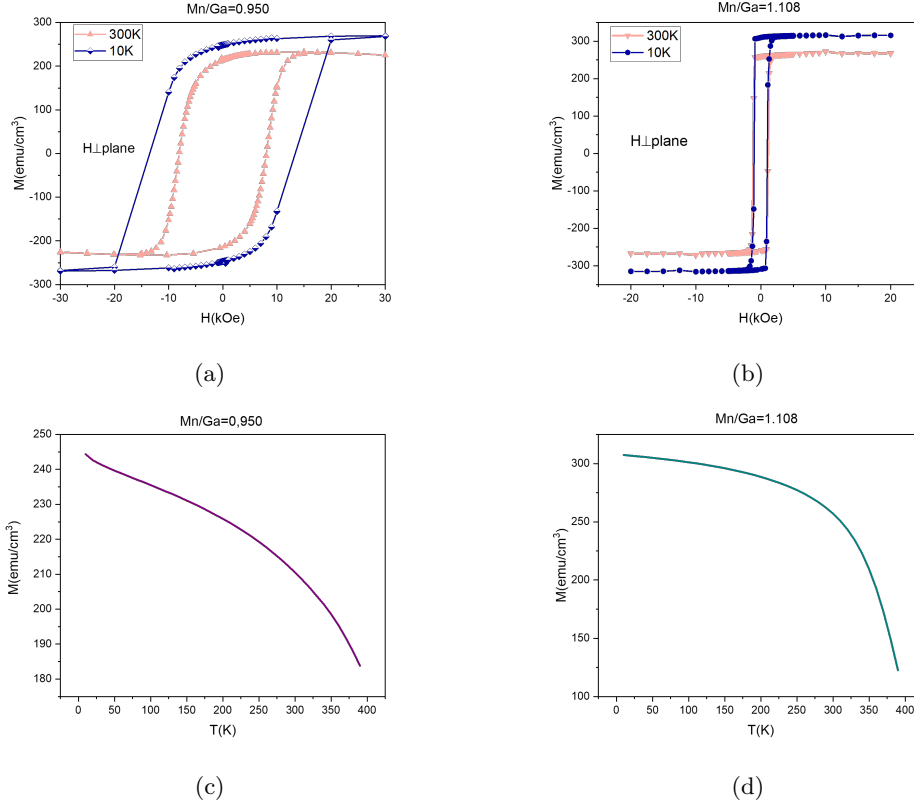


Figure 3.19: SQUID data of MnGa//GaAs(001) thin layers with the external field applied out of plane: (a) Hysteresis cycle for Mn/Ga ratio = 0.950 at 300K (in pink) and at 10K (in blue). (b) Hysteresis cycle for Mn/Ga ratio = 1.108 at 300K (in pink) and at 10K (in blue). Magnetization  $M$  as a function of temperature  $T$ : (c) for Mn/Ga ratio = 0.950, (d) for Mn/Ga ratio = 1.108.

| Mn/Ga ratio | $M_s$ ( $\text{emu}/\text{cm}^3$ ) | $H_c$ ( $\text{kOe}$ ) | $\mu$ ( $\mu_B/\text{atom}$ ) |
|-------------|------------------------------------|------------------------|-------------------------------|
| 0.950       | 10K: 260                           | 10K: 13                | 10K: 0.40                     |
|             | 300K: 220                          | 300K: 20               | 300K: 0.33                    |
| 1.108       | 10K: 315                           | 10K: 1                 | 10K: 0.48                     |
|             | 300K: 267                          | 300K: 1                | 300K: 0.41                    |

Table 3.3: Magnetic properties of MnGa//GaAs(001) thin layers for Mn/Ga BEP flux ratio=0.950 and 1.108.

However, for efficient SOT, it is necessary to have an ultra-thin FM layer of a few nm. Until now, we have used a 15 nm-thick MnGa layer for characterization, which is too thick to achieve efficient spin-orbit torque. Indeed, the SOT is inversely proportional to the FM thickness, as it acts on a thin layer at the interface. So in order to perform the SOT measurements, we made attempts to reduce the thickness of MnGa, which proved to be challenging. We observed that since the growth of MnGa occurs in 3D islands (VW growth mode), when the total thickness is only a few nanometers, so that there may not

be enough material to cover the entire surface of the substrate. This can result in poorer structural quality and an inability to achieve a PMA.

We grew MnGa layers with various nominal thicknesses: 4 nm, 5 nm, 6 nm, and 7 nm using the same conditions as the previously described method for growing 15-nm thick MnGa. Only the 4 nm- and 7 nm-thick MnGa layer exhibited the desirable ferromagnetic phase with the PMA, as evident from the hysteresis cycles obtained by AGFM with the magnetic field applied out of plane shown in Figure 3.20. However, as we will see later in the discussion about the structural quality that will be covered in Section 3.4 when we characterize the entire heterostructure BiSb/MnGa//GaAs(001) with STEM, the 4 nm-thick layer corresponds to the intermixing layer between the GaAs substrate and MnGa. So the thinnest ferromagnetic MnGa layer with PMA was of 7 nm, even though the magnetic properties of this layer are poorer than those of the 15 nm-thick layer.

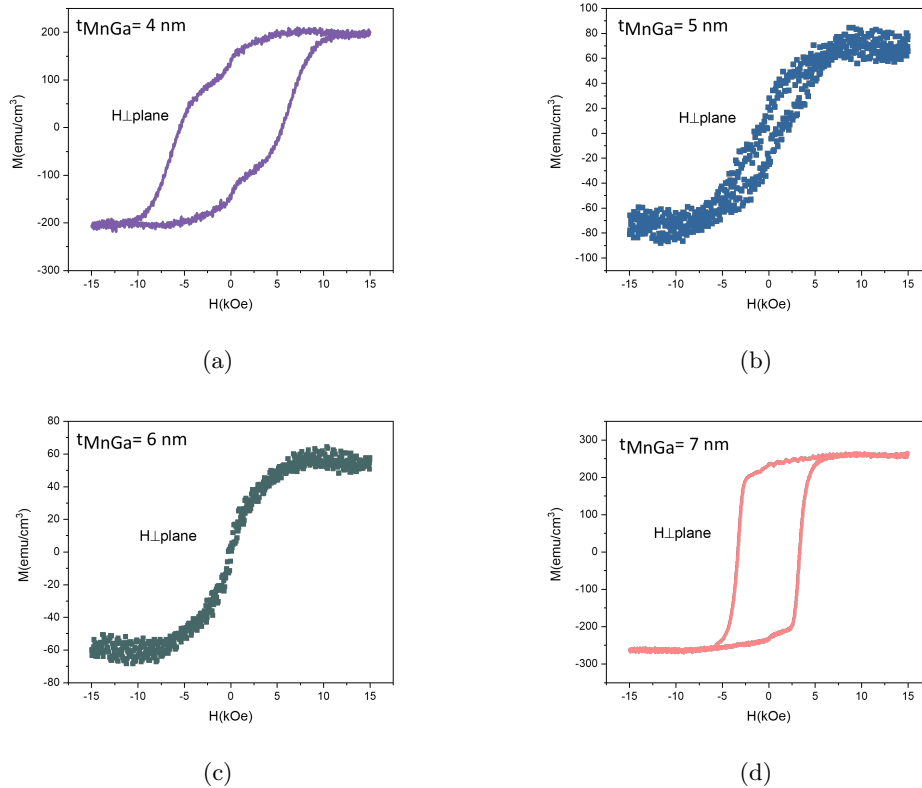


Figure 3.20: Magnetic hysteresis cycles measured with AGFM of the MnGa layers with varying nominal thicknesses with the magnetic field applied out of plane: (a) 4 nm, (b) 5 nm, (c) 6 nm, (d) 7 nm.

We can now proceed with the growth of a BiSb thin layer on top of the MnGa layer.

### 3.4 Growth and characterization of BiSb/MnGa//GaAs(001)

In this section, we will discuss the growth and structural characterization of the heterostructure of BiSb/MnGa//GaAs(001), as well as the challenges we encountered during

the process.

As mentioned previously, BiSb has a three-fold symmetric rhombohedral crystal structure, whereas MnGa has a four-fold tetragonal crystal structure. This presents a significant challenge in achieving monocrystalline thin films and a well-defined interface between the two thin layers. Consequently, this can negatively impact the efficiency of charge-to-spin interconversion.

#### Growth procedure, in-situ RHEED and ex-situ XRD characterizations

We started by depositing BiSb on top of a 15 nm-thick MnGa layer, which was grown using the optimized conditions described in Section 3.3. First, we deposited 9 nm of BiSb on top of MnGa at room temperature. The RHEED pattern appeared spotty and streaky initially. Then, the heterostructure underwent annealing at 180°C for 10 minutes, resulting in a streaky RHEED pattern without any spots. This indicates the formation of a flat two-dimensional surface. However, one can observe a doubling of the RHEED pattern of BiSb, which may indicate the presence of at least two domains. This will be discussed more in details in the next chapter. These patterns, as well as the one of MnGa before depositing of BiSb are shown in Figure 3.21

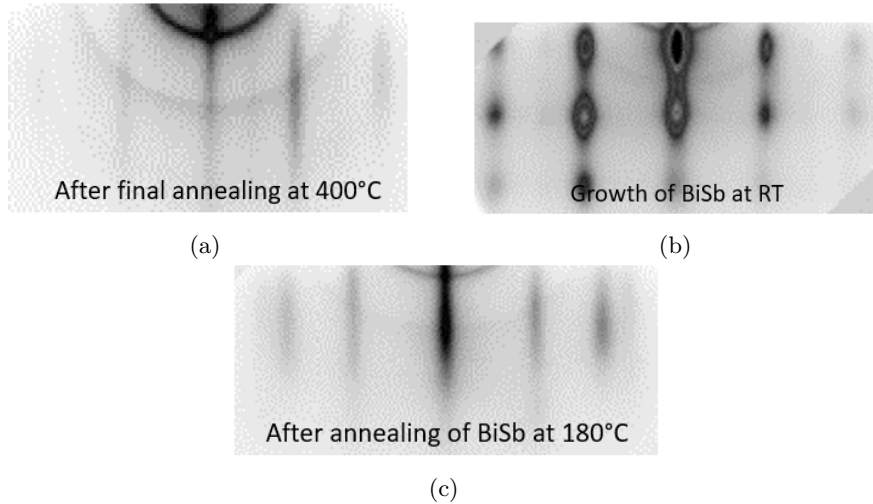


Figure 3.21: RHEED patterns with the MnGa  $\langle 110 \rangle$  azimuth during the growth of BiSb(9 nm)/MnGa(15 nm)//GaAs(001) heterostructure: (a) MnGa layer before depositing BiSb at room temperature. (b) During growth of BiSb at room temperature. (c) After annealing of BiSb at 180°C for 10 minutes.

Figure 3.22 shows an out-of-plane  $\theta-2\theta$  XRD diffractogram of the BiSb(9 nm)/MnGa(15 nm) bilayer. Besides the peaks of the GaAs(001) substrate, we can observe four other peaks. Two of them can be attributed to the rhombohedral structure of BiSb and two other peaks can be attributed to the tetragonal structure of MnGa, as expected. Both layers seem to be monocrystalline, as there is no other peaks observed.

#### STEM analysis

To go further in structural characterization, we performed cross-sectional scanning transmission electron microscopy (STEM) on three samples:

1. BiSb(9 nm)/MnGa(15 nm)//GaAs(001),

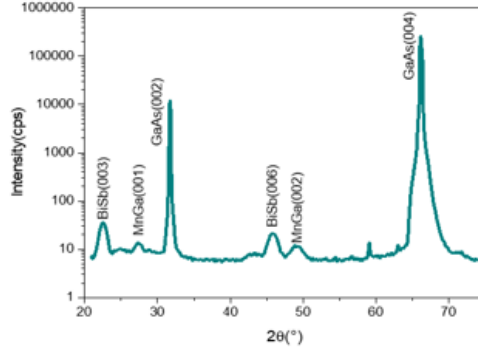


Figure 3.22: Out-of-plane  $\theta - 2\theta$  scan of the BiSb(9nm)/MnGa(15nm)//GaAs(001) bilayer. The curve was smoothed to enhance clarity.

2. BiSb(9 nm)/MnGa(7 nm)//GaAs(001)

3. BiSb(9 nm)/MnGa(12 nm)//GaAs(001)

The thickness in brackets indicates the nominal thickness of layers. The working principle of (S)TEM is given in Appendix. All STEM measurements in this work were conducted by L. Largeau at C2N.

#### BiSb(9 nm)/MnGa(15 nm)//GaAs(001)

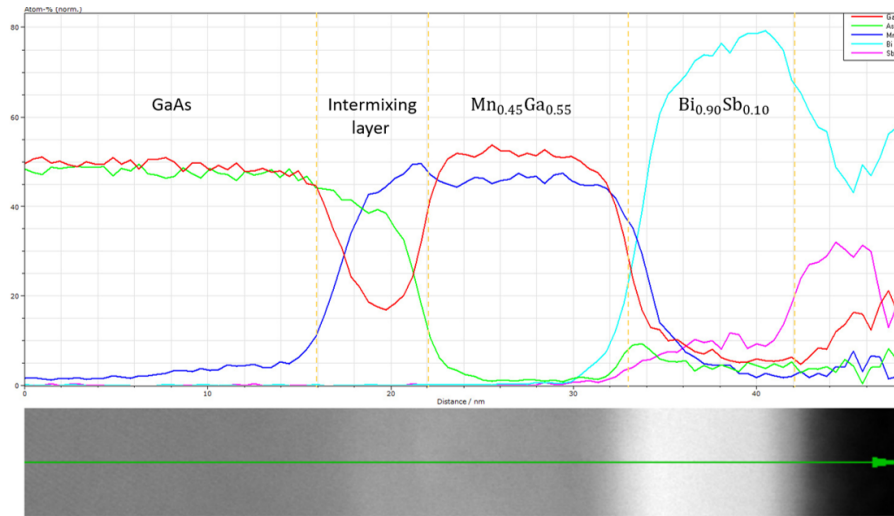
To gain a clear understanding of how the deposition of BiSb occurs on top of MnGa, we conducted STEM analysis on the BiSb(9 nm)/MnGa(15 nm)//GaAs(001) bilayer.

First of all, from this, we determined the stoichiometry of both layers:  $\text{Bi}_{0.90}\text{Sb}_{0.10}$  and  $\text{Mn}_{0.45}\text{Ga}_{0.55}$ , as seen in Figure 3.23(a) that shows the energy dispersive X-ray spectroscopy (EDX) profile. In addition, the STEM image in high-angle annular dark-field (HAADF) mode coupled with EDX scans showed that at the interface between the GaAs substrate and the MnGa layer, there is an intermixing of Mn, Ga, and As species (cf. Figure 3.23(a), (b)). This intermixing likely occurred during the final annealing stage at 400°C. The high temperature causes Mn to accumulate on the surface of the GaAs buffer and form complexes with elemental As atoms [33]. To prevent this, temperatures around 250°C are required, but unfortunately, this is not feasible in our case [122]. It is necessary to anneal the MnGa layer at around 400°C to achieve a ferromagnetic phase with a PMA. As a consequence, the actual thickness of  $\text{Mn}_{0.45}\text{Ga}_{0.55}$  is smaller (10 nm) than the nominal thickness (15 nm). The 10 nm-thick MnGa layer is crystalline and homogeneous, as well as the 10 nm-thick  $\text{Bi}_{0.90}\text{Sb}_{0.10}$  layer, as seen in Figure 3.24. The interface between the two layers looks sharp.

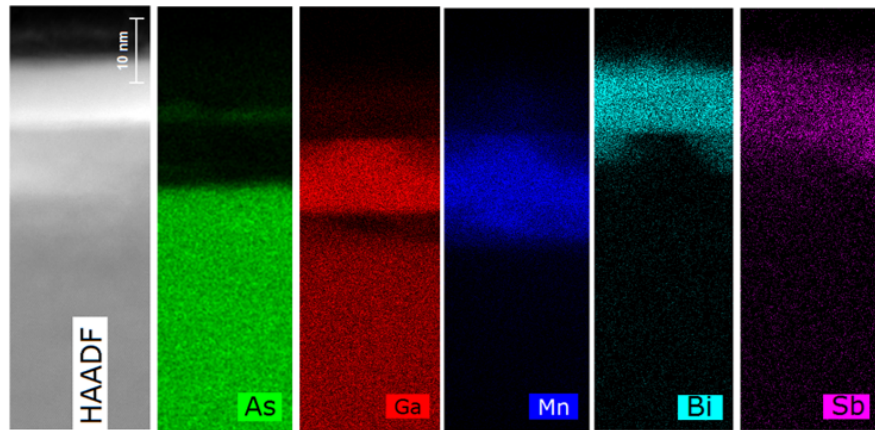
The role of the 5 nm-thick intermixing layer in the magnetic properties remains unclear. However, we can assume that this layer is not a ferromagnet with a PMA, as we observed in Section 3.3 that MnGa exhibits a ferromagnetic phase only when its nominal thickness exceeds 7 nm.

The indexing of fast Fourier transform (FFT) patterns from the measured zones by STEM in HAADF mode confirmed the epitaxial growth mode of BiSb with (001) orientation on MnGa and MnGa with (001) orientation on GaAs(001), as shown in Figure 3.25

#### BiSb(9 nm)/MnGa(7 nm)//GaAs(001)



(a)



(b)

Figure 3.23: (a) Top panel: EDX profile of the BiSb(9 nm)/MnGa(15 nm)//GaAs(001) bilayer: the formation of complexes of Mn with As atoms at the interface of the GaAs buffer and the MnGa layer is observed. Bottom panel: Corresponding STEM image of the measured zone. (b) EDX scans of the measured zone in STEM-HAADF mode (left) pictured on the right side. They provide a localization of each atomic species (As, Ga, Mn, Bi, and Sb).

As we discussed in Section 3.3, the minimum nominal thickness of MnGa to achieve a FM phase with a PMA is 7 nm. Thus, the BiSb(9 nm)/MnGa(7 nm)//GaAs(001) bilayer underwent the cross-sectional STEM. An image in HAADF mode is shown in Figure 3.26 (left). An EDX scan of the sample also provides a localization of each atomic species (As, Ga, Mn, Bi, and Sb, from left to right in Figure 3.26). It was observed that Mn still forms complexes with As atoms at the interface between the GaAs substrate and the MnGa layer. Additionally, the presence of cavities in the GaAs buffer filled with

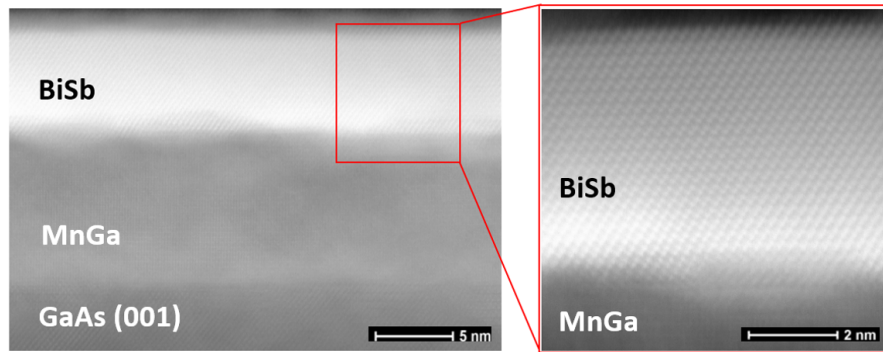


Figure 3.24: STEM micrograph of the BiSb/MnGa//GaAs(001) bilayer in HAADF mode: both layers are crystalline and homogeneous. The red frame represents the zoom on the interface between MnGa and BiSb layers.

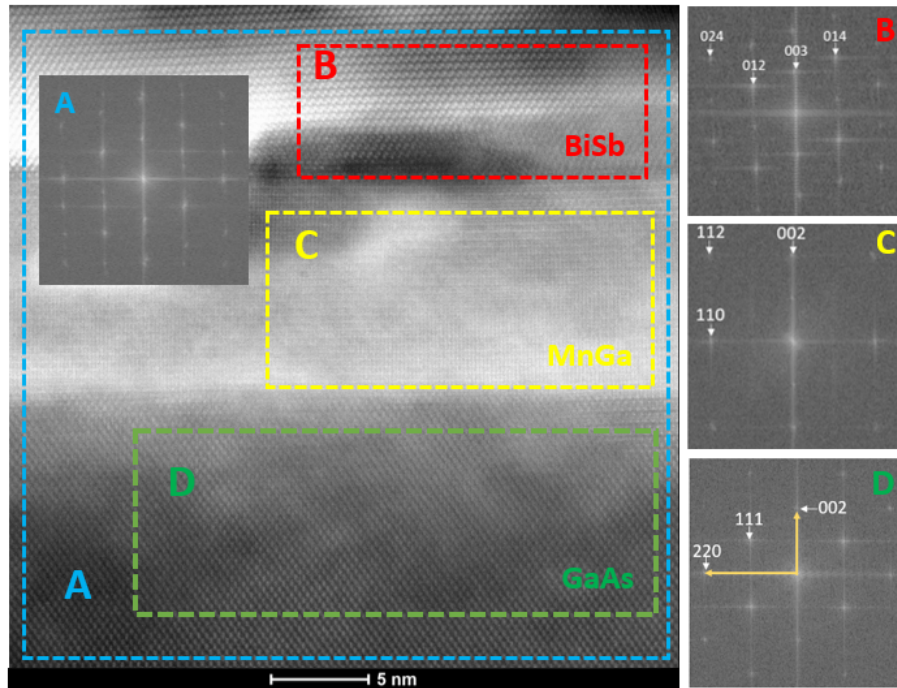


Figure 3.25: STEM micrograph in HAADF mode of BiSb(9 nm)/MnGa(15 nm)//GaAs(001) and its fast Fourier transform (FFT). The FFT labeled with letters A, B, C, and D corresponds to the measured zones framed with the same letters.

these MnAs complexes was observed, as shown in Figure 3.26. The MnGa layer appears amorphous and forms 3D islands (VW growth mode) on the surface, with BiSb filling the spaces between these MnGa islands, as seen in Figure 3.26. This phenomenon may occur because initially, the growth of MnGa starts in islands, and after reaching a certain

thickness, it forms a homogeneous layer covering the entire surface of the sample. The nominal thickness of 7 nm (the actual thickness of MnGa is 2 nm in this case) may not be sufficient to initiate layer-by-layer growth (SK growth mode).

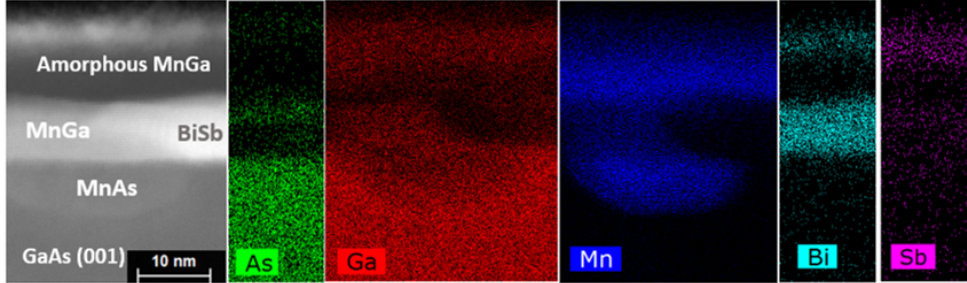


Figure 3.26: STEM image of the measured zone of BiSb(9 nm)/MnGa(7 nm)//GaAs(001) in HAADF mode pictured on the left side. Along with the EDX images on the right side, it reveals that MnGa initially grows in the form of 3D islands, suggesting that 7 nm of MnGa might not be sufficient to cover the entire surface of the substrate. As a result, BiSb, deposited afterward, grows in the spaces between the MnGa 3D islands. This phenomenon could be influenced by the fact that at temperatures above 250°C, Mn can form complexes with the As atoms present in the GaAs buffer layer.

#### BiSb(9 nm)/MnGa(12 nm)//GaAs(001)

Lastly, as we mentioned previously, a few nm-thick FM layer is necessary for the SOT measurements. Considering the 5-nm thick intermixing layer between MnGa and BiSb, we grew an MnGa layer of 12 nm nominal thickness following the procedure discussed previously. Thus, we obtain an MnGa layer with the actual thickness of 7 nm. This thickness represents the minimum thickness of a FM with a PMA that we could achieve. The AGFM measurements with the external magnetic field applied out of plane and in plane confirmed the ferromagnetic phase of the MnGa layer with a PMA. Figure 3.27(a) shows its characteristic hysteresis cycles with the magnetic field applied both in and out of plane.

Figure 3.27(b) shows an STEM image of BiSb(9 nm)/MnGa(12 nm)//GaAs(001) in HAADF mode. We can still observe the MnAs complexes at the interface between MnGa and GaAs(001). Even though the heterostructure presents more inhomogeneties, as compared to the BiSb(9 nm)/MnGa(15 nm)//GaAs(001) sample, it exhibits a good quality crystalline structure and epitaxial growth mode.

From now on, we will indicate in brackets the actual thickness of the MnGa layer without taking in account the intermixing layer.

## 3.5 Chapter conclusion

During the development of the BiSb/MnGa//GaAs(001) heterostructure, we encountered some challenges, such as differences in the symmetries of BiSb and MnGa, the interaction of Mn atoms with the GaAs substrate after an annealing phase, and consequently, the VW growth mode of MnGa that starts by forming 3D islands up until a certain thickness. Despite all these challenges, we were able to grow epitaxial layers that are crystallographically well-aligned. However, we were not able to obtain ultra-thin layers of MnGa (a few nm) that are more suitable for SCC experiments.

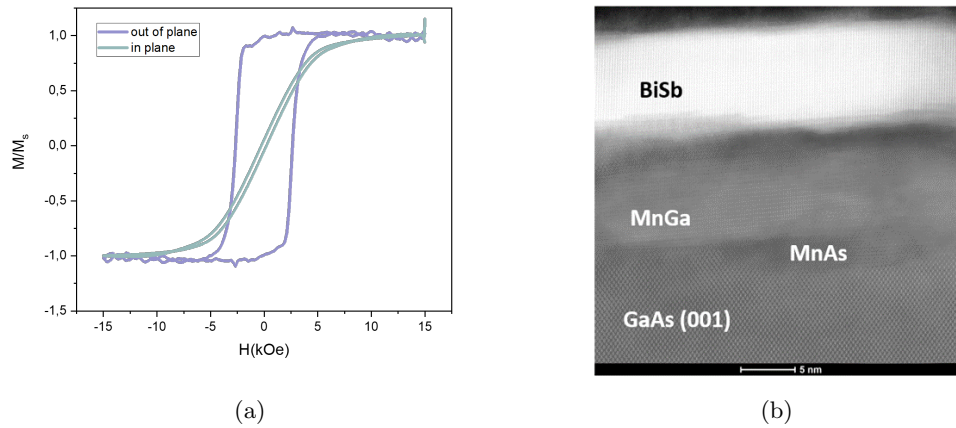


Figure 3.27: (a) Normalized hysteresis cycle  $M/M_s(H)$  of MnGa(12 nm)//GaAs(001) measured using AGFM with the external magnetic field applied out of plane (in purple) and in plane (in green). It shows that the MnGa layer exhibits a ferromagnetic phase with a PMA. (b) STEM image in HAADF mode of the BiSb(9 nm)/MnGa(12 nm)//GaAs(001) bilayer. Even though the heterostructure presents more inhomogeneties, as compared to the BiSb(9 nm)/MnGa(15 nm) bilayer, a good quality crystalline structure and epitaxial growth mode are observed.

Nevertheless, the MnGa(10 nm) thin films offer superior magnetic properties with a PMA, high Curie temperature (above room temperature), low coercive field ( $H_c = 0.1$  T), and significant saturation magnetization ( $M_s = 315$  emu/cm<sup>3</sup> at 15 K).

This work holds significant value, since it provides a detailed structural analysis of the BiSb/MnGa//GaAs(001) heterostructure, which has been lacking in the literature until now.

We will now proceed to the electronic characterisations of the system, including ARPES and magnetotransport measurements. The transport properties of both BiSb and MnGa layers will be discussed, as well.

## Chapter 4

# Electronic characterization of BiSb/MnGa//GaAs(001) bilayer

In the previous chapter, we discussed the growth procedure and structural properties of the BiSb/MnGa//GaAs(001) bilayer. In this chapter, we will describe its electronic properties. We will start with characterizations using ARPES, which is an indispensable tool for studying the electron band structure of topological insulators.

Following that, we will detail the results of the transport and magnetotransport properties measurements. Specifically, we will conduct electrical measurements and assess the conductivity properties of both BiSb and MnGa layers, as well as the magnetoresistance effects in the system arising from spin-orbit interactions.

### 4.1 ARPES to explore the topological nature of BiSb/MnGa

We performed ARPES measurements at the CASSIOPEE (Combined Angular- and Spin-resolved Spectroscopies Of PhotoEmitted Electrons) beamline at the SOLEIL Synchrotron. Synchrotron radiation as a light source has several assets:

- It is very intense and "brilliant": all the photons are concentrated in a small spot on the sample;
- It contains all the photon energies from infrared to hard X-rays. The photon energy can be chosen using a monochromator placed before the photoemission endstation;
- It is polarized. This can be useful to select the symmetry of the ground states to be excited.

The CASSIOPEE beamline operates with UV and soft X-rays in the energy range from 8 to 1200 eV, providing spin-and angle-resolved photoemission spectroscopy setups. It is also equipped with an MBE chamber, which is particularly convenient because samples can be grown and then directly transferred for (S)ARPES studies without exposure to the air [11].

#### 4.1.1 How does ARPES work?

ARPES has played an essential role in the experimental discovery of 3D topological insulators [61] and has become a leading technique for exploring their topological nature.

ARPES technique is based on the photoelectric effect, which microscopic mechanism was explained by A. Einstein in 1905 [39].

It involves shining monochromatic light, in the form of X-rays or ultraviolet photons with energy  $h\nu$ , onto the surface of a material. The source of photons can be a UV-lamp (e.g., He(I) radiation at 21.2 eV), a X-ray tube (usually using Al- $K\alpha$  or Mg- $K\alpha$  lines, at 1486.6 eV and 1253.6 eV, respectively) or, as in our case, a synchrotron radiation. When photons interact with the atoms in the material, the latter eject electrons mainly from the sample's surface. These so-called photoelectrons can be collected by an electron analyser, able to determine their kinetic energy and their emission angles  $(\theta, \varphi)$ , as shown in Figure 4.1(a) top panel. This information is directly connected to the energy and momentum of the electrons inside the material, prior to the excitation by the photon, by the conservation of energy and momentum. Consequently, one is able to determine the electronic band structure of the material.

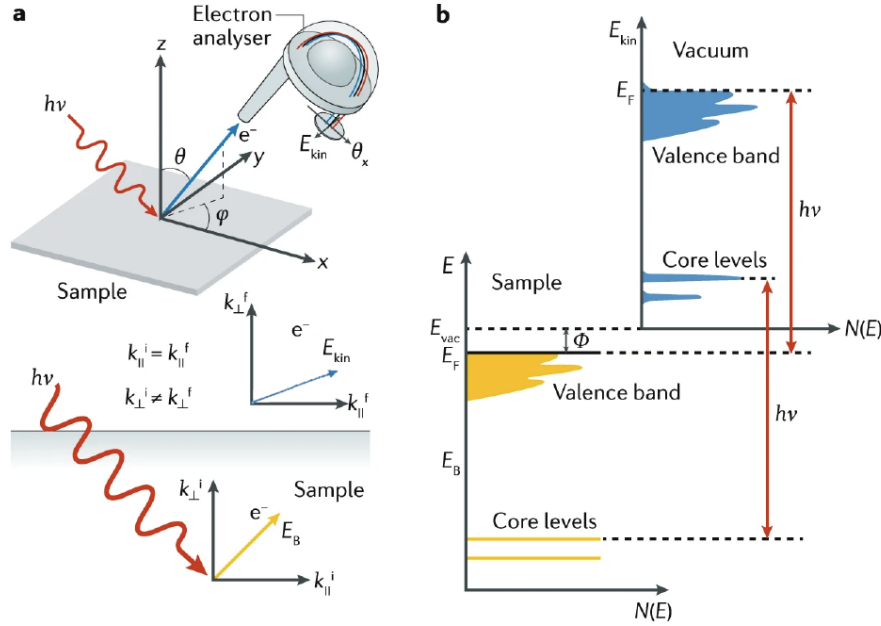


Figure 4.1: (a) Top panel: Schematic representation of the photoemission spectroscopy measurements. By shining light of energy  $h\nu$  onto the sample, electrons are ejected from the material in the vacuum at angles  $(\theta, \varphi)$  and collected by an electron analyser. Bottom panel: (Non-)conservation of the electron's momenta during the photoemission process. The component of the momentum parallel to the sample's plane is conserved:  $k_{||}^i = k_{||}^f$ . However, its perpendicular component is not:  $k_{\perp}^i \neq k_{\perp}^f$ , as the electron needs to go through the sample's surface which refracts it. (b) The schematic representation of the energy conservation of the electron during the photoemission experiment. The photon energy  $h\nu$  must be superior to  $E_B + \Phi$  to extract an electron from the material to the vacuum, so that  $E_{kin} = h\nu - \Phi - |E_B|$ . Adapted from [103].

If we define the kinetic energy of a photoelectron as  $E_{kin}$ , the binding energy of this electron inside the material as  $E_B$ , and the work function of the material (the energy required to extract an electron at the Fermi level  $E_F$  to the vacuum) as  $\Phi$  ( $\Phi > 0$ ), we

obtain the following energy conservation relation:

$$E_{\text{kin}} = h\nu - \Phi - |E_B| \quad (4.1)$$

The energy conservation during the photoemission process is illustrated in Figure 4.1(b).

One can also write the momentum conservation law. Let us define  $k$  as the electron momentum in its initial state and  $k^i$  its momentum in its excited state *inside* the solid. The momentum conservation writes:

$$k^i = k + k_{\text{photon}} \quad (4.2)$$

where  $k_{\text{photon}}$  is the momentum of the incident photon. In the photon energy range usually used for ARPES (10-100eV), it is negligible as compared to  $k$ , so:

$$k^i \simeq k \quad (4.3)$$

The photoelectron then needs to traverse the surface and overcome a potential barrier with a height  $\Phi$ . Since the symmetry is broken only perpendicular to the surface and not parallel to it, the component of the momentum parallel to the surface, denoted as  $k_{\parallel}$ , remains conserved (refer to Figure 4.1(a) bottom panel). Let  $k^f$  denote the photoelectron momentum outside the solid. Considering it behaves as a free electron, the measurement of  $E_{\text{kin}}$  directly provides its modulus:

$$E_{\text{kin}} = \frac{\hbar^2 (k^f)^2}{2m} \quad (4.4)$$

$$|k^f| = \frac{\sqrt{2mE_{\text{kin}}}}{\hbar} \quad (4.5)$$

A simple projection of  $k^f$  on the surface gives its component parallel to the surface  $k_{\parallel}^f$ , and therefore also  $k_{\parallel}$ :

$$k_{\parallel} = k_{\parallel}^i = k_{\parallel}^f = \frac{\sqrt{2mE_{\text{kin}}}}{\hbar} \sin(\theta) \quad (4.6)$$

However, the perpendicular component of the momentum is not conserved:  $k_{\perp}^i \neq k_{\perp}^f$  (see Figure 4.1(a) bottom panel). Calculating  $k_{\perp}$  as a function of the measured quantities  $E_{\text{kin}}$  and  $\theta$  requires assuming that the photoelectron's final state inside the solid lies on a free electron parabola (with its bottom located at an energy  $E_0$ ) to accurately calculate its energy outside the solid after crossing the  $\Phi$  potential barrier as a function of  $k$ . Knowing  $k_{\parallel}$ , it becomes straightforward to derive an expression for  $k_{\perp}$ :

$$k_{\perp} = \frac{\sqrt{2m(E_{\text{kin}} \cos^2 \theta + V_0)}}{\hbar} \quad (4.7)$$

where  $V_0$  is the so-called inner potential:  $V_0 = E_0 + \Phi$ .

Considering the equations 4.1, 4.6, and 4.7 and the measurements of  $E_{\text{kin}}$  and  $\theta$ , one can determine the electronic band structure of the material  $E_B(\mathbf{k})$ .

### 4.1.2 Surface states in BiSb//GaAs(001) and BiSb/MnGa//GaAs(001) probed by ARPES

#### ARPES experimental setup at the CASSIOPEE beamline

UV photons are directed onto the sample at a  $45^\circ$  angle with respect to the surface normal, causing the ejection of electrons from the vertically mounted sample. These ejected electrons are collected by the electron analyzer through a vertical entrance slit. The analyzer's entrance slit enables the collection of all electrons in the vertical plane that arrive at the analyzer within a  $\theta$  angular range of  $-15^\circ$  to  $+15^\circ$  with respect to the surface normal, as shown in Figure 4.2.

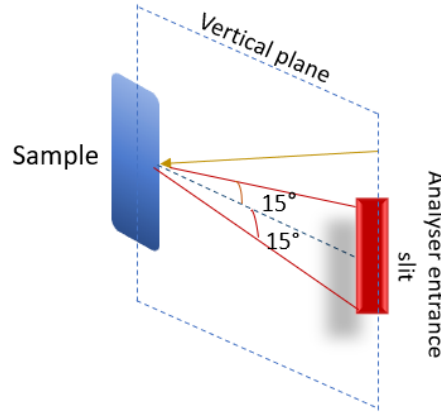


Figure 4.2: Scheme of the ARPES experimental setup at the CASSIOPEE beamline shows that photoelectrons ejected from the vertically mounted sample are collected by the electron analyzer through the vertical entrance slit within a  $\theta$  angular range of  $-15^\circ$  to  $+15^\circ$  with respect to the surface normal.

The 2D detector at the exit of the analyzer allows for the sorting of electrons based on their emission angle  $\theta$ , along one axis and their kinetic energy along another axis. The result of these measurements is represented as an image  $(E_{\text{kin}}, \theta)$ . By using the equations 4.1 and 4.6, this image  $(E_{\text{kin}}, \theta)$  can be transformed into the  $(E_{\text{B}}, k_{\parallel})$ . Note that  $k_{\perp}$  is expected to remain invariant for the 2D surface states.

#### Sample preparation

For the ARPES study, we prepared two samples inside the MBE system at C2N:

Sample 1: GaAs buffer(100 nm)//GaAs(001),

Sample 2: Mn<sub>0.45</sub>Ga<sub>0.55</sub>(10 nm)//GaAs(001).

The Sample 1 was grown following the growth procedure of the 100 nm-thick GaAs buffer, as detailed in Section 3.2. The Sample 2 was grown following the growth procedure of Mn<sub>0.45</sub>Ga<sub>0.55</sub> (10 nm)//GaAs(001) described in Section 3.3. Note that a pristine GaAs substrate was shown to be too insulating for ARPES measurements, so it was necessary to use Si-doped substrates. Both layers were capped by a 1 nm-thick amorphous As layer at room temperature to protect them from oxidation. The samples were then removed from the machine and transferred to the SOLEIL MBE machine to grow a BiSb layer. The MBE machine is connected to the ARPES module, so we do not expose the BiSb

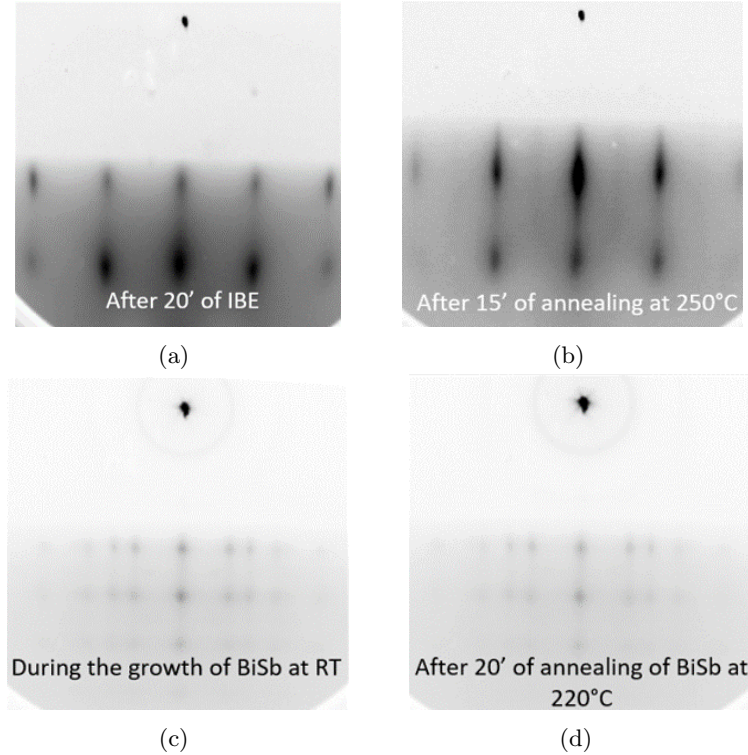


Figure 4.3: RHEED patterns during the decapping of As layer in the MnGa//GaAs(001) film and subsequent growth of BiSb inside the MBE chamber at CASSIOPEE beamline for further ARPES measurements: (a) After 20 minutes of IBE with Ar atoms: the surface is relatively rough. (b) The IBE step was followed by the annealing at 250°C for 15 minutes: surface appears smoother. (c) After the decapping of As layer, the  $\text{Bi}_{0.85}\text{Sb}_{0.15}$  (15 nm) layer was deposited at room temperature. (d) The deposited BiSb layer was then annealed at 220°C for 20 minutes. The RHEED pattern is streaky with spots which indicates a rough surface. The decapping may not be successful.

layer to the air, preserving the surface states.

Prior to growth of BiSb, one of the challenges was to remove the As capping layer and obtain a smooth surface of the already grown layers. The classic procedure consists of heating the samples to 300°C to evaporate the As layer. Sample 1 underwent this procedure, allowing us to obtain a smooth surface of GaAs.

Achieving a smooth surface for MnGa (Sample 2) proved to be more challenging. So we adopted another technique: performing ion beam etching (IBE) with Ar ions at an energy of 800 eV and an incident angle of 25° for 20 minutes, followed by annealing. The IBE allowed us to obtain a surface reconstruction, but this surface remained relatively rough, as evident from the streaky and spotty RHEED pattern (cf. Figure 4.3(a)).

To smooth the MnGa surface, we annealed it at 250°C for 15 minutes. This annealing step improved the surface quality, with the RHEED pattern appearing less spotty compared to the one just after the IBE (cf. Figure 4.3(b)).

After removing the As layer from the MnGa and GaAs layers (Samples 1 and 2), we deposited a 15 nm-thick layer of  $\text{Bi}_{0.85}\text{Sb}_{0.15}$  at room temperature on both samples (the

growth rate and the relative fluxes of Bi and Sb were measured using quartz microbalances). However, the RHEED pattern remained streaky and spotty even after annealing at 220°C for 20 minutes (cf. Figure 4.3(c), (d)). These RHEED patterns may indicate that the removal of As layer was not entirely successful and we were not able to obtain a smooth surface with a small roughness. Thus, this procedure needs to be further optimised.

#### ARPES measurements

Figure 4.4(a) displays the Fermi surface of Sample 1, measured at room temperature using a photon energy of 30 eV. In BiSb compounds, the typical Fermi surface consists of a hexagonal pocket centered at  $\Gamma$ . Along the six different  $\overline{\Gamma M}$  directions of the surface Brillouin zone, two colinear elongated petals are usually observed (see Figure 2.12(a)). In Figure 4.4(b), a sketch of this Fermi surface is presented, limited to the first petal in the  $\overline{\Gamma M}$  directions. However, in Sample 1, ten clearly visible petals (twelve under adjusted image contrast) extend from the central pocket. A plausible interpretation is that the BiSb film comprises two crystallographic domains of BiSb, rotated 30° with respect to each other. The total Fermi surface would then be a combination of the two single-domain Fermi surfaces, as depicted in Figure 4.4(b), with a predominance of domain 1 in this case.

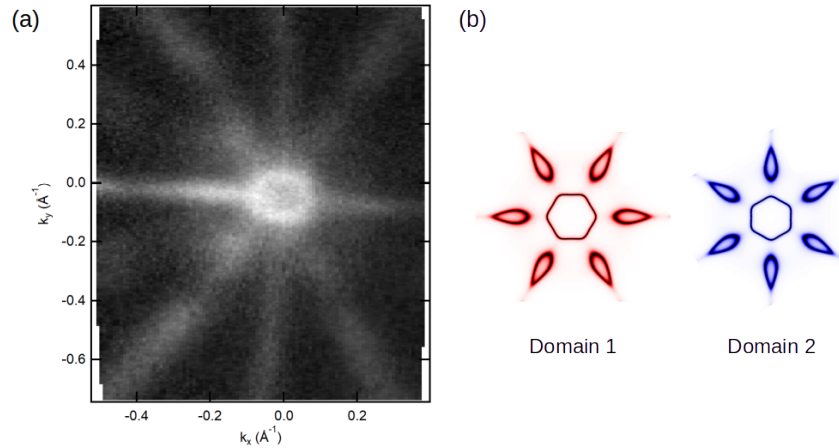


Figure 4.4: (a) Fermi surface measured at room temperature on Sample 1 using a photon energy of 30 eV. The Fermi level was found to be at a kinetic energy of 25.805 eV by fitting the angle-integrated spectrum recorded along one of the  $\overline{\Gamma M}$  direction with a Fermi function. The data are integrated over 15 meV. The analyzer entrance slit is along  $k_y$ . (b) Sketch of the expected Fermi surfaces for two domains rotated 30° one with respect to the other.

Due to the presence of these two crystallographic domains, the interpretation of the band structure becomes less straightforward. Both the band dispersion and Fermi surfaces are less structured compared to the case of BiSb/Si(111) [11], [12]. Nevertheless, we managed to find an orientation of the sample with a  $\overline{\Gamma M}$  direction along the slit of the electron analyzer. In this geometry, a simple measurement provides the band dispersion along this reciprocal space direction, as illustrated in Figure 4.5. Here, we can clearly observe the presence of the two surface states,  $S_1$  and  $S_2$ .

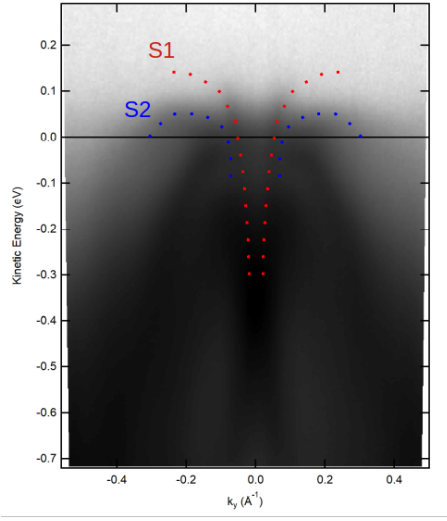


Figure 4.5: Band dispersion measured by ARPES along the  $\overline{\Gamma M}$  direction at room temperature on Sample 1 using a photon energy of 20 eV. The two  $S_1$  and  $S_2$  surface states are highlighted by red and blue dashed lines, respectively.

We then conducted a photon energy dependence study of these bands, utilizing photons in the range of 20 to 60 eV. In accordance with Equation 4.7 at  $\theta=0$ , this corresponds to varying the  $k$ -component perpendicular to the surface, denoted as  $k_{\perp}$ . If, as expected, the  $S_1$  and  $S_2$  states are 2D surface states, this component should remain constant. The results are shown in Figure 4.6 as a  $(k_{\perp}, k_y)$  Fermi surface. The intersections of  $S_1$  and  $S_2$  with the Fermi level appear as straight lines, indicating their non-dispersive nature perpendicular to the sample plane and affirming their 2D character.

As previously discussed, the BiSb growth on MnGa (Sample 2) was not really satisfactory with a relatively spotty final RHEED pattern. We were, nevertheless able to record a Fermi surface on this film, shown in Figure 4.7. It shows the same two-domain structure as on Sample 1, although a little bit less well-structured. As compared to the Sample 1, the two domains seem to have equivalent weights.

### 4.1.3 Complementary structural analysis of BiSb/MnGa//GaAs(001) by GIXRD

The identification of two domains through ARPES measurements prompted us to conduct a complementary structural analysis of BiSb(10 nm)/MnGa(7 nm)//GaAs(001) using grazing incidence X-ray diffraction (GIXRD). These measurements were performed using Smartlab Rigaku diffractometer with high-flux 9 kW rotating anode X-ray source, Ge(220) $\times$ 2 in-plane monochromator, and 0.5 $^{\circ}$  collimating optics. The grazing incidence angle was 0.3 $^{\circ}$ .

Upon analyzing the  $2\theta_{\chi}/\phi$  GIXRD spectra and identifying the peaks (see Figure 4.8), several observations emerged. We observed diffraction peaks associated to (110) and (300) planes perpendicular to the surface. It may indicate that the  $c$  axis of the BiSb cell is perpendicular to the surface. However, we also observed a less intense peak due to the secondary (015) orientation that might be related to the presence of grains with tilted

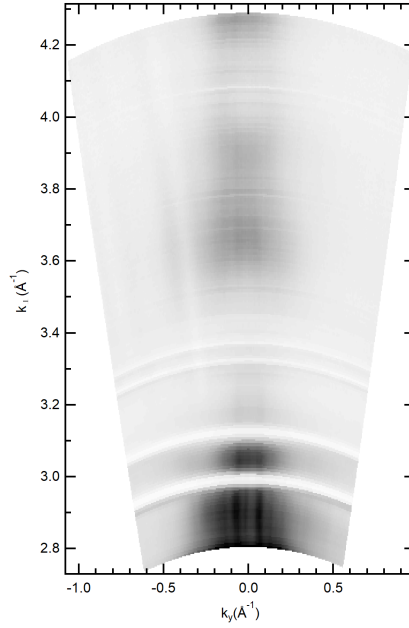


Figure 4.6:  $(k_{\perp}, k_y)$  Fermi surface recorded on Sample 1, calculated using  $V_0=10$  eV.

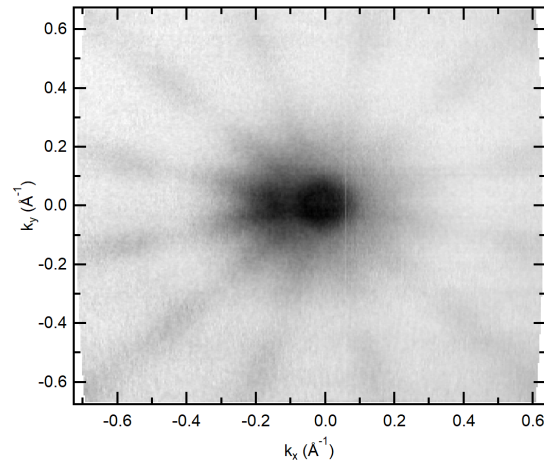


Figure 4.7: Fermi surface measured at room temperature on Sample 2 using a photon energy of 30 eV. The Fermi level was found to be at a kinetic energy of 25.83 eV by fitting the angle-integrated spectrum recorded along one of the  $\bar{\Gamma M}$  direction with a Fermi function. The data are integrated over 10 meV. The analyzer entrance slit is along  $k_y$ .

orientation [143].

Figure 4.9 shows a  $\phi$  scan of the BiSb(10 nm)/MnGa(7 nm)//GaAs(001) bilayer. This scan was obtained by rotating the sample in plane while keeping  $2\theta$  fixed.  $2\theta$  corresponds to the (110) BiSb diffraction peak. This experiment allows to identify crystal variants.

60 peaks are distinguishable. 24 of them are the most intense and correspond to the equivalent alignments of the hexagone along  $\langle 110 \rangle$  and  $\langle 100 \rangle$  directions grown on the square cell of MnGa (12 peaks along each direction). The remaining 36 peaks require further investigation to look for grains with different orientations.

These results indicate that the BiSb layer is not a single crystal and its growth on top of MnGa is far from being obvious. This explains two single-domain Fermi surface rotated  $30^\circ$  one with respect to the other observed with ARPES (cf. Section 4.1).

MnGa grows in the  $\langle 110 \rangle$  direction along GaAs(110). However, an additional (101) orientation is also observable.

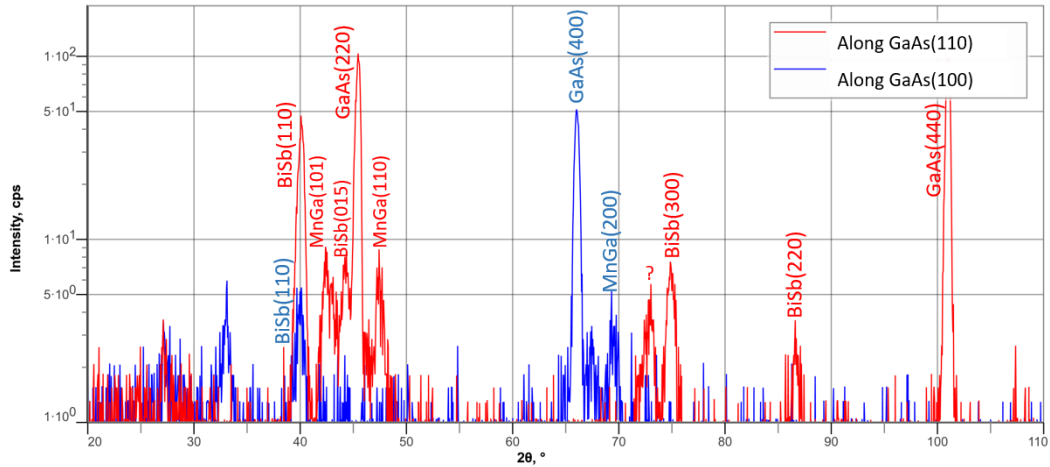


Figure 4.8:  $2\theta_\chi/\phi$  GIXRD spectra of the BiSb(10 nm)/MnGa(7 nm)//GaAs(001) bilayer along GaAs(100) (in blue) and GaAs(110) (in red) directions. We observe diffraction peaks associated to (110) and (300) planes perpendicular to the surface in the main  $\langle 110 \rangle$  epitaxial direction, parallel to the  $\langle 110 \rangle$  direction of MnGa. A secondary orientation (015) of BiSb is also detectable in this direction. MnGa grows in the  $\langle 110 \rangle$  direction along GaAs(110). However, an additional (101) direction is also observable.

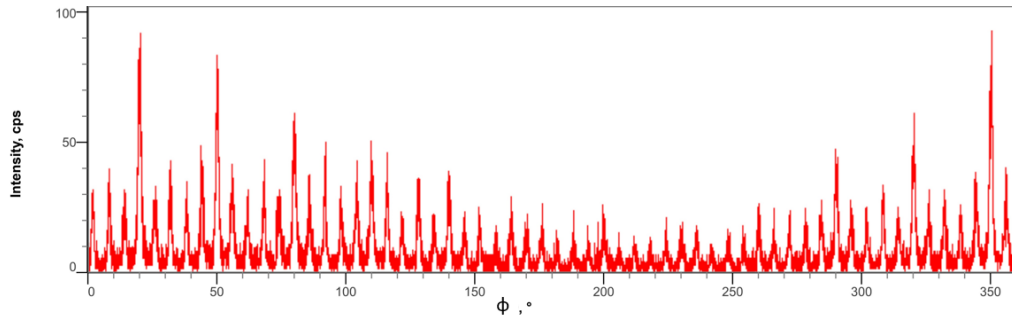


Figure 4.9:  $\phi$  scan of the BiSb(10 nm)/MnGa(7 nm)//GaAs(001). 60 peaks are observable. 24 of them are the most intense and correspond to the equivalent alignments of the hexagone along  $\langle 110 \rangle$  and  $\langle 100 \rangle$  directions grown on the square cell of MnGa (12 peaks along each direction). The remaining 36 peaks require further investigation.

## 4.2 Conductivity properties of BiSb and MnGa thin layers: is there current shunting?

Now, let us address a question of crucial importance concerning magnetotransport measurements in NM/FM thin layers, particularly in the context of spin-orbit torque efficiency evaluation: How much current flows through the BiSb layer in the BiSb/MnGa heterostructure?

One of the reasons we selected MnGa, as the ferromagnetic material is due to its expected conductivity, which is anticipated to be significantly lower than that of conventional FM metals. It is also characterised by high spin-polarized density of states at the Fermi level ( $\sim 70\%$ ) [136], [92], [113] that can result in low damping.

As we previously discussed in Section 2.3, there is a significant discrepancy in the SOT efficiency values reported in the literature for BiSb/FM layers. This may be partially attributed to the limited available information in the literature regarding the current distribution between the BiSb and FM layers. It raises the possibility that a substantial portion of the current predominantly flows through the FM layer, often a metallic material. This prompted us to conduct conductivity measurements to estimate the current ratio within this bilayer system.

### Sample preparation

For this study (conductivity and magnetotransport measurements (see Section 4.3)), we used the  $\text{Bi}_{0.90}\text{Sb}_{0.10}(9\text{ nm})/\text{Mn}_{0.45}\text{Ga}_{0.55}(7\text{ nm})//\text{GaAs}(001)$  system, which was deposited by MBE using the growth technique described in Section 3.4. Fabricating Hall bars for electrical measurements involved a one-step standard patterning process using UV lithography based on the design depicted in Figure 4.10. The one-step lithography was sufficient since there was no need to deposit metal contacts. It is possible to achieve a good electrical contact by wire-bonding directly on the BiSb layer. The Hall bar design allowed for the injection of current  $I$  (or current density  $\mathbf{j}$ ), along the  $+\mathbf{x}$  direction and the measurement of both longitudinal ( $R_{xx}$ ) and transverse ( $R_{xy}$ ) resistance. We can also apply an external magnetic field  $\mathbf{B}$  at angles  $(\theta, \varphi)$ , as shown in Figure 4.10. After the one-step lithography, the samples were etched using IBE, cleaned with oxygen plasma, and left in an acetone bath overnight. We chose to avoid using an ultrasonic cleaner to prevent potential deterioration of the layers. The dimensions of the Hall bar are: length  $L = 27\mu\text{m}$  and width  $w = 4\mu\text{m}$ .

### Conductivity measurements

These measurements, as well as the magnetotransport measurements (Section 4.3) were conducted by injecting a DC current with the Keithley 6221 current source inside the closed-cycle helium cryostat Attodry 1000, allowing temperatures as low as 5 K and equipped with a superconducting magnet enabling the reach of magnetic fields up to 9 T. The 3D sample rotator module allows the application of an external magnetic field both out-of-plane and in-plane of the sample. Figure 4.11 shows the longitudinal resistance as a function of temperature of the  $\text{Bi}_{0.90}\text{Sb}_{0.10}(9\text{ nm})/\text{Mn}_{0.45}\text{Ga}_{0.55}(7\text{ nm})$  bilayer and the  $\text{Mn}_{0.45}\text{Ga}_{0.55}(7\text{ nm})$  single layer capped with a 2 nm amorphous Bi layer. Both resistances increase with increasing temperature, which is characteristic of a conductor. From these measurements and taking into account the Hall bar dimensions, we can calculate the resistivity  $\rho = \frac{RA}{L}$  of the MnGa layer, where  $A$  is the surface of the cross section of the conduction channel and  $L$  is its length.

In determining the resistivity of the BiSb layer, we employed the parallel resistor

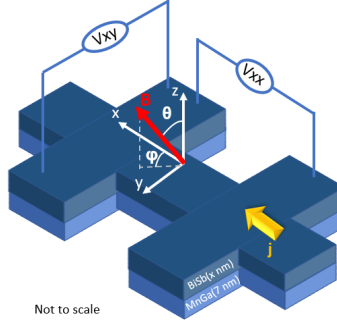


Figure 4.10: The geometry of a Hall bar for electrical measurements that involves injecting a current  $I$  (or current density  $\mathbf{j}$ ), in the  $+x$  direction. It allows to measure both the longitudinal voltage  $V_{xx}$  and the transverse voltage  $V_{xy}$ , from which we can then deduce the longitudinal resistance  $R_{xx}$  and the transverse resistance  $R_{xy}$ . In addition, we can also apply an external magnetic field  $\mathbf{B}$  at angles  $(\theta, \varphi)$ . The thickness of the MnGa layer remains constant at 7 nm for all measurements, whereas the thickness of the BiSb layer will vary.

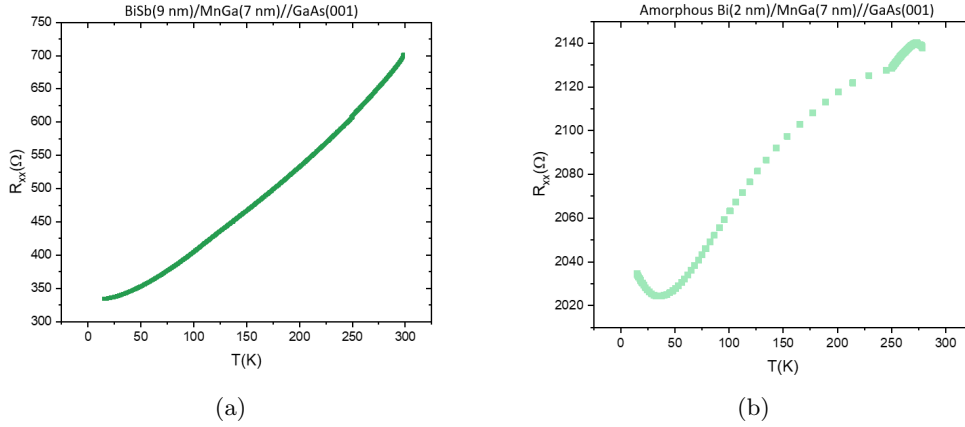


Figure 4.11: Longitudinal resistance as a function of temperature for the (a)  $\text{Bi}_{0.90}\text{Sb}_{0.10}$  (9 nm)/ $\text{Mn}_{0.45}\text{Ga}_{0.55}$  (7 nm) bilayer and (b)  $\text{Mn}_{0.45}\text{Ga}_{0.55}$  (7 nm) single layer capped with a 2 nm amorphous Bi layer.

model. If we designate  $R_1$  as the resistance of the first conductor and  $R_2$  as the resistance of the second conductor, with  $R_{\text{total}}$  being the total resistance for the bilayer, we can use the formula  $R_{\text{total}} = \frac{R_1 R_2}{R_1 + R_2}$ . Utilizing this expression, along with the known resistance of the single MnGa layer and the total resistance, we can calculate the resistance and thus the conductivity of the BiSb layer. At room temperature, we estimated the conductivity of  $\text{Bi}_{0.90}\text{Sb}_{0.10}$  to be  $7.3 \times 10^5 \Omega^{-1} \text{m}^{-1}$ . This value is twice as large than the maximal conductivity of the BiSb thin layers found in the literature [77, 20, 142, 10]. To understand the reason behind this large conductivity, it is necessary to conduct further Hall effect measurements on a single BiSb layer to estimate the surface carrier density and its mobility.

Furthermore, by considering the resistivity values of both single BiSb and MnGa

layers, we estimated the current distribution ratio within this bilayer system using the following formula:

$$\delta_{\text{BiSb}} = \frac{\rho_{\text{BiSb}}}{\rho_{\text{BiSb}} + \rho_{\text{MnGa}}} \cdot 100\% \quad (4.8)$$

where  $\delta_{\text{BiSb}}$  denotes the contribution (in %) of BiSb in total resistivity of the entire bilayer.

We found that at room temperature, the current ratio flowing through the BiSb(9 nm) layer amounts to 67%, and at low temperature (15 K) it reaches 78%. So the majority of the current contributes to the generation of a pure spin current at the topological insulator surface.

All of these calculated values representing conductivity properties are presented in Table 4.1.

|  | 290 K                                       | 15 K  |
|--|---|---|
| $\sigma$ (Bi <sub>0.90</sub> Sb <sub>0.10</sub> )            | $7.3 \times 10^5 \Omega^{-1} \text{m}^{-1}$ | $1.3 \times 10^6 \Omega^{-1} \text{m}^{-1}$ |
| $\sigma$ (Mn <sub>0.45</sub> Ga <sub>0.55</sub> )            | $4.5 \times 10^5 \Omega^{-1} \text{m}^{-1}$ | $4.7 \times 10^5 \Omega^{-1} \text{m}^{-1}$ |
| Current ratio (Bi <sub>0.90</sub> Sb <sub>0.10</sub> (9 nm)) | min. 67 %                                   | min. 78 %                                   |

Table 4.1: Conductivity properties of BiSb and MnGa thin films and current ratio flowing through the BiSb(9 nm) layer in the Bi<sub>0.90</sub>Sb<sub>0.10</sub>(9 nm)/Mn<sub>0.45</sub>Ga<sub>0.55</sub>(7 nm) system at room and low temperatures. These values were calculated using the longitudinal resistance measurements.

It is important to note that we made the assumption that only BiSb and MnGa layers are conducting. However, as we discussed in Section 3.4 there exists a 5-nm thick intermixing layer between the MnGa film and the GaAs substrate, and we do not have information regarding its conductivity properties. This may make the resistivity of MnGa and the intermixing layer even larger. Therefore, the 67% (78%) of current passing through the BiSb layer at room (low) temperature is likely an underestimate, and it is plausible that even more current is flowing through the BiSb layer. Consequently, current shunting to the MnGa layer is lower than what is typically observed in conventional FM metallic layers, such as Co.

To go deeper into the analysis, we conducted Van der Pauw measurements for BiSb ( $x$  nm)/MnGa (7 nm) bilayers with varying thicknesses ( $x$ ) of the BiSb layer at room temperature. These measurements served the dual purpose of not only calculating the conductivity of BiSb to estimate the current distribution, as mentioned earlier, but also to explore how the thickness of the BiSb layer affects its structural quality through its transport properties.

Figure 4.12(a) illustrates the calculated sheet resistance  $R_{\text{sheet}}$  ( $\Omega/\text{sq}$ ) for the heterostructure mentioned earlier, as determined through Van der Pauw measurements. The thickness of the MnGa layer remains constant at 7 nm, meaning that the variation in the total sheet resistance is exclusively attributed to changes in the thickness of the BiSb layer.

It is evident that the resistivity decreases as the thickness increases, which may suggest a uniform distribution of the deposited atoms as atomic layers.

The sheet resistance is then solely dependent on one independent variable, the thickness of BiSb  $x$ , so that  $R_{\text{sheet}} = \frac{\rho}{x} = R_{\text{sheet}}(1/x)$ . Given that the thickness of MnGa is held constant, we can fit a curve with parameters, such as the resistivity of the BiSb and MnGa layers. Consequently, we can determine their respective conductivities:  $\sigma(\text{Bi}_{0.90}\text{Sb}_{0.10}) =$

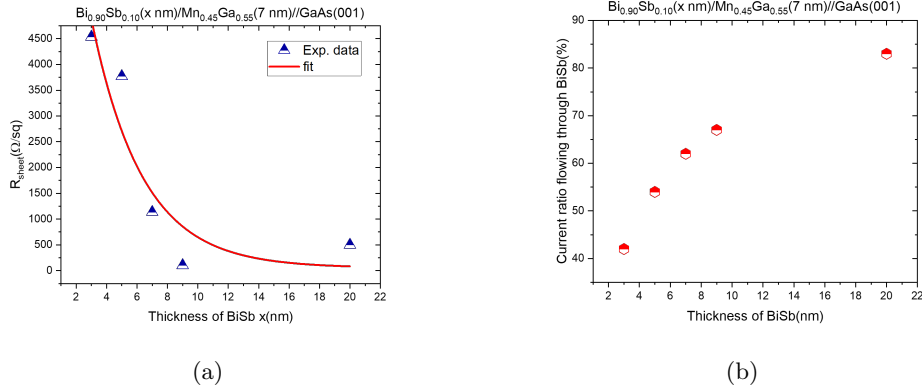


Figure 4.12: (a) Sheet resistance of the  $\text{Bi}_{0.90}\text{Sb}_{0.10}(x \text{ nm})/\text{Mn}_{0.45}\text{Ga}_{0.55}(7 \text{ nm})//\text{GaAs}(001)$  as a function of the thickness of the BiSb layer  $x$ . (b) Current ratio distribution flowing through the BiSb( $x \text{ nm}$ ) layer in the  $\text{Bi}_{0.90}\text{Sb}_{0.10}(x \text{ nm})/\text{Mn}_{0.45}\text{Ga}_{0.55}(7 \text{ nm})//\text{GaAs}(001)$  system.

$7.1 \times 10^5 \Omega^{-1} \text{m}^{-1}$  and  $\sigma(\text{Mn}_{0.45}\text{Ga}_{0.55}) = 4.2 \times 10^5 \Omega^{-1} \text{m}^{-1}$ . These values align closely with those calculated using longitudinal resistance measurements (cf. Table 4.1). This implies that the conductivity properties of the BiSb layers remain consistent, regardless of their thickness. This suggests a good structural quality of the BiSb layers, despite all the challenges we encountered during the development stage of the heterostructure, including differing symmetries of the TI and FM layers, intermixing between the substrate and MnGa, etc.

The behavior of the conductivity as a function of thickness also suggests that bulk states contribute more to the conductivity than surface states. If the contribution of the surface states is predominant, the sheet resistance remains constant irrespective of the layer's thickness. In our case, though, it varies as  $1/x$ .

We can now calculate the current distribution ratio through the BiSb layer in the BiSb( $x \text{ nm}$ )/MnGa(7 nm) bilayer system, as summarized in Figure 4.12(b). It is important to keep in mind that these values represent the lower limit of the current distribution, implying that even more current flows through the BiSb film in the studied bilayers.

### 4.3 Magnetotransport measurements

In this section, we will characterize our system using magnetotransport measurements that focus on various magnetoresistance effects arising from the spin-orbit interaction.

The magnetotransport measurements involve performing electrical measurements by injecting a current, denoted as  $I$ , and measuring both the longitudinal voltage  $V_{xx}$  and the transverse voltage  $V_{xy}$ , from which we can deduce the longitudinal resistance  $R_{xx}$  and the transverse resistance  $R_{xy}$ .

In the following, we will focus on basic magnetotransport measurements that confirm the ferromagnetic nature of MnGa, as well as the spin-to-charge interconversion behaviour of BiSb. It involves measuring anisotropic magnetoresistance (AMR), spin Hall magnetoresistance (SMR), and AHE effects. AMR and SMR both contribute to the longitudinal resistance, while AHE contributes to the transverse resistance.

### 4.3.1 Angular dependence measurements: AMR and SMR effects

First, we performed the scans in x-y, x-z, and y-z planes by rotating the sample at different angles  $\alpha$ ,  $\beta$ , and  $\gamma$  at a constant magnetic field of 4 T at 15 K, following the convention illustrated in Figure 4.13(a).

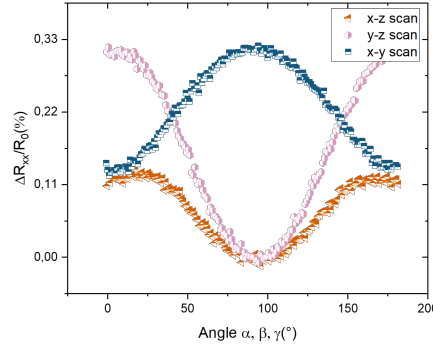
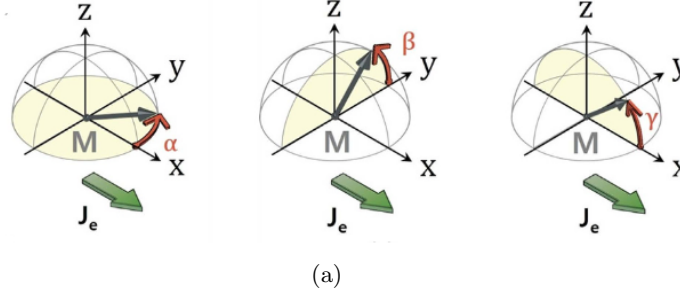


Figure 4.13: (a) Schematics of the magnetoresistance measurements by rotating the sample at angles  $\alpha$ ,  $\beta$ , and  $\gamma$  at a constant magnetic field. (b) The normalized longitudinal resistance  $\Delta R_{xx}/R_0$  in percentage (%) for BiSb(9 nm)/MnGa(7 nm), varies with different rotation angles  $\alpha$ ,  $\beta$ , and  $\gamma$ , following the convention illustrated in the panel above. The applied in-plane magnetic field of 4 T is strong enough to saturate magnetization of the MnGa layer in plane. The measurements were performed at 15 K.

Rotation in the x-z plane corresponds to the measurement of the anisotropic magnetoresistance effect. Indeed, the AMR refers to the dependence of the longitudinal resistance  $R_{xx}$  on the relative orientation of the injected current  $\mathbf{j}$  and the magnetization  $\mathbf{m}$  in a FM layer.

We apply a DC current along  $+\mathbf{x}$  direction and a magnetic field of 4 T in plane which is strong enough to saturate the magnetization of the MnGa film in plane of the sample. So by rotating the sample in the x-z plane, the angle  $\gamma$  between the magnetization and the current varies from  $0^\circ$  to  $90^\circ$ . The resistance is at its maximum, when the current and the magnetization are aligned ( $\mathbf{m} \parallel \mathbf{j}_x$ ), and at its minimum when they are perpendicular with respect to each other. Thus, the AMR can be expressed as:  $R_{xx,AMR} = R_{m_x} \cos^2 \gamma$ , where  $R_{m_x}$  is the resistance when the magnetization is along  $\mathbf{x}$  direction. This phenomenon arises from spin-dependent scattering due to the spin splitting of the d-states induced by

exchange interactions.

Rotation in the  $y$ - $z$  plane allows us to measure the spin Hall magnetoresistance. The SMR arises in NM/FM bilayer systems. It results from the absorption and/or partial reflection of the spin current generated by the spin Hall effect at the NM/FM interface. The reflected spin current is converted again into a charge current through the inverse spin Hall effect, resulting in resistance proportional to the square of the spin Hall angle.

The amount of the absorption of the spin current depends on the relative orientation of the magnetization  $\mathbf{m}$  and the spin accumulation  $\sigma$ . When they are aligned, the spin current is absorbed by the FM material over the spin diffusion length, which is larger than the mean free path [168]. On the other hand, when they are perpendicular with respect to each other, the spin current relaxes over a shorter length scale due to the Larmor precession of the conduction electron spins around the exchange field of the FM [130]. The shorter characteristic length is expected to lead to a larger absorption of the spin current compared to the first case when  $\mathbf{m} \parallel \sigma$ . Consequently, this results in a lower spin current converted in a lower charge current leading to a higher resistance.

The SMR can be also generated through the REE mechanism, which is known as Rashba magnetoresistance [116], [35].

To measure the SMR effect, similarly to AMR measurements, we apply a DC current along the  $+x$  direction and a 4 T magnetic field to saturate the magnetization within the plane of the sample. However, in this case, we rotate the sample in the  $y$ - $z$  plane, causing the angle  $\beta$  between the magnetization and the spin accumulation (aligned along  $+y$  direction) to vary from  $0^\circ$  to  $90^\circ$ . The resistance should be minimum when the spin accumulation and the magnetization are aligned ( $\mathbf{m} \parallel \sigma$ ) and maximum when they are perpendicular to each other. Thus, the SMR can be expressed as:  $R_{xx,SMR} = -R_{m_y} \cos^2 \beta$ .

Finally, rotation in the  $x$ - $y$  plane corresponds to the sum of the AMR and SMR effects.

Figure 4.13(b) displays the results of the measurements discussed above. The curves can be fitted with the square of the cosine of the corresponding angles. In the case of the AMR effect, its relative amplitude  $(R_{xx,AMR} - R_0)/R_0$  reached 0.11%.

Unexpectedly, for the SMR signal, we obtained a negative effect, i.e. the resistance is maximum when the spin accumulation and the magnetization are aligned ( $\mathbf{m} \parallel \sigma$ ) and minimum when they are perpendicular with respect to each other. Kang et al. reported a negative SMR in the Ta/NiFe bilayer [74]. According to their theoretical calculations, they attributed it to the combined effect of the interfacial spin current generation due to the spin-orbit coupling and its reciprocal effect: the interfacial spin-to-charge conversion enhances the resistivity, when the magnetization and spin accumulation are aligned.

Another possible explanation can be that the  $y$ - $z$  rotation signal contains contributions, other than the SMR, e.g., the anisotropic interfacial magnetoresistance (AIMR) that arises from the interfacial hybridization at the NM/FM interface [84], [66], [121].

In case if the measured signal when rotating the sample in the  $y$ - $z$  plane actually corresponds to the SMR effect, its relative magnitude, expressed as  $(R_{xx,SMR} - R_0)/R_0$ , is 0.35%. It is greater than what is typically observed for SMR in SOT reference systems, such as Pt/Co [106], [8], [76]. It is also higher than the SMR amplitude found in Bi<sub>0.90</sub>Sb<sub>0.10</sub>/FeCo bilayer (0.25%) by Binda et al. [20]. However, in this work, the expected positive SMR was reported. This significant SMR effect can serve us as an initial indicator of efficient spin-to-charge interconversion.

### 4.3.2 Anomalous Hall effect measurements

The anomalous Hall effect arises from spin-dependent scattering in a ferromagnetic material due to the spin-orbit interaction, as described in Section 1.2.1. It can be detected by

applying a current along the  $+x$  direction and using an out-of-plane magnetic field with sufficient strength to saturate the magnetization out of the plane. The effect is quantified by measuring the transverse resistance  $R_{xy}$  as a function of the magnetic field's amplitude. These measurements provide information about the magnetic properties of a ferromagnetic material.

Figure 4.14 displays the measurements of the anomalous Hall effect at various temperatures for the  $\text{Bi}_{0.90}\text{Sb}_{0.10}$  (9 nm)/ $\text{Mn}_{0.45}\text{Ga}_{0.55}$  (7 nm)//GaAs(001) bilayer (a) and the  $\text{Mn}_{0.45}\text{Ga}_{0.55}$  (7 nm) single layer capped with a 2 nm amorphous Bi layer (b). Both systems exhibit nearly square hysteresis resistance cycles, with their amplitudes strongly dependent on the measurement temperature, as expected. The single MnGa layer exhibits a large AHE amplitude of  $\sim 3.5 \Omega$  and a small coercive field,  $H_c = 0.1 \text{ T}$  at room temperature, indicating a ferromagnetic material with perpendicular magnetic anisotropy, consistent with our earlier SQUID measurements (cf. Section 3.3).

In the case of the BiSb/MnGa bilayer, the AHE amplitude is significantly reduced ( $\sim 0.30 \Omega$ ) compared to the single MnGa layer. This drop in AHE could be attributed to the fraction of the current passing through the BiSb (9 nm) layer. As we discussed previously approximately 33% of the current passes through the MnGa layer at room temperature. According to the parallel resistor model, the total AHE resistance of the BiSb/MnGa bilayer is equal to:  $R_{\text{AHE, BiSb/MnGa}} = \frac{R_{\text{BiSb}} R_{\text{MnGa}}}{R_{\text{BiSb}} + R_{\text{MnGa}}}$ . Assuming that  $R_{\text{BiSb}}$  stays constant (BiSb does not contribute to the AHE) and is negligible comparing to  $R_{\text{MnGa}}$ , the final expression of the AHE amplitude of the bilayer is [30]:

$$\Delta R_{\text{AHE, BiSb/MnGa}} \sim \Delta R_{\text{MnGa}} \left( \frac{R_{\text{BiSb}}}{R_{\text{MnGa}}} \right)^2 \quad (4.9)$$

In our case,  $\frac{R_{\text{BiSb}}}{R_{\text{MnGa}}} \sim 0.33$ . Therefore, in the BiSb/MnGa bilayer, the AHE amplitude will decrease to one-tenth of that observed in the single MnGa layer.

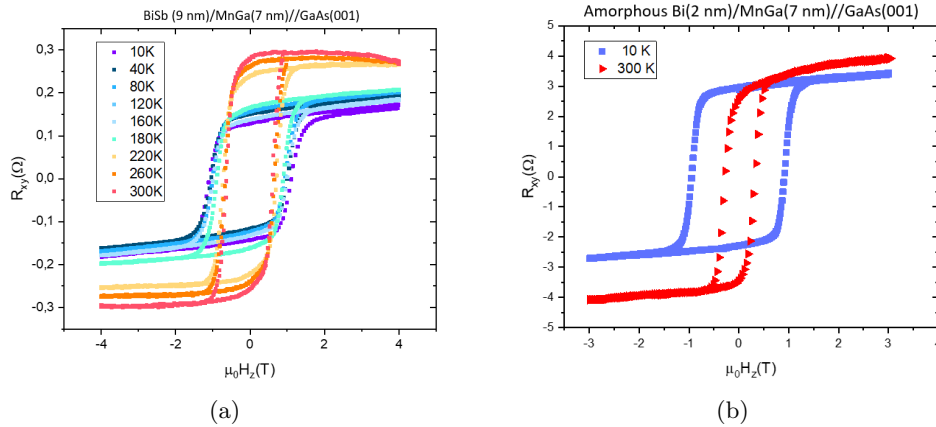


Figure 4.14: AHE hysteresis cycles at different temperatures with the magnetic field applied out of plane  $\mathbf{H} = H_z \mathbf{z}$  for the (a)  $\text{Bi}_{0.90}\text{Sb}_{0.10}$  (9 nm)/ $\text{Mn}_{0.45}\text{Ga}_{0.55}$  (7 nm) bilayer and (b)  $\text{Mn}_{0.45}\text{Ga}_{0.55}$  (7 nm) single layer capped with a 2 nm amorphous Bi layer.

## 4.4 Chapter conclusion

We investigated the surface states of the  $\text{Bi}_{0.85}\text{Sb}_{0.15}(15\text{ nm})/\text{Mn}_{0.45}\text{Ga}_{0.55}(10\text{ nm})//\text{GaAs}(001)$  and  $\text{Bi}_{0.85}\text{Sb}_{0.15}(15\text{ nm})//\text{GaAs}(001)$  systems using ARPES. One of the challenges we encountered was the removal of the As capping layer from the MnGa layer grown in the MBE machine at C2N. Decapping the As layer from the MnGa surface proved to be particularly challenging, resulting in a streaky and spotty RHEED pattern during the growth of the BiSb layer on top of this surface. This indicated that the removal of As was not entirely successful.

Nevertheless, we managed to record a Fermi surface on both systems, which was a combination of two single-domain Fermi surfaces, and observed two surface states,  $S_1$  and  $S_2$ , confirming the topological nature of BiSb on MnGa and BiSb on GaAs(001). The two-domain Fermi surface might stem from the BiSb layer grown in two crystallographic domains.

The presence of two structural domains of BiSb was further confirmed by a complementary structural analysis using GIXRD.

The magnetotransport studies unveiled the presence of various resistance components, including AMR, SMR, and AHE. If the measured signal when rotating in the y-z plane actually corresponds to the SMR effect, its significant amplitude in the BiSb/MnGa system can serve us as an initial indicator of spin-to-charge interconversion. The AHE confirmed the presence of perpendicular magnetic anisotropy in the MnGa layer, which is consistent with the magnetic characterization discussed in Section [3.3](#).

To assess the current distribution within the BiSb/MnGa systems, we studied their conductivity properties, which are crucial for understanding SOT measurements. Usually, in TI/FM systems, involving FM metals with high conductivity compared to the TI layer, most of the current probably flows through the FM layer, leading to current shunting. Our findings reveal that at least 67% (78%) of the current flows through the BiSb layer in the  $\text{BiSb}(9\text{ nm})/\text{MnGa}(7\text{ nm})$  heterostructure at room (low) temperature. The current shunting to the FM layer is thus limited and most of the current contributes to the generation of a pure spin current at the topological insulator surface. Consequently, our system might offer a significant gain in charge-to-spin conversion efficiency. In addition, we estimated the conductivity of  $\text{Bi}_{0.90}\text{Sb}_{0.10}$  thin layer to be twice as large than found in the literature. However, the reason behind this large conductivity is not clear yet.

Additionally, we measured the resistivity of the BiSb layer for various thicknesses of BiSb. The resistivity decreases with increasing thickness, suggesting a uniform distribution of deposited atoms in atomic layers. It also suggests that bulk states contributes in the conductivity more than surface states.

The consistent conductivity properties of BiSb regardless of its thickness, suggest a good structural quality of the BiSb layers, despite differing symmetries of BiSb and MnGa and their large lattice mismatch.



## Chapter 5

# Charge-to-spin interconversion in BiSb/MnGa//GaAs(001) bilayer

This chapter is dedicated to the characterization of the charge-to-spin interconversion properties in the BiSb/MnGa bilayer heterostructure. Firstly, we will discuss the charge-to-spin conversion, in particular the evaluation of spin-orbit torques, and the current-driven magnetization switching. We already described the fundamentals of SOT in Chapter 1, as well as the properties of TI for SOT in Chapter 2. Here, we will focus on the experimental aspect of the SOT. To begin, we will describe one of the main experimental technique typically used to measure SOT efficiency and applied in this work: the harmonic Hall voltage (HHV) technique, along with the macrospin model we used to extract SOT efficiency values. Subsequently, we will present and discuss the results of the HHV measurements, as well as the current-driven magnetization switching.

Finally, we will present preliminary results on the reciprocal effect, i.e. the characterization of spin-to-charge conversion in the BiSb/MnGa bilayer heterostructure. This will be accomplished using terahertz time-domain spectroscopy (THz-TDS), and we will compare our system with other well-known conventional metallic systems.

### 5.1 Charge-to-spin conversion: SOT in BiSb/MnGa//GaAs(001) heterostructure

In general, in HM/FM heterostructures, SOT measurements are based on the effect of the absorption of a spin current by the FM layer on the magnetization, leading to magnetization oscillations or switching. The magnetization dynamics signal can be detected through the variation of the transverse and longitudinal resistance, which have several contributions, primarily from the anomalous Hall effect, anisotropic magnetoresistance, spin Hall magnetoresistance, and non-linear magnetoresistance terms proportional to the current-induced spin density. In addition, charge current induces thermoelectric and thermomagnetic effects due to thermal gradients caused by the Joule effect and asymmetric heat dissipation. These effects are known as the anomalous Nernst effect and the spin Seebeck effect 7. These thermal gradients can exist in the plane of the sample along the  $x$  direction:  $\nabla T = \nabla_x T \mathbf{x}$ , or out of the plane:  $\nabla T = \nabla_z T \mathbf{z}$ .

Each of these contributions can be separated based on their distinct symmetries and magnetic field dependencies 7.

The main experimental techniques for measuring SOT include the harmonic Hall voltage (HHV), spin-torque ferromagnetic resonance (ST-FMR) [166], [89], [145], [99], [100], [13], [47], [90]. and magneto-optical Kerr effect (MOKE) [112], [40], [141], [144], [157], [45]. In this work, we used HHV to perform SOT measurements, which we will describe more in detail in the next section.

### 5.1.1 Harmonic Hall voltage technique

The HHV technique consists in injecting a low frequency AC current into the studied heterostructure patterned in a Hall bar device. The harmonic response of the magnetization oscillating at a frequency  $\omega$  around its equilibrium position  $(\theta, \varphi)$  induced by the AC current  $I = I_0 \sin(\omega t)$  can be thus detected. The variations of this equilibrium position  $(\Delta\theta, \Delta\varphi)$  are defined by a combination of the effective anisotropy field, external magnetic field and current-induced fields via magnetoresistance effects (AHE, planar Hall effect (PHE), etc.). So by measuring  $(\Delta\theta, \Delta\varphi)$ , the estimation of the components of the current-induced field is possible [87]. The time-dependent transverse Hall resistance  $R_{xy}(t)$  writes as:

$$R_{xy}(t) = R_{xy}(\mathbf{B}_0 + \mathbf{B}_I(t)) \quad (5.1)$$

where  $\mathbf{B}_0$  is the sum of the effective anisotropy field and the external magnetic field and  $\mathbf{B}_I$  is the sum of current-induced fields, i.e. damping-like  $\mathbf{B}_{DL}$ , field-like  $\mathbf{B}_{FL}$  SOTs, and Oersted field  $\mathbf{B}_{Oe}$ :  $\mathbf{B}_I = \mathbf{B}_{DL} + \mathbf{B}_{FL} + \mathbf{B}_{Oe}$ .

Assuming the small oscillations of the magnetization,  $R_{xy}(t)$  can be expanded in Taylor series to the first order as follows:

$$R_{xy}(t) \approx R_{xy}(\mathbf{B}_0) + \frac{dR_{xy}}{d\mathbf{B}_I} \cdot \mathbf{B}_I \sin(\omega t) \quad (5.2)$$

The transverse Hall voltage  $V_{xy}$  is given by the following equation:

$$V_{xy}(t) = R_{xy}(t)I_0 \sin(\omega t) \quad (5.3)$$

If we combine Equations [5.2] and [5.3], we obtain:

$$V_{xy}(t) = R_{xy}(\mathbf{B}_0)I_0 \sin(\omega t) + \frac{dR_{xy}}{d\mathbf{B}_I}(\mathbf{B}_I)I_0 \sin^2(\omega t) \quad (5.4)$$

Considering Equation [5.4], and recalling that  $\sin^2(x) = \frac{1}{2} - \frac{\cos(2x)}{2}$ ,  $V_{xy}$  writes as follows:

$$V_{xy} \approx I_0[R_{xy}^0 + R_{xy}^\omega \sin(\omega t) + R_{xy}^{2\omega} \cos(2\omega t)] \quad (5.5)$$

where  $R_{xy}^0 = \frac{1}{2} \frac{dR_{xy}}{d\mathbf{B}_I} \cdot \mathbf{B}_I$  is the 0<sup>th</sup> harmonic response,  $R_{xy}^\omega = R_{xy}(\mathbf{B}_0)$  is the 1<sup>st</sup> harmonic response, and  $R_{xy}^{2\omega} = -\frac{1}{2} \frac{dR_{xy}^\omega}{d\mathbf{B}_I} \cdot \mathbf{B}_I + R_{xy}^{2\omega T}$  is the 2<sup>nd</sup> harmonic response.

In addition, we need to take into account the anomalous Hall resistance  $R_{AHE}$ , the planar Hall resistance  $R_{PHE}$ , as well as the thermoelectric effect. We already discussed AHE in Section [4.3.2].

To study planar Hall effect, which originates from AMR, the Hall voltage is measured in the plane of the sample. It is sensitive to the in-plane component of the magnetization,

meaning that the resistance depends on the angle between the current direction and the magnetization direction in the plane of the sample:  $R_{\text{PHE}} \propto \sin(2\varphi_m)$ .

As for the thermoelectric effect, assuming that the thermal gradient is induced only by the Joule heating due to the injected current, we obtain  $\nabla T \propto I^2 R_s$ , where  $R_s$  is the sample resistance. If the injected current is an AC current,  $\nabla T$  becomes:

$$\nabla T \propto I_0^2 \sin^2(\omega t) R_s = \frac{1}{2} I_0^2 (1 - \cos(2\omega t)) R_s \quad (5.6)$$

Usually, in a FM layer, the main contribution to the thermal effect is due to the ANE. The in-plane current induces a perpendicular thermal gradient, so that correspondent voltage is defined as:  $V_{\text{ANE}} \sim \nabla T \times \mathbf{m}$ . This thermal gradient should be thus included in the 2<sup>nd</sup> harmonic response and contributes when the external magnetic field is applied along the current direction. It is possible to subtract this effect from the 2<sup>nd</sup> harmonic response. Another thermal contribution to the 2<sup>nd</sup> harmonic response is the ordinary Nernst effect (ONE) [139], [1], which is proportional to the applied magnetic field  $V_{\text{ONE}} \sim N \nabla T I_0 B_{\text{ext}}$  (where  $N$  is the ordinary Nernst coefficient), so that it is a predominant term at high fields.

So considering the effects mentioned above, the 1<sup>st</sup> harmonic response writes as:

$$V_{xy} = IR_0 + IR_{\text{AHE}} \cos \theta + IR_{\text{PHE}} \sin^2 \theta \sin(2\varphi) \quad (5.7)$$

$\Delta\theta$  and  $\Delta\varphi$  can be expanded in Taylor series to the first order:

$$\Delta\theta = \frac{\partial_{H_x} E}{\partial_\theta E} \Delta H_x + \frac{\partial_{H_y} E}{\partial_\theta E} \Delta H_y + \frac{\partial_{H_z} E}{\partial_\theta E} \Delta H_z \quad (5.8)$$

$$\Delta\varphi = \frac{\partial_{H_x} E}{\partial_\varphi E} \Delta H_x + \frac{\partial_{H_y} E}{\partial_\varphi E} \Delta H_y + \frac{\partial_{H_z} E}{\partial_\varphi E} \Delta H_z \quad (5.9)$$

where  $E$  is the total energy density of the thin film with uniaxial anisotropy, which can be expressed as follows:

$$E = -K_{\text{eff}} \cos^2 \theta - M_s (\sin \theta \cos \varphi H_x + \sin \theta \sin \varphi H_y + \cos \theta H_z) \quad (5.10)$$

where  $K_{\text{eff}}$  is the effective out-of-plane anisotropy, that verifies the relation:  $K_{\text{eff}} = \mu_0 H_k M_s / 2$ .

If we combine Equations [5.8], [5.9], and [5.10],  $\Delta\theta$  and  $\Delta\varphi$  can be rewritten as:

$$\Delta\theta = \frac{\cos \theta (\Delta H_x \cos \varphi + \Delta H_y \sin \varphi) - \Delta H_z \sin \theta}{H_k \cos(2\theta) + H \cos(\theta - \theta_H)} \quad (5.11)$$

$$\Delta\varphi = \frac{\Delta H_y \cos \varphi - \Delta H_x \sin \varphi}{H \sin \theta_H} \quad (5.12)$$

Since the injected AC current is time-dependent, we replace  $I$  with  $I_0 \sin(\omega t)$ ,  $\Delta H$  with  $\Delta H \sin(\omega t)$ ,  $\theta$  with  $\theta + \Delta\theta \sin(\omega t)$ , and  $\varphi$  with  $\varphi + \Delta\varphi \sin(\omega t)$ , so we can rewrite  $V_{xy}$  of Equation [5.7] as follows:

$$V_{xy} = V_0 + V_\omega \sin(\omega t) + V_{2\omega} \cos(2\omega t) \quad (5.13)$$

where  $V_\omega = I_0 (R_0 + R_{\text{AHE}} \cos \theta + R_{\text{PHE}} \sin^2(\theta) \sin(2\varphi))$  and  $V_{2\omega} = \frac{1}{2} (R_{\text{AHE}} \sin \theta - R_{\text{PHE}} \sin(2\theta) \sin(2\varphi)) \Delta\theta I_0 - R_{\text{PHE}} \sin^2(\theta) \cos(2\varphi) \Delta\varphi I_0$ .

Measurements of  $V_\omega$  provide information about the magnetization rotation ( $\theta, \varphi$ ), whereas  $V_{2\omega}$  contains information about the magnetization oscillation ( $\Delta\theta, \Delta\varphi$ ).

It is necessary to measure the 1<sup>st</sup> harmonic response, since it allows to estimate the polar angle of the magnetization  $\theta$ .

In our case, we have a system with a perpendicular magnetic anisotropy, so two distinctive measurements need to be done with the external magnetic field applied in the plane of the sample at angles ( $\theta_H = \frac{\pi}{2} + \delta\theta_H, \varphi_H = 0^\circ$ ) and ( $\theta_H = \frac{\pi}{2} + \delta\theta_H, \varphi_H = 90^\circ$ ). These measurements correspond respectively to the DLT and FLT, if  $R_{\text{AHE}} \gg R_{\text{PHE}}$  [50]. This condition is generally true in metallic systems, and it serves as the historical reason behind the names of these two geometries. To avoid multidomain states, the external magnetic field is slightly tilted with respect to the sample surface at angle  $\delta\theta_H$ . So, the DLT and FLT voltages can be expressed as follows:

$$V_{2\omega}^{\text{DL}} = -\frac{1}{2} \sin \theta \left( \frac{H_{\text{DL}}}{H_k \cos(2\theta) - H \sin(\delta\theta_H - \theta)} + \frac{2H_{\text{FL}}R_{\text{PHE}}/R_{\text{AHE}} \sec \delta\theta_H \sin \theta}{H} \right) R_{\text{AHE}}I_0 \quad (5.14)$$

$$V_{2\omega}^{\text{FL}} = \frac{1}{2} \cos \theta \sin \theta \left( \frac{H_{\text{FL}}}{H_k \cos(2\theta) - H \sin(\delta\theta_H - \theta)} + \frac{2H_{\text{DL}}R_{\text{PHE}}/R_{\text{AHE}} \sec \delta\theta_H \sin \theta}{H} \right) R_{\text{AHE}}I_0 \quad (5.15)$$

$\theta$  can be directly estimated from the  $V_\omega$  measurements:  $\theta = \cos^{-1}(V_\omega)$ .  $H_k$  and  $\delta\theta_H$  can be estimated from  $\cos \theta$  as a function of  $H$  using the Stoner-Wohlfarth model [176]:

$$\cos \theta = \frac{f}{6} \pm \frac{1}{6} \sqrt{2f^2 - 18e + \frac{54h_z(1 + h_{\text{IP}}^2)}{f} - \frac{h_{\text{OIP}}}{2}} \quad (5.16)$$

where  $h = H/H_k$ ,  $h_{\text{IP}}$  and  $h_{\text{OIP}}$  are in-plane and out-of-plane components of  $h$ , respectively,  $d = 1 - h^2$ ,  $e = d \cos(\frac{1}{3} \cos^{-1}(54h_{\text{IP}}^2 h_{\text{OIP}}^2/d^3 - 1))$ , and  $f = \pm \sqrt{9h_{\text{OIP}}^2 + 6d + 6e}$ .

By fitting the measured 2<sup>nd</sup> harmonic Hall voltage  $V_{2\omega}^{\text{DL,FL}}$  as a function of  $H/H_k$ , we can extract the values of  $H_{\text{DL}}$  and  $H_{\text{FL}}$ . Figure 5.1 shows the typical  $V_{2\omega}^{\text{DL,FL}}$  curves that can be obtained experimentally [87]. The peaks of  $V_{2\omega}^{\text{DL}}$  change the sign when the magnetization is reversed, while the peaks of  $V_{2\omega}^{\text{FL}}$  do not depend on the magnetization direction.

### 5.1.2 SOT efficiency dependence on the BiSb thickness

#### Sample preparation

For this study, a series of samples,  $\text{Bi}_{0.90}\text{Sb}_{0.10}$  ( $x$  nm)/ $\text{Mn}_{0.45}\text{Ga}_{0.55}$  (7 nm)//GaAs(001), with  $x$  as BiSb thickness values of 3 nm, 5 nm, 7 nm, 9 nm, and 20 nm were grown by MBE following the procedure described in Section 3.4

The harmonic Hall voltage measurements were conducted in Hall bars, the design of which is shown in Figure 5.2(a). These 27- $\mu\text{m}$  long and 4- $\mu\text{m}$  wide Hall bars were patterned using one-step projection photolithography, followed by dry etching.

#### Experimental results and discussion

We performed the harmonic Hall voltage measurements, by injecting an AC current  $\mathbf{j}_x$  with the Keithley 6221 current source and measuring the 1<sup>st</sup> and the 2<sup>nd</sup> harmonic of the transverse Hall voltage with the Signal recovery 7270 DSP lock-in amplifier as a function of the external magnetic field. These measurements were conducted inside

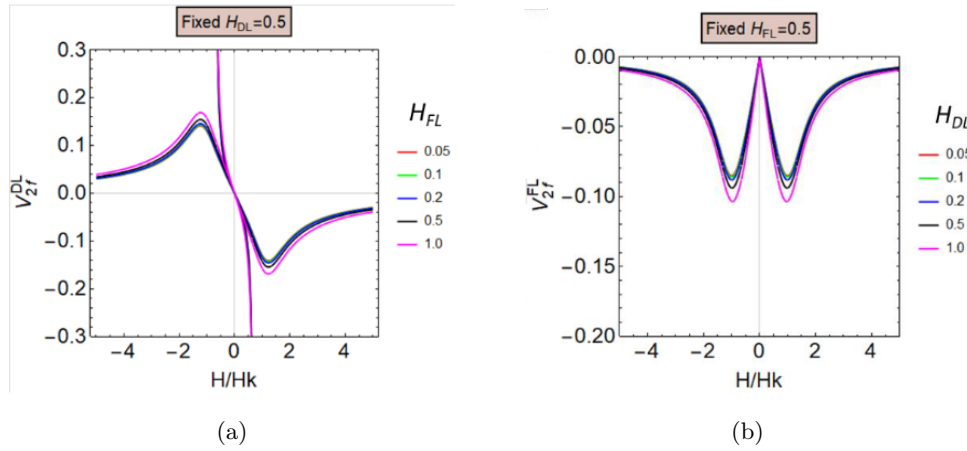


Figure 5.1: Numerical simulations of the 2<sup>nd</sup> harmonic Hall voltage  $V_{2\omega}$  as a function of the normalized external magnetic field  $H/H_k$  in the (a) damping-like geometry and (b) field-like geometry. Extracted from [87].

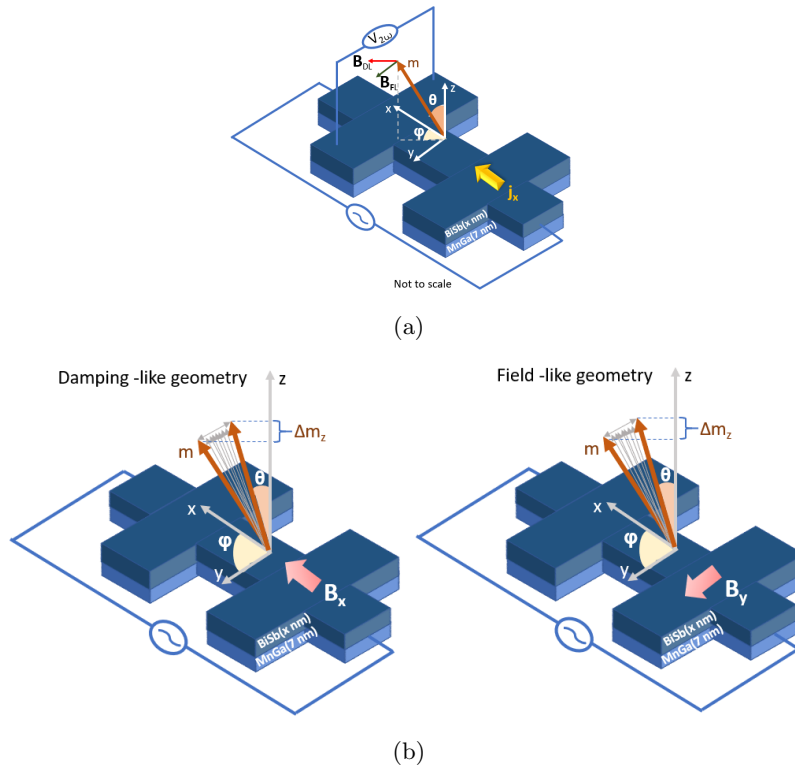


Figure 5.2: (a) Schematic representation of the harmonic Hall voltage technique experiments on a Hall bar. (b) Effect of a low-frequency AC current on the magnetization  $\mathbf{m}$  in the damping-like (left) and the field-like (right) geometries.

the closed-cycle helium cryostat Attodyr 1000, allowing temperatures as low as 5 K and equipped with a superconducting magnet enabling the reach of magnetic fields up to 9 T. The 3D sample rotator module allows the application of an external magnetic field both out-of-plane and in-plane of the sample. We used the spherical coordinates system with  $\varphi_m$  the azimuthal angle between the x-axis and the magnetization vector  $\mathbf{m}$  and  $\theta_m$  the polar angle between the y-axis and the magnetization vector. Schematic illustration of these experiments is represented in Figure 5.2(a).

The in-plane magnetic field is applied at  $\varphi_H = 0^\circ$  (along the  $\mathbf{x}$  direction) which corresponds to the damping-like geometry and at  $\varphi_H = 90^\circ$  (along the  $\mathbf{y}$  direction) which corresponds to the field-like geometry, as portrayed in Figure 5.2(b). It also shows the effect of the low-frequency AC current on the FM magnetization. We applied currents ranging from 1 mA to 4 mA. The corresponding current densities were calculated using the Hall bar width ( $4 \mu\text{m}$ ), the thickness of the BiSb layer, and, most importantly, by taking into account the current ratio flowing through the BiSb layer, as estimated in Section 4.2. All the results presented in this Section were obtained at room temperature.

As discussed previously, to extract  $B_{\text{DL,FL}}$ , we need the amplitudes of the AHE and PHE. So we measure these effects that contribute in the 1<sup>st</sup> harmonic resistance. Typical AHE and PHE curves measured in our samples are presented in Figure 5.3

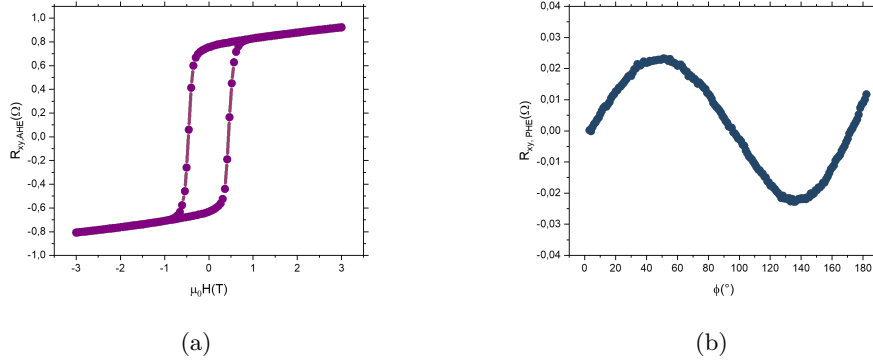


Figure 5.3: Typical AHE and PHE curves measured in the BiSb( $x$  nm)/MnGa(7 nm) samples: (a) AHE hysteresis cycle measured at 300 K with the out-of-plane magnetic field, (b) PHE effect measured at 300 K by rotating the sample in the x-y plane and applying the 4 T in-plane magnetic field.

The 2<sup>st</sup> harmonic resistance has the contributions from the current-induced DLT and FLT, the Oersted field, and the thermal effects, such as ANE, ONE, and the spin Seebeck effect.

Figure 5.4 shows the 2<sup>nd</sup> harmonic voltage as a function of applied in-plane magnetic field in the damping-like geometry for different thickness of the BiSb layer. We observe that up till 7 nm, the 2<sup>nd</sup> harmonic voltage is dominated by the thermal effects, so that the  $B_{\text{DL}}$  is relatively small. However, for the thickness above 7 nm, the 2<sup>nd</sup> harmonic voltage presents the expected anti-symmetric behaviour.

Figure 5.5 shows the 2<sup>nd</sup> harmonic voltage as a function of applied in-plane magnetic field in the field-like geometry for different thickness of the BiSb layer. The curves show the expected symmetric behaviour.

The extracted values of  $B_{\text{DL,FL}}$  as a function of thickness of BiSb are shown in Figure 5.6. We observed that the DLT increases with the increasing thickness of BiSb. This

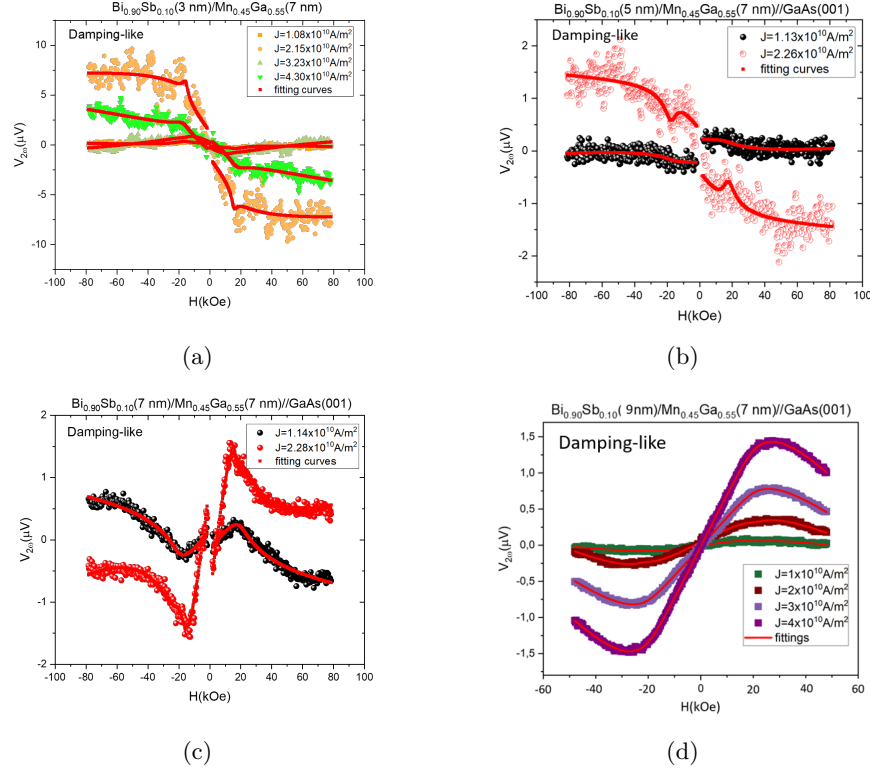


Figure 5.4: The 2<sup>nd</sup> harmonic Hall voltage measurements in the damping-like geometry in Bi<sub>0.90</sub>Sb<sub>0.10</sub>( $x$  nm)/Mn<sub>0.45</sub>Ga<sub>0.55</sub>(7 nm)//GaAs(001) heterostructure with  $x =$  (a) 3 nm, (b) 5 nm, (c) 7 nm, (d) 9 nm. All the measurements were performed at room temperature.

trend suggests the bulk SOT behaviour that should evolve as:  $\theta_{SH} \frac{g_{\uparrow\downarrow r_s} \tanh\left(\frac{x \text{BiSb}}{2\lambda_{sf}}\right)}{1 + g_{\uparrow\downarrow r_s} \coth\left(\frac{x \text{BiSb}}{\lambda_{sf}}\right)}$  [99], where  $\lambda_{sf}$  is the spin diffusion length and  $g_{\uparrow\downarrow r_s}$  is a material constant, a product of the spin mixing conductance of BiSb and MnGa and the spin resistance of BiSb. This formula was used to fit the DLT as a function of thickness by varying the parameters  $\lambda_{sf}$  and  $g_{\uparrow\downarrow r_s}$ . The fit is shown in Figure 5.6 and  $\lambda_{sf}$  is found to be  $15 \pm 5$  nm. This value differs from that found by Sharma et al. ( $\sim 8$  nm) [151].

As for the  $B_{FL}$ , the uncertainty estimation is significant, making it difficult to interpret these results properly.

The damping-like torque has been primarily considered as a result of the spin current generated by the bulk of the NM layer through the spin Hall effect. According to this paradigm, our findings suggest that bulk states of BiSb play a predominant role in generating SOTs via SHE, since we observed an increase of the DLT with increasing thickness of BiSb, and the interfacial REE contribution is expected to be thickness-independent according to the simplest theoretical models.

The predominance of the bulk states to the SOTs was also suggested by Binda et al. in MBE-grown BiSb/FeCo system [20], as well as by Chi et al. in sputtered BiSb/CoFeB [26]. The charge-to-spin conversion via REE mechanism, i.e. dominated by topological surface states in the BiSb-based system has not been reported yet.

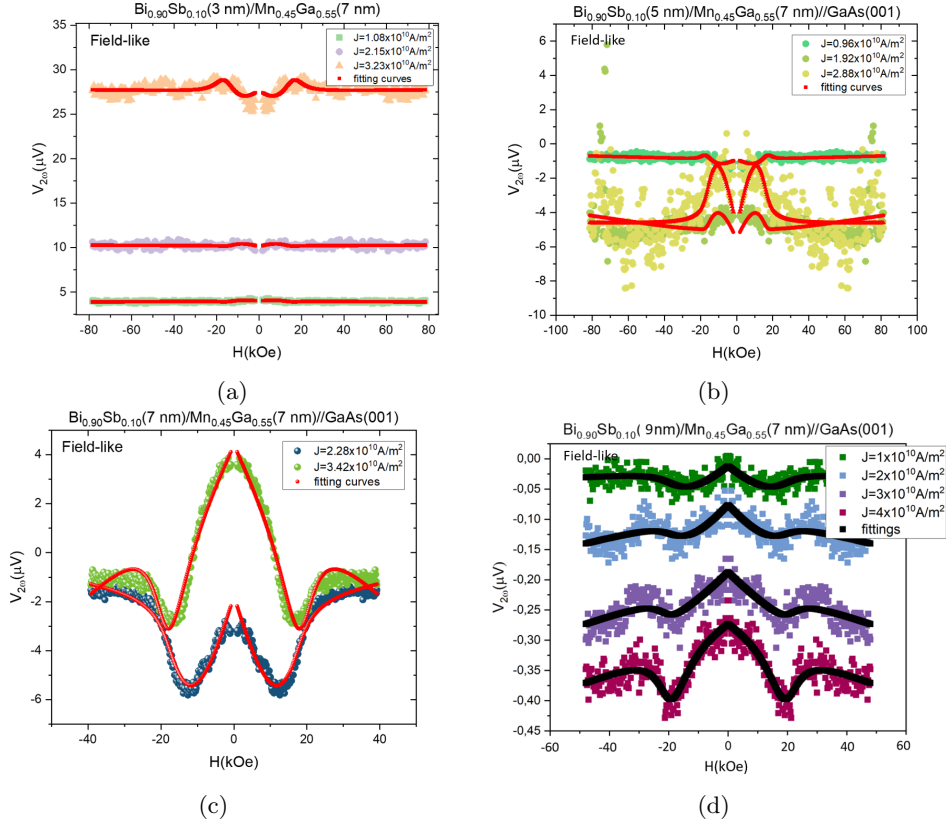


Figure 5.5: The 2<sup>nd</sup> harmonic Hall voltage measurements in the field-like geometry in  $\text{Bi}_{0.90}\text{Sb}_{0.10}(x \text{ nm})/\text{Mn}_{0.45}\text{Ga}_{0.55}(7 \text{ nm})$  with  $x =$  (a) 3 nm, (b) 5 nm, (c) 7 nm, (d) 9 nm. All the measurements were performed at room temperature.

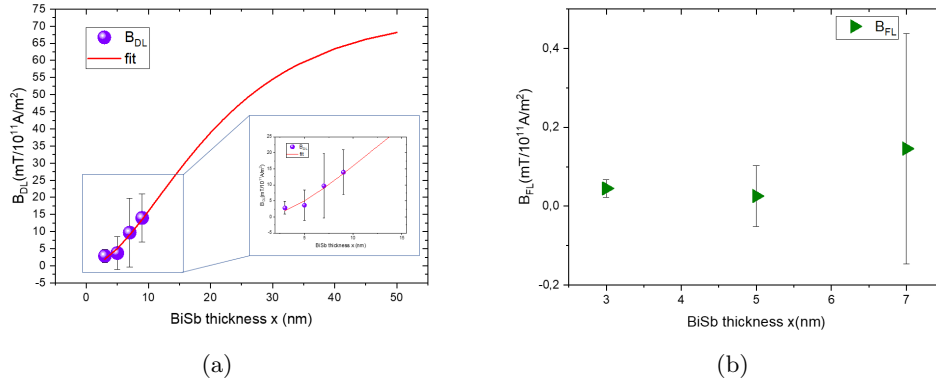


Figure 5.6: Extracted values of the (a)  $B_{DL}$  and its fit, and (b)  $B_{FL}$  as a function of BiSb thickness from the HHV measurements of the  $\text{Bi}_{0.90}\text{Sb}_{0.10}(x \text{ nm})/\text{Mn}_{0.45}\text{Ga}_{0.55}(7 \text{ nm})$  bilayer.

These observations contrast with the findings from our previous study, discussed in Section 2.3, where we obtained a significant thickness-independent THz signal confirming high SCC in BiSb/Co system [138]. Spin-to-charge conversion was attributed to the IREE, suggesting that the surface states of BiSb are mainly responsible for efficient SCC. However, it is important to note that this BiSb layer was grown on a different substrate (Si(111)) with a different FM material, and the SCC was evaluated by the THz-TDS technique.

Nonetheless, by probing the surface of the BiSb/MnGa//GaAs(001) bilayer, we confirmed the presence of topological surface states on the upper surface of BiSb, as discussed in Section 4.1. We currently lack information about the presence of non-trivial surface states on the bottom surface (BiSb/MnGa interface). Nevertheless, both surface and bulk states may coexist and may contribute to the generation of SOTs. Disentangling one contribution from another, however, remains challenging, since ideally the SOT thickness-dependence study requires that other properties of the thin layers do not change with varying thickness.

In recent theoretical studies by Haney et al. [56] and Amin and Stiles [3], the paradigm described above has shifted. Both DLT and FLT have interfacial nature, and Rashba-like DLT scales similarly to SHE-DLT with varying thickness. Thus, separating the two contributions to the DLT is not easy. The only certain claim that we can make for now is that experimentally DLT in the majority of systems has a strong contribution from the spin Hall effect. As for the Rashba effect, it can contribute to both DLT and FLT, since according to these calculations, the accumulated spin density at the interface can diffuse away from the interface towards the bulk due to the extrinsic scattering. Its actual contribution still remains unclear.

Similarly, the SHE not only generates the spin current from the bulk, but also results in a non-equilibrium spin density at the interface, thus can be expected to contribute to both DLT and FLT.

Theoretical calculations using the drift-diffusion model of the SHE suggest that both DLT and FLT have a similar thickness-dependent behavior and are proportional to the real and imaginary parts of the spin mixing conductance (SMC) of the interface, respectively. This results in  $\xi_{DL}^j \gg \xi_{FL}^j$  [56]. This is not, however, consistent with the experimental observations made in most systems.

Therefore, a more in-depth structural investigation of the BiSb/MnGa heterostructure, depending on the thickness of BiSb, becomes crucial. As mentioned previously, we have grown a 20 nm-thick BiSb sample, but unfortunately for technical reasons we were not able to measure it. In addition, since the SHE-DLT increases with the increasing thickness of BiSb until its saturation at  $x > 2\lambda_{sf}$ , it is necessary to produce more samples with higher thicknesses, going to at least 40 nm (since we found  $\lambda_{sf} = 15 \pm 5$  nm).

Nonetheless, for  $x_{\text{BiSb}} = 9$  nm, even for the relatively thick FM layer, we were able to obtain a significant effective damping-like field  $B_{DL} = 13.97$  mT for the injected current density of  $10^{11}$  A/m<sup>2</sup>. It is important to note that our model does not take into consideration a magnon-driven SOT that can be significant in some materials. We will discuss this effect in Section 5.1.3. The charge-to-spin conversion efficiency  $\xi_{DL,FL}$  can be calculated using the following formula:

$$\xi_{DL,FL}^j = \frac{2e}{\hbar} \frac{M_s t_{\text{FM}}}{j} B_{DL,FL} \quad (5.17)$$

The DLT efficiency of our heterostructure for the 9 nm-thick BiSb layer is estimated to be  $\simeq 0.65$ , which is larger than that in conventional 5d heavy metals based systems,

for example,  $\xi_{\text{Pt,DL}}^j = 0.06 - 0.2$  (cf. Section 1.4), making BiSb a promising candidate as an efficient spin current source. However, it is smaller compared to the SOT efficiency reported in some studies for BiSb-based heterostructures, as discussed in Section 2.3 where it varies from 0.01 to 61. It is important to note that the high SOT efficiencies of 52 and 61 were estimated indirectly, using measurement techniques, such as current-induced hysteresis loop shift and output voltage of a SOT reader, respectively [77], [64]. Studies involving more direct measurements of SOT, using techniques like HHV, report more modest SOT efficiencies, ranging from 0.01 to 3.5. Multiple factors, such as deposition mode, structural and interface quality can make the comparative analysis of the SOT efficiency highly misleading. In addition, lack of information on the current distribution in a stack can result in a wrong estimation of the SOTs, as well.

### 5.1.3 SOT temperature dependence discussion

All HHV measurements were conducted at both room and low (15 K) temperatures. Surprisingly, we did not detect a significant SOT signal at low temperature. Usually, in the TI-based systems the decrease in carrier conductivity for bulk states with lowering temperature suggests that surface state carriers should dominate the conductivity at lower temperatures, consequently enhancing SOT contributions from the topological surface states.

Our observations align with the study conducted by Chi et al. on the sputtered BiSb/CoFeB system, where the SOT increases with rising temperature [26]. Notably, this effect appears to be independent of material thickness, as we did not observe significant SOTs at various thicknesses of BiSb at low temperature. This suggests that the temperature-dependent spin diffusion length of BiSb does not influence this phenomenon. Additionally, we found that the saturation magnetization of the MnGa layer remains relatively constant when the temperature decreases (see Section 4.3). Therefore, the changes in DLT and FLT are likely attributable to variations in the injected spin current. This temperature dependence can be attributed to the fact that the spin-dependent scattering due to phonons and magnons may enhance the SOTs at room temperature. Thus, it is important to consider these contributions to the SOTs when evaluating them. For instance, the magnon-driven torque efficiency in the Bi<sub>2</sub>Se<sub>3</sub>/antiferromagnetic NiO system is 0.3, which surpasses the efficiency of current-driven SOTs in heavy metals [172]. These experiments can be conducted using quasi-static MOKE or time-resolved MOKE [104].

Chi et al. proposed that thermally excited Dirac-like electrons in the *L* valley with large Berry curvature of the bulk energy gap of BiSb are responsible for the SOT enhancement at higher temperatures [26].

In another study of the BiSb/FeCo system, a decreasing SOT with decreasing temperature was attributed to the fact that the contribution to SOT above 20 K arises from thermally excited bulk hole carriers at the T point (see Figure 2.7(a)) [20]. Theoretical calculations indicated that the T point carriers contribute positively to the spin Hall conductivity, while the contribution of the L point is negative. Therefore, reducing the temperature leads to a decrease in the contribution of the T point to conductivity, resulting in reduced SOT. For the temperatures under 20 K, however, the DLT efficiency increases, which was attributed to the increased spin polarisation of surface states around  $\Gamma$  point due to reduced electron scattering.

In contrast, an inverse effect is observed in other TI-based systems, such as sputtered Bi<sub>2</sub>Se<sub>3</sub>/CoFeB, where the SOT increases with decreasing temperature [174]. In this study, the temperature-dependent SOT was attributed to the intrinsic effect of topological surface states. Given that the bulk energy gap of a TI is typically around 0.1 eV,

the Fermi energy of surface states falls within the range of 0.01-0.1 eV, corresponding to Fermi temperatures of  $10^2 - 10^3$  K—well within the experimental temperature range. Consequently, the surface states cannot be considered as degenerate electron gas and thus, thermal effects appear to be a significant factor in charge-to-spin conversion. In addition, as mentioned previously, with the increasing temperature, the role of phonon scattering becomes important resulting in both intraband and interband scattering, i.e. from surface to bulk which can be detrimental for the spin current generation [59], [128].

#### 5.1.4 Current-induced magnetization switching

The pioneering work of Miron, Garello et al. demonstrated the reversible switching of perpendicular magnetization in Pt/Co/AlO<sub>x</sub> ultrathin layers upon the injection of AC current pulses and an in-plane applied magnetic field  $B_x$  at current densities of  $10^7 - 10^8$  A/cm<sup>2</sup> [112]. In the macrospin model, the current-induced damping-like effective field  $B_{DL}$  can switch the magnetization from  $+\mathbf{z}$  to  $-\mathbf{z}$ , and the threshold current for switching in samples with perpendicular magnetic anisotropy is given by [94]:

$$j_{sw} = \frac{2e}{\hbar} \frac{M_s t_{FM}}{\xi_{DL}^j} \left( \frac{B_K}{2} - \frac{B_x}{\sqrt{2}} \right) \quad (5.18)$$

where  $B_K$  is the perpendicular anisotropy field that determines the thermal stability of the FM layer.

Practically, the switching process is highly dependent on the temperature determined by the injected current density and thermal conductivity of the layers. This dependence can not only initiate the switching but also modify critical material properties, such as  $M_s$ ,  $B_K$ , and  $\xi_{DL}^j$  during the experiment.

The magnetization switching process occurs through the nucleation and propagation of magnetic domains. Micromagnetic simulations [48], [129], [108], [111], and spatially-resolved magneto-optical Kerr effect (MOKE) measurements [41], [141], [181] have supported the development of various switching models. According to these models, the nucleation of domains can be initiated thermally or by the combination of Dzyaloshinskii-Moriya interaction (DMI), applied magnetic field, and edge effects, while the propagation of domain walls is determined by the damping-like torque.

#### Experimental results

We conducted magnetization switching experiments using SOTs induced by in-plane current. These experiments were performed on a Bi<sub>0.90</sub>Sb<sub>0.10</sub>(9 nm)/Mn<sub>0.45</sub>Ga<sub>0.55</sub>(7 nm)//GaAs(001) sample, patterned into a 5- $\mu$ m wide Hall bar using one-step projection photolithography followed by dry etching. Current pulses of 100  $\mu$ s were applied in-plane, while an external magnetic field of 6 kOe was applied in the same direction as the current. It is important to note that the applied field was weaker than the field required to saturate the in-plane magnetization of MnGa. The AHE measurements were conducted after each current pulse to monitor change in resistance. All measurements were carried out at room temperature. The schematic diagram of the magnetization switching experiments is presented in Figure 5.7. The injected current pulses were from 11 mA to 16 mA, corresponding to the current densities of  $2.3 \times 10^9$  A/m<sup>2</sup> -  $3 \times 10^9$  A/m<sup>2</sup>.

Figure 5.8(a) shows that current-induced SOT magnetization switching was achieved at the current pulses of 11 mA. However, a complete magnetization reversal, which would typically be represented by a hysteresis loop of the transverse resistance as a function of current pulses, was not obtained in our case. Instead, we observed only a partial hysteresis

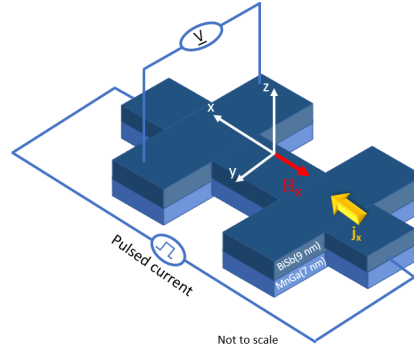


Figure 5.7: Schematic diagram of the current-induced magnetization switching experiment. Current pulses of  $100 \mu\text{s}$  are applied in a Hall bar, as well as the magnetic field of 6 kOe along the direction of the current.

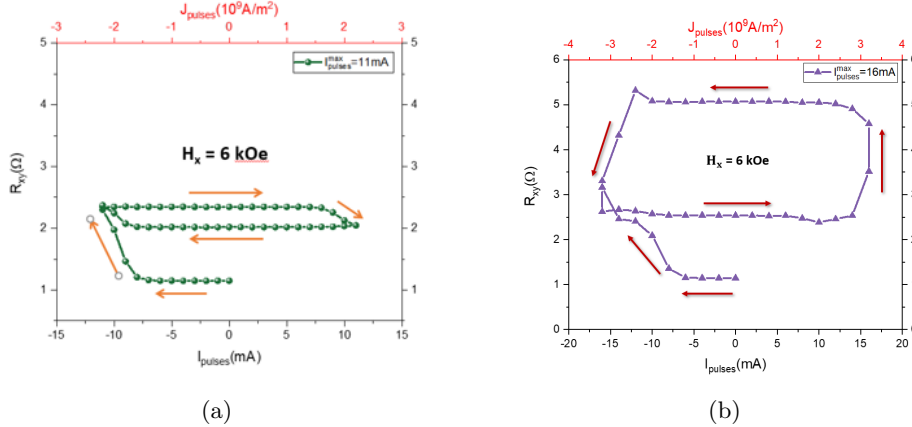


Figure 5.8: (a) Magnetization switching in the  $\text{Bi}_{0.90}\text{Sb}_{0.10}(9 \text{ nm})/\text{Mn}_{0.45}\text{Ga}_{0.55}(7 \text{ nm})//\text{GaAs}(001)$  system at room temperature. The maximal injected current pulses are 11 mA (b) and 16 mA. The correspondent current densities are shown on the top scale.

cycle, accounting for approximately 10% of the change in resistance between remanent states. The change in resistance between these remanent states corresponds to  $4 \Omega$ , as indicated by the AHE measurements in Figure 5.9(a).

This might result from the fact that the switching is limited by thermally induced magnetic domains nucleation, so that the intermediary magnetic states may be achieved. The magnetization reversal is obtained at a relatively low critical current density of  $2.3 \times 10^9 \text{ A/m}^2$  which is less than the critical current density necessary to switch magnetization in  $\text{Bi}_{0.90}\text{Sb}_{0.10}(5 \text{ nm})/\text{Mn}_{0.45}\text{Ga}_{0.55}(3 \text{ nm})$  demonstrated by Khang et al. ( $J = 1.5 \times 10^{10} \text{ A/m}^2$ ) [77].

The same behaviour of the reversal curve is observed at current pulses up to 13-14 mA, and the change in resistance remains constant, as shown by the plotted amplitudes of the AHE as a function of current pluses in Figure 5.9(b). However, when the injected current pulses exceed 14 mA, the magnetic properties seem to degrade, as the resistance

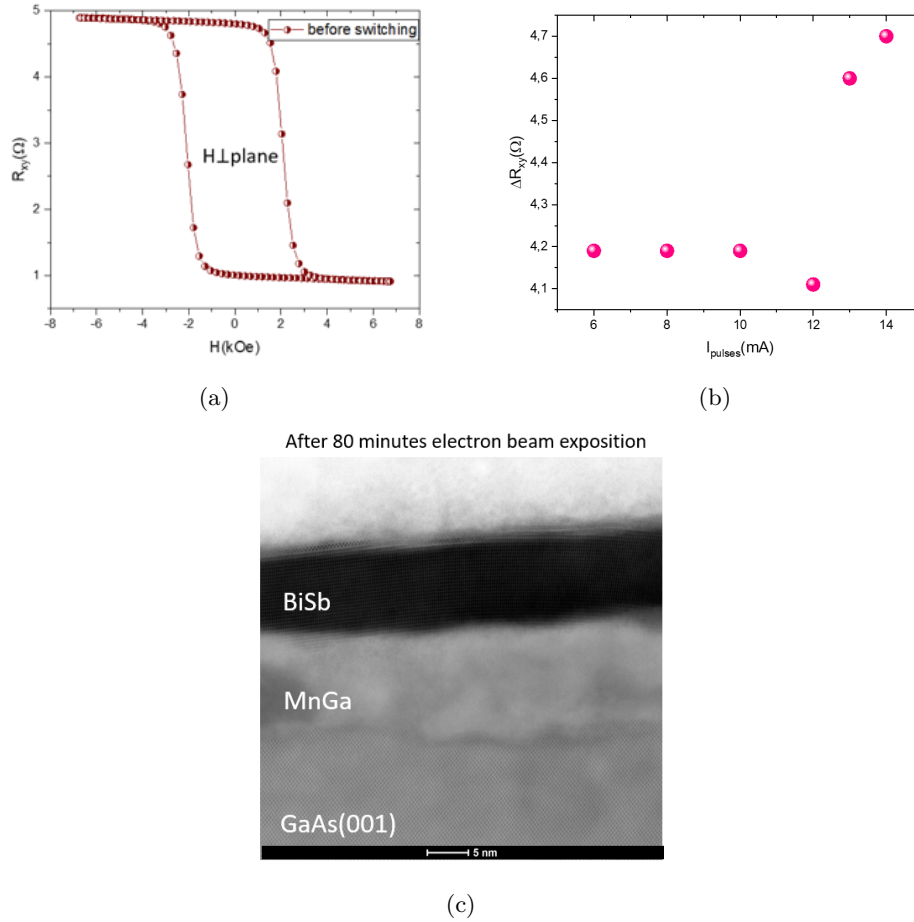


Figure 5.9: (a) The AHE measurements are done before each current pulse from 6 mA to 14 mA to monitor the change in resistance in the  $\text{Bi}_{0.90}\text{Sb}_{0.10}$  (9 nm)/ $\text{Mn}_{0.45}\text{Ga}_{0.55}$  (7 nm)//GaAs(001) system during the magnetization switching experiment. (b) The correspondent change in resistance as a function of the injected current pulses. (c) STEM measurements in BF mode of the  $\text{Bi}_{0.90}\text{Sb}_{0.10}$  (9 nm)/ $\text{Mn}_{0.45}\text{Ga}_{0.55}$  (7 nm)//GaAs(001) bilayer after 80 minutes of electron beam exposition: the MnGa layer becomes amorphous that may result from the thermal instability. The BiSb layer remains crystalline.

increases brutally (cf. Figure 5.8(b)). The AHE hysteresis cycle could not be obtained after this experiment, confirming the overheating of the sample and the deterioration of the ferromagnetic nature of MnGa.

This behavior might be attributed to the thermal instability of the MnGa layer that may modify the parameters appearing in Equation 5.18. STEM measurements in bright field (BF) mode revealed that after 80 minutes of electron beam exposure, the MnGa layer becomes amorphous, whereas the BiSb layer remains crystalline (cf. Figure 5.9(c)). However, we lack information about the specific temperature that degrades the MnGa layer. We also attempted to conduct magnetization switching probed by MOKE, but we were not able to obtain any magnetic contrast from MnGa.

## 5.2 Spin-to-charge conversion in BiSb/MnGa//GaAs(001) heterostructure

Thus far, our focus has been on characterizing the charge-to-spin conversion properties of the BiSb/MnGa heterostructure. This was the main goal of this thesis and the reason why we developed and fabricated perpendicularly magnetized FM material. While it may not be the most suitable geometry for studying the conversion of spin current to charge current by THz-TDS, which typically requires an in-plane magnetization, we were intrigued to explore it on the recently installed THz-TDS setup in the laboratory. This decision was influenced by the significant SCC observed in the Co/BiSb system [138]. The main limitation arises from the maximum magnetic field (200 mT) that can be applied which is insufficient to saturate the MnGa in the plane. Nonetheless, the preliminary results from these experiments are encouraging, warranting further in-depth investigation in the future.

### 5.2.1 Terahertz time-domain spectroscopy technique to study the spin-to-charge conversion properties

In 2013, THz-TDS was developed as a powerful all-optical technique for studying the SCC mechanism in NM/FM heterostructures [72]. Since then, SCC has been extensively investigated in a variety of materials using THz-TDS as an alternative tool to transport techniques [71, 188, 24, 25, 148, 28, 62]. The THz pulse typically has a width of  $\sim 100$  fs, enabling THz-TDS to detect SCC with sub-picosecond time resolution, thereby revealing the spin dynamics on the ultrafast timescale.

The THz-TDS consist in sending a femto-second pulse, typically from a Ti:sapphire laser in a sample that generates a spin current into a FM layer that diffuses into the NM layer. The generation of the spin current occurs through the absorption of photons that excite the  $3d$  electrons to the  $4sp$  band above the Fermi level, as illustrated in Figure 5.10(b). This is due to the difference in the density of states in the FM layer, populated with electrons of majority and minority spins in the  $sp$  and  $d$  bands, respectively.

The spin current that diffuses into the NM layer generates a charge current and emits THz radiation, following Maxwell's equations (see Reference [72]). The schematic representation of the THz-TDS working principle is shown in Figure 5.10(a). The detected THz signal depends on the SCC process, which is influenced by the quality of the NM/FM interface, the substrates used, and the thickness of the FM layer.

#### Experimental setup

Terahertz emission from BiSb/MnGa heterostructures is probed by THz-TDS in transmission mode. The sample is excited by 80 fs pulses with a center wavelength of 800 nm. The emitted monocycle THz pulse is then sampled by electro-optic detection using 150 fs pulses centered at 1030 nm as the probe beam, focused on a 500  $\mu\text{m}$ -thick ZnTe crystal. These measurements were performed by S. Massabeau at UMPy CNRS/Thales.

#### Sample preparation

It has been well established that Co/Pt systems are efficient in terms of spin-to-charge conversion, which was already characterized by THz-TDS on various substrates [62, 178, 131, 97]. That is why we used this system as reference sample, and for this study, we prepared three samples:

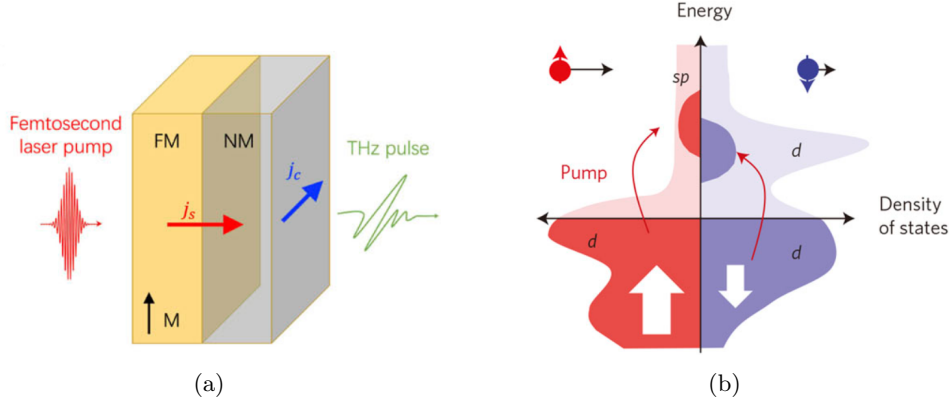


Figure 5.10: (a) Schematic illustration of the working principle of THz emission spectroscopy in NM/FM systems: by sending a femtosecond laser pulse into the FM layer, a spin current  $j_s$  is generated that diffuses into the NM layer. The generated spin current converts into a charge current  $j_c$ , emitting THz radiation on the sub-picosecond timescale. (b) Generation of a spin current in the FM layer: a femtosecond pulse excites  $d$  electrons with majority and minority spins to the  $sp$  and  $d$  bands, respectively.

1. Bi<sub>0.90</sub>Sb<sub>0.10</sub>(9 nm)/Mn<sub>0.45</sub>Ga<sub>0.55</sub>(7 nm)//single-side polished (ssp) GaAs(001) grown by MBE, as described in Section 3.4
2. Pt(2 nm)/Co(2 nm)//single-side polished GaAs(001),
3. Pt(2 nm)/Co(2 nm)//double-side polished (dsp) GaAs(001).

During the experiments, we encountered several challenges. Firstly, the ferromagnetic MnGa layer has perpendicular magnetic anisotropy, and its in-plane magnetization saturation reaches  $\simeq 1$  T (see Figure 3.27(a)). However, for the moment, our experimental setup allows us to apply a maximal magnetic field of up to 200 mT, which means that during the experiment, the magnetization of MnGa is not completely saturated in plane.

Secondly, the substrate on which the BiSb/MnGa heterostructure was deposited is a single-side polished GaAs substrate. To probe the influence of polished substrates on THz emission, we fabricated two Co/Pt samples grown on single and double-sided polished GaAs. We will see later that the influence of this parameter seems limited in our case.

### 5.2.1.1 Experimental results

Figure 5.11(a) shows the THz signal emitted by the BiSb(9 nm)/MnGa(7 nm)//ssp GaAs(001), as well as the THz signal emitted by the Co(2 nm)/Pt(2 nm)//ssp GaAs(001) for reference. For all samples we observe sharp oscillations within a 3 ps-wide envelope. As mentioned earlier, the magnetization of MnGa is only partially saturated when a magnetic field of 200 mT is applied in plane. Specifically, it reaches 25% of its full saturation, as seen in Figure 5.12. Consequently, we can conclude that the THz signal from the BiSb/MnGa bilayer is comparable to the THz signal from Co/Pt, as its THz amplitude corresponds to 25% of the THz amplitude from Co/Pt, where the Co magnetization is fully saturated.

As we already discussed, large SOC in NM layers results in a transverse charge current after injecting a spin current via ISHE or IREE. So the emitted THz signal originated

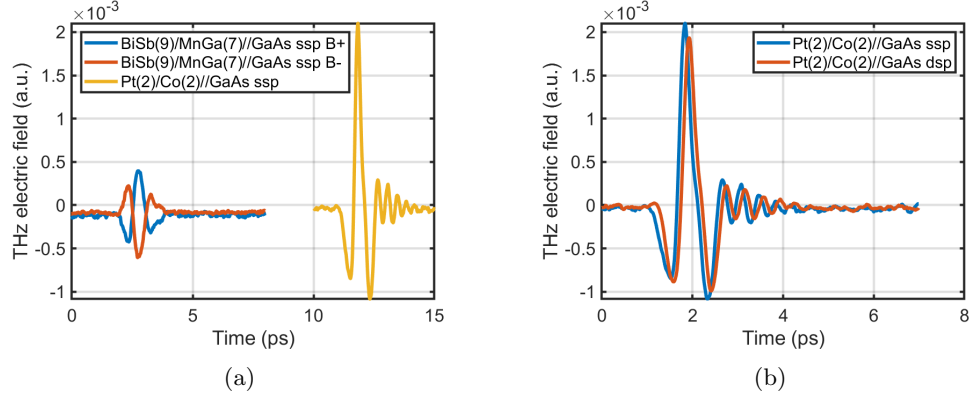


Figure 5.11: (a) THz emission from  $\text{Bi}_{0.90}\text{Sb}_{0.10}(9 \text{ nm})/\text{Mn}_{0.45}\text{Ga}_{0.55}(7 \text{ nm})//\text{ssp GaAs}(001)$  for two directions of 200 mT in-plane magnetic field  $\pm B$  compared to  $\text{Pt}(2 \text{ nm})/\text{Co}(2 \text{ nm})//\text{ssp GaAs}(001)$  for reference. Considering that the magnetization of MnGa only 25% saturated in plane, the signal from BiSb/MnGa is comparable to the signal from the reference sample. (b) THz emission from  $\text{Pt}(2 \text{ nm})/\text{Co}(2 \text{ nm})$  grown on both ssp GaAs(001) and dsp GaAs(001). There is no apparent difference in the THz signal emitted from these samples.

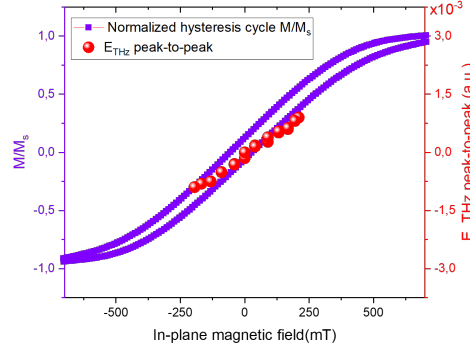


Figure 5.12: Normalized hysteresis cycle  $M/M_s$  of the MnGa(7 nm) layer (in red) and the THz signal amplitude emitted by BiSb(9 nm)/MnGa(7 nm) bilayer (in purple) as a function of the in-plane magnetic field. The magnetization of MnGa reaches 25% of its full saturation when a magnetic field of 200 mT is applied in the plane of the sample.

from the spin current must satisfy the following relation:

$$\mathbf{j}_c \propto \mathbf{j}_s \times \frac{\mathbf{m}}{|\mathbf{m}|} \quad (5.19)$$

According to Equation 5.19, the emitted THz is always perpendicular to the applied magnetic field and the injected spin current.

Figure 5.11(a) shows that the THz signal changes sign, when we reverse the applied magnetic field ( $\pm B$ ), so that the magnetization is also reversed, as expected. These observations are consistent with Equation 5.19, confirming that the observed THz signal

is a signature of the spin-to-charge conversion via ISHE or/and IREE.

In addition, we performed the same experiments on the Co(2 nm)/Pt(2 nm) bilayers deposited on both ssp GaAs(001) and dsp GaAs(001) substrates to estimate the absorption of the signal by the ssp substrate, compared to the dsp substrate. As it can be seen in Figure 5.11(b), there is no apparent difference in THz signal emitted from these samples.

To conclude on the origin of SCC, a study of the thickness dependence of BiSb must be carried out to disentangle the role of surface states and bulk states. It will be preferable for this study to fabricate a layer with an in-plane magnetization. The difficulty will be to define the magnetic compound compatible with our III-V MBE chamber and easy to grow with the BiSb layer.

### 5.3 Chapter conclusion

The charge-to-spin conversion properties were characterized by the second harmonic Hall voltage in the BiSb/MnGa//GaAs(001) heterostructure. The damping-like torque is relatively small for BiSb thicknesses under 7 nm, and then increases drastically for the 9 nm-thick BiSb. As for the field-like torque, interpreting these results is challenging, as the measurement uncertainty was significant.

According to the traditional paradigm, these findings suggest that bulk states play a predominant role in generating SOT. However, as discussed in Section 4.1, we confirmed the presence of topological surface states at the upper surface of the BiSb/MnGa system through ARPES. Event though we do not have information on the presence of non-trivial surface states at the BiSb/MnGa interface, the coexistence of both bulk and surface states is possible.

Therefore, further in-depth studies are necessary to disentangle these two contributions, since the SOT dependence study requires that other properties of layers do not change with varying thickness. In particular, investigating the structural quality of BiSb in relation to its thickness is crucial, as the layer quality and the quality of the interface FM/TI can reduce or eliminate the bulk gap.

Nevertheless, we obtained a significant DLT efficiency for BiSb with a thickness of 9 nm compared to other conventional metal systems. The obtained DLT is comparable to that found in BiSb in the literature measured by the HHV technique.

Partial current-induced magnetization switching was accomplished at a relatively low critical current density of  $2.3 \times 10^9$  A/m<sup>2</sup>, which is lower than what is typically reported in the literature. This partial reversal could potentially be attributed to the thermally induced magnetic domain nucleation of the MnGa (7 nm) layer. This may offer an explanation for the partial magnetization reversal observed in the BiSb(9 nm)/MnGa(7 nm) bilayer induced by the SOTs. In addition, the injected current densities exceeding  $2.3 \times 10^9$  A/m<sup>2</sup> may induce heating in the MnGa layer, leading to the degradation of its ferromagnetic properties. Being able to fabricate thinner and more stable layers of MnGa would be necessary but brings us back to a material problem which study can take time.

The efficient spin-to-charge conversion was also confirmed in the BiSb/MnGa bilayer by THz-TDS. However, during the experiments, we were limited by the maximum magnetic field that we could apply in our experimental setup, preventing the full in-plane saturation of the MnGa magnetization. Considering this, we found that the THz emission from BiSb/MnGa//ssp GaAs(001) was comparable to the THz emission from Pt/Co//ssp GaAs(001). For the later system, it has been well-established that it provides efficient spin-to-charge conversion by numerous THz-TDS experiments. These results constitute encouraging preliminary findings that need further exploration.



# General conclusion and perspectives

In this PhD work, the goal was to develop a  $\text{Bi}_{x-1}\text{Sb}_x/\text{FM}$  heterostructure using MBE, aiming to provide evidence of efficient charge-to-spin interconversion within this system. To facilitate the distinction between spin-orbit torque effects and thermal effects, the initial objective was to grow BiSb/FM material structures with a perpendicularly magnetized layer. We opted for the BiSb/MnGa//GaAs(001) heterostructure, as both materials could be deposited in the same MBE chamber, ensuring the preservation of the MnGa/BiSb interface's quality. A part of this thesis focused on the MBE growth, involving a comprehensive structural characterization through various experimental techniques, including RHEED, AFM, XRD, GIXRD, and STEM. Given our aim to fabricate a perpendicularly magnetized magnetic material, magnetic characterizations using SQUID and AGFM also guided this development phase.

The main results and achievements can be summarized as follows:

- The growth of a 10 nm-thick ferromagnetic MnGa layer on a GaAs(001) substrate with perpendicular magnetic anisotropy has been successfully completed, displaying sought-after magnetic properties. A magnetization of the order of  $315 \text{ emu/cm}^3$  at low temperature, a hysteresis cycle with a remanence close to 1 when the magnetic field is applied perpendicularly to the plane of the layers, and a coercivity of the order of 0.1 T were achieved. Structural studies have demonstrated the epitaxial relationship with the substrate. However, reducing the thickness of MnGa to a few nanometers showed deterioration in its ferromagnetic properties and thermal instability. We were able to observe perpendicular magnetic anisotropy down to 7 nm. The presence of an intermixing layer at the interface between the GaAs substrate and the MnGa layer was also observed.
- A high-quality, thermally stable, and epitaxial thin layer of BiSb was successfully grown on top of MnGa. GIXRD measurements revealed, however, the presence of two crystallographic orientations of BiSb.
- Beyond this specific structure, during this thesis I was interested in the growth of BiSb on various substrates. BiSb thin films were grown on InSb, GaAs(001), GaAs(111)A, and GaAs(111)B substrates. In anticipation of characterizing this topological insulator through transport measurements, I initiated a study of BiSb growth on AlInSb insulator, which has a lattice parameter close to that of BiSb. While this presents a promising alternative, further optimization will be necessary.
- The objective behind developing this specific heterostructure was to investigate the mechanisms involved in converting a charge current into a spin current, particularly through the spin-orbit torques exerted when this spin current is absorbed by a ferromagnetic material. In theory, the transport properties of BiSb, being a topological insulator, stem from its spin-polarized surface states. However, in practical scenarios, the narrow

bulk gap of BiSb can lead to a Fermi level shift into the conduction band, introducing a significant contribution from bulk states in the transport. This shift may result from unintentional doping, charge transfer, or band bending effects at the interface.

Utilizing the CASSIOPEE synchrotron beamline facilities, we successfully confirmed the presence of surface states on BiSb when grown on MnGa. It is important to note that our observations were limited to the top surface, providing no direct insight into the MnGa/BiSb interface.

- The charge-to-spin conversion was characterized using the second harmonic Hall voltage technique and current-induced magnetization switching. Due to the low conductivity of MnGa, a significant portion of the current flowed through the BiSb layer. This allowed for the estimation of a higher effective DLT field in the BiSb(9 nm)/MnGa(7 nm) system compared to conventional metallic systems. However, the FLT signal was found to be insignificant. These observations suggest a more probable origin of the bulk SHE-SOT. Additional support for this conclusion comes from the substantial decrease in the DLT field when reducing the BiSb thickness. Nevertheless, arriving at a definitive conclusion regarding the role of surface states versus bulk states remains challenging at this stage. Producing a substantial number of samples with varying thicknesses for both the TI and FM materials is necessary. This proves to be a limitation with MnGa on GaAs, where decreasing the thickness below 7 nm seems difficult. Further investigations into the origin of the high DLT are required. Additionally, only partial current-induced magnetization was achieved, likely due to the probable thermal instability of MnGa, which may deteriorate its magnetic properties.

- As a further test, the high spin-to-charge conversion efficiency of BiSb was demonstrated by THz time-domain spectroscopy. The THz signal emitted is comparable to that of the conventional Pt/Co SHE system. These preliminary results open the door to rapid characterization of SSCs (no lithography is required), but unlike for SOT measurements, an in-plane magnetization for the ferromagnetic layer would be a better configuration.

In the course of this thesis work, we successfully demonstrated that the MnGa/BiSb system fabricated by MBE exhibits intriguing characteristics for studying the conversion of a spin current into a charge current and vice versa. Nevertheless, the results presented here are preliminary, and a more thorough understanding of the system is needed. Specifically, to distinguish between the contributions of bulk and surface states, producing a considerable number of high-quality samples is essential. Overcoming certain challenges is, however, necessary. Firstly, reducing the thickness of the magnetic material to a few nanometers is crucial, given that spin-orbit torques are interfacial. Achieving this on GaAs substrates appears challenging, and the high anisotropy is suboptimal for minimizing the critical currents required for magnetization reversal. Despite these challenges, MnGa stands out as one of the rare perpendicularly magnetized materials grown in direct contact with BiSb.

The second point pertains to the growth of BiSb on MnGa. While the system is epitaxial, several crystalline orientations coexist due to the difference in structural symmetries, complicating the interpretation of the band structure using the currently available tight-binding model.

To investigate the role of surface states, it is crucial to control the Fermi level and position it within the BiSb gap. This remains an ongoing area of study.

Regardless of the origin of the spin current to charge current conversion, we have shown that the BiSb system is a promising alternative to traditional metallic materials. Its amenability to modulating electron properties through gate effects or combining with ferroelectric materials makes it an attractive system. However, mastery of low thicknesses

and the demonstration of such effects are still pending.

Finally, recent studies on the feasibility of growing BiSb by sputtering with crystalline quality comparable to that achieved by MBE [42] has encouraged our research group to embark on a new activity in this field. Initial results are encouraging, demonstrating significant spin-to-charge current efficiency using THz-TDS experiments.

In conclusion, both HHV and THz-TDS techniques offer advantages and drawbacks, and improving our understanding of the mechanisms underlying the observed large spin-to-charge current conversion in the BiSb topological insulator requires the production of high-quality samples. The literature on this topic remains scattered and controversial. To converge on this matter and position BiSb as a competitor to classical SHE materials in spintronics, a thorough control of the material is imperative. A substantial part of this thesis was dedicated to advancing this objective.



# Bibliography

- [1] Jeong Ung Ahn et al. “Observation of the Nernst effect in a GeTe/NiFe structure”. In: *Current Applied Physics* 49 (May 1, 2023), pp. 12–17. ISSN: 1567-1739. DOI: [10.1016/j.cap.2023.02.008](https://doi.org/10.1016/j.cap.2023.02.008). URL: <https://www.sciencedirect.com/science/article/pii/S1567173923000317>.
- [2] Mustafa Akyol et al. “Effect of heavy metal layer thickness on spin-orbit torque and current-induced switching in Hf|CoFeB|MgO structures”. In: *Applied Physics Letters* 109.2 (July 11, 2016). ISSN: 0003-6951. DOI: [10.1063/1.4958295](https://doi.org/10.1063/1.4958295). URL: <https://www.osti.gov/biblio/22590600>.
- [3] V. P. Amin and M. D. Stiles. “Spin transport at interfaces with spin-orbit coupling: Phenomenology”. In: *Physical Review B* 94.10 (Sept. 16, 2016). Publisher: American Physical Society, p. 104420. DOI: [10.1103/PhysRevB.94.104420](https://doi.org/10.1103/PhysRevB.94.104420). URL: <https://link.aps.org/doi/10.1103/PhysRevB.94.104420>.
- [4] P. W. Anderson and J. M. Rowell. “Probable Observation of the Josephson Superconducting Tunneling Effect”. In: *Physical Review Letters* 10.6 (Mar. 15, 1963). Publisher: American Physical Society, pp. 230–232. DOI: [10.1103/PhysRevLett.10.230](https://doi.org/10.1103/PhysRevLett.10.230). URL: <https://link.aps.org/doi/10.1103/PhysRevLett.10.230>.
- [5] K. Ando et al. “Electric Manipulation of Spin Relaxation Using the Spin Hall Effect”. In: *Physical Review Letters* 101.3 (July 18, 2008). Publisher: American Physical Society, p. 036601. DOI: [10.1103/PhysRevLett.101.036601](https://doi.org/10.1103/PhysRevLett.101.036601). URL: <https://link.aps.org/doi/10.1103/PhysRevLett.101.036601>.
- [6] Tomoyoshi Aono. “The Nernst Effect of Bi-Sb Alloys”. In: *Japanese Journal of Applied Physics* 9.7 (July 1, 1970). Publisher: IOP Publishing, p. 761. ISSN: 1347-4065. DOI: [10.1143/JJAP.9.761](https://doi.org/10.1143/JJAP.9.761). URL: <https://iopscience.iop.org/article/10.1143/JJAP.9.761/meta>.
- [7] Can Onur Avci et al. “Fieldlike and antidamping spin-orbit torques in as-grown and annealed Ta/CoFeB/MgO layers”. In: *Physical Review B* 89.21 (June 23, 2014). Publisher: American Physical Society, p. 214419. DOI: [10.1103/PhysRevB.89.214419](https://doi.org/10.1103/PhysRevB.89.214419). URL: <https://link.aps.org/doi/10.1103/PhysRevB.89.214419>.
- [8] Can Onur Avci et al. “Unidirectional spin Hall magnetoresistance in ferromagnet/normal metal bilayers”. In: *Nature Physics* 11.7 (July 2015), pp. 570–575. ISSN: 1745-2473, 1745-2481. DOI: [10.1038/nphys3356](https://doi.org/10.1038/nphys3356). arXiv: [1502.06898\[cond-mat\]](https://arxiv.org/abs/1502.06898). URL: <http://arxiv.org/abs/1502.06898>.
- [9] M. N. Baibich et al. “Giant Magnetoresistance of (001)Fe/(001)Cr Magnetic Superlattices”. In: *Physical Review Letters* 61.21 (Nov. 21, 1988). Publisher: American Physical Society, pp. 2472–2475. DOI: [10.1103/PhysRevLett.61.2472](https://doi.org/10.1103/PhysRevLett.61.2472). URL: <https://link.aps.org/doi/10.1103/PhysRevLett.61.2472>.

- [10] Laëtitia Baringthon. “Élaboration et caractérisation de phases topologiques de l’alliage pour la conversion spin charge”. These de doctorat. université Paris-Saclay, Jan. 20, 2022. URL: <https://www.theses.fr/2022UPASP007>.
- [11] Laëtitia Baringthon et al. “Topological surface states in ultrathin  $\text{Bi}_{1-x}\text{Sb}_x$  layers”. In: *Physical Review Materials* 6.7 (July 20, 2022). Publisher: American Physical Society, p. 074204. DOI: [10.1103/PhysRevMaterials.6.074204](https://doi.org/10.1103/PhysRevMaterials.6.074204). URL: <https://link.aps.org/doi/10.1103/PhysRevMaterials.6.074204>.
- [12] Hadj M. Benia et al. “Surface band structure of  $\text{Bi}_{1-x}\text{Sb}_x$  (111)”. In: *Physical Review B* 91.16 (Apr. 13, 2015), p. 161406. ISSN: 1098-0121, 1550-235X. DOI: [10.1103/PhysRevB.91.161406](https://doi.org/10.1103/PhysRevB.91.161406). URL: <https://link.aps.org/doi/10.1103/PhysRevB.91.161406>.
- [13] Andrew J. Berger et al. “Inductive detection of fieldlike and dampinglike ac inverse spin-orbit torques in ferromagnet/normal-metal bilayers”. In: *Physical Review B* 97.9 (Mar. 7, 2018). Publisher: American Physical Society, p. 094407. DOI: [10.1103/PhysRevB.97.094407](https://doi.org/10.1103/PhysRevB.97.094407). URL: <https://link.aps.org/doi/10.1103/PhysRevB.97.094407>.
- [14] L. Berger. “Emission of spin waves by a magnetic multilayer traversed by a current”. In: *Physical Review B* 54.13 (Oct. 1, 1996). Publisher: American Physical Society, pp. 9353–9358. DOI: [10.1103/PhysRevB.54.9353](https://doi.org/10.1103/PhysRevB.54.9353). URL: <https://link.aps.org/doi/10.1103/PhysRevB.54.9353>.
- [15] L. Berger. “Side-Jump Mechanism for the Hall Effect of Ferromagnets”. In: *Physical Review B* 2.11 (Dec. 1, 1970). Publisher: American Physical Society, pp. 4559–4566. DOI: [10.1103/PhysRevB.2.4559](https://doi.org/10.1103/PhysRevB.2.4559). URL: <https://link.aps.org/doi/10.1103/PhysRevB.2.4559>.
- [16] B. Andrei Bernevig, Taylor L. Hughes, and Shou-Cheng Zhang. “Quantum Spin Hall Effect and Topological Phase Transition in  $\text{HgTe}$  Quantum Wells”. In: *Science* 314.5806 (Dec. 15, 2006). Publisher: American Association for the Advancement of Science, pp. 1757–1761. DOI: [10.1126/science.1133734](https://doi.org/10.1126/science.1133734). URL: <https://www.science.org/doi/10.1126/science.1133734>.
- [17] Michael Victor Berry. “Quantal phase factors accompanying adiabatic changes”. In: *Proceedings of the Royal Society of London. A. Mathematical and Physical Sciences* 392.1802 (Jan. 1997). Publisher: Royal Society, pp. 45–57. DOI: [10.1098/rspa.1984.0023](https://doi.org/10.1098/rspa.1984.0023). URL: <https://royalsocietypublishing.org/doi/10.1098/rspa.1984.0023>.
- [18] Gustav Bihlmayer et al. “Rashba-like physics in condensed matter”. In: *Nature Reviews Physics* 4.10 (Aug. 24, 2022), pp. 642–659. ISSN: 2522-5820. DOI: [10.1038/s42254-022-00490-y](https://doi.org/10.1038/s42254-022-00490-y). URL: <https://www.nature.com/articles/s42254-022-00490-y>.
- [19] G. Binasch et al. “Enhanced magnetoresistance in layered magnetic structures with antiferromagnetic interlayer exchange”. In: *Physical Review B* 39 (Mar. 1, 1989). ADS Bibcode: 1989PhRvB..39.4828B, pp. 4828–4830. ISSN: 0163-1829/1098-0121. DOI: [10.1103/PhysRevB.39.4828](https://doi.org/10.1103/PhysRevB.39.4828). URL: <https://ui.adsabs.harvard.edu/abs/1989PhRvB..39.4828B>.
- [20] Federico Binda et al. “Spin–Orbit Torques and Spin Hall Magnetoresistance Generated by Twin-Free and Amorphous  $\text{Bi}_{0.9}\text{Sb}_{0.1}$  Topological Insulator Films”. In: *Advanced Materials* (), p. 2304905. ISSN: 1521-4095. DOI: [10.1002/adma.202304905](https://doi.org/10.1002/adma.202304905). URL: <https://onlinelibrary.wiley.com/doi/abs/10.1002/adma.202304905>.

- [21] Yu. A. Bychkov and É. I. Rashba. “Properties of a 2D electron gas with lifted spectral degeneracy”. In: *Soviet Journal of Experimental and Theoretical Physics Letters* 39 (Jan. 1, 1984). ADS Bibcode: 1984JETPL..39...78B, p. 78. ISSN: 0021-3640. URL: <https://ui.adsabs.harvard.edu/abs/1984JETPL..39...78B>.
- [22] A. D. Caviglia et al. “Tunable Rashba Spin-Orbit Interaction at Oxide Interfaces”. In: *Physical Review Letters* 104.12 (Mar. 26, 2010). Publisher: American Physical Society, p. 126803. DOI: [10.1103/PhysRevLett.104.126803](https://doi.org/10.1103/PhysRevLett.104.126803). URL: <https://link.aps.org/doi/10.1103/PhysRevLett.104.126803>.
- [23] Cui-Zu Chang et al. “Experimental Observation of the Quantum Anomalous Hall Effect in a Magnetic Topological Insulator”. In: *Science* 340.6129 (Apr. 12, 2013). Publisher: American Association for the Advancement of Science, pp. 167–170. DOI: [10.1126/science.1234414](https://doi.org/10.1126/science.1234414). URL: <https://www.science.org/doi/10.1126/science.1234414>.
- [24] Mengji Chen et al. “Current-Enhanced Broadband THz Emission from Spintronic Devices”. In: *Advanced Optical Materials* 7.4 (2019), p. 1801608. ISSN: 2195-1071. DOI: [10.1002/adom.201801608](https://doi.org/10.1002/adom.201801608). URL: <https://onlinelibrary.wiley.com/doi/abs/10.1002/adom.201801608>.
- [25] Liang Cheng et al. “Far out-of-equilibrium spin populations trigger giant spin injection into atomically thin MoS<sub>2</sub>”. In: *Nature Physics* 15.4 (Apr. 2019). Number: 4 Publisher: Nature Publishing Group, pp. 347–351. ISSN: 1745-2481. DOI: [10.1038/s41567-018-0406-3](https://doi.org/10.1038/s41567-018-0406-3). URL: <https://www.nature.com/articles/s41567-018-0406-3>.
- [26] Zhendong Chi et al. “The spin Hall effect of Bi-Sb alloys driven by thermally excited Dirac-like electrons”. In: *Science Advances* 6.10 (Mar. 6, 2020). Publisher: American Association for the Advancement of Science, eaay2324. DOI: [10.1126/sciadv.aay2324](https://doi.org/10.1126/sciadv.aay2324). URL: <https://www.science.org/doi/full/10.1126/sciadv.aay2324>.
- [27] Sunglae Cho et al. “Bi epitaxy on polar InSb(111) *A/B* faces”. In: *Journal of Vacuum Science & Technology A: Vacuum, Surfaces, and Films* 20.4 (July 2002), pp. 1191–1194. ISSN: 0734-2101, 1520-8559. DOI: [10.1116/1.1479735](https://doi.org/10.1116/1.1479735). URL: <http://avs.scitation.org/doi/10.1116/1.1479735>.
- [28] Joel Cramer et al. “Complex Terahertz and Direct Current Inverse Spin Hall Effect in YIG/Cu<sub>1-x</sub>Ir<sub>x</sub> Bilayers Across a Wide Concentration Range”. In: *Nano Letters* 18.2 (Feb. 14, 2018). Publisher: American Chemical Society, pp. 1064–1069. ISSN: 1530-6984. DOI: [10.1021/acs.nanolett.7b04538](https://doi.org/10.1021/acs.nanolett.7b04538). URL: <https://doi.org/10.1021/acs.nanolett.7b04538>.
- [29] P. Cucka and C. S. Barrett. “The crystal structure of Bi and of solid solutions of Pb, Sn, Sb and Te in Bi”. In: *Acta Crystallographica* 15.9 (Sept. 10, 1962). Number: 9 Publisher: International Union of Crystallography, pp. 865–872. ISSN: 0365-110X. DOI: [10.1107/S0365110X62002297](https://doi.org/10.1107/S0365110X62002297). URL: [//scripts.iucr.org/cgi-bin/paper?a03586](http://scripts.iucr.org/cgi-bin/paper?a03586).
- [30] T. H. Dang et al. “Anomalous Hall effect in 3 d / 5 d multilayers mediated by interface scattering and nonlocal spin conductivity”. In: *Physical Review B* 102.14 (Oct. 2, 2020), p. 144405. ISSN: 2469-9950, 2469-9969. DOI: [10.1103/PhysRevB.102.144405](https://doi.org/10.1103/PhysRevB.102.144405). URL: <https://link.aps.org/doi/10.1103/PhysRevB.102.144405>.

- [31] Mahendra Dc et al. “Room-temperature high spin-orbit torque due to quantum confinement in sputtered  $\text{Bi}_x\text{Se}_{(1-x)}$  films”. In: *Nature Materials* 17.9 (Sept. 2018). Number: 9 Publisher: Nature Publishing Group, pp. 800–807. ISSN: 1476-4660. DOI: [10.1038/s41563-018-0136-z](https://doi.org/10.1038/s41563-018-0136-z). URL: <https://www.nature.com/articles/s41563-018-0136-z>.
- [32] Praveen Deorani et al. “Observation of inverse spin Hall effect in bismuth selenide”. In: *Physical Review B* 90.9 (Sept. 3, 2014). Publisher: American Physical Society, p. 094403. DOI: [10.1103/PhysRevB.90.094403](https://doi.org/10.1103/PhysRevB.90.094403). URL: <https://link.aps.org/doi/10.1103/PhysRevB.90.094403>.
- [33] D. DeSimone, C. E. C. Wood, and C. A. Evans Jr. “Manganese incorporation behavior in molecular beam epitaxial gallium arsenide”. In: *Journal of Applied Physics* 53.7 (July 1, 1982), pp. 4938–4942. ISSN: 0021-8979. DOI: [10.1063/1.331328](https://doi.org/10.1063/1.331328). URL: <https://doi.org/10.1063/1.331328>.
- [34] G. Dresselhaus. “Spin-Orbit Coupling Effects in Zinc Blende Structures”. In: *Physical Review* 100.2 (Oct. 15, 1955). Publisher: American Physical Society, pp. 580–586. DOI: [10.1103/PhysRev.100.580](https://doi.org/10.1103/PhysRev.100.580). URL: <https://link.aps.org/doi/10.1103/PhysRev.100.580>.
- [35] Ye Du, Saburo Takahashi, and Junsaku Nitta. “Spin-current-related magnetoresistance in epitaxial Pt/Co bilayers in the presence of spin Hall effect and Rashba-Edelstein effect”. In: *Physical Review B* 103.9 (Mar. 12, 2021), p. 094419. ISSN: 2469-9950, 2469-9969. DOI: [10.1103/PhysRevB.103.094419](https://doi.org/10.1103/PhysRevB.103.094419). arXiv: [1807.10867](https://arxiv.org/abs/1807.10867) [cond-mat]. URL: <http://arxiv.org/abs/1807.10867>.
- [36] Nguyen Huynh Duy Khang et al. “Growth and characterization of MnGa thin films with perpendicular magnetic anisotropy on BiSb topological insulator”. In: *Journal of Applied Physics* 122.14 (). Publisher: American Institute of Physics, p. 143903. ISSN: 0021-8979. DOI: [10.1063/1.4999617](https://doi.org/10.1063/1.4999617). URL: <https://aip.scitation.org/doi/abs/10.1063/1.4999617> (visited on 01/09/2021).
- [37] M. I. Dyakonov and V. I. Perel. “Current-induced spin orientation of electrons in semiconductors”. In: *Physics Letters A* 35.6 (July 12, 1971), pp. 459–460. ISSN: 0375-9601. DOI: [10.1016/0375-9601\(71\)90196-4](https://doi.org/10.1016/0375-9601(71)90196-4). URL: <https://www.sciencedirect.com/science/article/pii/0375960171901964>.
- [38] V. M. Edelstein. “Spin polarization of conduction electrons induced by electric current in two-dimensional asymmetric electron systems”. In: *Solid State Communications* 73.3 (Jan. 1, 1990), pp. 233–235. ISSN: 0038-1098. DOI: [10.1016/0038-1098\(90\)90963-C](https://doi.org/10.1016/0038-1098(90)90963-C). URL: <https://www.sciencedirect.com/science/article/pii/003810989090963C>.
- [39] A. Einstein. “On a Heuristic Point of View about the Creation and Conversion of Light”. In: *The Old Quantum Theory*. Elsevier, 1967, pp. 91–107. ISBN: 978-0-08-012102-4. DOI: [10.1016/B978-0-08-012102-4.50014-0](https://doi.org/10.1016/B978-0-08-012102-4.50014-0). URL: <https://linkinghub.elsevier.com/retrieve/pii/B9780080121024500140>.
- [40] Satoru Emori et al. “Current-driven dynamics of chiral ferromagnetic domain walls”. In: *Nature Materials* 12.7 (July 2013), pp. 611–616. ISSN: 1476-4660. DOI: [10.1038/nmat3675](https://doi.org/10.1038/nmat3675).
- [41] Satoru Emori et al. “Interfacial spin-orbit torque without bulk spin-orbit coupling”. In: *Physical Review B* 93.18 (May 4, 2016). Publisher: American Physical Society, p. 180402. DOI: [10.1103/PhysRevB.93.180402](https://doi.org/10.1103/PhysRevB.93.180402). URL: <https://link.aps.org/doi/10.1103/PhysRevB.93.180402>.

- [42] Tuo Fan et al. “Crystal growth and characterization of topological insulator BiSb thin films by sputtering deposition on sapphire substrates”. In: *Japanese Journal of Applied Physics* 59.6 (June 2020). Publisher: IOP Publishing, p. 063001. ISSN: 1347-4065. DOI: [10.35848/1347-4065/ab91d0](https://doi.org/10.35848/1347-4065/ab91d0). URL: <https://doi.org/10.35848/1347-4065/ab91d0>.
- [43] Tuo Fan et al. “Low power spin-orbit torque switching in sputtered BiSb topological insulator/perpendicularly magnetized CoPt/MgO multilayers on oxidized Si substrate”. In: *Applied Physics Letters* 119.8 (Aug. 26, 2021), p. 082403. ISSN: 0003-6951. DOI: [10.1063/5.0062625](https://doi.org/10.1063/5.0062625). URL: <https://doi.org/10.1063/5.0062625>.
- [44] Xin Fan et al. “Observation of the nonlocal spin-orbital effective field”. In: *Nature Communications* 4.1 (Apr. 30, 2013). Number: 1 Publisher: Nature Publishing Group, p. 1799. ISSN: 2041-1723. DOI: [10.1038/ncomms2709](https://www.nature.com/articles/ncomms2709). URL: <https://www.nature.com/articles/ncomms2709>.
- [45] Xin Fan et al. “Quantifying interface and bulk contributions to spin-orbit torque in magnetic bilayers”. In: *Nature Communications* 5.1 (Jan. 9, 2014). Number: 1 Publisher: Nature Publishing Group, p. 3042. ISSN: 2041-1723. DOI: [10.1038/ncomms4042](https://www.nature.com/articles/ncomms4042). URL: <https://www.nature.com/articles/ncomms4042>.
- [46] Yabin Fan et al. “Magnetization switching through giant spin-orbit torque in a magnetically doped topological insulator heterostructure”. In: *Nature Materials* 13.7 (July 2014). Number: 7 Publisher: Nature Publishing Group, pp. 699–704. ISSN: 1476-4660. DOI: [10.1038/nmat3973](https://www.nature.com/articles/nmat3973). URL: <https://www.nature.com/articles/nmat3973>.
- [47] D Fang et al. “Spin-orbit-driven ferromagnetic resonance”. In: *Nature nanotechnology* 6.7 (May 1, 2011), pp. 413–417. ISSN: 1748-3395. DOI: [10.1038/nnano.2011.68](https://doi.org/10.1038/nnano.2011.68). URL: <https://doi.org/10.1038/nnano.2011.68>.
- [48] G. Finocchio et al. “Switching of a single ferromagnetic layer driven by spin Hall effect”. In: *Applied Physics Letters* 102.21 (May 30, 2013), p. 212410. ISSN: 0003-6951. DOI: [10.1063/1.4808092](https://doi.org/10.1063/1.4808092). URL: <https://doi.org/10.1063/1.4808092>.
- [49] Liang Fu, C. L. Kane, and E. J. Mele. “Topological Insulators in Three Dimensions”. In: *Physical Review Letters* 98.10 (Mar. 7, 2007). Publisher: American Physical Society, p. 106803. DOI: [10.1103/PhysRevLett.98.106803](https://link.aps.org/doi/10.1103/PhysRevLett.98.106803). URL: <https://link.aps.org/doi/10.1103/PhysRevLett.98.106803>.
- [50] Kevin Garello et al. “Symmetry and magnitude of spin-orbit torques in ferromagnetic heterostructures”. In: *Nature Nanotechnology* 8.8 (Aug. 2013), pp. 587–593. ISSN: 1748-3395. DOI: [10.1038/nnano.2013.145](https://doi.org/10.1038/nnano.2013.145).
- [51] Abhijit Ghosh et al. “Interface-Enhanced Spin-Orbit Torques and Current-Induced Magnetization Switching of Pd/Co/Al/O Layers”. In: *Physical Review Applied* 7.1 (Jan. 6, 2017). Publisher: American Physical Society, p. 014004. DOI: [10.1103/PhysRevApplied.7.014004](https://link.aps.org/doi/10.1103/PhysRevApplied.7.014004). URL: <https://link.aps.org/doi/10.1103/PhysRevApplied.7.014004>.
- [52] Dongwook Go and Hyun-Woo Lee. “Orbital torque: Torque generation by orbital current injection”. In: *Physical Review Research* 2.1 (Feb. 20, 2020). Publisher: American Physical Society, p. 013177. DOI: [10.1103/PhysRevResearch.2.013177](https://link.aps.org/doi/10.1103/PhysRevResearch.2.013177). URL: <https://link.aps.org/doi/10.1103/PhysRevResearch.2.013177>.

- [53] F. D. M. Haldane. “Model for a Quantum Hall Effect without Landau Levels: Condensed-Matter Realization of the ”Parity Anomaly””. In: *Physical Review Letters* 61.18 (Oct. 31, 1988). Publisher: American Physical Society, pp. 2015–2018. DOI: [10.1103/PhysRevLett.61.2015](https://doi.org/10.1103/PhysRevLett.61.2015). URL: <https://link.aps.org/doi/10.1103/PhysRevLett.61.2015>.
- [54] E. H. Hall. “On a New Action of the Magnet on Electric Currents”. In: *American Journal of Mathematics* 2.3 (1879). Publisher: Johns Hopkins University Press, pp. 287–292. ISSN: 0002-9327. DOI: [10.2307/2369245](https://doi.org/10.2307/2369245). URL: <https://www.jstor.org/stable/2369245>.
- [55] Xiufeng Han et al. “Spin-orbit torques: Materials, physics, and devices”. In: *Applied Physics Letters* 118.12 (Mar. 24, 2021), p. 120502. ISSN: 0003-6951. DOI: [10.1063/5.0039147](https://doi.org/10.1063/5.0039147). URL: <https://doi.org/10.1063/5.0039147>.
- [56] Paul M. Haney et al. “Current induced torques and interfacial spin-orbit coupling: Semiclassical modeling”. In: *Physical Review B* 87.17 (May 7, 2013). Publisher: American Physical Society, p. 174411. DOI: [10.1103/PhysRevB.87.174411](https://doi.org/10.1103/PhysRevB.87.174411). URL: <https://link.aps.org/doi/10.1103/PhysRevB.87.174411>.
- [57] Qiang Hao and Gang Xiao. “Giant Spin Hall Effect and Switching Induced by Spin-Transfer Torque in a W/Co<sub>40</sub>/Fe<sub>40</sub>B<sub>20</sub>/MgO Structure with Perpendicular Magnetic Anisotropy”. In: *Physical Review Applied* 3.3 (Mar. 26, 2015). Publisher: American Physical Society, p. 034009. DOI: [10.1103/PhysRevApplied.3.034009](https://doi.org/10.1103/PhysRevApplied.3.034009). URL: <https://link.aps.org/doi/10.1103/PhysRevApplied.3.034009>.
- [58] M. Z. Hasan and C. L. Kane. “Colloquium: Topological insulators”. In: *Reviews of Modern Physics* 82.4 (Nov. 8, 2010). Publisher: American Physical Society, pp. 3045–3067. DOI: [10.1103/RevModPhys.82.3045](https://doi.org/10.1103/RevModPhys.82.3045). URL: <https://link.aps.org/doi/10.1103/RevModPhys.82.3045>.
- [59] Richard C. Hatch et al. “Stability of the Bi<sub>2</sub>Se<sub>3</sub>(111) topological state: Electron-phonon and electron-defect scattering”. In: *Physical Review B* 83.24 (2011). DOI: [10.1103/physrevb.83.241303](https://doi.org/10.1103/physrevb.83.241303). URL: <https://doi.org/10.1103/physrevb.83.241303>.
- [60] T. Hirahara et al. “Topological metal at the surface of an ultrathin Bi<sub>1-x</sub>Sb<sub>x</sub> alloy film”. In: *Physical Review B* 81.16 (Apr. 15, 2010). Publisher: American Physical Society, p. 165422. DOI: [10.1103/PhysRevB.81.165422](https://doi.org/10.1103/PhysRevB.81.165422). URL: <https://link.aps.org/doi/10.1103/PhysRevB.81.165422>.
- [61] D. Hsieh et al. “A topological Dirac insulator in a quantum spin Hall phase”. In: *Nature* 452.7190 (Apr. 2008). Number: 7190 Publisher: Nature Publishing Group, pp. 970–974. ISSN: 1476-4687. DOI: [10.1038/nature06843](https://doi.org/10.1038/nature06843). URL: <https://www.nature.com/articles/nature06843> (visited on 08/01/2023).
- [62] T. J. Huisman et al. “Femtosecond control of electric currents in metallic ferromagnetic heterostructures”. In: *Nature Nanotechnology* 11.5 (May 2016). Number: 5 Publisher: Nature Publishing Group, pp. 455–458. ISSN: 1748-3395. DOI: [10.1038/nnano.2015.331](https://doi.org/10.1038/nnano.2015.331). URL: <https://www.nature.com/articles/nnano.2015.331>.
- [63] Van Hulst. “Epitaxial growth of Bi and BiSb heterostructures”. In: (1995).
- [64] Ho Hoang Huy et al. “Large inverse spin Hall effect in BiSb topological insulator for 4 Tb/in<sup>2</sup> magnetic recording technology”. In: *Applied Physics Letters* 122.5 (Jan. 30, 2023), p. 052401. ISSN: 0003-6951, 1077-3118. DOI: [10.1063/5.0135831](https://doi.org/10.1063/5.0135831). URL: <https://pubs.aip.org/aip/apl/article/2874871>.

- [65] Hironari Isshiki et al. “Phenomenological model for the direct and inverse Edelstein effects”. In: *Physical Review B* 102.18 (Nov. 10, 2020). Publisher: American Physical Society, p. 184411. DOI: [10.1103/PhysRevB.102.184411](https://doi.org/10.1103/PhysRevB.102.184411), URL: <https://link.aps.org/doi/10.1103/PhysRevB.102.184411>.
- [66] Loghman Jamilpanah, Mohammadreza Hajiali, and Seyed Majid Mohseni. “Interfacial magnetic anisotropy in Py/MoS<sub>2</sub> bilayer”. In: *Journal of Magnetism and Magnetic Materials* 514 (Nov. 15, 2020), p. 167206. ISSN: 0304-8853. DOI: [10.1016/j.jmmm.2020.167206](https://doi.org/10.1016/j.jmmm.2020.167206), URL: <https://www.sciencedirect.com/science/article/pii/S0304885320308532>.
- [67] Mi-Jin Jin et al. “Nonlocal Spin Diffusion Driven by Giant Spin Hall Effect at Oxide Heterointerfaces”. In: *Nano Letters* 17.1 (Jan. 11, 2017). Publisher: American Chemical Society, pp. 36–43. ISSN: 1530-6984. DOI: [10.1021/acs.nanolett.6b03050](https://doi.org/10.1021/acs.nanolett.6b03050), URL: <https://doi.org/10.1021/acs.nanolett.6b03050>.
- [68] Jing Jing et al. “Epitaxial growth of ultrathin films of bismuth: an atomic force microscopy study”. In: *Applied Surface Science* 62.3 (Jan. 1, 1992), pp. 105–114. ISSN: 0169-4332. DOI: [10.1016/0169-4332\(92\)90135-K](https://doi.org/10.1016/0169-4332(92)90135-K), URL: <https://www.sciencedirect.com/science/article/pii/016943329290135K>.
- [69] M. Julliere. “On the “Rotational Coefficient” in nickel and cobalt”. In: *Philos. Mag.* (1881), p. 157.
- [70] M. Julliere. “Tunneling between ferromagnetic films”. In: *Physics Letters A* 54.3 (Sept. 8, 1975), pp. 225–226. ISSN: 0375-9601. DOI: [10.1016/0375-9601\(75\)90174-7](https://doi.org/10.1016/0375-9601(75)90174-7), URL: <https://www.sciencedirect.com/science/article/pii/0375960175901747>.
- [71] Matthias B. Jungfleisch et al. “Control of Terahertz Emission by Ultrafast Spin-Charge Current Conversion at Rashba Interfaces”. In: *Physical Review Letters* 120.20 (May 18, 2018). Publisher: American Physical Society, p. 207207. DOI: [10.1103/PhysRevLett.120.207207](https://doi.org/10.1103/PhysRevLett.120.207207), URL: <https://link.aps.org/doi/10.1103/PhysRevLett.120.207207>.
- [72] T. Kampfrath et al. “Terahertz spin current pulses controlled by magnetic heterostructures”. In: *Nature Nanotechnology* 8.4 (Apr. 2013). Number: 4 Publisher: Nature Publishing Group, pp. 256–260. ISSN: 1748-3395. DOI: [10.1038/nnano.2013.43](https://doi.org/10.1038/nnano.2013.43), URL: <https://www.nature.com/articles/nnano.2013.43>.
- [73] C. L. Kane and E. J. Mele. “Quantum Spin Hall Effect in Graphene”. In: *Physical Review Letters* 95.22 (Nov. 23, 2005). Publisher: American Physical Society, p. 226801. DOI: [10.1103/PhysRevLett.95.226801](https://doi.org/10.1103/PhysRevLett.95.226801), URL: <https://link.aps.org/doi/10.1103/PhysRevLett.95.226801>.
- [74] Min-Gu Kang et al. “Negative spin Hall magnetoresistance of normal metal/ferromagnet bilayers”. In: *Nature Communications* 11.1 (July 17, 2020). Number: 1 Publisher: Nature Publishing Group, p. 3619. ISSN: 2041-1723. DOI: [10.1038/s41467-020-17463-3](https://doi.org/10.1038/s41467-020-17463-3), URL: <https://www.nature.com/articles/s41467-020-17463-3>.
- [75] Y. K. Kato et al. “Observation of the spin Hall effect in semiconductors”. In: *Science (New York, N.Y.)* 306.5703 (Dec. 10, 2004), pp. 1910–1913. ISSN: 1095-9203. DOI: [10.1126/science.1105514](https://doi.org/10.1126/science.1105514).
- [76] Masashi Kawaguchi et al. “Anomalous spin Hall magnetoresistance in Pt/Co bilayers”. In: *Applied Physics Letters* 112.20 (May 16, 2018), p. 202405. ISSN: 0003-6951. DOI: [10.1063/1.5021510](https://doi.org/10.1063/1.5021510), URL: <https://doi.org/10.1063/1.5021510>.

- [77] Nguyen Huynh Duy Khang, Yugo Ueda, and Pham Nam Hai. “A conductive topological insulator with large spin Hall effect for ultralow power spin-orbit torque switching”. In: *Nature Materials* 17.9 (Sept. 2018). Number: 9 Publisher: Nature Publishing Group, pp. 808–813. ISSN: 1476-4660. DOI: [10.1038/s41563-018-0137-y](https://doi.org/10.1038/s41563-018-0137-y). URL: <https://www.nature.com/articles/s41563-018-0137-y>.
- [78] Nguyen Huynh Duy Khang et al. “Nanosecond ultralow power spin orbit torque magnetization switching driven by BiSb topological insulator”. In: *Applied Physics Letters* 120.15 (Apr. 11, 2022), p. 152401. ISSN: 0003-6951, 1077-3118. DOI: [10.1063/5.0084927](https://doi.org/10.1063/5.0084927). URL: <https://pubs.aip.org/aip/apl/article/2833332>.
- [79] Nguyen Huynh Duy Khang et al. “Ultralow power spin-orbit torque magnetization switching induced by a non-epitaxial topological insulator on Si substrates”. In: *Scientific Reports* 10.1 (July 22, 2020). Number: 1 Publisher: Nature Publishing Group, p. 12185. ISSN: 2045-2322. DOI: [10.1038/s41598-020-69027-6](https://doi.org/10.1038/s41598-020-69027-6). URL: <https://www.nature.com/articles/s41598-020-69027-6>.
- [80] Junyeon Kim et al. “Anomalous temperature dependence of current-induced torques in CoFeB/MgO heterostructures with Ta-based underlayers”. In: *Physical Review B* 89.17 (May 23, 2014). Publisher: American Physical Society, p. 174424. DOI: [10.1103/PhysRevB.89.174424](https://doi.org/10.1103/PhysRevB.89.174424). URL: <https://link.aps.org/doi/10.1103/PhysRevB.89.174424>.
- [81] Junyeon Kim et al. “Layer thickness dependence of the current-induced effective field vector in Ta|CoFeB|MgO”. In: *Nature Materials* 12.3 (Mar. 2013), pp. 240–245. ISSN: 1476-4660. DOI: [10.1038/nmat3522](https://doi.org/10.1038/nmat3522).
- [82] P. D. C. King et al. “Large Tunable Rashba Spin Splitting of a Two-Dimensional Electron Gas in Bi<sub>2</sub>Se<sub>3</sub>”. In: *Physical Review Letters* 107.9 (Aug. 25, 2011). Publisher: American Physical Society, p. 096802. DOI: [10.1103/PhysRevLett.107.096802](https://doi.org/10.1103/PhysRevLett.107.096802). URL: <https://link.aps.org/doi/10.1103/PhysRevLett.107.096802>.
- [83] K. v. Klitzing, G. Dorda, and M. Pepper. “New Method for High-Accuracy Determination of the Fine-Structure Constant Based on Quantized Hall Resistance”. In: *Physical Review Letters* 45.6 (Aug. 11, 1980). Publisher: American Physical Society, pp. 494–497. DOI: [10.1103/PhysRevLett.45.494](https://doi.org/10.1103/PhysRevLett.45.494). URL: <https://link.aps.org/doi/10.1103/PhysRevLett.45.494>.
- [84] A. Kobs et al. “Anisotropic Interface Magnetoresistance in Pt / Co / Pt Sandwiches”. In: *Physical Review Letters* 106.21 (May 27, 2011), p. 217207. ISSN: 0031-9007, 1079-7114. DOI: [10.1103/PhysRevLett.106.217207](https://doi.org/10.1103/PhysRevLett.106.217207). URL: <https://link.aps.org/doi/10.1103/PhysRevLett.106.217207>.
- [85] Julian Koch et al. “Surface state conductivity in epitaxially grown Bi<sub>1-x</sub>Sb<sub>x</sub>(111) films”. In: *New Journal of Physics* 18.9 (Sept. 2016). Publisher: IOP Publishing, p. 093012. ISSN: 1367-2630. DOI: [10.1088/1367-2630/18/9/093012](https://doi.org/10.1088/1367-2630/18/9/093012). URL: <https://dx.doi.org/10.1088/1367-2630/18/9/093012>.
- [86] K. Kondou et al. “Fermi-level-dependent charge-to-spin current conversion by Dirac surface states of topological insulators”. In: *Nature Physics* 12.11 (Nov. 2016). Number: 11 Publisher: Nature Publishing Group, pp. 1027–1031. ISSN: 1745-2481. DOI: [10.1038/nphys3833](https://doi.org/10.1038/nphys3833). URL: <https://www.nature.com/articles/nphys3833>.
- [87] S. Krishnia et al. “Spin-Orbit Coupling in Single-Layer Ferrimagnets: Direct Observation of Spin-Orbit Torques and Chiral Spin Textures”. In: *Physical Review Applied* 16 (Aug. 24, 2021). DOI: [10.1103/PhysRevApplied.16.024040](https://doi.org/10.1103/PhysRevApplied.16.024040).

- [88] Viola Krizakova et al. “Spin-orbit torque switching of magnetic tunnel junctions for memory applications”. In: ().
- [89] Hitoshi Kubota et al. “Quantitative measurement of voltage dependence of spin-transfer torque in MgO-based magnetic tunnel junctions”. In: *Nature Physics* 4.1 (Jan. 2008). Number: 1 Publisher: Nature Publishing Group, pp. 37–41. ISSN: 1745-2481. DOI: [10.1038/nphys784](https://doi.org/10.1038/nphys784). URL: <https://www.nature.com/articles/nphys784>.
- [90] H. Kurebayashi et al. “An antidamping spin-orbit torque originating from the Berry curvature”. In: *Nature Nanotechnology* 9.3 (Mar. 2014), pp. 211–217. ISSN: 1748-3395. DOI: [10.1038/nnano.2014.15](https://doi.org/10.1038/nnano.2014.15).
- [91] K. Kuroda et al. “Hexagonally Deformed Fermi Surface of the 3D Topological Insulator Bi<sub>2</sub>Se<sub>3</sub>”. In: *Physical Review Letters* 105.7 (Aug. 10, 2010). Publisher: American Physical Society, p. 076802. DOI: [10.1103/PhysRevLett.105.076802](https://doi.org/10.1103/PhysRevLett.105.076802). URL: <https://link.aps.org/doi/10.1103/PhysRevLett.105.076802>.
- [92] H. Kurt et al. “High spin polarization in epitaxial films of ferrimagnetic Mn<sub>3</sub>Ga”. In: *Physical Review B* 83.2 (Jan. 12, 2011). Publisher: American Physical Society, p. 020405. DOI: [10.1103/PhysRevB.83.020405](https://doi.org/10.1103/PhysRevB.83.020405). URL: <https://link.aps.org/doi/10.1103/PhysRevB.83.020405>.
- [93] Markus König et al. “Quantum Spin Hall Insulator State in HgTe Quantum Wells”. In: *Science* 318.5851 (Nov. 2, 2007). Publisher: American Association for the Advancement of Science, pp. 766–770. DOI: [10.1126/science.1148047](https://doi.org/10.1126/science.1148047). URL: <https://www.science.org/doi/10.1126/science.1148047>.
- [94] Ki-Seung Lee et al. “Threshold current for switching of a perpendicular magnetic layer induced by spin Hall effect”. In: *Applied Physics Letters* 102.11 (Mar. 18, 2013), p. 112410. ISSN: 0003-6951, 1077-3118. DOI: [10.1063/1.4798288](https://doi.org/10.1063/1.4798288). URL: <https://pubs.aip.org/apl/article/102/11/112410/25568/Threshold-current-for-switching-of-a-perpendicular>.
- [95] B. Lenoir et al. “Bi-Sb alloys: an update”. In: *Fifteenth International Conference on Thermoelectrics. Proceedings ICT '96*. Fifteenth International Conference on Thermoelectrics. Proceedings ICT '96. Mar. 1996, pp. 1–13. DOI: [10.1109/ICT.1996.553246](https://doi.org/10.1109/ICT.1996.553246).
- [96] E. Lesne et al. “Highly efficient and tunable spin-to-charge conversion through Rashba coupling at oxide interfaces”. In: *Nature Materials* 15.12 (Dec. 2016), pp. 1261–1266. ISSN: 1476-4660. DOI: [10.1038/nmat4726](https://doi.org/10.1038/nmat4726).
- [97] G. Li et al. “THz emission from Co/Pt bilayers with varied roughness, crystal structure, and interface intermixing”. In: *Physical Review Materials* 3.8 (Aug. 19, 2019). Publisher: American Physical Society, p. 084415. DOI: [10.1103/PhysRevMaterials.3.084415](https://doi.org/10.1103/PhysRevMaterials.3.084415). URL: <https://link.aps.org/doi/10.1103/PhysRevMaterials.3.084415>.
- [98] Luqiao Liu et al. “Current-induced switching of perpendicularly magnetized magnetic layers using spin torque from the spin Hall effect”. In: *Physical Review Letters* 109.9 (Aug. 31, 2012), p. 096602. ISSN: 1079-7114. DOI: [10.1103/PhysRevLett.109.096602](https://doi.org/10.1103/PhysRevLett.109.096602).

- [99] Luqiao Liu et al. “Spin-Torque Ferromagnetic Resonance Induced by the Spin Hall Effect”. In: *Physical Review Letters* 106.3 (Jan. 20, 2011). Publisher: American Physical Society, p. 036601. DOI: [10.1103/PhysRevLett.106.036601](https://doi.org/10.1103/PhysRevLett.106.036601) URL: <https://link.aps.org/doi/10.1103/PhysRevLett.106.036601> (visited on 11/15/2023).
- [100] Luqiao Liu et al. “Spin-torque switching with the giant spin Hall effect of tantalum”. In: *Science (New York, N.Y.)* 336.6081 (May 4, 2012), pp. 555–558. ISSN: 1095-9203. DOI: [10.1126/science.1218197](https://doi.org/10.1126/science.1218197).
- [101] Yi Liu and Roland E. Allen. “Electronic structure of the semimetals Bi and Sb”. In: *Physical Review B* 52.3 (July 15, 1995). Publisher: American Physical Society, pp. 1566–1577. DOI: [10.1103/PhysRevB.52.1566](https://doi.org/10.1103/PhysRevB.52.1566) URL: <https://link.aps.org/doi/10.1103/PhysRevB.52.1566>.
- [102] H. C. Longuet-Higgins et al. “Studies of the Jahn-Teller Effect. II. The Dynamical Problem”. In: *Proceedings of the Royal Society of London Series A* 244 (Feb. 1, 1958), pp. 1–16. ISSN: 0080-4630/1364-5021. DOI: [10.1098/rspa.1958.0022](https://doi.org/10.1098/rspa.1958.0022) URL: <https://ui.adsabs.harvard.edu/abs/1958RSPSA.244...1L>.
- [103] Baiqing Lv, Tian Qian, and Hong Ding. “Angle-resolved photoemission spectroscopy and its application to topological materials”. In: *Nature Reviews Physics* 1.10 (Oct. 2019). Number: 10 Publisher: Nature Publishing Group, pp. 609–626. ISSN: 2522-5820. DOI: [10.1038/s42254-019-0088-5](https://doi.org/10.1038/s42254-019-0088-5) URL: <https://www.nature.com/articles/s42254-019-0088-5>.
- [104] Igor Lyalin, Shuyu Cheng, and Roland K. Kawakami. “Spin-Orbit Torque in Bilayers of Kagome Ferromagnet  $\text{Fe}_3\text{Sn}_2$  and Pt”. In: *Nano Letters* 21.16 (Aug. 25, 2021), pp. 6975–6982. ISSN: 1530-6984, 1530-6992. DOI: [10.1021/acs.nanolett.1c02270](https://doi.org/10.1021/acs.nanolett.1c02270) URL: <https://pubs.acs.org/doi/10.1021/acs.nanolett.1c02270>.
- [105] D. MacNeill et al. “Control of spin-orbit torques through crystal symmetry in  $\text{WTe}_2$ /ferromagnet bilayers”. In: *Nature Physics* 13 (Mar. 1, 2017). ADS Bibcode: 2017NatPh..13..300M, pp. 300–305. ISSN: 1745-2473. DOI: [10.1038/nphys3933](https://doi.org/10.1038/nphys3933) URL: <https://ui.adsabs.harvard.edu/abs/2017NatPh..13..300M>.
- [106] A. Manchon et al. “Current-induced spin-orbit torques in ferromagnetic and antiferromagnetic systems”. In: *Reviews of Modern Physics* 91.3 (Sept. 9, 2019), p. 035004. ISSN: 0034-6861, 1539-0756. DOI: [10.1103/RevModPhys.91.035004](https://doi.org/10.1103/RevModPhys.91.035004) URL: <https://link.aps.org/doi/10.1103/RevModPhys.91.035004>.
- [107] A. Manchon et al. “New perspectives for Rashba spin-orbit coupling”. In: *Nature Materials* 14.9 (Sept. 2015). Number: 9 Publisher: Nature Publishing Group, pp. 871–882. ISSN: 1476-4660. DOI: [10.1038/nmat4360](https://doi.org/10.1038/nmat4360) URL: <https://www.nature.com/articles/nmat4360>.
- [108] Eduardo Martinez et al. “Universal chiral-triggered magnetization switching in confined nanodots”. In: *Scientific Reports* 5.1 (June 10, 2015). Number: 1 Publisher: Nature Publishing Group, p. 10156. ISSN: 2045-2322. DOI: [10.1038/srep10156](https://doi.org/10.1038/srep10156) URL: <https://www.nature.com/articles/srep10156>.
- [109] A. R. Mellnik et al. “Spin-transfer torque generated by a topological insulator”. In: *Nature* 511.7510 (July 2014). Number: 7510 Publisher: Nature Publishing Group, pp. 449–451. ISSN: 1476-4687. DOI: [10.1038/nature13534](https://doi.org/10.1038/nature13534) URL: <https://www.nature.com/articles/nature13534>.

- [110] Ioan Mihai Miron et al. “Current-driven spin torque induced by the Rashba effect in a ferromagnetic metal layer”. In: *Nature Materials* 9.3 (Mar. 2010). Number: 3 Publisher: Nature Publishing Group, pp. 230–234. ISSN: 1476-4660. DOI: [10.1038/nmat2613](https://doi.org/10.1038/nmat2613). URL: <https://www.nature.com/articles/nmat2613>.
- [111] N. Mikuszeit et al. “Spin-orbit torque driven chiral magnetization reversal in ultrathin nanostructures”. In: *Physical Review B* 92.14 (Oct. 26, 2015). Publisher: American Physical Society, p. 144424. DOI: [10.1103/PhysRevB.92.144424](https://doi.org/10.1103/PhysRevB.92.144424). URL: <https://link.aps.org/doi/10.1103/PhysRevB.92.144424>.
- [112] Kevin Miron Ioan Mihai and et al. “Perpendicular switching of a single ferromagnetic layer induced by in-plane current injection”. In: *Nature* 476.7359 (Aug. 11, 2011), pp. 189–193. ISSN: 1476-4687. DOI: [10.1038/nature10309](https://doi.org/10.1038/nature10309).
- [113] S. Mizukami et al. “Mn-based hard magnets with small saturation magnetization and low spin relaxation for spintronics”. In: *Scripta Materialia* 118 (June 1, 2016), pp. 70–74. ISSN: 1359-6462. DOI: [10.1016/j.scriptamat.2016.01.045](https://doi.org/10.1016/j.scriptamat.2016.01.045). URL: <https://www.sciencedirect.com/science/article/pii/S1359646216300446>.
- [114] J. E. Moore and L. Balents. “Topological invariants of time-reversal-invariant band structures”. In: *Physical Review B* 75.12 (Mar. 26, 2007). Publisher: American Physical Society, p. 121306. DOI: [10.1103/PhysRevB.75.121306](https://doi.org/10.1103/PhysRevB.75.121306). URL: <https://link.aps.org/doi/10.1103/PhysRevB.75.121306>.
- [115] Nevill Francis Mott and Niels Henrik David Bohr. “The scattering of fast electrons by atomic nuclei”. In: *Proceedings of the Royal Society of London. Series A, Containing Papers of a Mathematical and Physical Character* 124.794 (Jan. 1997). Publisher: Royal Society, pp. 425–442. DOI: [10.1098/rspa.1929.0127](https://doi.org/10.1098/rspa.1929.0127). URL: <https://royalsocietypublishing.org/doi/abs/10.1098/rspa.1929.0127>.
- [116] Hiroyasu Nakayama et al. “Rashba-Edelstein Magnetoresistance in Metallic Heterostructures”. In: *Physical Review Letters* 117.11 (Sept. 7, 2016). Publisher: American Physical Society, p. 116602. DOI: [10.1103/PhysRevLett.117.116602](https://doi.org/10.1103/PhysRevLett.117.116602). URL: <https://link.aps.org/doi/10.1103/PhysRevLett.117.116602>.
- [117] Kulothungasagaran Narayanapillai et al. “Current-driven spin orbit field in LaAlO<sub>3</sub>/SrTiO<sub>3</sub> heterostructures”. In: *Applied Physics Letters* 105.16 (Oct. 21, 2014), p. 162405. ISSN: 0003-6951. DOI: [10.1063/1.4899122](https://doi.org/10.1063/1.4899122). URL: <https://doi.org/10.1063/1.4899122>.
- [118] Douglas Natelson. *nanoscale views: What is Berry phase?* nanoscale views. July 31, 2018. URL: <http://nanoscale.blogspot.com/2018/07/what-is-berry-phase.html>.
- [119] N.F.Mott. “The scattering of fast electrons by atomic nuclei”. In: *Proceedings of the Royal Society of London. Series A, Containing Papers of a Mathematical and Physical Character* 124.794 (June 4, 1929), pp. 425–442. ISSN: 0950-1207, 2053-9150. DOI: [10.1098/rspa.1929.0127](https://doi.org/10.1098/rspa.1929.0127). URL: <https://royalsocietypublishing.org/doi/10.1098/rspa.1929.0127>.
- [120] Minh-Hai Nguyen, D. C. Ralph, and R. A. Buhrman. “Spin Torque Study of the Spin Hall Conductivity and Spin Diffusion Length in Platinum Thin Films with Varying Resistivity”. In: *Physical Review Letters* 116.12 (Mar. 24, 2016). Publisher: American Physical Society, p. 126601. DOI: [10.1103/PhysRevLett.116.126601](https://doi.org/10.1103/PhysRevLett.116.126601). URL: <https://link.aps.org/doi/10.1103/PhysRevLett.116.126601>.

- [121] Takayuki Nozaki et al. “Enhancing the interfacial perpendicular magnetic anisotropy and tunnel magnetoresistance by inserting an ultrathin LiF layer at an Fe/MgO interface”. In: *NPG Asia Materials* 14.1 (Jan. 28, 2022). Number: 1 Publisher: Nature Publishing Group, pp. 1–7. ISSN: 1884-4057. DOI: [10.1038/s41427-021-00350-8](https://doi.org/10.1038/s41427-021-00350-8). URL: <https://www.nature.com/articles/s41427-021-00350-8>.
- [122] H. Ohno. “Making Nonmagnetic Semiconductors Ferromagnetic”. In: *Science* 281.5379 (Aug. 14, 1998). Publisher: American Association for the Advancement of Science, pp. 951–956. DOI: [10.1126/science.281.5379.951](https://doi.org/10.1126/science.281.5379.951). URL: <https://www.science.org/doi/10.1126/science.281.5379.951>.
- [123] Ryo Ohshima et al. “Strong evidence for d-electron spin transport at room temperature at a LaAlO<sub>3</sub>/SrTiO<sub>3</sub> interface”. In: *Nature Materials* 16.6 (June 2017). Number: 6 Publisher: Nature Publishing Group, pp. 609–614. ISSN: 1476-4660. DOI: [10.1038/nmat4857](https://doi.org/10.1038/nmat4857). URL: <https://www.nature.com/articles/nmat4857>.
- [124] Akihiro Ohtake et al. “Surface structures of GaAs{111}A, B - (2 × 2)”. In: *Physical Review B* 64.4 (June 29, 2001). Publisher: American Physical Society, p. 045318. DOI: [10.1103/PhysRevB.64.045318](https://doi.org/10.1103/PhysRevB.64.045318). URL: <https://link.aps.org/doi/10.1103/PhysRevB.64.045318>.
- [125] Chi-Feng Pai et al. “Enhancement of Perpendicular Magnetic Anisotropy and Transmission of Spin-Hall-Effect-Induced Spin Currents by a Hf Spacer Layer in W/Hf/CoFeB/MgO Layer”. In: *Applied Physics Letters* 104 (Jan. 18, 2014). DOI: [10.1063/1.4866965](https://doi.org/10.1063/1.4866965).
- [126] Chi-Feng Pai et al. “Spin transfer torque devices utilizing the giant spin Hall effect of tungsten”. In: *Applied Physics Letters* 101 (Sept. 1, 2012). ADS Bibcode: 2012ApPhL.10112404P, p. 122404. ISSN: 0003-6951. DOI: [10.1063/1.4753947](https://doi.org/10.1063/1.4753947). URL: <https://ui.adsabs.harvard.edu/abs/2012ApPhL.10112404P>.
- [127] S. Pancharatnam. “Generalized theory of interference, and its applications”. In: *Proceedings of the Indian Academy of Sciences - Section A* 44.5 (Nov. 1, 1956), pp. 247–262. ISSN: 0370-0089. DOI: [10.1007/BF03046050](https://doi.org/10.1007/BF03046050). URL: <https://doi.org/10.1007/BF03046050>.
- [128] Akiyoshi Park et al. “Quasiparticle scattering in 3 MeV proton irradiated BaFe<sub>2</sub>(As<sub>0.67</sub>P<sub>0.33</sub>)<sub>2</sub>”. In: *Physical Review B* 98.5 (Aug. 20, 2018). Publisher: American Physical Society, p. 054512. DOI: [10.1103/PhysRevB.98.054512](https://doi.org/10.1103/PhysRevB.98.054512). URL: <https://link.aps.org/doi/10.1103/PhysRevB.98.054512>.
- [129] N. Perez et al. “Chiral magnetization textures stabilized by the Dzyaloshinskii-Moriya interaction during spin-orbit torque switching”. In: *Applied Physics Letters* 104.9 (Mar. 3, 2014), p. 092403. ISSN: 0003-6951, 1077-3118. DOI: [10.1063/1.4867199](https://doi.org/10.1063/1.4867199). URL: <https://pubs.aip.org/aip/apl/article/132732>.
- [130] Cyril Petitjean, David Luc, and Xavier Waintal. “Unified Drift-Diffusion Theory for Transverse Spin Currents in Spin Valves, Domain Walls, and Other Textured Magnets”. In: *Physical Review Letters* 109.11 (Sept. 13, 2012). Publisher: American Physical Society, p. 117204. DOI: [10.1103/PhysRevLett.109.117204](https://doi.org/10.1103/PhysRevLett.109.117204). URL: <https://link.aps.org/doi/10.1103/PhysRevLett.109.117204>.
- [131] H. S. Qiu et al. “Layer thickness dependence of the terahertz emission based on spin current in ferromagnetic heterostructures”. In: *Optics Express* 26.12 (June 11, 2018). Publisher: Optica Publishing Group, pp. 15247–15254. ISSN: 1094-4087. DOI: [10.1364/OE.26.015247](https://doi.org/10.1364/OE.26.015247). URL: <https://opg.optica.org/oe/abstract.cfm?uri=oe-26-12-15247>.

- [132] Xuepeng Qiu et al. “Angular and temperature dependence of current induced spin-orbit effective fields in Ta/CoFeB/MgO nanowires”. In: *Scientific Reports* 4.1 (Mar. 27, 2014). Number: 1 Publisher: Nature Publishing Group, p. 4491. ISSN: 2045-2322. DOI: [10.1038/srep04491](https://doi.org/10.1038/srep04491). URL: <https://www.nature.com/articles/srep04491>.
- [133] *Quantum Matter Theory Research Team | Akira Furusaki | Center for Emergent Matter Science (CEMS) | RIKEN*. URL: <https://cems.riken.jp/laboratory/qmtrt>.
- [134] Rajagopalan Ramaswamy et al. “Hf thickness dependence of spin-orbit torques in Hf/CoFeB/MgO heterostructures”. In: *Applied Physics Letters* 108.20 (May 16, 2016). DOI: [10.1063/1.4951674](https://doi.org/10.1063/1.4951674). URL: <https://digitalcommons.memphis.edu/facpubs/6669>.
- [135] E I Rashba and V I Sheka. “Symmetry of Energy Bands in Crystals of Wurtzite Type II. Symmetry of Bands with Spin-Orbit Interaction Included”. In: ().
- [136] Karsten Rode et al. “Site-specific order and magnetism in tetragonal Mn<sub>3</sub>Ga thin films”. In: *Physical Review B* 87.18 (May 24, 2013). Publisher: American Physical Society, p. 184429. DOI: [10.1103/PhysRevB.87.184429](https://doi.org/10.1103/PhysRevB.87.184429). URL: <https://link.aps.org/doi/10.1103/PhysRevB.87.184429>.
- [137] J.-C. Rojas-Sánchez and A. Fert. “Compared Efficiencies of Conversions between Charge and Spin Current by Spin-Orbit Interactions in Two- and Three-Dimensional Systems”. In: *Physical Review Applied* 11.5 (May 17, 2019). Publisher: American Physical Society, p. 054049. DOI: [10.1103/PhysRevApplied.11.054049](https://doi.org/10.1103/PhysRevApplied.11.054049). URL: <https://link.aps.org/doi/10.1103/PhysRevApplied.11.054049> (visited on 01/09/2021).
- [138] E. Rongione et al. “Spin-Momentum Locking and Ultrafast Spin-Charge Conversion in Ultrathin Epitaxial Bi<sub>1-x</sub>Sb<sub>x</sub> Topological Insulator”. In: *Advanced Science* 10.19 (2023), p. 2301124. ISSN: 2198-3844. DOI: [10.1002/advs.202301124](https://doi.org/10.1002/advs.202301124). URL: <https://onlinelibrary.wiley.com/doi/abs/10.1002/advs.202301124>.
- [139] Niklas Roschewsky et al. “Spin-orbit torque and Nernst effect in Bi-Sb/Co heterostructures”. In: *Physical Review B* 99.19 (May 2, 2019), p. 195103. ISSN: 2469-9950, 2469-9969. DOI: [10.1103/PhysRevB.99.195103](https://doi.org/10.1103/PhysRevB.99.195103). URL: <https://link.aps.org/doi/10.1103/PhysRevB.99.195103>.
- [140] Rahul Roy. “Topological phases and the quantum spin Hall effect in three dimensions”. In: *Physical Review B* 79.19 (May 21, 2009). Publisher: American Physical Society, p. 195322. DOI: [10.1103/PhysRevB.79.195322](https://doi.org/10.1103/PhysRevB.79.195322). URL: <https://link.aps.org/doi/10.1103/PhysRevB.79.195322>.
- [141] Kwang-Su Ryu et al. “Chiral spin torque at magnetic domain walls”. In: *Nature Nanotechnology* 8.7 (July 2013). Number: 7 Publisher: Nature Publishing Group, pp. 527–533. ISSN: 1748-3395. DOI: [10.1038/nnano.2013.102](https://doi.org/10.1038/nnano.2013.102). URL: <https://www.nature.com/articles/nnano.2013.102>.
- [142] Dima Sadek et al. “Growth of BiSb on GaAs (001) and (111)A surfaces: A joint experimental and theoretical study”. In: *Applied Surface Science* 622 (Feb. 14, 2023), p. 156688. DOI: [10.1016/j.apsusc.2023.156688](https://doi.org/10.1016/j.apsusc.2023.156688). URL: <https://hal.laas.fr/hal-04017077>.

- [143] Dima Sadek et al. “Integration of the Rhombohedral BiSb(0001) Topological Insulator on a Cubic GaAs(001) Substrate”. In: *ACS Applied Materials & Interfaces* 13.30 (Aug. 4, 2021), pp. 36492–36498. ISSN: 1944-8244, 1944-8252. DOI: [10.1021/acsami.1c08477](https://doi.org/10.1021/acsami.1c08477). URL: <https://pubs.acs.org/doi/10.1021/acsami.1c08477>.
- [144] C. K. Safeer et al. “Spin-orbit torque magnetization switching controlled by geometry”. In: *Nature Nanotechnology* 11.2 (Feb. 2016). Number: 2 Publisher: Nature Publishing Group, pp. 143–146. ISSN: 1748-3395. DOI: [10.1038/nnano.2015.252](https://doi.org/10.1038/nnano.2015.252). URL: <https://www.nature.com/articles/nnano.2015.252>.
- [145] J. C. Sankey et al. “Spin-Transfer-Driven Ferromagnetic Resonance of Individual Nanomagnets”. In: *Physical Review Letters* 96.22 (June 5, 2006). Publisher: American Physical Society, p. 227601. DOI: [10.1103/PhysRevLett.96.227601](https://doi.org/10.1103/PhysRevLett.96.227601). URL: <https://link.aps.org/doi/10.1103/PhysRevLett.96.227601>.
- [146] J. Sasaki et al. “Improvement of the Effective Spin Hall Angle by Inserting an Interfacial Layer in Sputtered BiSb Topological Insulator (Bottom)/Ferromagnet With In-Plane Magnetization”. In: *IEEE Transactions on Magnetism* 58.4 (Apr. 2022). Conference Name: IEEE Transactions on Magnetism, pp. 1–4. ISSN: 1941-0069. DOI: [10.1109/TMAG.2021.3115169](https://doi.org/10.1109/TMAG.2021.3115169).
- [147] Julian Sasaki et al. “Highly efficient spin current source using BiSb topological insulator/NiO bilayers”. In: *Japanese Journal of Applied Physics* 62 (SC Dec. 20, 2022). Publisher: IOP Publishing, SC1005. ISSN: 1347-4065. DOI: [10.35848/1347-4065/aca772](https://doi.org/10.35848/1347-4065/aca772). URL: <https://iopscience.iop.org/article/10.35848/1347-4065/aca772/meta>.
- [148] T. Seifert et al. “Terahertz Spin Currents and Inverse Spin Hall Effect in Thin-Film Heterostructures Containing Complex Magnetic Compounds”. In: *SPIN* 07.3 (Sept. 2017). Publisher: World Scientific Publishing Co., p. 1740010. ISSN: 2010-3247. DOI: [10.1142/S2010324717400100](https://doi.org/10.1142/S2010324717400100). URL: <https://www.worldscientific.com/doi/abs/10.1142/S2010324717400100>.
- [149] Qiming Shao et al. “Roadmap of Spin-Orbit Torques”. In: *IEEE Transactions on Magnetism* 57.7 (July 2021), pp. 1–39. ISSN: 0018-9464, 1941-0069. DOI: [10.1109/TMAG.2021.3078583](https://doi.org/10.1109/TMAG.2021.3078583). URL: <https://ieeexplore.ieee.org/document/9427163/>.
- [150] Qiming Shao et al. “Strong Rashba-Edelstein Effect-Induced Spin-Orbit Torques in Monolayer Transition Metal Dichalcogenide/Ferromagnet Bilayers”. In: *Nano Letters* 16.12 (Dec. 14, 2016). Publisher: American Chemical Society, pp. 7514–7520. ISSN: 1530-6984. DOI: [10.1021/acs.nanolett.6b03300](https://doi.org/10.1021/acs.nanolett.6b03300). URL: <https://doi.org/10.1021/acs.nanolett.6b03300>.
- [151] Vinay Sharma et al. “Light and microwave driven spin pumping across FeGaB-BiSb interface”. In: *Phys. Rev. Mater.* 5 (12 2021), p. 124410. DOI: [10.1103/PhysRevMaterials.5.124410](https://doi.org/10.1103/PhysRevMaterials.5.124410). URL: <https://link.aps.org/doi/10.1103/PhysRevMaterials.5.124410>.
- [152] Y. Shiomi et al. “Spin-Electricity Conversion Induced by Spin Injection into Topological Insulators”. In: *Physical Review Letters* 113.19 (Nov. 3, 2014). Publisher: American Physical Society, p. 196601. DOI: [10.1103/PhysRevLett.113.196601](https://doi.org/10.1103/PhysRevLett.113.196601). URL: <https://link.aps.org/doi/10.1103/PhysRevLett.113.196601>.
- [153] J. C. Slonczewski. “Current-driven excitation of magnetic multilayers”. In: *Journal of Magnetism and Magnetic Materials* 159.1 (June 1, 1996), pp. L1–L7. ISSN: 0304-8853. DOI: [10.1016/0304-8853\(96\)00062-5](https://doi.org/10.1016/0304-8853(96)00062-5). URL: <https://www.sciencedirect.com/science/article/pii/0304885396000625>.

- [154] P. C. van Son, H. van Kempen, and P. Wyder. “Boundary Resistance of the Ferromagnetic-Nonferromagnetic Metal Interface”. In: *Physical Review Letters* 58.21 (May 25, 1987). Publisher: American Physical Society, pp. 2271–2273. DOI: [10.1103/PhysRevLett.58.2271](https://doi.org/10.1103/PhysRevLett.58.2271). URL: <https://link.aps.org/doi/10.1103/PhysRevLett.58.2271>.
- [155] Cheng Song et al. “Spin-orbit torques: Materials, mechanisms, performances, and potential applications”. In: *Progress in Materials Science* 118 (May 1, 2021), p. 100761. ISSN: 0079-6425. DOI: [10.1016/j.pmatsci.2020.100761](https://doi.org/10.1016/j.pmatsci.2020.100761). URL: <https://www.sciencedirect.com/science/article/pii/S0079642520301250>.
- [156] Qi Song et al. “Observation of inverse Edelstein effect in Rashba-split 2DEG between SrTiO<sub>3</sub> and LaAlO<sub>3</sub> at room temperature”. In: *Science Advances* 3.3 (Mar. 17, 2017). Publisher: American Association for the Advancement of Science, e1602312. DOI: [10.1126/sciadv.1602312](https://doi.org/10.1126/sciadv.1602312). URL: <https://www.science.org/doi/10.1126/sciadv.1602312>.
- [157] C. Stamm et al. “Magneto-Optical Detection of the Spin Hall Effect in Pt and W Thin Films”. In: *Physical Review Letters* 119.8 (Aug. 25, 2017). Publisher: American Physical Society, p. 087203. DOI: [10.1103/PhysRevLett.119.087203](https://doi.org/10.1103/PhysRevLett.119.087203). URL: <https://link.aps.org/doi/10.1103/PhysRevLett.119.087203> (visited on 11/29/2023).
- [158] Veronika Sunko et al. “Maximal Rashba-like spin splitting via kinetic-energy-coupled inversion-symmetry breaking”. In: *Nature* 549.7673 (Sept. 28, 2017). Publisher: Nature Publishing Group, pp. 492–497. ISSN: 00280836. URL: <https://go.gale.com/ps/i.do?p=AONE&sw=w&issn=00280836&v=2.1&it=r&id=GALE%7CA507194990&sid=googleScholar&linkaccess=abs>.
- [159] J. C. Rojas Sánchez et al. “Spin-to-charge conversion using Rashba coupling at the interface between non-magnetic materials”. In: *Nature Communications* 4.1 (Dec. 17, 2013). Number: 1 Publisher: Nature Publishing Group, p. 2944. ISSN: 2041-1723. DOI: [10.1038/ncomms3944](https://doi.org/10.1038/ncomms3944). URL: <https://www.nature.com/articles/ncomms3944>.
- [160] M. Tanaka et al. “Epitaxial growth of ferromagnetic ultrathin MnGa films with perpendicular magnetization on GaAs”. In: *Applied Physics Letters* 62.13 (Mar. 29, 1993). Publisher: American Institute of Physics, pp. 1565–1567. ISSN: 0003-6951. DOI: [10.1063/1.108642](https://doi.org/10.1063/1.108642). URL: <https://aip.scitation.org/doi/10.1063/1.108642> (visited on 04/26/2021).
- [161] Masaaki Tanaka. “Epitaxial ferromagnetic thin films and superlattices of Mn-based metallic compounds on GaAs”. In: *Materials Science and Engineering: B. Proceedings of the 5th NEC Symposium on Fundamental Approaches to New Material Phases: Spin-Dependent Phenomena in Multilayer Systems* 31.1 (Apr. 1, 1995), pp. 117–125. ISSN: 0921-5107. DOI: [10.1016/0921-5107\(94\)08013-5](https://doi.org/10.1016/0921-5107(94)08013-5). URL: <https://www.sciencedirect.com/science/article/pii/0921510794080135>.
- [162] Shuang Tang and Mildred S. Dresselhaus. “Electronic properties of nano-structured bismuth-antimony materials”. In: *Journal of Materials Chemistry C* 2.24 (May 30, 2014). Publisher: The Royal Society of Chemistry, pp. 4710–4726. ISSN: 2050-7534. DOI: [10.1039/C4TC00146J](https://doi.org/10.1039/C4TC00146J). URL: <https://pubs.rsc.org/en/content/articlelanding/2014/tc/c4tc00146j>.

- [163] D. J. Thouless et al. “Quantized Hall Conductance in a Two-Dimensional Periodic Potential”. In: *Physical Review Letters* 49.6 (Aug. 9, 1982). Publisher: American Physical Society, pp. 405–408. DOI: [10.1103/PhysRevLett.49.405](https://doi.org/10.1103/PhysRevLett.49.405). URL: <https://link.aps.org/doi/10.1103/PhysRevLett.49.405>.
- [164] Jacob Torrejon et al. “Interface control of the magnetic chirality in CoFeB/MgO heterostructures with heavy-metal underlayers”. In: *Nature Communications* 5.1 (Aug. 18, 2014). Number: 1 Publisher: Nature Publishing Group, p. 4655. ISSN: 2041-1723. DOI: [10.1038/ncomms5655](https://doi.org/10.1038/ncomms5655). URL: <https://www.nature.com/articles/ncomms5655>.
- [165] M. Tsoi et al. “Excitation of a Magnetic Multilayer by an Electric Current”. In: *Physical Review Letters* 80.19 (May 11, 1998). Publisher: American Physical Society, pp. 4281–4284. DOI: [10.1103/PhysRevLett.80.4281](https://doi.org/10.1103/PhysRevLett.80.4281). URL: <https://link.aps.org/doi/10.1103/PhysRevLett.80.4281>.
- [166] A. A. Tulapurkar et al. “Spin-torque diode effect in magnetic tunnel junctions”. In: *Nature* 438.7066 (Nov. 2005). Number: 7066 Publisher: Nature Publishing Group, pp. 339–342. ISSN: 1476-4687. DOI: [10.1038/nature04207](https://doi.org/10.1038/nature04207). URL: <https://www.nature.com/articles/nature04207>.
- [167] Yugo Ueda et al. “Epitaxial growth and characterization of Bi<sub>1-x</sub>Sb<sub>x</sub> spin Hall thin films on GaAs(111)A substrates”. In: *Applied Physics Letters* 110.6 (Feb. 6, 2017). Publisher: American Institute of Physics, p. 062401. ISSN: 0003-6951. DOI: [10.1063/1.4975492](https://doi.org/10.1063/1.4975492). URL: <https://aip.scitation.org/doi/10.1063/1.4975492>.
- [168] T. Valet and A. Fert. “Theory of the perpendicular magnetoresistance in magnetic multilayers”. In: *Physical Review B* 48.10 (Sept. 1, 1993). Publisher: American Physical Society, pp. 7099–7113. DOI: [10.1103/PhysRevB.48.7099](https://doi.org/10.1103/PhysRevB.48.7099). URL: <https://link.aps.org/doi/10.1103/PhysRevB.48.7099>.
- [169] W. Van Roy et al. “Epitaxial MnGa/(Mn,Ga,As)/MnGa trilayers: Growth and magnetic properties”. In: *Applied Physics Letters* 69.5 (July 29, 1996), pp. 711–713. ISSN: 0003-6951. DOI: [10.1063/1.117815](https://doi.org/10.1063/1.117815). URL: <https://doi.org/10.1063/1.117815>.
- [170] F. T. Vas’ko. “Spin splitting in the spectrum of two-dimensional electrons due to the surface potential”. In: *ZhETF Pisma Redaktsiiu* 30 (Nov. 1, 1979). ADS Bibcode: 1979ZhPmR..30..574V, p. 574. URL: <https://ui.adsabs.harvard.edu/abs/1979ZhPmR..30..574V>.
- [171] Hong Wang et al. “Crystallographic structure and defects in epitaxial bismuth films grown on mica”. In: *Journal of Crystal Growth* 130.3 (June 1, 1993), pp. 571–577. ISSN: 0022-0248. DOI: [10.1016/0022-0248\(93\)90546-9](https://doi.org/10.1016/0022-0248(93)90546-9). URL: <https://www.sciencedirect.com/science/article/pii/0022024893905469>.
- [172] Yi Wang et al. “Magnetization switching by magnon-mediated spin torque through an antiferromagnetic insulator”. In: *Science (New York, N.Y.)* 366.6469 (Nov. 29, 2019), pp. 1125–1128. ISSN: 1095-9203. DOI: [10.1126/science.aav8076](https://doi.org/10.1126/science.aav8076).
- [173] Yi Wang et al. “Room-Temperature Giant Charge-to-Spin Conversion at the SrTiO<sub>3</sub>-LaAlO<sub>3</sub> Oxide Interface”. In: *Nano Letters* 17.12 (Dec. 13, 2017), pp. 7659–7664. ISSN: 1530-6992. DOI: [10.1021/acs.nanolett.7b03714](https://doi.org/10.1021/acs.nanolett.7b03714).

- [174] Yi Wang et al. “Topological Surface States Originated Spin-Orbit Torques in  $\text{Bi}_2\text{Se}_3$ ”. In: *Physical Review Letters* 114.25 (June 24, 2015), p. 257202. ISSN: 0031-9007, 1079-7114. DOI: [10.1103/PhysRevLett.114.257202](https://doi.org/10.1103/PhysRevLett.114.257202). URL: <https://link.aps.org/doi/10.1103/PhysRevLett.114.257202>.
- [175] Xiao-Gang Wen. “Topological orders and edge excitations in fractional quantum Hall states”. In: *Advances in Physics* 44.5 (Oct. 1, 1995). Publisher: Taylor & Francis eprint: <https://doi.org/10.1080/00018739500101566>, pp. 405–473. ISSN: 0001-8732. DOI: [10.1080/00018739500101566](https://doi.org/10.1080/00018739500101566). URL: <https://doi.org/10.1080/00018739500101566>.
- [176] Roger Wood. “Exact Solution for a Stoner–Wohlfarth Particle in an Applied Field and a New Approximation for the Energy Barrier”. In: *IEEE Transactions on Magnetics* 45.1 (Jan. 2009). Conference Name: IEEE Transactions on Magnetics, pp. 100–103. ISSN: 1941-0069. DOI: [10.1109/TMAG.2008.2006286](https://doi.org/10.1109/TMAG.2008.2006286). URL: <https://ieeexplore.ieee.org/document/4773629>.
- [177] Feng Wu et al. “Epitaxial  $\text{Mn}_2.5\text{Ga}$  thin films with giant perpendicular magnetic anisotropy for spintronic devices”. In: *Applied Physics Letters* 94.12 (Mar. 23, 2009). Publisher: American Institute of Physics, p. 122503. ISSN: 0003-6951. DOI: [10.1063/1.3108085](https://doi.org/10.1063/1.3108085). URL: <https://aip-scitation-org.proxy.scd.u-psud.fr/doi/10.1063/1.3108085>.
- [178] Yang Wu et al. “High-Performance THz Emitters Based on Ferromagnetic/ Non-magnetic Heterostructures”. In: *Advanced Materials* 29.4 (2017), p. 1603031. ISSN: 1521-4095. DOI: [10.1002/adma.201603031](https://doi.org/10.1002/adma.201603031). URL: <https://onlinelibrary.wiley.com/doi/abs/10.1002/adma.201603031>.
- [179] Y. Xia et al. “Observation of a large-gap topological-insulator class with a single Dirac cone on the surface”. In: *Nature Physics* 5.6 (June 2009). Number: 6 Publisher: Nature Publishing Group, pp. 398–402. ISSN: 1745-2481. DOI: [10.1038/nphys1274](https://doi.org/10.1038/nphys1274). URL: <https://www.nature.com/articles/nphys1274>.
- [180] Kenichiro Yao, Nguyen Huynh Duy Khang, and Pham Nam Hai. “Influence of crystal orientation and surface termination on the growth of  $\text{BiSb}$  thin films on  $\text{GaAs}$  substrates”. In: *Journal of Crystal Growth* 511 (Apr. 1, 2019), pp. 99–105. ISSN: 0022-0248. DOI: [10.1016/j.jcrysgro.2019.01.041](https://doi.org/10.1016/j.jcrysgro.2019.01.041). URL: <http://www.sciencedirect.com/science/article/pii/S002202481930065X>.
- [181] Guoqiang Yu et al. “Switching of perpendicular magnetization by spin-orbit torques in the absence of external magnetic fields”. In: *Nature Nanotechnology* 9.7 (July 2014), pp. 548–554. ISSN: 1748-3395. DOI: [10.1038/nnano.2014.94](https://doi.org/10.1038/nnano.2014.94).
- [182] Shinji Yuasa et al. “Giant room-temperature magnetoresistance in single-crystal  $\text{Fe/MgO/Fe}$  magnetic tunnel junctions”. In: *Nature Materials* 3 (Dec. 1, 2004). ADS Bibcode: 2004NatMa...3..868Y, pp. 868–871. ISSN: 1476-1122. DOI: [10.1038/nmat1257](https://doi.org/10.1038/nmat1257). URL: <https://ui.adsabs.harvard.edu/abs/2004NatMa...3..868Y> (visited on 11/21/2023).
- [183] Jia Zhang et al. “Band structure and spin texture of  $\text{Bi}_2\text{Se}_3$  3d ferromagnetic metal interface”. In: *Physical Review B* 94.1 (July 27, 2016). Publisher: American Physical Society, p. 014435. DOI: [10.1103/PhysRevB.94.014435](https://doi.org/10.1103/PhysRevB.94.014435). URL: <https://link.aps.org/doi/10.1103/PhysRevB.94.014435>.

- [184] S. Zhang and A. Fert. “Conversion between spin and charge currents with topological insulators”. In: *Physical Review B* 94.18 (Nov. 18, 2016). Publisher: American Physical Society, p. 184423. DOI: [10.1103/PhysRevB.94.184423](https://doi.org/10.1103/PhysRevB.94.184423), URL: <https://link.aps.org/doi/10.1103/PhysRevB.94.184423>.
- [185] Wei Zhang et al. “Determination of the Pt spin diffusion length by spin-pumping and spin Hall effect”. In: *Applied Physics Letters* 103.24 (Dec. 12, 2013), p. 242414. ISSN: 0003-6951. DOI: [10.1063/1.4848102](https://doi.org/10.1063/1.4848102). URL: <https://doi.org/10.1063/1.4848102>.
- [186] Weifeng Zhang et al. “Role of transparency of platinum-ferromagnet interface in determining intrinsic magnitude of spin Hall effect”. In: *Nature Physics* 11.6 (June 2015), pp. 496–502. ISSN: 1745-2473, 1745-2481. DOI: [10.1038/nphys3304](https://doi.org/10.1038/nphys3304), arXiv: [1504.07929\[cond-mat\]](https://arxiv.org/abs/1504.07929), URL: <http://arxiv.org/abs/1504.07929>.
- [187] Siqian Zhao and Takao Suzuki. “Magnetic and structural properties of Mn-Ga thin films”. In: *AIP Advances* 6.5 (Mar. 17, 2016). Publisher: American Institute of Physics, p. 056025. DOI: [10.1063/1.4944655](https://doi.org/10.1063/1.4944655). URL: <https://aip.scitation.org/doi/full/10.1063/1.4944655>.
- [188] C. Zhou et al. “Broadband Terahertz Generation via the Interface Inverse Rashba-Edelstein Effect”. In: *Physical Review Letters* 121.8 (Aug. 20, 2018). Publisher: American Physical Society, p. 086801. DOI: [10.1103/PhysRevLett.121.086801](https://doi.org/10.1103/PhysRevLett.121.086801), URL: <https://link.aps.org/doi/10.1103/PhysRevLett.121.086801>.
- [189] L. J. Zhu et al. “Tailoring magnetism of multifunctional Mn<sub>x</sub>Ga films with giant perpendicular anisotropy”. In: *Applied Physics Letters* 102.13 (Apr. 1, 2013). Publisher: American Institute of Physics, p. 132403. ISSN: 0003-6951. DOI: [10.1063/1.4799344](https://doi.org/10.1063/1.4799344). URL: <https://aip.scitation.org/doi/10.1063/1.4799344>.
- [190] Lijun Zhu et al. “Multifunctional L1<sub>0</sub>-Mn<sub>1.5</sub>Ga Films with Ultrahigh Coercivity, Giant Perpendicular Magnetocrystalline Anisotropy and Large Magnetic Energy Product”. In: *Advanced Materials* 24.33 (2012), pp. 4547–4551. ISSN: 1521-4095. DOI: [10.1002/adma.201200805](https://doi.org/10.1002/adma.201200805), URL: <https://onlinelibrary.wiley.com/doi/abs/10.1002/adma.201200805>.

# Appendix: Experimental structural characterization techniques used in this work

## Reflection high-energy electron diffraction (RHEED)

RHEED is a powerful surface-sensitive technique primarily probing the top few atomic layers of the crystal lattice. It is widely used in-situ in thin film growth processes. It provides real-time information about the growth and quality of thin films by analyzing the diffraction patterns of high-energy electrons reflected off a crystalline surface. It also can be used to determine lattice parameters of the material and the epitaxial relation with the substrate.

It is based on the principle of electron diffraction, utilizing high-energy electrons emitted from a tungsten filament (typically in the range of 10-100 keV) directed at a surface sample under UHV conditions at grazing incident angles. As electrons interact with the crystal lattice, they undergo diffraction, resulting in a diffraction pattern on a fluorescent screen, as shown in Figure 5.13

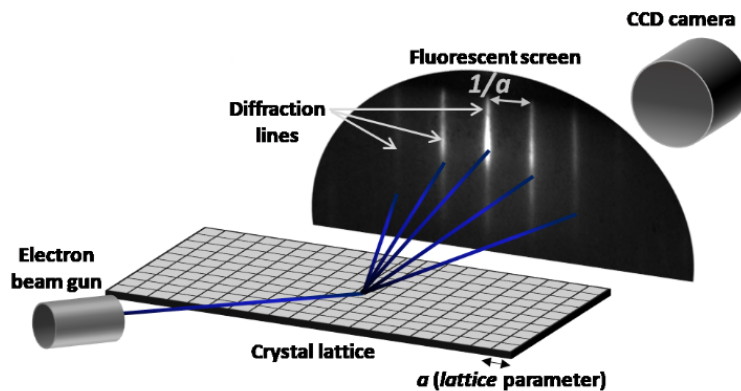


Figure 5.13: Schematic illustration of the working principle of the RHEED technique. High-energy electrons emitted from a tungsten filament are directed at a surface sample at grazing incident angles. As electrons interact with the crystal lattice, they undergo diffraction, resulting in a diffraction pattern on a fluorescent screen.

The intersection of the Ewald sphere with a reciprocal lattice of a crystalline surface, which is a lattice of regular rods, results in a streaky pattern. An array of dots evenly

distributed on rings is an indicator of a perfectly smooth surface. Broad streak pattern result from a lattice with defects or strain. Spotty and streaky pattern suggests a rough surface, while concentric rings pattern suggests a polycrystalline thin film. An amorphous sample results in a diffuse pattern. As a result, RHEED patterns served us as initial indicators of the quality of the surfaces of the growing thin layers.

### Atomic force microscopy (AFM)

AFM is a characterization technique used to provide information about the topography of a sample. The key principle behind AFM is the use of a flexible cantilever with a sharp tip attached to its free end. The cantilever is typically made of silicon, which acts as a mechanical spring. As the tip interacts with the sample surface, the forces between them cause deflection in the cantilever. This deflection can be recorded using the laser beam reflection by the cantilever on a four-sectional photodiode detector, as illustrated in Figure 5.14

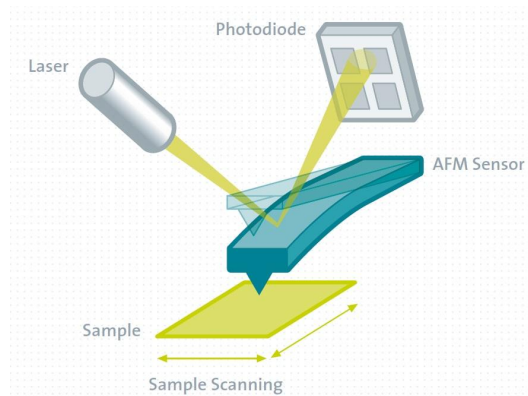


Figure 5.14: Schematic illustration of the working principle of the AFM technique. A flexible cantilever with a sharp tip acts as a mechanical spring. As the tip interacts with the sample surface, the forces between them cause deflection in the cantilever. This deflection can be recorded by a photodiode detector giving information about the topography of the sample.

AFM can operate in various modes, including contact mode, tapping mode, and non-contact mode, depending on the specific requirements due to different materials. Each mode utilizes different techniques to maintain a suitable interaction force between the tip and the sample.

### (Scanning) transmission electron microscopy ((S)TEM)

(S)TEM is a powerful tool to explore the structural quality of thin layers. Its working principle is based on the interaction of a beam of electrons with a thin sample, which allows for high-resolution imaging and analysis of its structure at the atomic scale.

In TEM, the entire transmitted electron beam passes through the sample, and the resulting image is formed based on the intensity and phase changes of the transmitted electrons. In STEM, a focused electron beam is scanned across the sample, and the transmitted electrons are collected using a detector. The image is formed by analyzing the variations in transmitted electron intensity.

In this work we used STEM to characterize our samples.

A beam of electrons is emitted from a heated filament or a field emission gun. It is then accelerated by a high voltage and focused using electromagnetic lenses into a thin sample.

As the electron beam passes through the sample, it interacts with the atoms and electrons within the material. These interactions include elastic scattering, inelastic scattering, and absorption of electrons by the sample. The transmitted electrons are then collected by a fluorescent screen or a digital camera, which records the intensity and spatial distribution of the transmitted electrons.

(S)TEM can operate in various imaging modes, including bright-field (BF) imaging, high annular dark-field (HAADF) imaging, and energy dispersive X-ray (EDX) spectroscopy.

In BF mode, the objective lens collects the transmitted electrons, and an image is formed by variations in electron intensity, resulting from the differences in electron absorption or scattering within the sample. Regions with higher electron density appear darker, while less dense regions appear brighter.

In HAADF mode, an annular detector is positioned above the sample, collecting electrons scattered at high angles. Heavier elements scatter electrons more effectively, leading to higher (brighter) intensity in the image.

EDX provides information about the elemental composition of a sample. A high-energy electron beam is focused onto a sample and interactions occur between the electrons and the atoms in the sample. The core electrons may be ejected. Electrons from higher energy levels then fill these vacancies, emitting X-rays that are detected. The detected X-rays produce a spectrum, where peaks correspond to the characteristic X-ray energies of specific elements. The intensity of each peak is proportional to the amount of the corresponding element in the sample.

The working principle of STEM is illustrated in Figure 5.15.

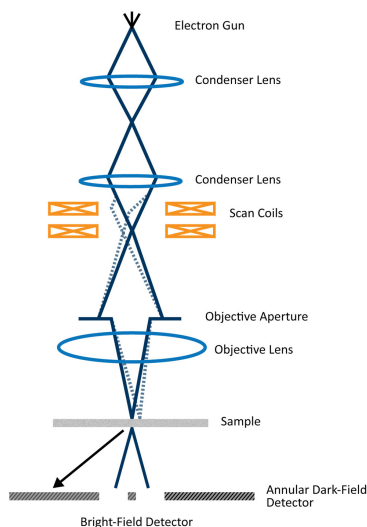


Figure 5.15: Schematic illustration of the working principle of the STEM technique. A focused electron beam is scanned across the sample, and the transmitted electrons are collected using a detector. The image is formed by analyzing the variations in transmitted electron intensity.

### X-ray diffraction (XRD)

XRD is a versatile technique used for characterizing the crystal structure of materials. It allows to identify crystalline phases, determine lattice parameters, and analyze the quality of materials.

A coherent monochromatic X-ray beam is directed towards a crystalline sample and interacts with the electrons in the crystal. The excited core electrons relax and emit the X-ray beam that is detected, in our case, by a non-monochromatic detector. The diffraction peaks position allows us to identify the material phase.

The relationship between the angle of incidence  $\theta$ , the wavelength of the X-rays  $\lambda$ , and the interplane distance  $d_{hkl}$  is described by Bragg's Law:

$$n\lambda = 2d_{hkl} \sin(\theta) \quad (5.20)$$

where  $n$  is a positive integer.

In this work, we used two configurations of XRD: out-of plane  $\theta - 2\theta$  XRD and in-plane grazing incidence XRD (GIXRD). Out-of plane  $\theta - 2\theta$  XRD allows to identify the out-of-plane crystalline phases, evaluate crystalline quality, and estimate lattice parameters. GIXRD provides information about in-plane crystalline phases and lattice parameter.

Typically, for out-of-plane XRD measurements, the Bragg-Brentano ( $\theta - 2\theta$ ) geometry is employed, as illustrated in Figure 5.16(a). The incident angle  $\omega$  defines the angle between the X-ray source and the plane of the sample, while  $2\theta$  represents the diffraction angle, indicating the angle between the incident beam and the detector. In the Bragg-Brentano configuration, the diffraction vector  $\mathbf{s}$  is always normal to the surface of the sample. This setting allows for the detection of diffraction peaks from lattice planes parallel to the surface, with their normal collinear with the surface normal.

In the GIXRD configuration (see Figure 5.16(b)), the incident X-ray beam strikes the sample at a very low angle  $\alpha$ , typically  $\alpha < 1^\circ$ . This allows the beam to travel along the sample surface, significantly reducing the X-ray penetration depth. The incident beam then undergoes diffraction from lattice planes perpendicular to the sample surface.

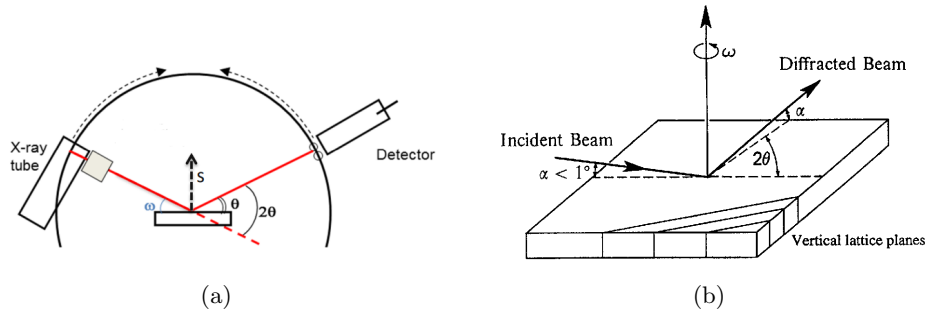


Figure 5.16: (a) Bragg-Brentano geometry: The incident angle  $\omega$  is the angle between the X-ray source and the plane of the sample.  $2\theta$  is the diffraction angle that defines the angle between the incident beam and the detector. In this configuration the diffraction vector  $\mathbf{s}$  is always normal to the sample surface. (b) GIXRD configuration: the incident X-ray beam strikes the sample at a very low angle  $\alpha$ . This allows the beam to travel along the sample surface and to experience diffraction from lattice planes perpendicular to the sample surface.

### Alternating gradient field magnetometry (AGFM)

AGFM is a technique used to measure the magnetic properties of materials. It operates based on the principles of alternating magnetic fields and the interaction between the material's magnetic moments and the applied field.

The sample, mounted on a probe, is placed between two electromagnetic coils, so that it is exposed to a uniform applied magnetic field generated by coils, as illustrated in Figure 5.17. Simultaneously, it encounters an alternating magnetic field produced by another set of gradient coils. This interaction results in a force acting on the magnetic moments of the sample, influenced by both the magnetic properties of the sample and the gradient of the magnetic field. The magnetic moments align with the alternating magnetic field and undergo oscillations. The amplitude of these oscillations, directly proportional to the magnetic moment of the sample, can be detected by a displacement sensor, such as a capacitive or fiber-optic sensor.

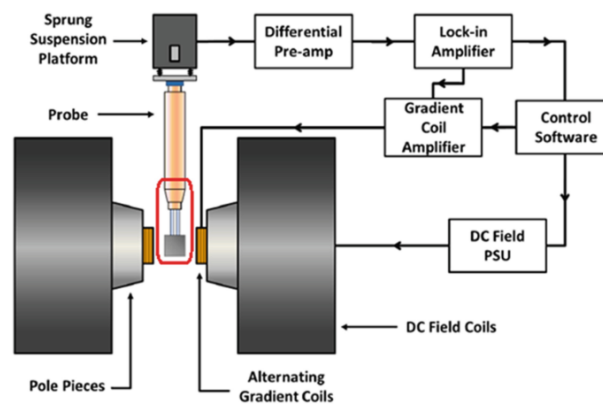


Figure 5.17: Schematic illustration of the working principle of the AGFM technique.

#### Direct current superconducting quantum interference device (DC-SQUID)

DC-SQUID is a highly sensitive magnetometer that used to exploit magnetic properties of materials. SQUID operates at cryogenic temperatures, typically close to absolute zero.

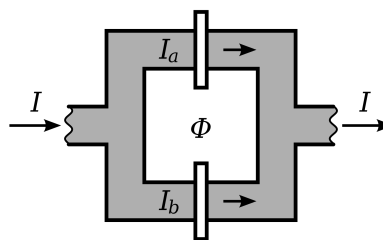


Figure 5.18: Schematic representation of a DC-SQUID device. The current  $I$  splits into the two paths with currents  $I_a$  and  $I_b$ . The barriers in each path are Josephson junctions.  $\Phi$  is the magnetic flux going through the superconducting loop.

The core component of a SQUID device is the two Josephson junctions in parallel creating a closed superconducting loop. According to the DC Josephson effect [4], the induced by splitting current phase difference (cf. Figure 5.18), a Josephson phase, is quantized and directly proportional to the magnetic flux. This quantization allows SQUID to measure extremely small changes in magnetic flux with high precision.

The sample is placed in a uniform magnetic field where it acquires magnetization. The sample is vertically moved. The change in magnetic flux generated by this movement induces an electric current in a superconducting circuit. This current is converted by a SQUID sensor into an electrical signal proportional to the magnetization of the sample.